

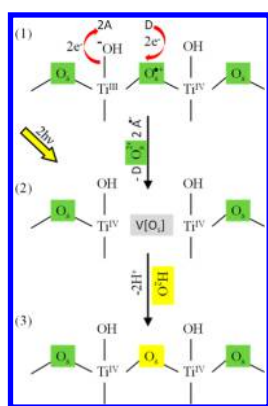
Understanding TiO₂ Photocatalysis: Mechanisms and Materials

Jenny Schneider,^{*,†} Masaya Matsuoka,[‡] Masato Takeuchi,[‡] Jinlong Zhang,[§] Yu Horiuchi,[‡] Masakazu Anpo,[‡] and Detlef W. Bahnemann^{*,†}

[†]Institut für Technische Chemie, Leibniz Universität Hannover, Callinstrasse 3, D-30167 Hannover, Germany

[‡]Faculty of Engineering, Osaka Prefecture University, 1 Gakuen-cho, Sakai Osaka 599-8531, Japan

[§]Key Lab for Advanced Materials and Institute of Fine Chemicals, East China University of Science and Technology, Shanghai 200237, China



CONTENTS

1. Introduction	9920
2. Progress in TiO ₂ Photocatalysis: A Short Historical Overview	9920
3. Time-Resolved Analysis of the Photocatalytic Process: From Femto- to Microseconds	9922
3.1. Dark Processes in TiO ₂	9922
3.2. Photoinduced Charge Carrier Generation and Fate	9924
3.2.1. Charge Carrier Recombination	9925
3.2.2. Hole Trapping	9926
3.2.3. Electron Trapping	9927
3.3. Photoinduced Electron Transfer at the TiO ₂ Surface	9930
3.3.1. Photoinduced Reduction Reactions at the TiO ₂ Surface	9931
3.3.2. Photoinduced Oxidation Reactions at the TiO ₂ Surface	9932
4. Novel Mechanistic Aspects of TiO ₂ Photocatalysis	9935
5. Synthesis of TiO ₂ Nanoparticles and Nanoparticle Structures	9938
6. Preparation and Properties of Doped TiO ₂ Photocatalysts	9943
6.1. Preparation of Visible Light-Responsive TiO ₂ Photocatalysts by Chemical Doping	9943
6.1.1. Metal Ion Doping	9945
6.1.2. Nonmetal Ion Doping	9948
6.1.3. Codoping of TiO ₂	9949
6.2. Preparation of Visible Light-Responsive TiO ₂ Photocatalysts by Doping Using Physical Methods	9951
6.2.1. Transition Metal Ion-Implantation	9951
6.2.2. Anion-Implantation	9954

6.3. Preparation of Visible Light-Responsive TiO ₂ Photocatalysts by Other Doping Methods: Plasmon Enhanced Photocatalysis and Metal Organic Frameworks (MOF)	9955
6.3.1. Plasmon Enhanced Photocatalysis with TiO ₂	9955
6.3.2. Metal Organic Frameworks (MOF)	9957
7. Titanium-Based Single-Site Photocatalysts	9958
7.1. Local Structure of a Single-Site Photocatalyst	9959
7.2. Decomposition of Harmful Organic Compounds	9960
7.3. Decomposition of NO	9961
7.4. Photocatalytic Reduction of CO ₂ with H ₂ O	9962
7.5. Other Single-Site Photocatalysts with Different Metal Centers	9964
7.6. Surface Functionality of Single-Site Photocatalyst Thin Films	9964
7.7. Platform for the Formation of Fine Metal Nanoparticles	9965
8. Applications of Visible Light-Responsive TiO ₂ Thin Films: Solar Water Splitting, Solar Cells, and Photofuel Cells	9967
8.1. Visible Light-Responsive TiO ₂ Photocatalyst Thin Films	9967
8.2. Evolution of H ₂ and O ₂ by Visible Light-Induced Water Splitting	9968
8.3. Design of Solid Thin Film Solar Cell without Use of Any Dye Sensitization	9969
8.4. Photofuel Cells Based on Vis-TiO ₂	9970
9. Photoinduced Surface Wettability Changes	9971
9.1. Introduction	9971
9.2. Preparation of TiO ₂ and TiO ₂ -Based Binary Oxide Films by the Ionized Cluster Beam (ICB) Deposition Method	9971
9.3. Photoinduced Surface Wettability of TiO ₂ -Based Binary Oxide Thin Films	9972
9.4. Proposed Mechanism of Photoinduced Wettability Changes on TiO ₂ Photocatalyst Surfaces	9972
9.4.1. Effect of UV Irradiation on the Microstructure of H ₂ O Clusters Adsorbed on the TiO ₂ Surface	9973

Special Issue: 2014 Titanium Dioxide Nanomaterials

Received: April 3, 2014

Published: September 19, 2014

9.4.2. Photocatalytic Reactivity versus Wettability Control of TiO ₂ Surfaces	9975
9.4.3. Mechanism of the Wettability Control on TiO ₂ Surfaces	9976
10. Conclusions	9976
Author Information	9976
Corresponding Authors	9976
Notes	9976
Biographies	9977
Acknowledgments	9978
References	9978

1. INTRODUCTION

Environmental pollution and destruction as well as the lack of sufficient clean and natural energy resources are some of the most serious problems presently faced on a global scale. The increase in world population and the rampant unregulated industrial growth have all led to accelerated energy consumption, while the unabated release of toxic agents and industrial waste into the air and waterways has resulted in pollution-related diseases, global warming, and abnormal climatic changes. In addition, the earthquake-tsunami disaster of March 11, 2011, which crippled the nuclear reactors in Fukushima, Japan, has raised serious concerns over the supply of electrical power and environmental pollution due to nuclear waste and coolants polluted with radioactive materials. It should therefore be our goal to contribute to the development of environmentally harmonious, ecologically clean and safe, sustainable, and energy-efficient chemical technologies, the most urgent challenges scientists are facing today.

Photocatalysis, in which the inexhaustibly abundant, clean, and safe energy of the sun can be harnessed for sustainable, nonhazardous, and economically viable technologies, is a major advance in this direction. Titanium–oxide materials in different types and forms have shown great potential as ideal and powerful photocatalysts for various significant reactions due to their chemical stability, nontoxicity, and high reactivity. Investigations of well-defined photocatalytic reaction systems and of their detailed reaction mechanisms and kinetics using a number of molecular spectroscopies have led to the development of various Ti–oxide-based photocatalytic materials. In particular, photocatalysts have been employed for such significant applications as the purification of polluted water and air, self-cleaning glasses, tiles, and tents coated with Ti–oxide materials with unique photoinduced superhydrophilicity, and bone-implant fixation using photofunctionalized titanium enabling more rapid and complete bone-titanium integration, just to name a few. Investigations have also been carried out into the development of visible light-responsive Ti–oxide photocatalysts by adding small amounts of components such as cations and metal oxides by both chemical doping and physical ion-implantation methods. Moreover, it has also been possible to prepare Ti–oxide photocatalysts, enabling the absorption of light not only in the ultraviolet but also in the visible light wavelength region to operate effectively under natural sunlight irradiation.

The decomposition of H₂O for the separate evolution of pure H₂ and O₂ is also being developed using visible light-responsive titanium oxide thin film photocatalysts under sunlight irradiation. It has, moreover, been reported that Ti–oxide single site photocatalysts constructed within zeolite frameworks can induce the reduction of CO₂ with H₂O to form hydrocarbons and O₂. At present, scientists are investigating how to raise the efficiency and

selectivity of these photocatalytic reactions. It is the aim of this Review to summarize the progress of the research carried out into Ti–oxide-based photocatalysts, including our own research, to gain insights into the future development of photocatalysis and into the use of solar energy for environmental remediation and other useful systems and processes.

2. PROGRESS IN TiO₂ PHOTOCATALYSIS: A SHORT HISTORICAL OVERVIEW

The important breakthroughs in the research on TiO₂ photocatalysis that have led to many practical applications are summarized below. As early as in the 1960s, many research groups studied the photoinduced phenomena proceeding on semiconducting solids such as TiO₂ and ZnO under UV light irradiation. It was found that some molecules such as O₂ and H₂O are adsorbed on or desorbed from the solid semiconductor surfaces under UV illumination depending on the respective surface conditions. These phenomena have been explained and are now well understood by the band theory of semiconductors.^{1–4} S. Kato and F. Masuo reported in 1964 (in the journal *Kogyo Kagaku Zasshi*) the oxidation reaction of tetralin in the liquid phase using UV-illuminated TiO₂ as photocatalyst.⁵ This paper can perhaps be considered as one of the first articles to report a photocatalytic reaction on TiO₂ under UV irradiation. Subsequently, many researchers such as Steinbach,⁶ Teichner,⁷ Tanaka,⁸ Yoneyama,⁹ and others^{10,11} have reported various reactions in the gas phase employing UV-illuminated semiconducting TiO₂ as catalysts.

In 1972, K. Honda and A. Fujishima discovered the photosensitization effect of a TiO₂ electrode for the electrolysis of H₂O into H₂ and O₂ using a Pt metal electrode as cathode and a TiO₂ photoanode irradiated with UV light. They found that, under UV light irradiation of the TiO₂ electrode, the electrolysis of H₂O proceeded at a much lower bias voltage as compared to normal electrolysis.¹² In 1977, G. N. Schrauzer and T. D. Guth reported the photocatalytic decomposition of H₂O on powdered TiO₂ photocatalysts loaded with small amounts of Pt or Rh metal particles.¹³ This led to the development of the mechanistic picture that, on such Pt/TiO₂ catalysts, the electrons photoformed in TiO₂ move to the Pt metal site where they induce reduction reactions, while photoformed holes remain in the TiO₂ particle and migrate to its surface where they induce oxidation reactions.^{14,15} Thus, the charge separation of electrons and holes is without doubt the most important process in photocatalysis employing semiconducting materials, that is, the so-called photoelectrochemical mechanism.¹⁶ Since the pioneering works by Honda/Fujishima and Schrauzer/Guth, photocatalysis employing various semiconductors has been the focus of intense investigations by a number of researchers.^{17–41} Considerable efforts have been devoted to the design of photocatalytic systems exhibiting a high conversion efficiency of light into chemical energy such as the decomposition of H₂O into H₂ and O₂^{14–22} as well as related reactions.^{23,24} Some research groups have focused on colloidal semiconductors, extremely small-sized particles in which quantization effects are expected,^{25–37} as well as on semiconductors incorporated on inert supports such as porous glass and zeolites.^{38–42} Various binary oxide catalysts have also been shown to be promising photocatalysts.^{43–45}

Although it has been established that surface ions in low coordination play a significant role in heterogeneous catalysis, their exact role is still unclear in photocatalysis. To investigate the mechanisms driving these reactions, chemical treatment to functionalize the surface can be used to control the degree of

coordinative unsaturation of the surface ions. Focusing on this issue, Anpo et al. reported in a series of ground-breaking papers that with Ti–oxide single sites anchored onto porous Vycor glass, unique photocatalytic reactions that are not observed with bulk semiconducting TiO_2 can take place with a high efficiency.^{46–51} This particular and high photocatalytic reactivity of such single site catalysts has been attributed to the high reactivity of the electron–hole pair state of the Ti–oxide single site by investigations employing various molecular spectroscopies such as ESR, photoluminescence, XAFS, and FT-IR.^{46–51} Similar characteristics of oxide single site catalysts have meanwhile been reported for various transition metal oxides such as vanadium,^{52–54} molybdenum,^{55–57} and chromium.⁵⁸ The photocatalytic reactions on such oxide single site catalysts have subsequently been investigated by various research groups, for example, by Anpo, Matsuoka, and Horiuchi et al.^{59–62} and by Yamashita and Mori et al.^{63–65}

The efficiency of photocatalytic processes can be evaluated by the measurement of the photonic efficiency ζ , that is, the rate of the formation of reaction products divided by the incident photon flow,⁶⁶ and is, unfortunately, usually found to be rather small. In fact, time-resolved spectroscopic studies reveal that most of the photogenerated e^-/h^+ pairs ($\sim 90\%$) recombine rapidly after excitation. This is assumed to be one reason for the relatively low ζ -values ($<10\%$) of most semiconductor-based photocatalytic reactions.⁶⁶

Despite these drawbacks, there are already various applications of photocatalytic systems, the number of which is steadily growing worldwide. For example, different water treatment facilities have been realized utilizing (inexpensive) solar photons for the photocatalytic depollution.⁶⁷ For example, Figure 1 shows



Figure 1. View of a pilot plant for the solar photocatalytic treatment of biologically pretreated wastewater installed in Wolfsburg, Germany. Reprinted with permission from ref 67. Copyright 2000 Elsevier.

a pilot plant that has been realized in Germany for the solar photocatalytic treatment of biologically pretreated industrial wastewater with the aim to reuse this water in the production process.⁶⁷

Identifying the factors that govern the kinetics of photocatalytic processes and understanding the role that they play is inherent to achieve the desired goal of developing more efficient systems. Although great strides have been made in the past 25 years, a lot more still remains unknown, making TiO_2 photocatalysis an interesting challenge not only for engineers but also for basic scientists. Figure 2 illustrates one successful

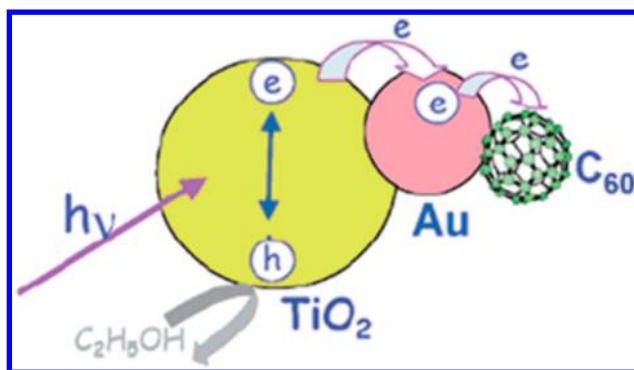


Figure 2. Photoelectron transfer in Au/TiO_2 probed by a $\text{C}_{60}/\text{C}_{60}^-$ couple. Reproduced with permission from ref 68. Copyright 2009 The Royal Society of Chemistry.

experimental approach to quantify the number of charge carriers that can be transferred from an excited photocatalyst (TiO_2) particle via a noble metal nanocontact (Au) to a suitable electron acceptor (C_{60}).⁶⁸

Obviously, even within such a simple system, it is rather difficult to resolve the individual reaction steps, which, however, is a prerequisite for the focused development of highly efficient photocatalytic systems in the future.

Another important aspect that needs to be resolved before photocatalytic systems can be employed on a large scale is the benign character of the employed photocatalysts, that is, the absence of any toxicity or other undesired side effects. As for most applications, it has been found to be essential to utilize photocatalysts with a high surface area; usually particles with diameters considerably smaller than 100 nm are being used. Because the health aspects of the entire class of nanomaterials are currently discussed intensively, it is of utmost importance to also assess the respective toxicological parameters of those nanoparticles fabricated for photocatalytic applications. The results of one of these studies are presented in Figure 3 evincing that the commercial TiO_2 nanoparticles tested here do not exhibit any cytotoxic effect on HEP-G2 liver cells even when applied at very

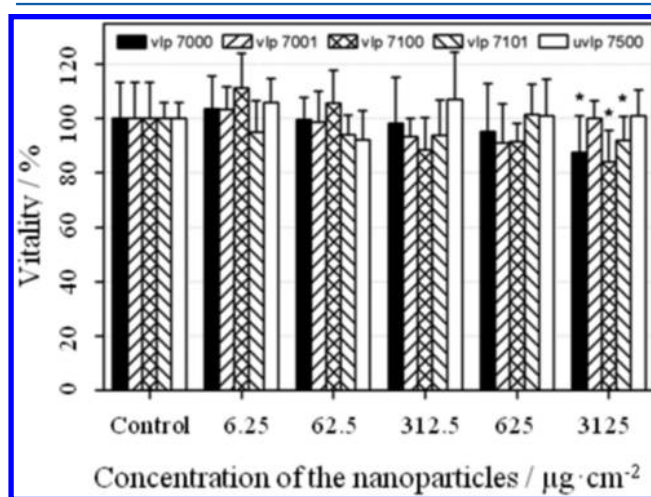


Figure 3. Vitality of HEP-G2 cells after 3 days of incubation in the presence of different commercial TiO_2 nanoparticles (Kronos International Inc., particle diameters $d_{\text{vlp7000}} = 144$ nm, $d_{\text{vlp7001}} = 51.9$ nm, $d_{\text{vlp7100}} = 9.8$ nm, $d_{\text{vlp7101}} = 14.6$ nm, $d_{\text{vlp7500}} = 128.6$ nm) without UV-illumination. Adapted with permission from ref 69. Copyright 2010 John Wiley and Sons Ltd.

high loadings ($>3 \text{ mg/cm}^3$).⁶⁹ Further investigations are currently being carried out, the results of which will be of crucial importance for future applications of photocatalysis.

The field of photocatalysis can be regarded as a very active research area with more than 2000 papers published yearly in peer-reviewed journals and an overwhelming number of review articles aiming to summarize these findings. This Review will focus on some issues of TiO_2 photocatalysis that are, however, often neglected in these summaries, that is, charge carrier transfer kinetics, novel mechanistic aspects, and unusual doping strategies to enhance photocatalytic activities and to broaden the accessible wavelength range.

3. TIME-RESOLVED ANALYSIS OF THE PHOTOCATALYTIC PROCESS: FROM FEMTO- TO MICROSECONDS

The absorption of photons by a semiconductor provokes photocatalytic reactions at its surface, for example, water splitting or the degradation of organic compounds. As compared to other semiconductor photocatalysts, titanium dioxide (TiO_2) has so far been shown to be the most promising material used for both fundamental research and practical applications, because it exhibits a higher photoreactivity (usually up to ζ (photonic efficiency) = 10%) and it is cheap, nontoxic, chemically and biologically inert, and photostable.⁷⁰ Although the detailed mechanism of photocatalysis varies with different pollutants, it is commonly agreed that the primary reactions responsible for the photocatalytic effect are interfacial redox reactions of electrons and holes that are generated when the semiconductor catalyst is exposed to light of sufficient energy^{71–73} (see Figure 4).

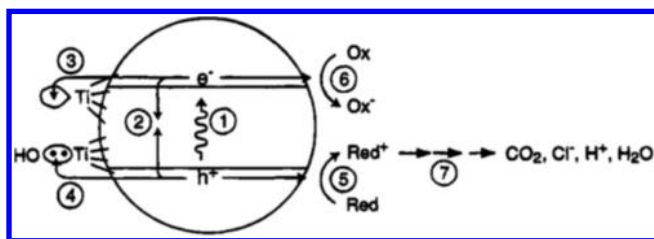


Figure 4. Primary steps in the mechanism of photocatalysis: (1) formation of charge carriers by photon absorption; (2) charge carrier recombination; (3) trapping of a conduction-band electron at a Ti(IV) site to yield Ti(III); (4) trapping of a valence-band hole at a surficial titanol group; (5) initiation of an oxidative pathway by a valence-band hole; (6) initiation of a reductive pathway by a conduction-band electron; and (7) further thermal (e.g., hydrolysis or reactions with active oxygen species) and photocatalytic reactions to yield mineralization products. Adapted with permission from ref 66. Copyright 1995 American Chemical Society.

Fundamental studies concerning the initial and usually very fast photocatalytic processes, induced by the absorption of a photon, the energy of which exceeds the bandgap energy of the photocatalyst, inside and at the surface of the semiconductor, are not carried out very often. The knowledge of these processes is, however, of utmost importance for the understanding of the photocatalytic reaction mechanism and thus for a better design of photocatalytic systems. Figure 5 provides an overview of the possible photoinduced events inside and on the surface of a TiO_2 photocatalyst in the time scale region from femtoseconds to microseconds.

The reaction dynamics of the photogenerated charge carriers in TiO_2 , shown in Figure 5, are usually obtained by means of

time-resolved absorption spectroscopy (TAS), being a widely employed technique to study the formation, relaxation, recombination, and transfer processes of photogenerated charge carriers in photocatalysts. In this technique, the samples are excited by a laser pulse with the absorption of the formed intermediates being detected by time-resolved optical spectroscopy usually in the UV/vis/NIR region employing white light for analysis. While during the past decade the measuring techniques have been improved, and it is, e.g., now possible to measure on the femtosecond time scale, a meaningful interpretation of the observed kinetics or even a chemical assignment of the detected absorption transients has rarely been executed. Hence, in the following section, kinetic and mechanistic studies of TiO_2 -based photocatalysts published previously will be discussed in a comprehensive manner with the aid of the band bending model.

3.1. Dark Processes in TiO_2

Before discussing the processes occurring in TiO_2 under illumination, at first, the situation before UV light exposure needs to be understood. At any interface the electronic bulk structure of the semiconductor will experience considerable interferences due to charge-transfer processes resulting, for example, in band bending phenomena. Even for a clean surface, that is, of a crystalline semiconductor in contact with vacuum, surface states are formed that alter the electronic structure drastically. In general, two types of surface states are distinguished, ionic states (Tamm states) and covalent surface states (Shockley states).⁷⁴ The first type is mostly found in semiconductors with strong ionic interactions, such as CdS or ZnS. In these materials, the heteronuclear splitting of the bonds, that is, the formation of strongly polarized bonds, leads to the formation of such surface states, which are located close to the band edges, and thus no band bending appears. The Shockley states are mainly distributed at the surfaces of covalently bound semiconductors, such as Ge and Si, and can be described as dangling bonds. These surface states introduce additional energy levels in the middle of the bandgap. To achieve electronic equilibrium between the surface and the bulk, a positively charged space charged layer is formed just beneath the surface of an n-type semiconductor because some of the midbandgap electrons are transferred to its surface states.⁷⁵ Accordingly, the energy distance between the Fermi level and the conduction band increases at the surface, leading to a corresponding band bending.

For TiO_2 with a stoichiometric (clean) surface, flat bands have been found from photoemission experiments.⁷⁶ Usually, however, in n-type TiO_2 , as it is often used in photocatalytic systems, the surface contains a lot of defects, with the most common being oxygen vacancies O_v . Such surface defects can be understood as unpaired electrons, which were located initially in an O 2p orbital and were then transferred, by the removal of the corresponding oxygen atom, into the conduction band formed by Ti 3d orbitals.^{77,78} Diebold⁷⁹ concluded from a detailed analysis of this electronic situation that these extra electrons in the vacancies act as donor-like states, thus creating an accumulation layer in the near-surface region that results in a downward band bending as shown in Figure 6. It is, however, important to realize that the sign of this effect strongly depends on details of the surface composition. Hence, for more realistic cases, for example, including the adsorption of different molecules at the electron-rich surface, the band bending may even be reverted. These energetic considerations are very

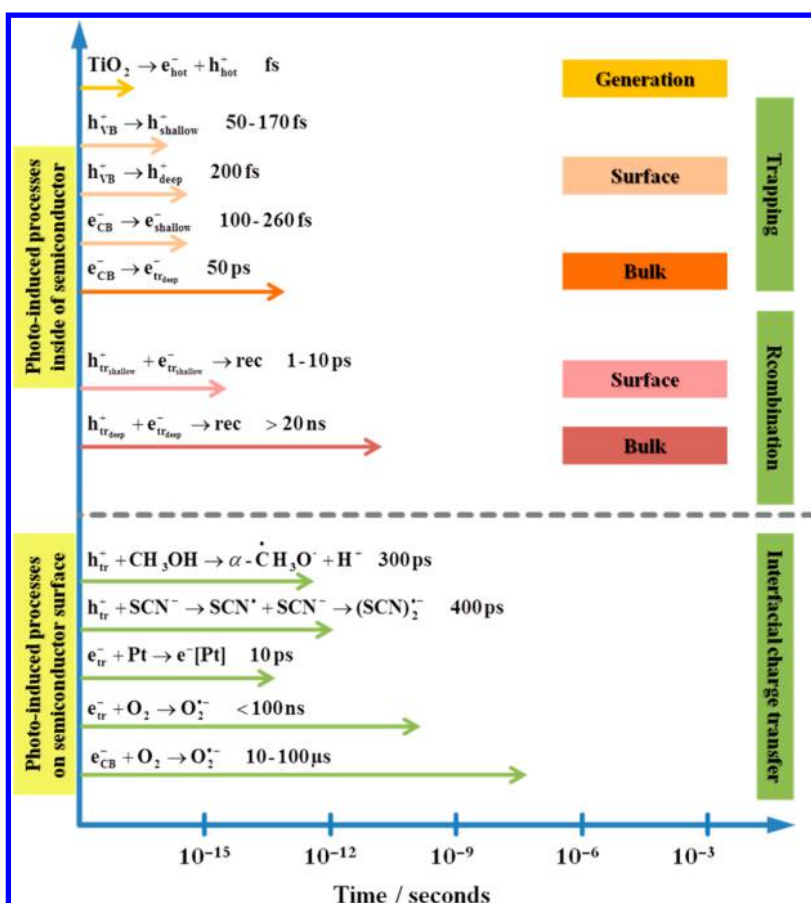


Figure 5. Photoinduced reactions in TiO_2 photocatalysis and the corresponding time scales.

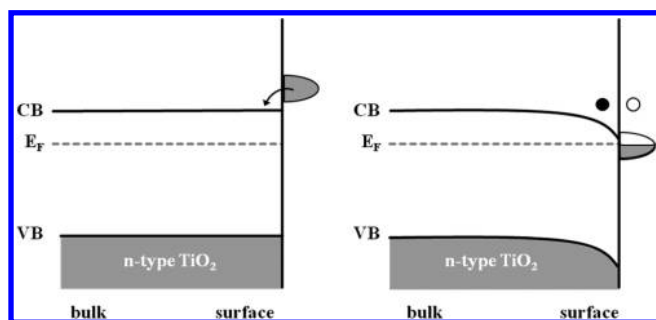


Figure 6. Schematic diagram of the surface band bending of a clean n-type TiO_2 in vacuum due to the presence of donor-like surface defect states (\bullet , electron; \circ , hole). An alternative energy diagram of a clean n-type TiO_2 has been suggested by Diebold.⁷⁹

important, because most photocatalytic studies are performed in atmospheric conditions rather than in a vacuum.

The accumulation of electrons at the surface determines the surface chemistry of TiO_2 . All processes occurring at the surface of semiconductors are driven to achieve an equilibrium between the Fermi level potential and the chemical potential of the adsorbates, with the position of the Fermi level being equal to the work function of the semiconductor. Deskins et al.⁸⁰ performed calculations using the density functional theory to define the influence of excess electrons on the adsorption behavior of adsorbates at the surface of rutile TiO_2 . According to these calculations, the charge transfer from the reduced surface to the adsorbate occurs provided that the electronegativity of the adsorbate exceeds the surface electronegativity of TiO_2 , χ_{TiO_2} ,

(see Figure 7a). Upon adsorption of species with low electronegativity (<4.5 eV), no electron transfer occurs (see Figure 7b).

Figure 7c shows a plot of the adsorption energies for a variety of species as a function of the electronegativity of the adsorbate, that is, the electronegativity difference between the surface containing oxygen vacancies O_v and the stoichiometric surface ($\Delta E_{\text{ads}} = E_{\text{ads-Ov}} - E_{\text{ads-clean}}$). Large negative values of ΔE_{ads} indicate a strong effect of the excess electrons on the adsorbate binding energies due to the enhanced charge transfer, while small values of ΔE_{ads} reveal that no or only little surface-to-adsorbate charge transfer occurs, that is, that the binding energy is not affected by the presence of excess electrons.

Martinez et al. investigated the adsorption properties of atoms and molecules with high, low, and intermediate electron affinity for a variety of TiO_2 surfaces, that is, stoichiometric, reduced, and oxidized, by means of the DFT theory.⁸¹ They found that depending on the oxidation state of the surface and the redox potential of the adsorbate, electrons can flow from or to the adsorbate, and therefore negatively or positively charged species can be formed. A direct consequence of this observation is that, by tuning the oxidation state of the surface, it is possible to control the surface chemistry of TiO_2 . Moreover, these authors demonstrated that when the adsorbate is not able to donate or to accept electrons, no charge transfer occurs, and the interaction strength does not depend on the oxidation state of the surface.

Considering the above results, we can conclude that depending on the electronegativity of the adsorbed species, either a stronger downward band bending, a band flattening, or even an upward band bending is to be expected. By the

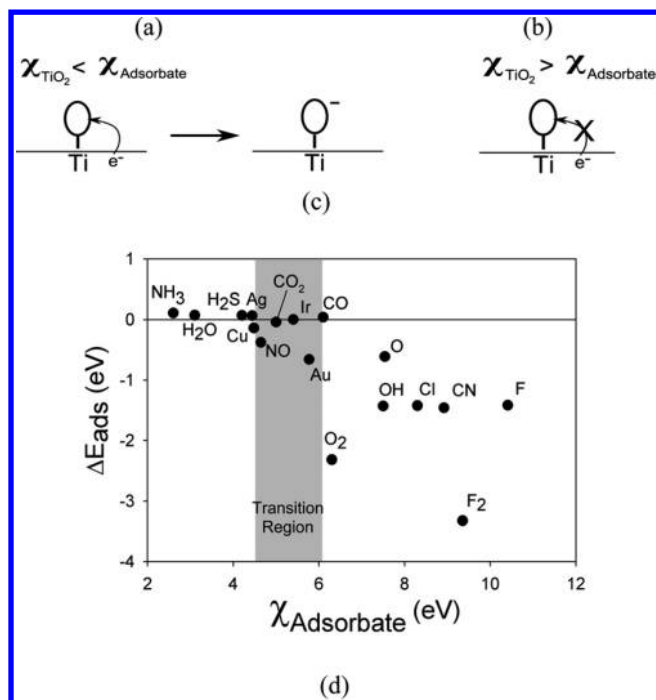


Figure 7. Illustration of the effect of electronegativity on the adsorption energies. Reprinted with permission from ref 80. Copyright 2010 American Chemical Society.

adsorption of gas molecules with their lowest unoccupied molecular orbital (LUMO) located more negatively than the Fermi level of TiO₂, the electrons will be transferred from TiO₂ to the adsorbed molecules, resulting in the development of an upward band bending. This charge transfer occurs as long as the LUMO orbital is filled being accompanied by a Fermi level decrease to the LUMO energy level (see Figure 8). Basically, the

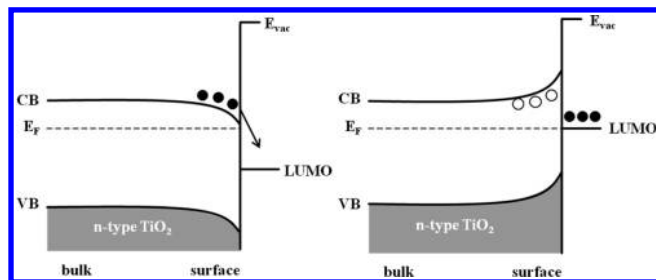


Figure 8. Schematic diagram of the surface band bending of TiO₂ in the presence of an acceptor-like molecule (E), for example, water.

band bending is defined as the difference between the electrode potential (Fermi level) of the semiconductor and the flat band potential, that is, the electrode potential at which the semiconductor bands are flat (zero space charge in the semiconductor). In n-type semiconductors, the band bending potential can be approximated as the difference between the electronegativity of the adsorbed molecule, χ_{molecule} , and the work function, W_{TiO_2} , of the surface.⁸² Experimental values for W_{TiO_2} extend from 5.8 to 4.4 eV depending on the degree of its reduction.⁸³ For example, by the adsorption of oxygen molecules with $\chi_{\text{O}_2} = 6.3$ eV,⁸⁴ band bending potentials between 0.5 and 1.9 eV can be expected.

The water molecule is well-known to act as electron donor upon the illumination of the semiconductor with UV light

leading to the formation of hydroxyl radicals. However, what is the effect of water molecules on the band bending of TiO₂ without excitation, because in this case the valence band is filled and water cannot inject electrons into TiO₂? To answer this question, the water adsorption process on the TiO₂ surface has to be considered.

As soon as TiO₂ is exposed to the ambient atmosphere, the adsorption of water occurs. The water adsorption process has already been widely discussed in many review articles, with the most controversial aspect being that the H₂O adsorption can either occur as a molecular, a mixed, or a dissociative process.^{79,85–87} In case water adsorbs molecularly at the TiO₂ surface, no charge transfer is expected according to the scheme shown in Figure 7. Nevertheless, He et al. reported that the molecular water adsorption on anatase (101) leads to a reduction of the charge density at the Ti_{5c} sites, indicating a surface-to-adsorbate charge transfer.⁸⁸ The dissociative water adsorption is usually described as the interaction of the OH group with a surficial Ti atom acting as a strong electron acceptor, while the H atom will form a bond with a bridging oxygen atom acting as electron donor. Shi et al. have shown in their ab initio study that during the water adsorption at a stoichiometric TiO₂ surface, the O atom accepts 0.84 e^- while the two H atoms donate 0.80 e^- , resulting in 0.04 net electrons being transferred from the solid to each water molecule.⁸⁹ However, experiments have shown that water molecules predominantly dissociate at the O_v sites, resulting in the formation of paired hydroxyl groups, a result that has been supported by theoretical calculations.^{90–92} According to Car–Parrinello molecular dynamic (CPMD) simulations on the rutile (110) surface performed by Tiloca et al., the water dissociation occurs only in the presence of surface oxygen vacancies, a process that is likely driven by a charge transfer from the 3d Ti orbitals of Ti³⁺ to the molecular π -orbitals of OH.⁹³ On the basis of these results, we conclude that in the absence of bandgap illumination the adsorption of water at the TiO₂ surface leads to an upward band bending due to the formation of negatively charged species at this surface and thus to a decrease of the charge carrier density in the near surface region as shown in Figure 8.

3.2. Photoinduced Charge Carrier Generation and Fate

If TiO₂ is exposed to ultrabandgap illumination, electron–hole pairs are created in the outer surface region of the material because of the short penetration depth δ_p ($\delta_p \approx 160$ nm)⁹⁴ of the UV light. In the space charge region, the electron–hole recombination is retarded as the photogenerated charge carriers move in different directions due to the near surface electric field. Continuous illumination will result in the annihilation of this electric field, that is, a band flattening. Yates et al.^{95,96} explained the appearance of this band flattening by a band shifting at the surface, because the free electrons move to the bulk, while free holes accumulate at the surface where the negative charge is neutralized (see Figure 9b). However, band flattening can also be explained by a band shifting in the bulk region, as the number of electrons increases in the bulk upon illumination (see Figure 9c). Consequently, the Fermi level, which can be regarded as the average energy of the electrons in the system, becomes more negative in the bulk. The energy of the surface states is usually pinned, in particular, when the capacitance of the Helmholtz layer is significantly higher than that of the depletion layer, which is true in most cases.

Different experimental methods can be applied for the detection of photogenerated charge carriers accumulated at the

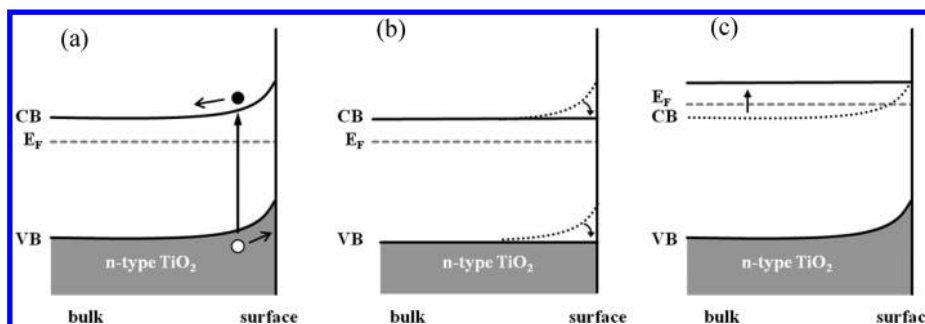


Figure 9. Schematic diagram of the photoinduced band flattening of bare TiO₂. (a) Photogeneration of an electron–hole pair in the space charge layer. (b) Band flattening due to the hole accumulation at the surface causing a band shifting at the surface. (c) Band flattening due to the electron accumulation in the bulk region causing a band shifting in the bulk.

TiO₂ surface. For example, using scanning tunneling microscopy (STM), Komiyama et al. observed a change of the local surface structure at the nanoscale on the TiO₂ (110) surface due to a local accumulation of the photoexcited states.^{97,98} Time-resolved optical second harmonic generation (SHG) is a further technique, which is often used to probe variations in the electrostatic surface fields induced under pulsed UV illumination. Employing an n-TiO₂ (001) electrode, Corn et al. demonstrated that the SHG signal decreases sharply upon UV illumination due to the creation of a steady-state population of photogenerated holes at the interface.^{99,100} The photoinduced band flattening is found to occur within a time scale of 3–4 ns as evinced by the fact that the SHG intensity returns to its steady-state level, because the excess holes at the surface are removed by electrochemical charge transfer and surface recombination processes.

3.2.1. Charge Carrier Recombination. The photocatalytic activities of TiO₂ photocatalysts are usually limited by the fast recombination of the photogenerated electron–hole pairs. Recently, an excellent review article showing the significance of the recombination of the photogenerated charge carriers on the photocatalytic process has been published.¹⁰¹ Although this process is undesirable, its study provides crucial information concerning the charge carrier dynamics in TiO₂. The recombination of the charge carriers can occur upon heat evolution via nonirradiative pathways or be accompanied by light emission via irradiative routes.¹⁰²

Photoluminescence (PL) spectroscopy is widely used to follow the irradiative recombination of photogenerated charge carriers in TiO₂ and to determine the energetic distribution of midbandgap states.^{102–104} Ordinary PL equipment consists of an excitation source and an optical power meter or a spectrophotometer to measure the PL intensity. The illumination of a semiconductor with light of an appropriate wavelength induces the excitation of an electron to the conduction band, leaving a hole behind in the valence band. The photogenerated charge carriers recombine subsequently; however, this recombination can proceed via different pathways due to the presence of trap states. Being a semiconductor with an indirect bandgap,⁷⁵ TiO₂ exhibits only very weak bandgap emission upon the recombination of conduction band electrons with valence band holes, while the irradiative recombination involving trap states is optically allowed.¹⁰⁵ For both anatase and rutile, the PL spectra in the visible and the near-IR wavelength range, respectively, have been reported, whereas the PL for anatase has been related to self-trapped excitons, and, for rutile, to intrinsic sites or to surface-bound species.^{106–111} For example, Knorr et al. observed for anatase a broad visible PL band, which they interpreted as a combination of the recombination of mobile electrons with

trapped holes (1 PL) and the recombination of trapped electrons with holes in the valence band (2 PL) (Figure 10a).¹¹² Through a

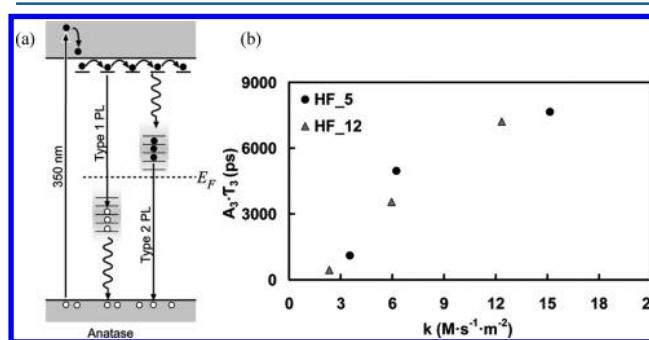


Figure 10. (a) Model for trap state photoluminescence in anatase. Wavy and straight lines indicate nonradiative and radiative transitions, respectively. The photoluminescence of anatase is considered to be a combination of both type 1 and type 2 PL, involving spatially separated hole and electron traps, respectively. The shaded regions represent the energetic distributions of traps estimated from the wavelengths spanned by the PL spectra. Adapted with permission from ref 112. Copyright 2008 American Chemical Society. (b) Correlation between the long-lasting PL component ($A_3\tau_3$) and the surface-normalized photocatalytic reaction rates of formic acid degradation for the HF_5 and HF_12 (fluorine doped TiO₂ with F/Ti nominal percent molar ratios of 5 and 12, respectively) photocatalyst series. Reprinted with permission from ref 114. Copyright 2013 American Chemical Society.

detailed analysis of the respective PL data, the surface trapped electrons in anatase are found to be located about 0.7–1.6 eV below the conduction band edge referring to oxygen vacancies, while the trapped holes are located about 1.8–2.5 eV below the conduction band edge.

Yamada et al.¹¹³ investigated the charge carrier recombination dynamics in rutile and anatase TiO₂ single crystals employing a combination of time-resolved PL, PC, and TA measurements and found longer lifetime for electrons in anatase (>few ms) in comparison to rutile (24 ns), while the decay for the holes in both crystal phases occurs on the nanosecond time scale.

Moreover, Dozzi et al.¹¹⁴ could observe a clear correlation between the photoactivity of the fluorine-doped TiO₂ materials and the recombination kinetics of the trapped electrons derived from the long-lasting component of the PL signal as shown in Figure 10b. Longer lifetimes of the photogenerated charge carriers result in higher photocatalytic formic acid degradation rates.

Generally, it is assumed that in TiO₂ the photogenerated electron–hole pairs predominantly recombine via nonirradiative

pathways. The nonirradiative recombination in photoexcited systems leads to the rapid release of heat, which can, for example, be detected by time-resolved photoacoustic spectroscopy (TRPAS). Employing this method, Leytnar and Hupp found that approximately 60% of all trapped electron–hole pairs recombine on the time scale of about 25 ns, releasing 154 kJ/mol of energy as heat.¹¹⁵ It was also demonstrated that if the heat is released nonadiabatically, this recombination energy is sufficient to provoke the deaggregation of TiO₂ nanoparticle aggregates.^{116–118} This photodeaggregation process increases the adsorption capacity of the photocatalyst, for example, for water molecules, without increasing its mass.

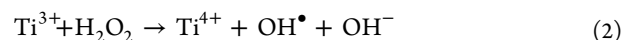
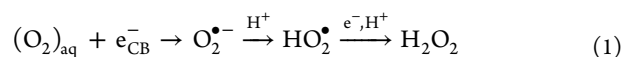
Moreover, the recombination kinetics of the photogenerated charge carriers have also been studied using time-resolved absorption spectroscopy. According to the reported results, the electron–hole recombination can be affected by many factors such as the sample preparation, the reaction temperature, the charge trapping, the interfacial charge transfer, and the excitation light intensity.^{119–125} Consequently, the lifetime of the charge carrier recombination in TiO₂ extends from the picosecond to the millisecond time scale. The reaction order of the recombination process appears to depend on the light intensity. For example, Rothenberger et al. observed second-order kinetics at high pulse energies (2 mJ) and first-order kinetics at low electron–hole concentrations obtained at a pulse energy of 0.5 mJ.¹²⁶

3.2.2. Hole Trapping. Usually, the photogenerated charge carriers do not recombine directly due to the fact that different possibilities for the charge carrier, for example, the hole trapping, exist at the semiconductor's surface; thus the band flattening will be retained for some nanoseconds. Many studies have been performed to establish the nature of the trapping sites for photogenerated holes in titanium dioxide.¹²⁷ Generally, it is assumed that holes can be trapped either at a bridging O^{2−} or they can be transferred to surface-bound OH[−] anions resulting in the formation O^{•−} or/and OH[•] centers, respectively. The most controversial point in the discussions concerning the nature of the hole trapping sites is whether superficially adsorbed hydroxyl groups, that is, Ti⁴⁺OH_ν, can trap the photogenerated charge carriers.^{128,129} Electron spin resonance spectroscopy (EPR) is a very useful experimental technique to clarify this issue as it enables the monitoring of the formation of paramagnetic species produced upon the irradiation of photocatalysts such as TiO₂. A drawback of this method is the low temperature requirement for the detection of the trapped states, although Iorio et al. detected Ti³⁺ species in ethanolic TiO₂ sols at room temperature.¹³⁰ However, the analysis of some EPR spectra evinces that the oxidation of water on the TiO₂ surface through valence band holes leads to the formation of the OH[•] radicals.^{131,132} These experimental results are supported by the thermodynamic analysis of the possible photoreactions. Because the standard redoxpotentials $E^0(\text{OH}_{\text{aq}}^-/\text{OH}_{\text{aq}}^{\bullet}) = 1.9 \text{ V}$ (vs NHE) and $E^0(\text{H}_2\text{O}_{\text{aq}}/\text{OH}_{\text{aq}}^{\bullet} + \text{H}_{\text{aq}}^+) = 2.73 \text{ V}$ (vs NHE) are located at a less positive potential than the valence band edge of TiO₂, the photogenerated holes are principally able to produce such species.¹³³ However, Bredow et al. found in their model calculations that the potential barriers for the desorption of free OH[•] radicals are too high; that is, the formation of free hydroxyl radicals in TiO₂ photocatalysis is considered to be highly unlikely. This is moreover supported by recent ab initio molecular dynamics (AIMD) simulations.¹³⁴ Following the initial generation of surface-bound hydroxyl radicals, the

formation of hydrogen peroxide and of peroxide radicals bound to the surface is rather favored.^{135,136}

Nevertheless, Imanischi et al. estimated the energy levels of the O 2p orbitals for H₂O_{aq} and OH_{aq}[−] from the reported photoelectron emission spectra and of Ti–OH at the TiO₂/water interface from the respective UV photoelectron spectra.^{137–139} On the basis of these results, the effective O 2p levels were found to be far below the valence band of TiO₂; thus the oxidation of adsorbed water molecules to OH_{aq}[•] radicals through the photogenerated holes was excluded. This conclusion was supported by various reported results, which clearly showed that the primary products of the hole trapping are not superficially bound or free OH_{aq}[•] radicals but rather O_s^{•−} radical ions in the TiO₂ lattice.^{140–143}

The formation of OH[•] radicals during the photocatalytic process cannot be completely excluded, because OH[•] radical species can be formed either through the electroreduction of dissolved oxygen by photogenerated electrons via reactions 1–5 or/and in acidic solution via the trapping of the holes by lattice bound O_s^{2−}.¹⁴⁴



According to the results discussed above, the trapped holes are considered to be localized at certain surface sites. This can be the case at very low temperatures, as for example during the EPR spectroscopic measurements, with the hopping of the charge carriers being limited, and thus more localized trapped states will be formed. Nevertheless, at room temperature the photogenerated holes will rather be trapped at different locations distributed over a certain radius within the surface layer, with this surface of the particles having a thickness that can range between 0.35 nm¹⁴⁵ and several atomic layers.¹⁴⁶ In this way, the trapped holes do not stay localized at certain surface sites, but are delocalized over the surface region. Shapovalov et al. have suggested that the holes can be delocalized over at least two surface oxygen atoms, and can be transferred between surface oxygen atoms and adsorbed species; thus, both O^{•−}–Ti(IV)–OH[−] and OH[•] species can be formed.¹⁴⁷ The concentrations of these species depend on the surrounding. For example, hydroxyl radical scavengers will shift the equilibrium toward the formation of OH[•], while strong acids and bases will result in a less pronounced generation of hydroxyl radicals. These results are supported by the theoretical DFT–U calculations performed for the TiO₂ (110) surface by Ji et al.¹⁴⁸ They reported that in the presence of a water molecule the electron can be transferred from water to a bridging oxygen atom through the formation of a hydroxyl radical. The latter is adsorbed on the Ti row and shares the hole with an in-plane oxygen. Moreover, Bredow et al. concluded from their theoretical calculations performed using the SCF MO method MSINDO (modified symmetrically orthogonalized intermediate neglect of differential overlap) that only delocalized electron–hole pairs can be directly formed through the interaction of the solid with photons, while more localized electron–hole pairs may not be directly created by light

absorption.¹⁴⁹ Figure 11 presents two representative examples of a “dark” state with essentially zero intensity (a), and a “bright”

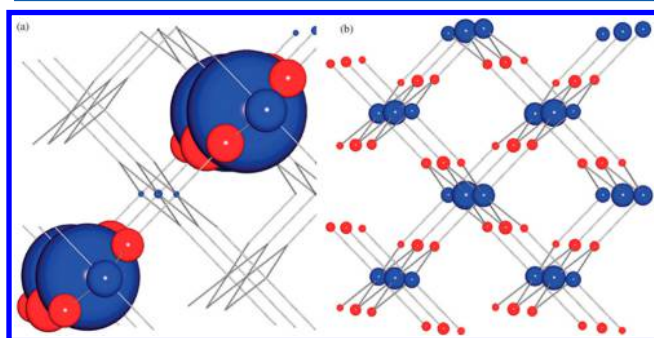


Figure 11. Difference densities of selected excited states in rutile: (a) a low-lying “dark” state, (b) a higher excited state with large oscillator strength. The size of the spheres is proportional to the charge difference at this center between the excited S_n state and the ground state. Blue denotes an increase of electronic population, and red denotes a decrease. Reproduced with permission from ref 149. Copyright 2012 The Royal Society of Chemistry.

state with high oscillator strength (b) for rutile. In the low-lying “dark” state, the electron–hole pair is strongly localized, only a few titanium atoms exhibit an increased electron density, while in the other case (see Figure 11b), where a higher-lying “bright” state is present, every Ti atom shows nearly the same increase of the electron density. Here, the electron–hole pairs are delocalized over the entire cyclic cluster.

The transient absorption spectroscopy provides another useful technique to study reaction dynamics and the formation of the trapped states at the TiO_2 surface. For example, free OH^\bullet and free $\text{O}_s^{\bullet-}$ exhibit a transient absorption with maxima located around 260 nm.¹⁵⁰ When these free radical groups are, however, located at surficial Ti sites, usually a substantial red-shift of the transient absorption spectrum results.¹²⁸ As can be seen from Table 1, the transient optical absorption of the trapped holes extends from the UV to the IR region. The transient spectra of the trapped holes are found to be slightly different when comparing the results reported by different researchers, indicating that apparently different trapped states for the holes coexist in TiO_2 particles. Bahnemann et al.¹⁵¹ performed a laser flash photolysis study employing colloidal TiO_2 suspensions and found that at least two different types of holes have to be considered, deeply trapped holes, which are unreactive and exhibit a transient absorption at 450 nm, and shallowly trapped holes, which exist in a thermally activated equilibrium with free holes and possess a very high oxidation potential. Moreover, the shallowly trapped holes do not exhibit any transient absorption between 400 and 650 nm as shown in Figure 12. These differences in the transient absorption spectra of the trapped holes can also be attributed to the fact that the charge carriers are delocalized over different trapping sites, with the charge carriers being trapped at different energetic depths resulting in broad transient absorption spectra.

The analysis of the decay kinetics of the transient absorption signals allows the determination of the trapped charge carrier lifetimes. The lifetime of the trapped holes can be extended from the picosecond to the millisecond time scale in the presence of electron acceptors such as Pt as shown in Table 1.^{33,102,119,151–154} Their transient absorption signal at 450 nm decays, most likely, resulting in the formation of surface peroxides according to



It is a real challenge to assign the optical transitions derived from the transient absorption spectra to individual electronically excited states and to unambiguously determine the corresponding chemical identity. The precise assignment of a transient absorption can be hindered by several factors such as the broadness and the overlap of the transient absorption spectra, the simultaneous formation and hence trapping of holes and electrons, and the various trapping states or the sensitivity of the transient absorption spectra to the experimental conditions as well as to the chemical and physical properties of the investigated TiO_2 particles.

As was already mentioned, it cannot unambiguously be predicted at which sites photogenerated holes are localized, that is, either at adsorbed hydroxyl groups or at bridging oxygen atoms forming $\text{OH}_{\text{aq}}^\bullet$ or $\text{O}_s^{\bullet-}$ radicals, respectively. Some studies even predict that the OH_s^\bullet radicals exhibit different transient absorption features as compared to $\text{O}_s^{\bullet-}$, with the former absorbing primarily light in the ultraviolet range, while the latter absorb photons in the visible range.^{128,157} Thus, the transient absorption in the visible range (2.5–2.8 eV) can be attributed to the transition either from the trap state to the CB forming unstable O atoms in the lattice. In other words, the detected transient absorption can be attributed to the $(\text{Ti}^{4+}-\text{O}_s^{\bullet-})-(\text{Ti}^{3+}\cdots\text{O})$ transition. Alternatively, the observed optical transition can also be due to the electron transfer from the valence band to the trap state forming $\text{O}_s^{\bullet-}$ radicals. Henderson et al., however, assumed that the latter transition may not be optically allowed.¹²⁷

For the first time, Zawadzki calculated the transient absorption spectra of trapped holes in bulk anatase TiO_2 and on its 001 and 101 surfaces.¹⁶² According to these calculations, the transient absorption can be assigned to the $(\text{O}^{2-}-\text{O}^-)$ transition, called the inter-polaron transition. Depending on the distance between neighboring O atoms, the transition energy will vary, with higher transition energies corresponding to longer distances. As the result of these calculations, the absorption spectra of trapped holes extend from 300 to 800 nm (see Figure 12). Bulk trapped holes exhibit long wavelength transient absorptions due to the fact that the difference between the hole trapping strength at oxygen lattice sites in the bulk is zero while on the surface it is high, because the surface exhibits different oxygen lattice sites. Hence, no difference of the transient absorption spectra of trapped holes can be expected for different metal oxide semiconductors. The drawback of these calculations is the assumption that holes are directly localized after their photo-generation at the surface bridging oxygen atoms.

3.2.3. Electron Trapping. Because of the upward band bending in hydroxylated n-type TiO_2 , the photogenerated electrons are forced to move from its surface into the bulk (see Figure 9a), where they can be delocalized over different Ti sites. Both theoretical and experimental studies are predicting bulk (subsurface) trapping rather than surface trapping of these electrons.^{135,143,147,148,163} However, alternative studies also exist demonstrating that Ti^{4+}OH groups located at the TiO_2 surface can act as trapping centers for the electrons, resulting in the formation of Ti^{3+}OH species. Such species can attract holes, thus behaving as recombination centers.^{132,141,164} Di Valentin et al. reported that holes and electrons populate surface sites due to the following reasons: (1) The lattice relaxation associated with

Table 1. Trapping Dynamics of Electrons and Holes Photogenerated in TiO₂ Photocatalysts

transient absorption		conditions	ref
trapped holes	trapped electrons		
475 nm pH < 7, decays ms pH > 7, decays μ s	650 nm	TiO ₂ colloidal solution, platinum as electron scavenger, alcohol as hole scavenger, $\lambda_{\text{ex}} = 347$ nm (15 ns, 0.7–7 J)	33
not reported 250 ns (formation)	620 nm <30 ps (formation) 30 ns (lifetime)	TiO ₂ colloidal solution (12 nm), $\lambda_{\text{ex}} = 355$ nm (30 ps, 0.5–2 mJ)	126
630 nm $t_{50\%} = 1.3$ ns	not reported	TiO ₂ colloidal solution (2.5–25 nm), dye as an electron scavenger, $\lambda_{\text{ex}} = 350$ nm (20 ps, 2–3 mJ)	152
430 nm $t_{50\%} = 53$ ns	650 nm $t_{50\%} = 53$ ns	TiO ₂ colloidal solution (2.4 nm), $\lambda_{\text{ex}} = 347$ nm (20 ns, 5.4 J)	151
520 nm <50 fs (trapping)	700 nm 260 fs (trapping)	TiO ₂ colloidal solution, $\lambda_{\text{ex}} = 360$ nm (200 fs, 5.4 J)	155
520/1200 nm $t_{50\%} = 1$ μ s	770/>1500 nm $t_{50\%} = 1$ μ s	TiO ₂ nc-films (10–15 nm) $\lambda_{\text{ex}} = 355$ nm (10 ns, 160 μ J)	119
550 nm 200 fs (formation) 100 ps (relaxation)	not reported	TiO ₂ nc-films (20 nm) $\lambda_{\text{ex}} = 266$ nm (130 fs, 1 mJ)	156
not reported	800 nm (25 μ s)	TiO ₂ nc-films (\sim 15 nm) $\lambda_{\text{ex}} = 377$ nm (400 μ J/cm ²)	122
400/550 nm $t_{50\%} = 0.2$ – 0.4 μ s	not reported	TiO ₂ nc-films (10–15 nm) $\lambda_{\text{ex}} = 355$ nm (10 ns, 0.14–1.1 mJ)	157
400 nm \sim 220 fs	800/2500 nm, \sim 170 fs (trapping), 500 ps (relaxation)	TiO ₂ nc-films (10–15 nm), $\lambda_{\text{ex}} = 355$ nm (120 fs, <160 nJ)	153
520 nm	770 nm	TiO ₂ nc-films (10–15 nm), $\lambda_{\text{ex}} = 355$ nm (150 ps, 0.4–14 mJ)	158
465 nm $t_{50\%} = 40$ μ s	not reported	TiO ₂ nc-films, $\lambda_{\text{ex}} = 335$ nm (6 ns, 200 μ J)	159
450 nm $t_{50\%} = 2$ μ s	800 nm, $t_{50\%} = 2$ μ s	TiO ₂ nc-films in water (pH = 7), $\lambda_{\text{ex}} = 337$ nm (1 ns, 0.4 mJ)	160
520 nm $t_{50\%} = 1.1$ μ s	not reported	TiO ₂ powder, $\lambda_{\text{ex}} = 355$ nm (5 ns)	161
470 nm/decay rate 0.5 ps (UV-100) 3.6 ps (P25)	600 nm	TiO ₂ powder, $\lambda_{\text{ex}} = 389$ nm (150 fs, 0.6–0.7 mJ)	154

the trapping is more feasible at the surface than in the bulk because of the possibility for the surface structure to relax with fewer constraints. (2) At the surface the energy levels calculated for the self-trapped charge carriers are deeper in the gap with respect to the bulk levels, confirming that there is a driving force for electrons and holes to migrate to the surface.¹⁶⁵

When debating whether the electrons are rather trapped at the surface or in the bulk of a TiO₂ particle, the particle size effect should also be considered, because the upward band bending will decrease with the particle size according to the following relationship:¹⁶⁶

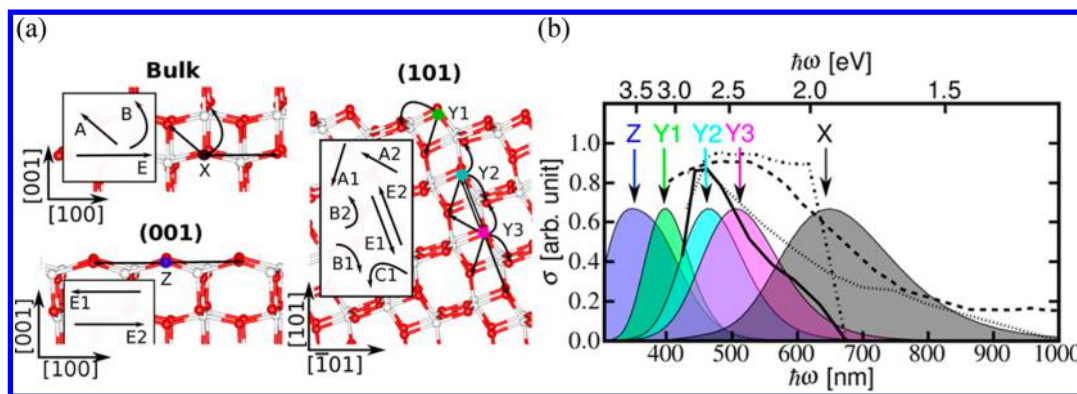


Figure 12. (a) Locations of the most stable O^- centers X, Z, Y1, Y2, and Y3 in anatase TiO_2 . (b) Calculated and experimental optical absorption spectra of the self-trapped holes in anatase TiO_2 . Absorption bands due to the X, Z, Y1, Y2, and Y3 trapping centers are marked by shaded curves. The experimental spectra are marked with lines: solid (time resolution 50 ns); dashed (measured after 5 ms); dash-dotted (measured after 20 ns); dotted (measured after 20 ms). Reprinted with permission from ref 162. Copyright 2013 American Chemical Society.

$$V_{BB} = \frac{kT}{6e} \left(\frac{r_0}{L_D} \right)^2 \quad (8)$$

where r_0 is the radius of the particle and L_D is the Debye length. In small particles with a radius $r_0 \ll d_{SC}$ (d_{SC} : thickness of the space charge layer), no space charge layer or rather band bending exists, and thus both electrons and holes are available at the surface resulting in very broad transient absorption spectra observed in the respective laser flash photolysis experiments, where the transient absorption bands of electrons and holes overlap as shown in Figure 13. In the presence of electron acceptors such as

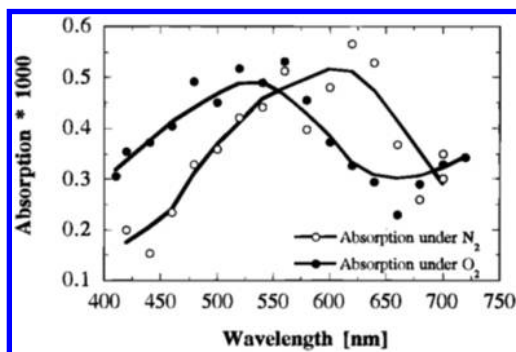


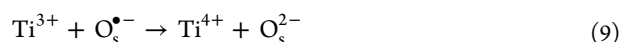
Figure 13. Transient absorption spectra measured 20 ns after laser excitation ($\lambda_{ex} = 350$ nm) in O_2 -saturated and N_2 -saturated solutions, respectively: pH = 2.3, 1×10^{-4} mol/L colloidal TiO_2 particles, absorbed photon concentration per pulse 9×10^{-6} mol/L. Reprinted with permission from ref 151. Copyright 1997 American Chemical Society.

O_2 , the maximum of these transient absorption spectra is shifted toward shorter wavelengths evincing distinctive trapping of the holes at the surface. Saturation of the solution with N_2 , on the other hand, supports the electron trapping resulting in the formation of Ti^{3+} centers with their transient absorption maxima located around 650 nm.

Table 1 summarizes the transient absorption maxima that have been reported for the trapped electrons, with most of them having been observed in the presence of hole scavengers. The broad transient absorption spectrum with a maximum around 650 nm (as shown in Figure 13) is usually associated with the excitation of a trapped electron from the trapping site to the conduction band.¹²⁵ Some studies report an additional transient

absorption in the IR range that has been attributed to the presence of free electrons, which are distributed in the bulk of the semiconductor particle.¹¹⁹ Such a transient absorption in the near-IR region can be assigned to the transition from the bottom of the conduction band to upper levels within the same band.

Peiro et al.¹²² studied the lifetime of trapped electrons in nc (nanocrystalline) TiO_2 films employing transient absorption spectroscopy and reported in the absence of ethanol (electron donor) and O_2 (electron acceptor) a half-life of its absorption signal of $\sim 25 \mu s$. The corresponding decay has been attributed to the recombination at trap sites:



In the presence of ethanol but still in the absence of O_2 , the lifetime of the trapped electrons was found to increase up to 500 ms. Principally, in the absence of electron acceptors, the transient absorption of the trapped electrons should not exhibit any decay behavior in the presence of a hole scavenger such as ethanol, because no recombination according to reaction 9 can proceed due to the complete removal of the holes, and the remaining Ti^{3+}/e^- do not react with each other. The organic radicals formed

upon the oxidation of the hole scavengers, such as $CH_3\dot{C}HOH$ obtained by the one-electron oxidation of ethanol used as hole scavenger, are also not likely to act as acceptors for the electrons even though this has been suggested in ref 122. The most likely

fate of α -hydroxyalkyl radicals like $CH_3\dot{C}HOH$ is, however, to inject an additional electron into the conduction band forming the respective aldehyde as stable product, that is, CH_3CHO (this is the so-called current doubling effect, vide infra). Thus, the slow decay of the Ti^{3+} absorption observed by Piero et al. may be due to the reaction of the trapped electrons with electron acceptors A, which might have been present in the TiO_2 matrix as impurities:



On the other hand, Kuznetsov et al. investigated the charge separation and storage in media-wet TiO_2 gels (anatase) and observed that under UV illumination more than 14% of the Ti^{4+} centers are converted into Ti^{3+} .¹⁶⁷ The trapped electron lifetime was found to be on time scales of months in the absence of oxygen.

Time-resolved microwave conductivity (TRMC) provides another feasible technique to study the reaction dynamics of photogenerated charge carriers in TiO_2 . The TRMC method is

based on the measurement of the relative change of the microwave power reflected from the sample. Photogenerated charge carriers will induce changes of the sample's conductivity, thus resulting in changes of the microwave power reflected by the sample. The signal obtained by this technique is called microwave conductivity. For TiO_2 , the interpretation of the observed TRMC signals is usually based on the assumption that the electrons have a much higher mobility than the holes; thus the observed conductivity can be attributed to the presence of excess electrons in the conduction band.¹⁶⁸ One difficulty to interpret the TRMC signals of different TiO_2 samples lies in the fact that numerous phenomena can be responsible for the decay of the microwave conductivity being merely the result of the decrease of the number of excess electrons in the conduction band. This could be either due to the electron–hole recombination but also to the electron trapping, because the trapping of the electrons leads to a drastic decrease of their mobility. However, a recently published review by Colbeau-Justin provides an excellent overview concerning the use of time-resolved conductivity measurements for the detection of mobile electrons in different systems.¹⁶⁹ For example, the TRMC method has been applied to study the charge carrier lifetime in anatase, rutile, anatase/rutile mixtures, and in quantum-sized TiO_2 .^{170–174} The signals for anatase and rutile are presented in Figure 14. The longer electron lifetime observed for the anatase

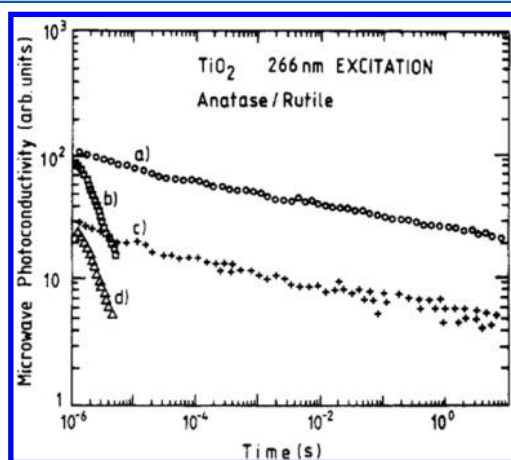


Figure 14. Photoconductivity of TiO_2 powders after a 20 ns (fwhm) laser flash excitation at 266 nm: (a) anatase, 0.5 mJ/cm²; (b) rutile, 1 mJ/cm²; (c) anatase, 0.1 mJ/cm²; (d) rutile, 0.2 mJ/cm². Reprinted with permission from ref 172. Copyright 1990 American Chemical Society.

in comparison to the rutile sample has been attributed to the fact that anatase has a higher amount of surficial OH groups, where the holes can be trapped leading to an enhanced charge separation. In the presence of water, a faster decay has been observed for the anatase sample, while the lifetime of the mobile electrons in rutile does not show any change after this surface treatment.¹⁷⁰ Principally, water can either decrease the stability of the surface-bound radicals, formed by the trapping of the holes, or it may promote the trapping of the mobile electrons, hence reducing their lifetime. The influence of the water treatment on the TRMC signals has been taken as evidence that while in rutile the dominant effect is the bulk charge carrier recombination, in anatase surface trapping appears to prevail.

The correlation of the results obtained by means of the TRMC and the TAS technique should provide a deeper understanding concerning the dynamics of the photogenerated charge carriers

in TiO_2 , provided that the experiments have been carried out under similar conditions. For example, using TRMC, Mul et al. investigated the dependence of the lifetime of free bulk electrons on the anatase TiO_2 particle size and found a faster decay of the mobile charge carriers in smaller particles. Assuming that the decay is predominantly caused by the trapping of the conduction band electrons, these TRMC data indicate that the samples with an average particle diameter below 15 nm are likely to contain a larger concentration of trapping sites as compared to the larger particles.¹⁷⁵ In good agreement with these results, Murakami et al. reported that for pure anatase TiO_2 , the height of the transient absorption signal of the trapped electrons at 600 nm increases with a decrease of the primary particle size from 40 to 6 nm, suggesting the electron-trapping process is more efficient for smaller TiO_2 particles exhibiting a larger surface area.¹⁵⁴

3.3. Photoinduced Electron Transfer at the TiO_2 Surface

Following their formation by light excitation, electrons and holes can easily be transferred to electron and hole acceptors, respectively, provided that the respective energetic requirements are fulfilled. The quantum efficiency¹⁷⁶ of these reactions depends on the charge-transfer rate at the interface, on the recombination rate within the particle, and on the transit time of the photogenerated charge carriers to the surface. The latter process can be observed either by means of the TAS method, where the transit time is derived from the decay of the transient absorption of the trapped charge carriers, or by means of the TRMC method, where the transit time can be derived from the effective mobilities of the free charge carriers, which are usually estimated from the magnitude of the end-of-pulse or rather of the initial transient microwave conductivity. One of the first studies that focused on the charge-transfer dynamics was performed by Rothenberger et al. employing colloidal TiO_2 nanoparticles.¹²⁶ The respective time for the electron transfer to their respective surface traps was found to be >30 ps, while the hole trapping time was reported to be 250 ns. In contrast to these values, Enright et al. observed in nanocrystalline (nc) TiO_2 films by means of spectroelectrochemical techniques that the diffusion coefficient for the holes is higher ($D_h = 4 \times 10^{-5} \text{ m}^2/\text{s}$) than that of the electrons ($D_e < 1 \times 10^{-6} \text{ m}^2/\text{s}$).¹⁷⁷ Using these values, the average transit time of the photogenerated charge carriers from the bulk to the surface of the particle can be calculated by¹⁷⁸

$$\tau = \frac{r_0^2}{\pi^2 D} \quad (11)$$

Taking a particle radius r_0 of 10 nm, the trapping time for the holes is thus calculated to be 250 fs and for the electrons 10 ps. Yang and Tamai studied the charge carrier dynamics on colloidal TiO_2 particles by means of femtosecond laser flash photolysis spectroscopy and observed longer trapping times of the electrons (260 fs) in comparison to the holes (50 fs).¹⁵⁵ According to Tamaki et al., both the photogenerated electrons and holes in nc TiO_2 films reach the surface in 170 and 220 fs, respectively.¹⁵³ Apparently, the calculated hole trapping times correlate very well with the experimentally observed values. In contrast, a considerable discrepancy exists for the electron trapping time. Furube et al. supposed the reason for this discrepancy to be that free electrons generated upon 355 nm excitation still contain part of the excess energy and may therefore have a larger diffusion coefficient than the reported value.¹⁵³ However, Warman et al. have found by means of TRMC measurements that the electron mobility of the photogenerated free electrons increases markedly from 0.05×10^{-4} to $1.5 \times 10^{-4} \text{ m}^2/\text{V}\cdot\text{s}$ with increasing particle

size from 5 to 50 nm; thus the bulk-to-surface transit time is calculated to increase from 19 to 65 ps.¹⁷⁹ These values are in agreement with above-discussed dependency of the lifetime of the photogenerated charge carriers on the particle size.¹⁷⁵

Tamaki et al. have also shown that after reaching the surface (within 170 fs) the photogenerated electrons migrate between surface and shallow bulk trap sites that are in equilibrium.¹⁵³ These shallowly trapped electrons relax into deeper sites within 500 ps through hopping processes involving energetically distributed trapping sites as shown in Figure 15.

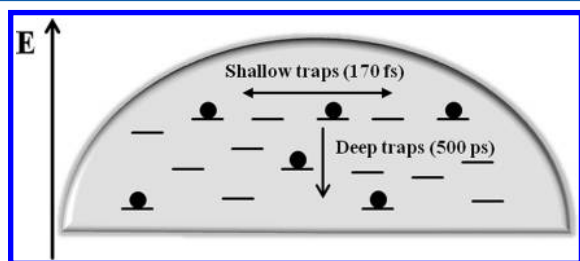
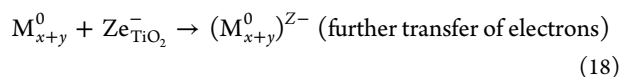
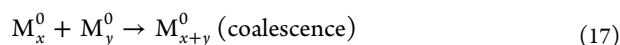
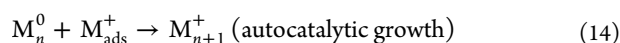
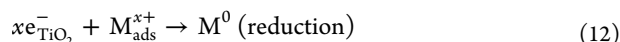


Figure 15. Schematic diagram illustrating the spatial and energetic distribution of electron traps in a TiO₂ particle. An alternative energy diagram of TiO₂ has been suggested by Tamaki et al.¹⁵³

3.3.1. Photoinduced Reduction Reactions at the TiO₂ Surface. The above-discussed results evince that photo-generated electrons are not directly available at the surface for the desired reactions but that TiO₂ should rather be modified to activate the photogenerated electrons for reduction reactions. This can, for example, be facilitated through a surface modification with noble metal nanocontacts. During the frequently employed photodeposition method, the loading of the metal onto the TiO₂ surface proceeds via the reduction of metal ions by electrons photogenerated in the photocatalytic system. Hereby the reduction step occurs, depending on the oxidation state of the metal ions, through single-, two-, or three-electron transfer reactions according to the following reaction sequence:^{180–183}



Noble metal-modified TiO₂ nanoparticles usually exhibit enhanced photocatalytic activity resulting from an improved charge separation. According to the Schottky barrier model, this enhanced charge separation can be attributed to the transfer of the photogenerated holes to the surface and the simultaneous migration of the electrons into the bulk induced by the electric field in the space charge layer as shown in Figure 16 for the example of platinum-modified TiO₂.

However, results from diffuse reflectance spectroscopy experiments apparently contradict the Schottky barrier model,

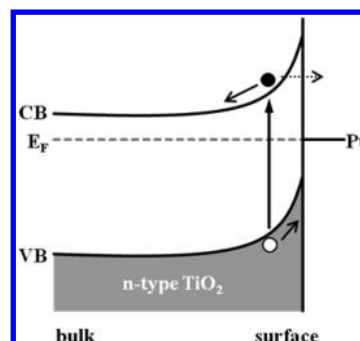


Figure 16. Schematic diagram illustrating the influence of Pt on the photogenerated charge carriers in TiO₂ (the straight arrow indicates the transfer of the electrons due to the Schottky barrier, and the dotted arrow indicates the transfer of the electrons initiated by the thermodynamic driving force).

indicating that both trapped electrons and free bulk electrons migrate to the Pt contact and thus to the TiO₂ surface within a time interval of 1.4 and 2.3 ps, respectively (values have been reported for 1% Pt/TiO₂).^{184,185} As shown in Figure 17a, the decay rate of the transient absorption at 600 nm increases with increasing Pt-loading, indicating that a larger Pt coverage on the TiO₂ surface enhances the probability of electron migration from TiO₂ to Pt.¹⁸⁴ These results are in agreement with the results of EPR measurements evincing the transfer of electrons from TiO₂ to Pt⁰ as shown in Figure 17b.¹⁸³ The ESR signal intensity of photoformed active Ti³⁺ sites on bare TiO₂ was found to increase linearly with the irradiation time, while Pt⁰-loaded catalysts showed almost no change in the signal intensity. The electron transfer depends upon the respective thermodynamic driving force because the electrons have to cross the energetic (Schottky) barrier. This explains the fact that the bulk-to-surface transit time is slower (1.4 ps) than the surface trapping time (170 fs) observed in the absence of Pt. However, the appearance of both characteristic signals for the Ti³⁺ species, that is, their transient absorption and the EPR signal, in the presence of Pt leads to the conclusion that not all electrons are transferred to the Pt catalyst but that rather a certain number of the photo-generated electrons remain in the TiO₂ particle.

The TRMC results denote that the electron migration from TiO₂ to Pt depends on the properties of the applied TiO₂ powder. For example, the photoconductivity of the photo-generated mobile electrons in P25 modified with Pt decays faster in comparison to bare P25, indicating an electron transfer to the Pt islands, where the subsequent reduction of a substrate such as a proton can take place.^{172,186,187} These results can not be explained by the Schottky-barrier model, according to which an increase in the electron lifetime would be the expected result. Nevertheless, in case of Pt/PC 50 (a Crystal Global photocatalyst, pure anatase phase), an increase of the electron lifetime after the modification with Pt has been observed as expected due to the enhanced separation of the photogenerated electron–hole pairs.

Upon the illumination of metal loaded TiO₂, the influence of the excitation of the metal particle on the reaction dynamics of the photogenerated charge carriers needs to be taken into account. The metal nanoparticles can be characterized by their surface plasmon resonance (SPR), which is readily explained by the photoinduced collective oscillations of electrons at the surface of these nanoparticles.^{188,189} Thus, an increased local electromagnetic field is generated upon illumination of the metal

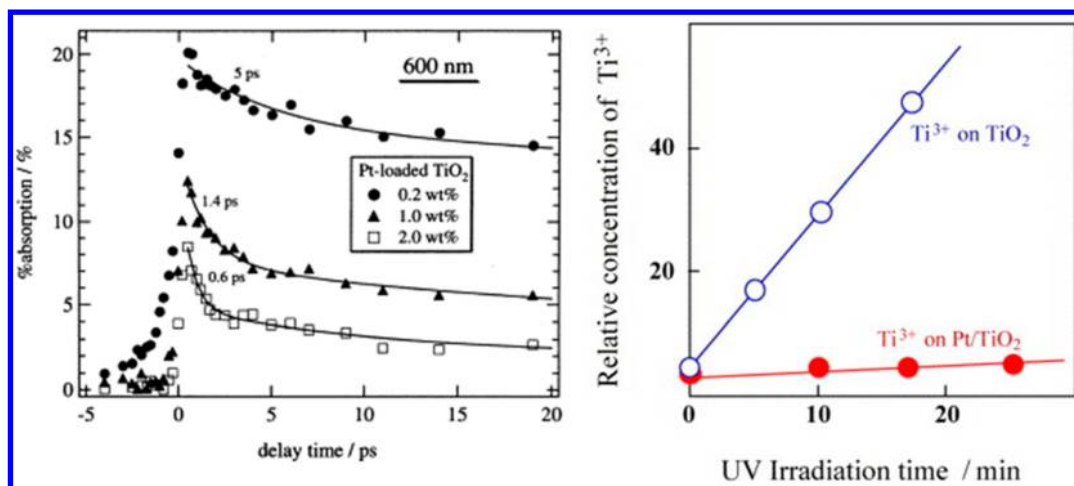


Figure 17. (a) Dependence of the transient absorption decay curves measured at 600 nm for Pt-loaded TiO₂ powder on the Pt-loading (wt %) following 390 nm laser excitation. Reprinted with permission from ref 184. Copyright 2003 Elsevier. (b) Growth of the ESR signal intensity of the photoformed Ti³⁺ active site on Pt-loaded and unloaded on TiO₂ catalysts (recorded at 77 K). Reprinted with permission from ref 183. Copyright 2001 Elsevier.

particles. The interaction of this localized electric field with the semiconductor induces the formation of charge carriers near the surface of the semiconductor; hence, these charge carriers can reach the respective surface sites on the semiconductor readily. This enhances the electron–hole separation and can, for example, lead to an increased visible light-induced photocatalytic H₂ evolution (vide infra).¹⁹⁰

This SPR effect has been applied for the development of visible active TiO₂ materials. Hereby, the loading of TiO₂ with Au provides an essential advantage over Pt-loading, because Pt⁰/TiO₂ can only be excited by UV light, while Au⁰/TiO₂ has been reported to be excitable also in the visible light region. For example, Fang et al. observed 3 times higher H₂ evolution rates for Au⁰/TiO₂ as compared to Pt⁰/TiO₂ upon excitation at $\lambda > 400$ nm.¹⁹¹ Figure 18 explains one of the proposed models of the

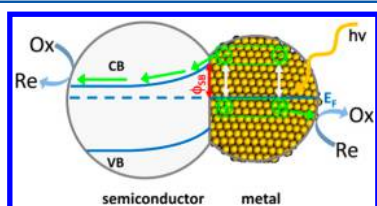


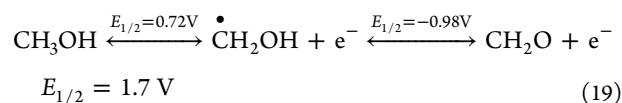
Figure 18. Schematic diagram of the plasmon-induced charge separation and the associated photochemistry at a metal/semiconductor heterojunction. Here, the charge separation is achieved in the metal by the transfer of electrons to the semiconductor. Reprinted with permission from ref 82. Copyright 2012 American Chemical Society.

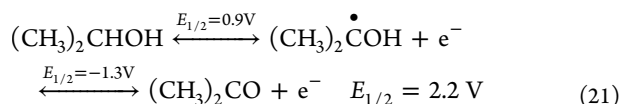
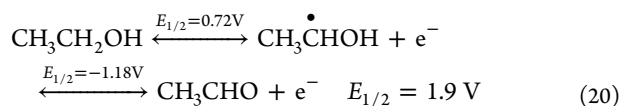
surface plasmon resonance-induced charge carrier formation and the associated charge transfer mechanism. Electrons excited in the metal particles by light absorption with energies exceeding the band bending potential can be transferred from the metal to the semiconductor; thus the reduction and the oxidation reaction will occur spatially separated. However, it should be noted at this point that alternative mechanisms are currently discussed intensely and that no final and definite explanation can therefore be given here. In particular, it seems rather unlikely that the oxidation reaction should take place on the metal surface in these plasmonic systems.

Recently, Furbe et al. published a study concerning the plasmon-induced charge-transfer mechanisms between excited

gold NPs (nanoparticles) and TiO₂, which was performed by means of femtosecond visible-pump/infrared-probe transient absorption spectroscopy.¹⁹² These authors found that the electron transfer from the gold NPs to the conduction band of TiO₂ occurs within 50 fs and that the electron injection yield reached 20–50% upon 550 nm laser excitation. Moreover, they suggested two possible pathways for the injection of the electrons: one through a direct electron–hole generation, and another one related to an enhanced electric field by the excited plasmon.

3.3.2. Photoinduced Oxidation Reactions at the TiO₂ Surface. The latter example demonstrates that metal nanoparticles can not only act as electron acceptors but, following light excitation, also as electron donors. However, in photocatalytic systems, usually more efficient electron donors are applied, such as different alcohols. Tamaki et al. investigated the reaction dynamics of the trapped holes by means of TAS and found that in the presence of alcohols the transient absorption of the trapped holes decayed more rapidly, clearly indicating that trapped holes can react with these alcohols.¹⁹³ The lifetime of the trapped holes in methanol, ethanol, and 2-propanol was found to be 300, 1000, and 3000 ps, respectively. The charge-transfer rate was also reported to be effected by the adsorption behavior of the adsorbates at the TiO₂ surface. For example, it was found that methanol and ethanol adsorb predominately via a dissociative pathway on the rutile surface, resulting in the formation of surface alkoxide and hydroxyl groups, with the charge transfer from the alkoxide group to the surface causing an increase of the adsorption strength.^{194–196} Nevertheless, under UV irradiation of the TiO₂ particles, these surface alkoxide groups serve as effective hole trapping centers. Generally, it is assumed that the hole or •OH-induced alcohol oxidation proceeds via two reaction steps according to eqs 19–21 (values taken from ref 197): the first step includes the cleavage of the C–H bond resulting in the formation of the respective α -hydroxyalkyl radicals, while the formation of the respective aldehyde occurs in the second step under injection of an electron into the conduction band of TiO₂, called “current doubling”.^{198–200}





The thermodynamic driving force for the oxidation of the different alcohols correlates very well with the kinetic values observed by Tamaki et al. However, it should be noted that the charge transfer can be inhibited, for example, through the formation of a hydrate shell. For example, no reduction of Ag^+ cations by the α -hydroxyalkyl radical has been observed, although the difference in the respective half-wave potentials is very large.²⁰¹ Nevertheless, it is important to mention here that the reduction of Ag^+ and the corresponding formation of Ag^0 is not such a simple process as the formation of atomic Ag is energetically difficult.²⁰² It usually requires an accumulation of electrons leading to the formation of silver clusters. Moreover, Henderson et al. demonstrated that chemisorbed water molecules have no influence on the methoxy photochemistry, while water molecules hydrogen-bonded in the second layer to bridging oxygen (O_{br}) sites inhibit the methoxy photodecomposition to formaldehyde.²⁰³ These sites act as proton acceptors for the photochemical cleavage of C–H bonds during the photoconversion of adsorbed methoxy-groups to formaldehyde. Morris et al.¹⁹⁶ proposed an overall photooxidation mechanism of methanol on the surface of TiO_2 nanoparticles as shown in Figure 19. Their experimental data showed that

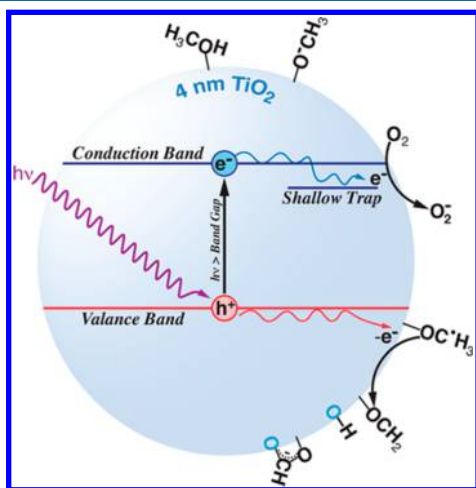


Figure 19. Photooxidation mechanism of methanol on rutile TiO_2 nanoparticles in the presence of molecular oxygen. Reprinted with permission from ref 196. Copyright 2012 American Chemical Society.

methanol adsorbs predominantly via a dissociative pathway on the surface of 4 nm rutile nanoparticles to produce surface methoxy and hydroxyl groups. These surface methoxy groups serve as effective hole trapping centers under irradiation with UV light. The hole trapping by methoxy groups leads to an effective charge separation as supported by the IR absorption of long-lived free and shallowly trapped electrons. A two-electron transfer process involving the initial formation of a radical anion through the direct hole oxidation of the methanol molecule followed by a prompt electron injection from this radical anion into the TiO_2 conduction band is suggested (i.e., the above-mentioned current-

doubling process). Furthermore, the studies by Morris et al.¹⁹⁶ showed that the role of O_2 in promoting methanol photodecomposition is to scavenge free electrons, which opens acceptor sites for the injection of new electrons during the methoxy group oxidation. In this way, O_2 increases the photonic efficiency by a factor of 5 without affecting the hole-mediated oxidation mechanism.

In summary, the photo-oxidation of methanol leads to the relocation of the trapped holes and to the accumulation of the electrons on the TiO_2 surface causing a downward band bending in the semiconductor as shown in Figure 20. In the absence of molecular oxygen as effective electron scavenger, TiO_2 changes its color from white to blue, indicating the formation of Ti^{3+} centers. The photogenerated electrons are located in the respective traps at the photocatalyst surface and are available now for different reduction reactions.^{180,181}

Montoya et al.^{204,205} investigated the photooxidation of benzene as an alternative electron donor. It is the crucial point of this work that the important role of the 2-fold-coordinated TiO_2 surface bridging oxygens has been emphasized. The latter's ability to trap photogenerated holes and to act as the main oxidizing agents, leaving the surface of the catalyst and becoming part of the intermediates and final reaction products, has been probed by using isotopic labeling reactions. Time evolution of the $\text{C}^{16}\text{O}^{18}\text{O}/\text{C}^{16}\text{O}_2$ QMS (quadrupole mass spectrometer) ratios of several benzene photo-oxidation experiments using labeled (Ti^{18}O_2) or unlabeled (Ti^{16}O_2) titania as photocatalysts are shown in Figure 21a, upper. When Ti^{16}O_2 was used as photocatalyst, a constant $\text{C}^{16}\text{O}^{18}\text{O}/\text{C}^{16}\text{O}_2$ ratio of 0.7% was obtained, which is readily explained by the natural content of ^{18}O in the water. In contrast, experiments with Ti^{18}O_2 showed a fast increase of the $\text{C}^{16}\text{O}^{18}\text{O}/\text{C}^{16}\text{O}_2$ ratio immediately after the illumination was started. Notably, it has been observed that the increase of the $\text{C}^{16}\text{O}^{18}\text{O}/\text{C}^{16}\text{O}_2$ ratio was more pronounced as the water concentration decreased. To gain information on the number of surface lattice oxygen atoms O_s that have been incorporated into the evolved CO_2 , the definite integral of the curve of C^{16}O_2 (in mmol h^{-1}) versus time (see Figure 21a, lower) and the definite integral of the QMS signal ration versus time in the time range $35\text{ min} < t < 270\text{ min}$ have been calculated. By combining the above results, values of 1.45×10^{16} , 1.93×10^{17} , 5.72×10^{17} , and 0.0 were found for curves 1, 2, 3, and 4 of Figure 21a, upper and lower. From the observed results, Montoya et al.²⁰⁵ derived the TOIET (terminal-oxygen indirect electron-transfer) mechanism involving three reaction steps: (1) hole trapping at surface lattice oxygen atoms resulting in the formation of terminal oxygen radicals, which are able to react with dissolved substrate species; (2) the incorporation of terminal oxygen radicals into photo-oxidation products with the simultaneous generation of TiO_2 surface oxygen vacancies; and (3) the dissociative adsorption of O_2 or H_2O molecules into terminal oxygen vacancies resulting in the “healing” of the catalyst surface (see Figure 21b).

The proposed TOIET mechanism excludes the participation of free and also of surface-bound hydroxyl radicals in photocatalytic oxidation reactions, thus contradicting most commonly assumed mechanisms involving hydroxyl radicals as major oxidative species. It is interesting to note here that Hoffmann and co-workers have actually suggested superficially adsorbed hydroxyl groups to act as electron trapping sites as shown in Figure 21b.²⁰⁶

While a fast reaction of the trapped holes with different alcohol molecules on the time scale of several picoseconds has been

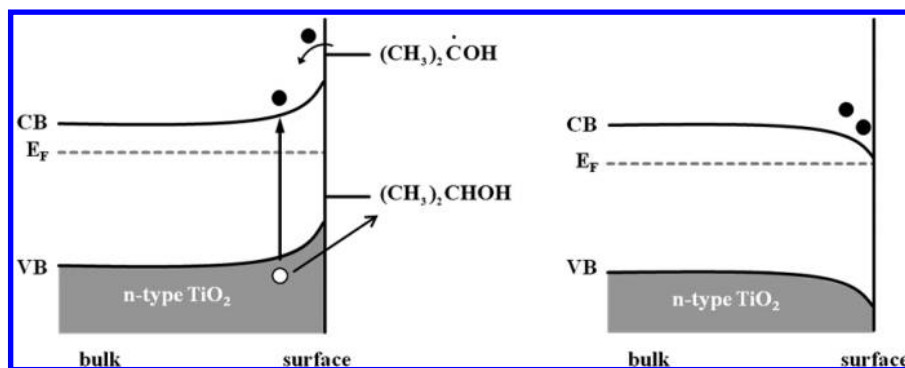


Figure 20. Schematic diagram of the photoinduced downward band bending of TiO_2 in the presence of 2-propanol acting as electron donor. An alternative energy diagram of TiO_2 in the presence of 2-propanol has been suggested by Kira et al.²⁰⁰

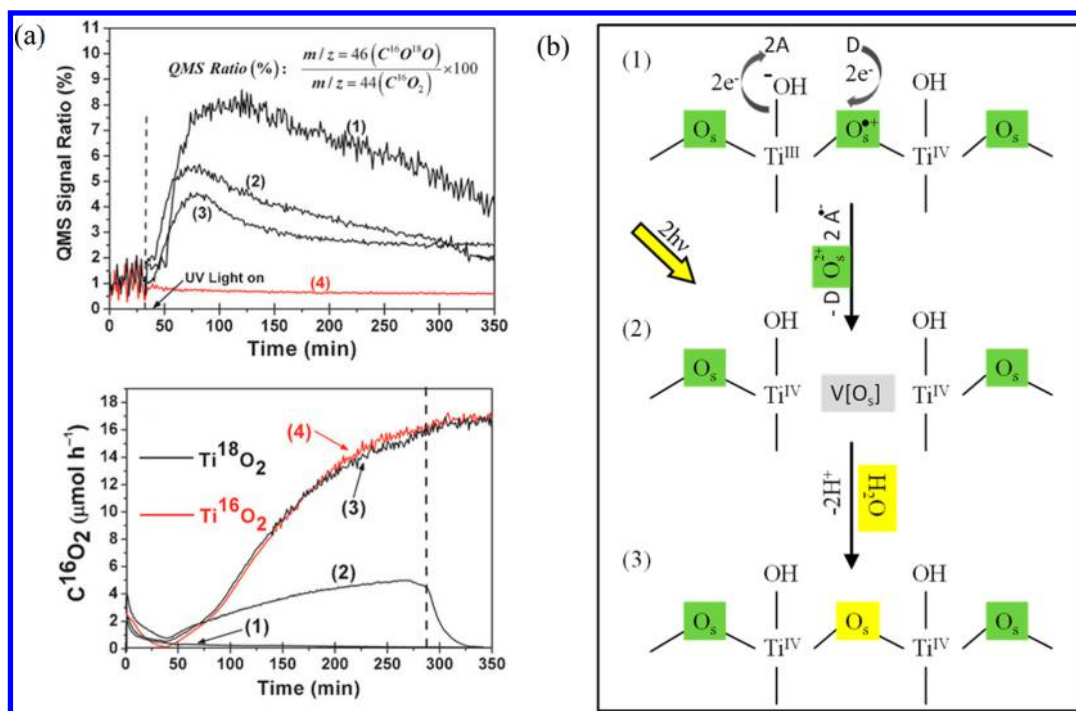


Figure 21. (a) Time evolution of the $\text{C}^{16}\text{O}^{18}\text{O}/\text{C}^{16}\text{O}_2$ QMS signal ratio from benzene photo-oxidation experiments with Ti^{18}O_2 (curves 1, 2, and 3 (black)) and Ti^{16}O_2 (curve 4 (red)) and water concentrations of $[\text{H}_2\text{O}] = 0.560 \text{ mM}$ (1), $[\text{H}_2\text{O}] = 10 \text{ mM}$ (2), $[\text{H}_2\text{O}] = 24 \text{ mM}$ (3), and $[\text{H}_2\text{O}] = 24 \text{ mM}$ (4) (upper). Time evolution of C^{16}O_2 production rate (r_{CO_2}) from benzene photocatalytic mineralization experiments (lower). All experiments were carried out under Ar flow in the presence of Ag^+ ions as electron acceptors. Adapted with permission from ref 205. Copyright 2014 John Wiley and Sons Ltd. (b) Photocatalytic oxidation process under active participation of the surface lattice oxygen atoms leading to the reconstruction of the TiO_2 surface.

observed, it was shown that holes that manage to survive until the nanosecond time scale exhibit lower reactivity. These deeply trapped holes exhibiting characteristic transient absorption maxima at 450 nm are neither able to oxidize dichloroacetate, DCA^- , nor thiocyanate, SCN^- , anions. Bahnemann et al.¹⁵¹ concluded from these results that just shallowly trapped holes, h^+_{tr} , being in a thermally activated equilibrium with free holes, are able to initiate such oxidation reactions. Moreover, calculations using the Marcus electron transfer theory for adiabatic processes resulted in a reorientation energy $\lambda = 0.64 \text{ eV}$, suggesting that in the case of SCN^- the hole transfer should occur in the adsorbed state. Furube et al. have observed an ultrafast hole transfer from TiO_2 to surface adsorbed SCN^- taking place in less than 1 ps followed by a subsequent structural stabilization of the formed $(\text{SCN})_2^{\bullet-}$ within a few picoseconds.²⁰⁷

The photocatalytic alcohol oxidation via trapped hole states clearly showed that the charge transfer depends on the difference between the oxidation potential of the substrate molecules and the oxidation potential of the trapped holes. However, one of the most interesting predictions of the electron transfer theory has been developed by Hush and Marcus. According to their theory, the electron transfer rate constant increases with an increasing electrochemical driving force in the so-called normal region, while in the so-called inverted region the reactivity decreases again with a further rise of the electrochemical driving force.^{208,209} Most studies of electron-transfer processes from the semiconductor conduction band to oxidized adsorbed dye molecules (i.e., the undesired back reaction of the dye-sensitized solar cell, DSSC) indeed exhibit the expected trend.^{210–212} Figure 22 shows the dependency of the electron transfer rate constant on the redox potential of various inorganic

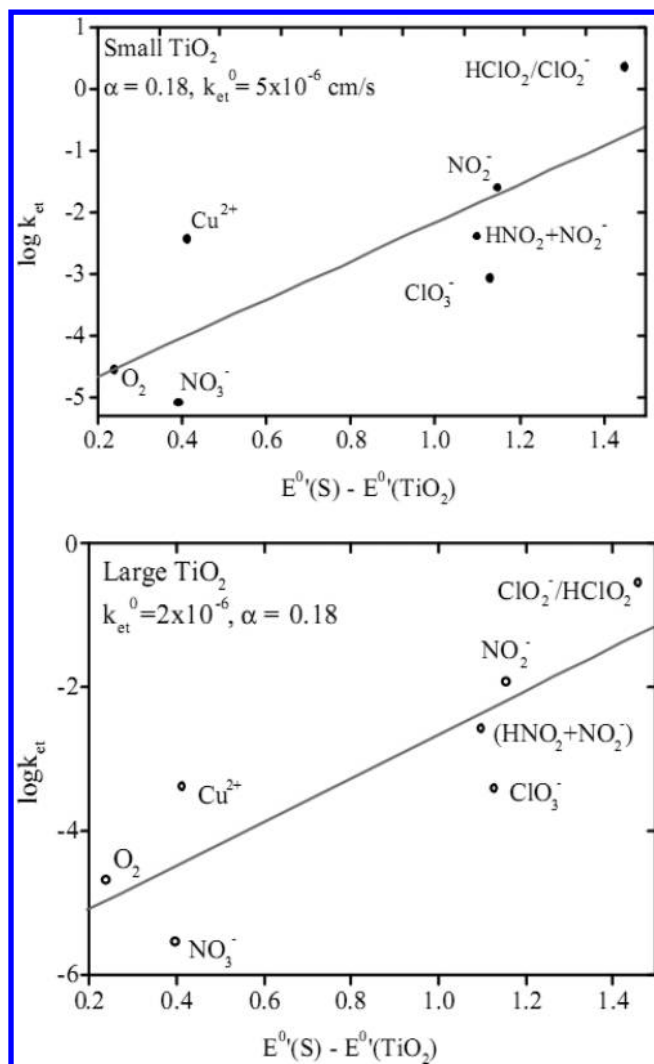


Figure 22. Dependency of interfacial electron transfer rates on the redox potentials. The individual points are average values (small TiO_2 , 16 TiO_2 molecules/particle, surface area $3.8 \times 10^{-14} \text{ cm}^2$; large TiO_2 , 1640 TiO_2 molecules/particle, surface area $7.4 \times 10^{-13} \text{ cm}^2$; k_{et} and k_{et}^0 are the interfacial electron transfer rate constants for single-first order process). Reprinted with permission from ref 213. Copyright 2003 Elsevier.

molecules.²¹³ For both small and large particles, an increase of the one-electron redox potential of the scavenger E_s leads, in most cases, to an improvement of the electron transfer kinetics. These results indicate that the electron transfer rate constant can be predetermined on the basis of the redox potential of the reducing species.

In Figure 22 only reduction reactions involving conduction band electrons are considered. In the case of trapped electrons, the driving force will be reduced, because the trap states are located below the conduction band edge (see Figure 15). During the reactions of the trapped electrons at the TiO_2 surface, the oxidation state of the lattice bound Ti atoms changes from 3 to 4, resulting in a higher reorganization energy and consequently a lower electron transfer rate constant.²¹⁴ Moreover, electrons localized at trap states exhibit lower reactivity as compared to free charge carriers.

However, these electron transfer processes compete with the surface trapping of the conduction band electrons. Because the trapping processes proceed within a time span of less than 1 ps, the electron transfer times should attain 10^{-15} s to dominate within this competition.^{153,214} Because most interfacial charge-transfer processes are, however, found to be much slower, interfacial electron transfer processes usually involve trapped charged carriers, that is, electrons.

4. NOVEL MECHANISTIC ASPECTS OF TiO_2 PHOTOCATALYSIS

Selected examples concerning new and/or alternative mechanistic concepts that have been proposed during recent years to explain certain peculiarities of photocatalytic reactions will be given below. As illustrated in Figure 4 (vide supra), the mechanism of redox processes induced in a photocatalytic system by light absorption is usually presented in diagrams showing one single semiconductor nanoparticle in which the absorption of a photon with an energy exceeding its bandgap energy generates an electron/hole pair (process 1) that either recombines (process 2) or induces two redox processes (processes 5 and 6), both of which take place in close vicinity on the particle's surface. However, considerable evidence has been collected that this mechanistic picture is highly oversimplified.^{215–221} As illustrated in Figure 23, metal oxide nanoparticles tend to form three-dimensional networks via a self-aggregation mechanism when suspended in aqueous solution.²¹⁸ HRTEM analysis of these aggregates showed that

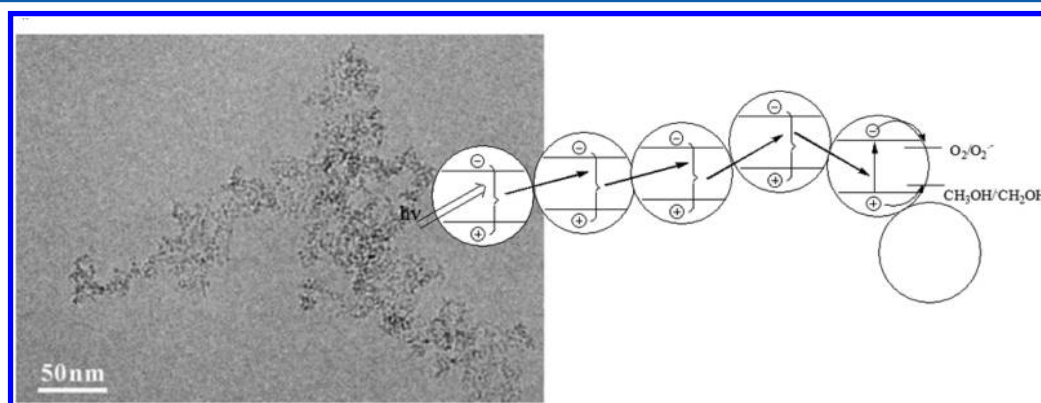


Figure 23. Cryo-TEM image of 0.5 at. % Fe(III)-doped TiO_2 nanoparticles (left) and scheme explaining the increased photocatalytic activity through energy/exciton transfer in aggregated photocatalyst particles, that is, the antenna effect (right). Reproduced with permission from ref 218. Copyright 2003 The Royal Society of Chemistry.

herein the particle–particle contacts do not form in an arbitrary manner but rather involve the exact alignment of the atomic planes of all involved particles. Consequently, the resulting aggregates can be regarded as arrays of nanowires that should allow the transfer of charge carriers without much interference of interfacial trap processes (see Figure 23, right). It should be noted that even though the materials studied here contained 0.5% of Fe^{3+} , this did not result in any measurable shift of the TiO_2 bandgap; that is, it did not result in the formation of visible light active photocatalysts.

This so-called “antenna effect” has meanwhile been observed by various research groups (i.e., list of references given in ref 218) and should in fact be regarded as a new basic concept for photocatalytic systems. Excitons formed through the absorption of light in one of the nanoparticles within this particle framework are likely to be transported throughout until arriving at a suitable trap site. The latter can, for example, be formed through the adsorption of electron acceptors and/or donors on one of the particles belonging to the aggregate. Once one of the charge carriers has been trapped, that is, has been involved in a redox reaction with the adsorbate, the other charge carrier can continue its “journey” through the particle network until reacting itself.²¹⁸ Obviously, the particle network replaces the individual photocatalyst particle shown in Figure 4, thus resulting in an improved photocatalytic activity of the overall system, that is, through a cooperative effect within the network. The good electron mobility within three-dimensional TiO_2 agglomerates actually presents one of the basic functionalities of dye-sensitized solar cells (DSSCs, vide infra) and has thus been thoroughly investigated.

Another interesting aspect of the self-assembled networks of nanoparticles is illustrated in Figure 24. On the basis of the

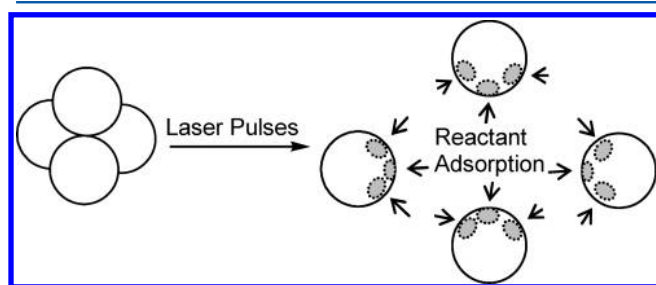


Figure 24. Laser-pulse-induced deaggregation of a close-packed TiO_2 particle tetramer resulting in single particles with additional sites for reactant adsorption. Reprinted with permission from ref 220. Copyright 2004 American Chemical Society.

observation that considerably higher photonic efficiencies can be achieved when the illumination is carried out by a sequence of high-intensity laser pulses rather than by continuous (c.w.) illumination employing an identical amount of photons, the “deaggregation concept” has been proposed to explain these observations.²²⁰

As was already described in detail above, a typical photocatalytic system “wastes” most of the absorbed light energy; that is, more than 90% of the photogenerated electron/hole pairs recombine generating heat and/or light, the energy content of which is considerably lower than the excitation energy (usually, the luminescence maximum is shifted by 100 nm or more toward longer wavelengths, i.e., lower energies). The photodeaggregation model assumes that part of the absorbed energy is used to break the (most likely hydrogen) bonds between the particles,

thus producing additional surface area for the photocatalytic process (resulting in increased photonic efficiencies). The subsequent establishment of the thermodynamic equilibria on the additional surface comprises protonation of the TiO_2 particles, reactant adsorption, and formation of the electrochemical double layer. All of these processes are exothermic, while the enthalpy of deaggregation has been calculated to be ca. +30 kJ/mol.¹¹⁷ Photons at a wavelength of 350 nm (as is usually employed in TiO_2 photocatalysis) possess an energy content of 342 kJ/mol; hence following their absorption there will be sufficient energy deposited within each particle to achieve the deaggregation process.

The above discussion clearly shows that the surface of the photocatalyst particle plays a major role within the individual redox processes that constitute the overall photocatalytic process. Therefore, a detailed study of the chemical transformations occurring at the photocatalyst’s surface should yield important information concerning the individual reaction steps. Unfortunately, the number of experimental techniques suitable to investigate the metal oxide/water interface in vitro, that is, in the presence of bulk water, is very limited. Employing diffuse reflectance infrared spectroscopy (DRIFTS), M. R. Hoffmann and co-workers have studied surface intermediates generated by band gap irradiation of polycrystalline, hydroxylated TiO_2 in great detail.^{206,223–225} A new absorbance at 3716 cm^{-1} was assigned to a Ti(III)O-H^- vibration resulting from the trapping of conduction band electrons at acidic Ti(IV)OH centers.²⁰⁶ A second new absorption band at 3683 cm^{-1} was ascribed to surface-bound $\cdot\text{OH}$ radicals with continuous UV(A) illumination resulting in an extended surface reconstruction of the photocatalyst due to a buildup of the trapped charge carrier concentration.²⁰⁶ The authors observed extended free charge carrier lifetimes, in particular, in dehydrated samples and attributed a very broad IR absorption peak centered at 3380 cm^{-1} to electronic transitions from occupied surface electron trap states located 0.42 eV below the conduction band back into the conduction band.²²⁴

While deeply trapped electrons were found to produce a Stark effect, shallowly trapped electrons apparently induce homogeneous electric fields and react rapidly with O_2 . Szczepankiewicz et al. interpret their results by a model envisaging shallow electron traps that are not associated with localized structures but are rather delocalized across the TiO_2 surface, thus explaining their photon-dependent wettability.²²⁵ Additional DRIFT studies of the same group of authors showed the formation of surficially adsorbed water and carbon dioxide molecules as well as a poisoning of the photocatalytic degradation of dimethyl methylphosphonate.²²³

Employing FTIR spectroscopy as a sensitive tool to study the individual reaction steps during the photocatalytic adsorption and oxidation of oxalate, a series of studies have been executed by Bahnemann and co-workers since 2005.^{226–233}

Following an initial study at an illuminated Degussa P-25 film²²⁷ suffering from the drawback of the material being a mixture of the anatase and the rutile form of TiO_2 and from the problem of distorted adsorption equilibria due to a lack of pH-control during the illumination process, all subsequent studies concerning the adsorption and photoreaction of oxalic acid were carried out on the surface of pure anatase or rutile TiO_2 nanoparticles, respectively, employing strict pH-control throughout (pH-stat conditions).^{229,232,233} In the dark, the adsorption of oxalate was found to attain an equilibrium state that can be

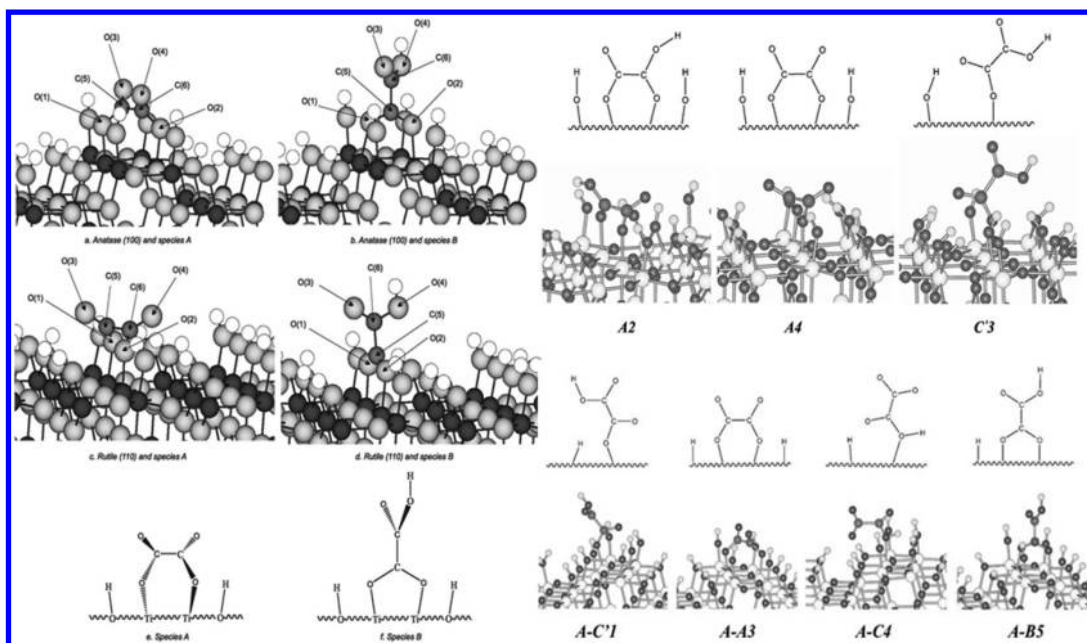


Figure 25. Left: (a and b) Most stable structures for adsorbed oxalic acid on hydrated anatase (100). (c and d) Most stable structures for adsorbed oxalic acid on hydrated rutile (110). The complexes correspond to bidentate structures. (e) Schematic drawing for adsorbed species A on either anatase or rutile. (f) Schematic drawing for adsorbed species B on either anatase or rutile. Black, titanium; dark gray, carbon; light gray, oxygen; white, hydrogen. For better visualization, all atoms belonging to oxalic acid are indicated with arrows and labels. Reproduced with permission from ref 229. Copyright 2006 PCCP Owner Societies. Right upper: Adsorption structures on rutile in the dark. A scheme of every structure is provided. Ti, O, H, and C atoms are represented by large light, dark, small light, and dark-dashed spheres, respectively. Reproduced with permission from ref 232. Copyright 2008 PCCP Owner Societies. Right lower: Adsorption structures on anatase in equilibrium in the dark. A scheme of every structure is provided. Ti, O, H, and C atoms are represented by large-light, dark, small-light, and dark-dashed-gray spheres, respectively. Reproduced with permission from ref 233. Copyright 2009 PCCP Owner Societies.

described as a mixture of adsorbed water and oxalate species, with the latter forming two different surface complexes on anatase and one on rutile particles (Figure 25, left). When the system is subsequently illuminated with UV(A) light, the surface becomes enriched with adsorbed oxalic acid replacing photodesorbed water molecules and one of the adsorbed oxalic acid structures on anatase being favored over the other (for details of the proposed mechanism, see Figure 12 in ref 229).

Subsequent more detailed studies combining ATR-FTIR measurements with quantum-chemical calculations employing the semiempirical method MSINDO revealed that the inclusion of solvation effects is crucial for the determination of the type of denticity and of the structure of the adsorbed complexes. By comparison of the experimental ATR-FTIR data with the theoretical MSINDO calculations, the most likely surface species and the effect of hydration for their relative stabilities were determined.^{232,233} While as shown in Figure 25 (right upper) for the case of rutile the most stable species consist of two bidentate surface complexes followed “in third place” by a monodentate form (ref 232), anatase allows the formation of four species with reversed stability (Figure 25, right lower). In the case of anatase, the main contributors to the surface speciation are two monodentate species differing in the position of the H atom within the molecule (being more stable when placed in the O–C–O moiety remote from the surface) followed by a deprotonated and a monoprotonated bidentate species with their C–C bond being parallel or perpendicular to the TiO₂ surface, respectively.²³³

It is another interesting aspect of the theoretical calculations that they are also able to predict the change in electron density of each individual bond of the various oxalate surface complexes

upon (photo)-excitation. Some selected results of the latter type of calculations are shown in Figure 26A–C.

While the excitation of the monodentate surface structure of oxalic acid on TiO₂ apparently results in a significant increase in electron density directly at the titania surface (Figure 26A), the bidentate surface structure shown in Figure 26B is expected to face increased electron densities at both anchoring positions, that is, very close to one another. In the former case, the increased electron density at one single location at the TiO₂ surface can be expected to lead to the formation of a recombination center, thus lowering the overall photonic efficiency¹⁷⁶ of the photocatalytic process. In the latter case, however, the C–C bond of the oxalate molecule should break, yielding 2 CO₂ molecules (the only detected product of the photocatalytic oxalate degradation). The last case shown in Figure 26C predicts an even more interesting reaction for the other excited bidentate surface complex, that is, the formation of a hydroxyl radical following the breaking of the weakened C–OH bond. Additional experimental evidence is most certainly required to verify these predictions from the theoretical calculations.

Besides the experimental techniques described so far, the combination of electrochemical investigations and measurements of the photocatalytic activity can provide interesting information concerning the properties of nanosized photocatalytic materials. A comparison of the results of Mott–Schottky measurements carried out on different TiO₂ thin film electrodes with the photocatalytic activities of these films for the photocatalytic reduction of methylviologen and the oxidation of methylene blue, respectively, revealed a good correlation of both the flatband potential and the donor density with the photonic efficiencies of the photocatalytic methylviologen

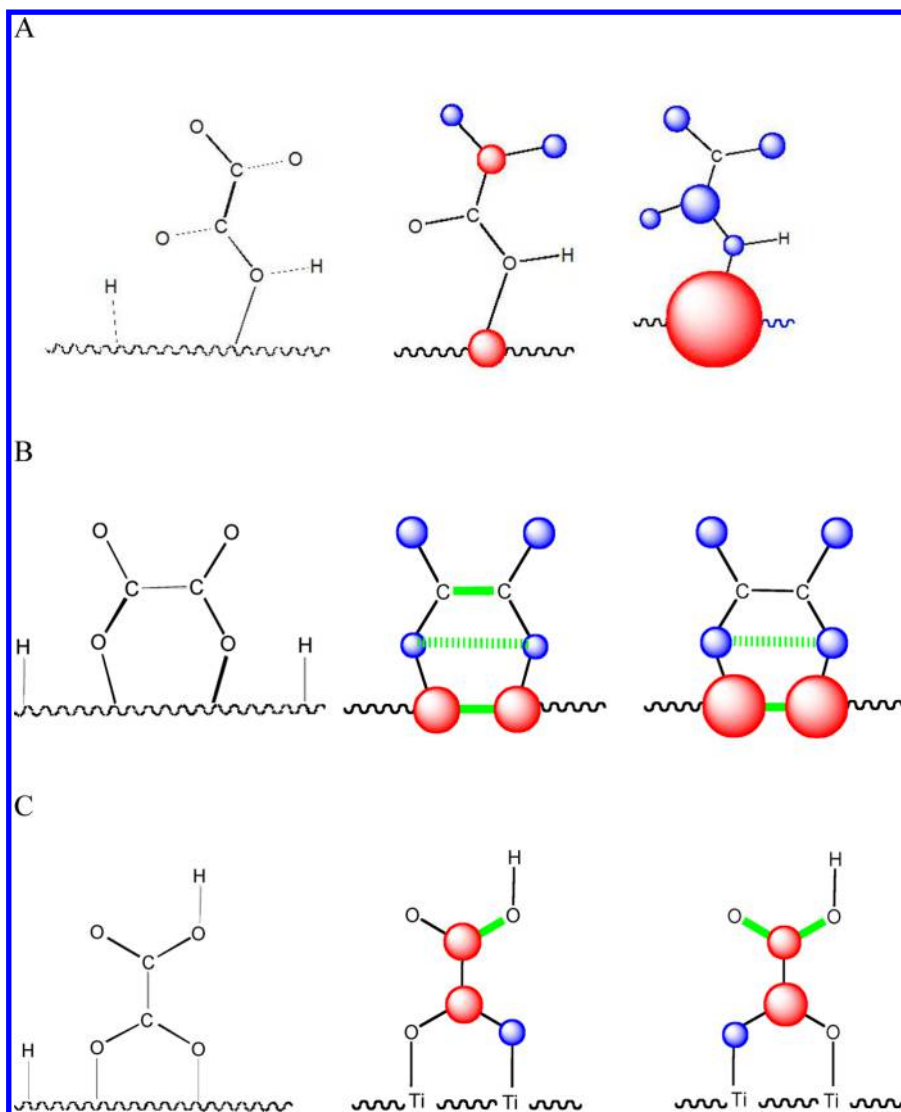


Figure 26. (A) Predicted first (middle) and second (right) excited structures of adsorbed oxalate in the ground structure with a single surface bond (left) evincing the formation of a surficial recombination center upon excitation; red, increased electron density; blue, decreased electron density. Reproduced with permission from ref 233. Copyright 2009 PCCP Owner Societies. (B) Predicted first (middle) and second (right) excited structures of adsorbed oxalate in the ground structure with two surface bonds to different carbon atoms (left) evincing the generation of CO_2 upon excitation; red, increased electron density; blue, decreased electron density; green, weakened bonds. Reproduced with permission from ref 233. Copyright 2009 PCCP Owner Societies. (C) Predicted first (middle) and second (right) excited structures of adsorbed oxalate in the ground structure with two surface bonds to the same carbon atom (left) suggesting the formation of hydroxyl radicals upon excitation; red, increased electron density; blue, decreased electron density; green, weakened bonds. Reproduced with permission from ref 233. Copyright 2009 PCCP Owner Societies.

reduction.²³⁴ This is readily explained by the fact that the more negative is the flatband potential, the higher are both the donor density and the photonic efficiency of the photocatalytic methylviologen reduction. However, no such dependency was found for the photonic efficiency of the photocatalytic methylene blue oxidation. Hence, for an n-type semiconductor, the electrochemical results obtained in the dark can always be expected to be very useful for the prediction of its reductive photocatalytic properties, while for a p-type semiconductor the reverse prediction should be possible. This is in good agreement with the quasi-Fermi-level concept known from fundamental photoelectrochemistry. This is described in detail by Memming et al.^{235,236}

5. SYNTHESIS OF TiO_2 NANOPARTICLES AND NANOPARTICULATE STRUCTURES

Two fundamentally different approaches are usually used to synthesize nanoparticles. While the so-called top-down approach starts with the bulk material and employs various techniques such as mechanical milling, laser ablation, sputtering, etc., to finally obtain the desired particle sizes, the so-called bottom-up approach uses chemical synthesis methods starting from appropriate molecular precursors. Here, the focus will be on the latter methodology as this has been shown to yield materials with higher photocatalytic activity.

The optical absorption spectra measured during the synthesis of transparent colloidal solutions of extremely small titanium dioxide particles ($d < 3$ nm) in water are presented in Figure 27a. So-called quantum-size effects are observed during particle growth and at the final stages of synthesis. They can be

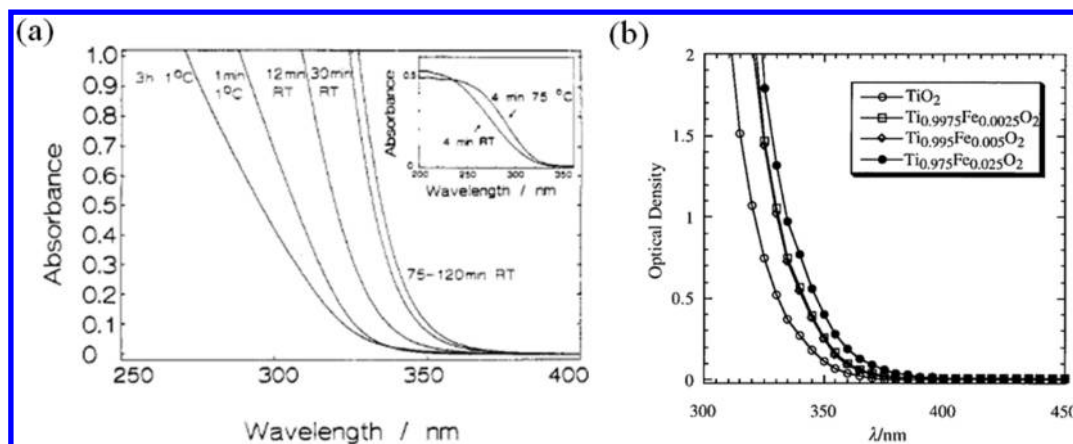


Figure 27. (a) Absorption spectra of TiO_2 colloids at various growth stages, obtained by hydrolysis of 5 mM TiCl_4 . Reprinted with permission from ref 237. Copyright 2014 American Chemical Society. (b) Absorbance spectra of TiO_2 and iron-doped TiO_2 nanoparticles in colloidal aqueous solution. Reproduced with permission from ref 215. Copyright 2000 The Royal Society of Chemistry.

qualitatively interpreted by using a simple molecular orbital (MO) picture as shown in Figure 28 and have been quantitatively

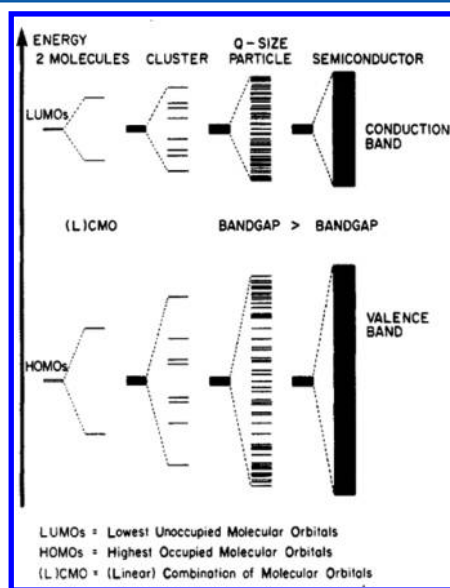


Figure 28. MO model for the particle growth of colloidal TiO_2 particles. Reprinted with permission from ref 238. Copyright 1987 American Chemical Society.

explained by using a quantum mechanical model developed by Brus.³² The particles prepared in aqueous solution were found to possess the anatase structure and consisted of about 200 TiO_2 molecules at their final growth stage. The colloidal particles can be isolated from solution as white powders that are soluble in water and ethanol with no apparent change in their properties. In organic solvents the quantum-sized TiO_2 particles appear to form with rutile rather than with anatase structure. Excess negative charge on the particles resulting either from deprotonated surface hydroxyl groups or from photogenerated or externally injected charge carriers causes a blue shift in the electronic absorption spectrum, which is readily explained by an electrostatic model. Electrons can be trapped in the solid as Ti^{3+} species exhibiting a characteristic visible absorption spectrum. As much as 10% of the available Ti^{4+} ions can be reduced photochemically in the solid with a quantum yield of 3%.

Molecular oxygen reoxidizes the Ti^{3+} centers, leading to detectable amounts of surface-bound peroxides.²³⁷

Because the photocatalytic activity of most “pure” metal oxide photocatalysts such as these prepared in refs 237,238 is in most cases found to be rather small and, moreover, limited to illumination by UV(A) light, various attempts have been made to improve both the efficiency as well as the capability to utilize visible photons for the photocatalytic process. Doping with transition metal ions presents one approach that has been widely employed. Often the respective research has been focused on the incorporation of Fe^{3+} ions into the TiO_2 matrix; for example, colloidal Ti/Fe mixed oxide nanoparticles have been synthesized in aqueous solution with the Fe^{3+} content varying from 0.05 to 50 at. % and particle diameters between 4 and 6 nm.²³⁹ The photocatalytic activity of these Ti/Fe mixed oxide particles was compared to that of pure colloidal TiO_2 , and it was noted that the efficiency of the destruction of the model pollutant dichloroacetate (DCA) obtained with the former particles is always higher than that of the latter.²³⁹

Fe(III) -doped TiO_2 nanoparticles have also been prepared from organometallic precursors and were found to exhibit strongly enhanced photocatalytic activity as demonstrated by the quantum yields measured for the formation of formaldehyde during the photocatalyzed oxidation of methanol in aqueous solution (Φ up to ca. 15%).²¹⁵ Figure 27b shows the absorbance spectra of as-prepared samples of neat TiO_2 and of TiO_2 doped with different amounts of Fe(III) . From these spectra, the bandgap energies, E_g , of the colloidal particles were obtained as 3.32, 3.25, 3.22, and 3.07 eV for 0, 0.25, 0.5, and 2.5 at. % iron, respectively. Clearly, E_g decreases with increasing iron content, thus enabling the absorption and hopefully also the utilization of longer wavelengths (visible) photons for the photocatalytic process.²¹⁵ Three-dimensional networks of these Fe(III) -doped TiO_2 nanoparticles (2–4 nm) have been detected by cryo-TEM (transmission electron microscopy) in an aqueous environment.²¹⁹ High-resolution TEM studies show that the nanoparticles prefer to align along their crystallographic orientation. Consequently, as a novel energy transfer mechanism, the antenna mechanism described above (see Figure 23, right) has been suggested here for the first time to explain the enhanced photocatalytic activities of these colloidal preparations.²¹⁹

Another promising approach to increase the photocatalytic activity of metal oxide semiconductor particles has been shown to be the deposition of (in most cases noble metal) catalysts on

their surfaces (as was already illustrated in Figure 2). Aiming to investigate this concept concerning its suitability for technical applications, three commercially available TiO_2 -photocatalysts, Degussa (now named Evonik-Degussa Airoxide) P25, Sachtleben Hombikat UV100, and Millennium (now named Crystal Global) PC50, were platinized by a photochemical impregnation method employing two ratios of platinum deposits (0.5 and 1 wt %).²⁴⁰ The photocatalytic activities of these samples were determined using three different model compounds: EDTA, 4-chlorophenol (4-CP), and dichloroacetic acid (DCA). While in the case of EDTA its disappearance was studied, total mineralization was measured for 4-CP and DCA. In all cases, the photocatalytic activity was found to increase with rising amounts of Pt, for example, the photonic efficiency for DCA degradation increased from $\zeta = 12.2\%$ for pure Hombikat UV100 to $\zeta = 32.1\%$ for Hombikat UV100/0.5 wt % Pt and to $\zeta = 42.7\%$ for Hombikat UV100/1 wt % Pt. Promising results were also achieved for the total mineralization of 4-CP. The photonic efficiency rose from $\zeta = 0.82\%$ using unmodified PC50 to $\zeta = 1.14\%$ with PC50/0.5 wt % Pt (zero-order kinetics assumed in all cases). Similar results were obtained with the other newly synthesized catalyst samples and for the model compound EDTA. No immediate relationship between the photocatalytic activity of the catalyst samples and their physical properties (surface area, adsorption of pollutants, absorption of light) could be observed. The proposed mechanism of the photocatalytic process in the presence of surficial Pt nanocontacts is illustrated in Figure 29.²⁴⁰

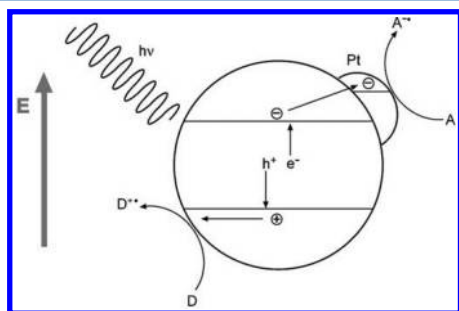


Figure 29. Fate of electron–hole pairs in platinized semiconductors: diffusion of the charge carriers to the surface competes with their recombination, leading to the production of heat before trapping at the surface by acceptors A and donors D. Trapping of the electrons from the semiconductor conduction band is enhanced by platinum islands due to a Schottky barrier at the metal–semiconductor interface, thus leading to reduced recombination of the charge carriers. Reprinted with permission from ref 240. Copyright 2002 Elsevier.

Materials prepared in the form of nanoparticles or powders usually do not present the most suitable form for practical applications. In particular, separation steps following, for example, the successful treatment of a pollutant aquifer present a (mostly very costly) technological problem. Therefore, it is of great importance to develop routes for the immobilization of the particulate photocatalysts resulting in stable surface coatings of the desired substrates without losing the photocatalytic activity of the nanopowder. A very successful example for this approach has been the preparation of TiO_2 coatings on sintered borosilicate glass (100–160 mm pore size) employing a synthetic route based on the hydrolysis of titanium oxysulfate (TiOSO_4).²⁴¹ The morphology of the coatings was studied by scanning electron microscopy (SEM), showing TiO_2 layers with

a smooth and homogeneous structure covering the entire surface of the particles forming the sintered glass (shown in Figure 30, upper). The photocatalytic activity of the TiO_2 coatings was analyzed employing the photooxidation of glucose in water as test reaction. The influence of the preparation conditions of the coatings on their photoactivities was studied. It was found that the starting concentration of the precursor and the aging time were two parameters of significant relevance for the final properties of the catalysts. With specific preparation parameters, photonic efficiencies up to 4% for the total mineralization of glucose in water could be reached. The effect of the reaction pH during the photocatalytic tests on the efficiency of these coatings was also studied, with the glucose degradation being more favorable at high pH values. Stability and lifetime of the coatings were tested following the evolution of their photocatalytic activity for more than 4000 h of continuous operation. No appreciable degradation of the coatings could be observed during this entire operation time.²⁴¹

An optimization of this preparation method to obtain more stable and photoactive supported TiO_2 layers was achieved by the control of the different preparation parameters influencing the final properties of the supported TiO_2 (see Figure 30, lower left). A comparative study with other coatings prepared by sol–gel or hydrolysis methods on sintered glass was performed. The examination of the coatings by scanning electron microscopy (SEM) showed a notably different morphology depending on the preparation method. The optimized supported TiO_2 prepared by thermal hydrolysis of TiOSO_4 exhibited a considerably higher photoactivity as compared with the other studied coatings, reaching values of the photonic efficiencies as high as 7%. The stability and lifetime of the most active supported TiO_2 were tested following the evolution of its photocatalytic activity for more than 5 months of continuous operation (see Figure 30, lower right). No decrease of the efficiency could be observed during this time.^{241,242}

It has been pointed out at various stages throughout this Review that self-assembled structures often exhibit extraordinarily high photocatalytic activities that are explained by the antenna (exciton and/or charge carrier transport) effect. Hence, it appears to be highly desirable to deliberately synthesize such structures. Therefore, well-ordered (often mesoporous) structures have been prepared by Ismail et al., and their photocatalytic properties have been examined. Some examples will be given in the following.

Well-ordered TiO_2/Au nanocomposites were prepared using a sol–gel process in the presence of the poly(ethylene oxide)106–poly(propylene oxide)70–poly(ethylene oxide)106 triblock copolymer (Pluronic F127) as structure directing agent. The content of Au in the TiO_2 network was 0.3, 0.5, 1, and 2 wt %, respectively. The TEM images of the 2 wt % Au/TiO_2 nanocomposites shown in Figure 31 (left) reveal a network of anatase nanoparticles with sizes of 12 ± 2 nm, while the Au particles exhibit diameters of 20 ± 5 nm. The results of the photocatalytic performance tests (Figure 31, right) show higher photonic efficiencies for the oxidation of methanol to formaldehyde for the TiO_2/Au nanocomposites as compared to pure TiO_2 nanocomposites and commercial Degussa P25, respectively, with the 1 wt % Au/TiO_2 sample being most active.²⁴³

Interesting results have also been obtained when titanium dioxide nanoparticles were modified with Pt–polypyrrole nanocomposites through the simultaneous in situ reduction of Pt(IV) and the oxidative polymerization of pyrrole monomers at ambient temperature. The photonic efficiencies of H_2 production

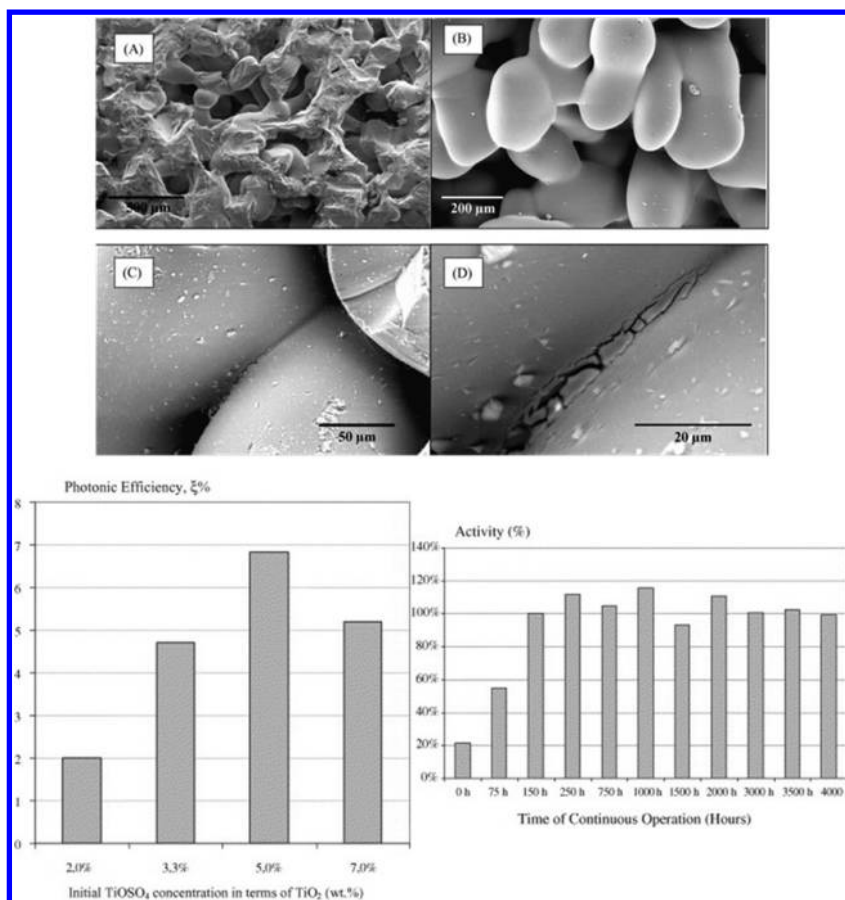


Figure 30. Scanning electron microscopy images for uncoated sintered glass (A and B) and TiO₂ coating on borosilicate sintered glass (C and D) (upper²⁴¹) and influence of the initial concentration of titanium oxydisulfate in the dipping solutions (in terms of the content of TiO₂) on the photonic efficiencies for the total photocatalytic mineralization of glucose ($\zeta\%$) of the supported TiO₂ on sintered glass (lower left²⁴²). Percentage of the initial activity of the supported TiO₂ on sintered glass prepared by thermal hydrolysis of TiOSO₄ over 4000 h of continuous operation (ca. 5.5 months) in the photocatalytic degradation of glucose in water. Flow rate 40 L/h, photon flow 1.6×10^{18} photons s⁻¹ (lower right²⁴²). Adapted with permission from refs 241 and 242. Copyright 2004 and 2005 Elsevier.

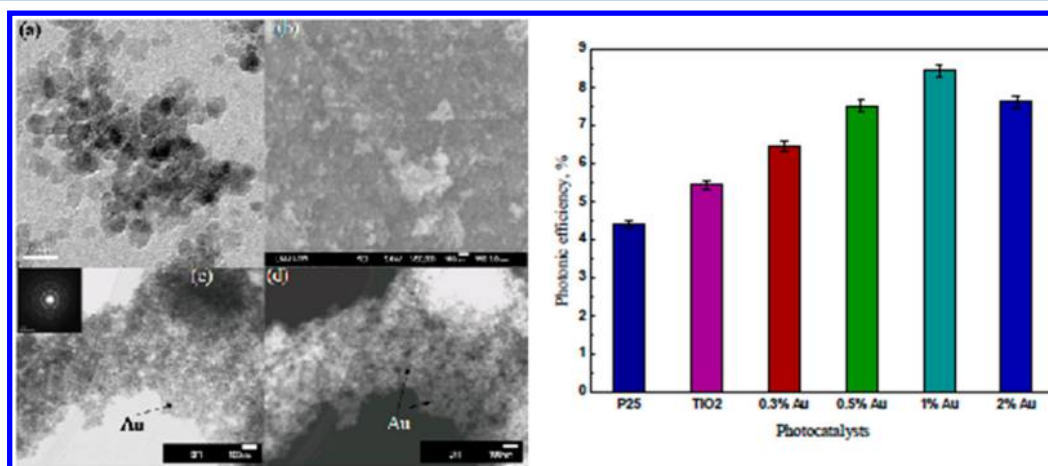


Figure 31. TEM image of 2% Au/TiO₂ nanocomposites (left (a)); SEM image of 2% Au/TiO₂ calcined at 500 °C for 4 h (left (b)); BF-STEM (with Au electron-diffraction as inset) and DF-STEM images of 2% Au/TiO₂ (left (c) and d). Photonic efficiencies of photocatalytic formaldehyde formation from methanol over commercial Degussa P25, pure TiO₂, and 0.3, 0.5, 1, and 2 wt % Au/TiO₂. Photocatalyst loading 0.5 g/L, 30 mM methanol, O₂-saturated, photon flow 4.5×10^{-6} einstein L⁻¹ s⁻¹ ($\lambda > 320$ nm). Error bars represent standard deviations (right). Reprinted with permission from ref 243. Copyright 2009 Journal of Advanced Oxidation Technologies.

in aqueous solutions containing methanol as sacrificial electron donor were found to be $\zeta = 10.6 \pm 0.5$ and $\zeta = 4.5 \pm 0.2\%$ for TiO₂ modified with Pt–polypyrrole nanocomposites and for Pt-loaded TiO₂ prepared by a photochemical deposition method,

respectively.²⁴⁴ As shown in Figure 32, a synergistic effect between Pt nanoparticles and polypyrrole yielding a better charge carrier separation is proposed to explain the enhanced activity of the newly synthesized photocatalysts.

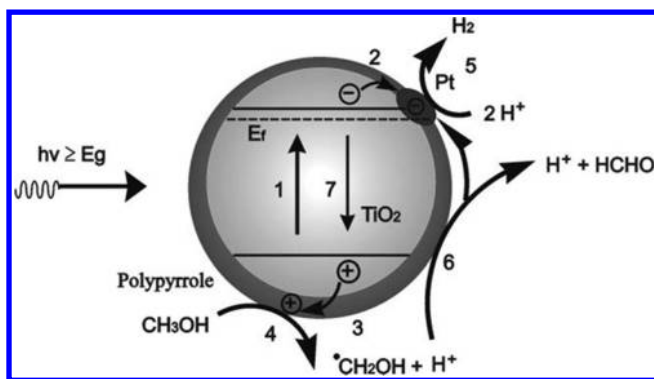


Figure 32. Scheme representing the enhancement of the charge carrier separation and the photocatalytic activity of TiO_2 modified with Pt-polypyrrole nanocomposites: (1) photogeneration of charge carriers, e^- and h^+ ; (2) trapping of e^- at Pt islands; (3) channeling of photogenerated holes by polypyrrole to the polymer/solution interface; (4) first oxidation step of CH_3OH ; (5) reduction of H^+ ; (6) formation of HCHO through e^- injection into the conduction band of TiO_2 (current-doubling); and (7) recombination channel. Reproduced with permission from ref 244. Copyright 2009 The Royal Society of Chemistry (RSC) on behalf of the European Society for Photobiology, the European Photochemistry Association, and RSC.

Highly ordered hexagonal $P6m$ mesoporous palladium-doped titania nanoarchitectures can be readily prepared using the F127 triblock copolymer as a template. They exhibit high surface areas (up to $223 \text{ m}^2/\text{g}$) and large pore volumes (up to $0.42 \text{ cm}^3/\text{g}$).²²² Transmission electron microscopy (TEM) measurements evince that the mesoporous framework is composed of aligned anatase phase grown along the $[101]$ direction (Figure 33 (upper), for details see ref 222). The Pd nanoparticles are well dispersed with sizes of about 20 nm.

This study revealed that mesoporous Pd/ TiO_2 nanostructures exhibit a 2.5 times higher activity for the photooxidation of CH_3OH than Pd/Hombikat UV-100 (i.e., a commercial photocatalyst in the presence of Pd nanocontacts). This increased activity was explained by a three-dimensional antenna effect as illustrated in the scheme shown in Figure 33 (middle). The photocatalytic oxidations of methanol using either highly ordered hexagonal networks in samples calcined at 350°C , catalysts with randomly ordered mesoporous channels after calcinations at 450°C , or disordered mesostructures prepared at 550°C are comparable (Figure 33, lower), although the crystallinity of the TiO_2 nanoparticles increases strongly only with calcination temperatures exceeding 500°C . From an economic point of view, ordered mesochannels prepared upon calcination at 450°C are considered to be the optimum for saving energy in the photocatalyst preparation without much loss of photocatalytic performance.

There seems to be a general agreement in the scientific community working in the area of photocatalysis that the anatase crystal structure of TiO_2 exhibits higher photocatalytic activities than the rutile structure. However, other polymorphs of titanium dioxide such as brookite have so far hardly been studied, one reason being that this material is neither commercially available nor very easy to prepare. A novel synthesis route for brookite nanopowder has recently been described by Kandiel et al., who also assessed the photocatalytic activity of this TiO_2 polymorph in detail.²⁴⁵

High-quality brookite TiO_2 nanorods have been obtained by the thermal hydrolysis of commercially available aqueous solutions of titanium bis(ammonium lactate) dihydroxide in

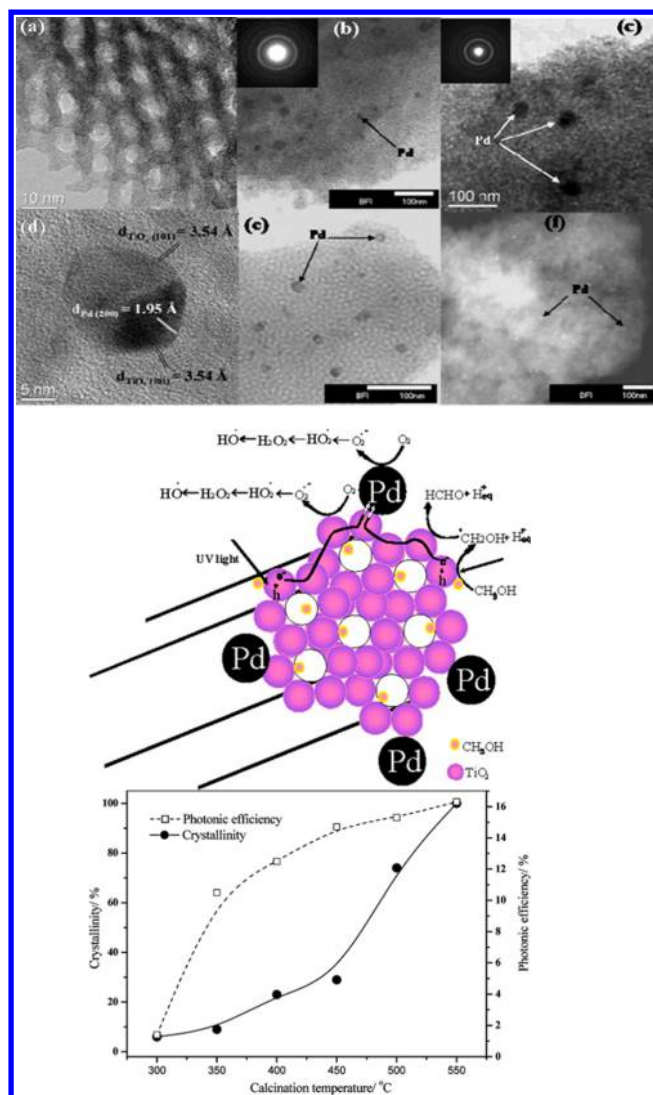


Figure 33. TEM images of two-dimensional hexagonal mesoporous Pd/ TiO_2 nanocomposites calcined at 350°C (a), 400°C (b), and 450°C (c). The insets show the SAED patterns for the anatase phase at 400°C (b) and 450°C (c). HRTEM image of Pd cuboctahedron using the (200) reflection beams and TiO_2 anatase phase using (101) (d), the bright-field TEM images of Pd/ TiO_2 at 350°C (e), and dark-field TEM image of Pd/commercial Hombikat UV-100 (f) (upper). Proposed antenna and reaction mechanism for methanol photooxidation to illustrate the enhanced photonic efficiency of mesostructured Pd/ TiO_2 photocatalysts (middle). Correlation between calcination temperature, crystallinity, and photonic efficiency of mesoporous Pd/ TiO_2 nanocomposites calcined at 300°C , 350°C , 400°C , 450°C , 500°C , and 550°C (lower). Adapted with permission from ref 222. Copyright 2010 American Chemical Society.

the presence of high concentrations of urea ($\geq 6.0 \text{ M}$) as in situ OH^- source, while biphasial anatase/brookite mixtures are obtained at lower urea concentrations (see Figure 34, left).²⁴⁵ It is interesting to note that rutile nanorods are obtained when urea is replaced by NaOH in this synthesis method.²⁴⁶ The ratios between anatase and brookite can readily be tailored by the control of the urea concentration. HRTEM analysis reveals the perfect crystallinity of the material as shown in Figure 34 (upper right). The photocatalytic activity of pure anatase nanoparticles, of anatase/brookite mixtures, and of pure brookite nanorods has been assessed by hydrogen evolution from aqueous methanol

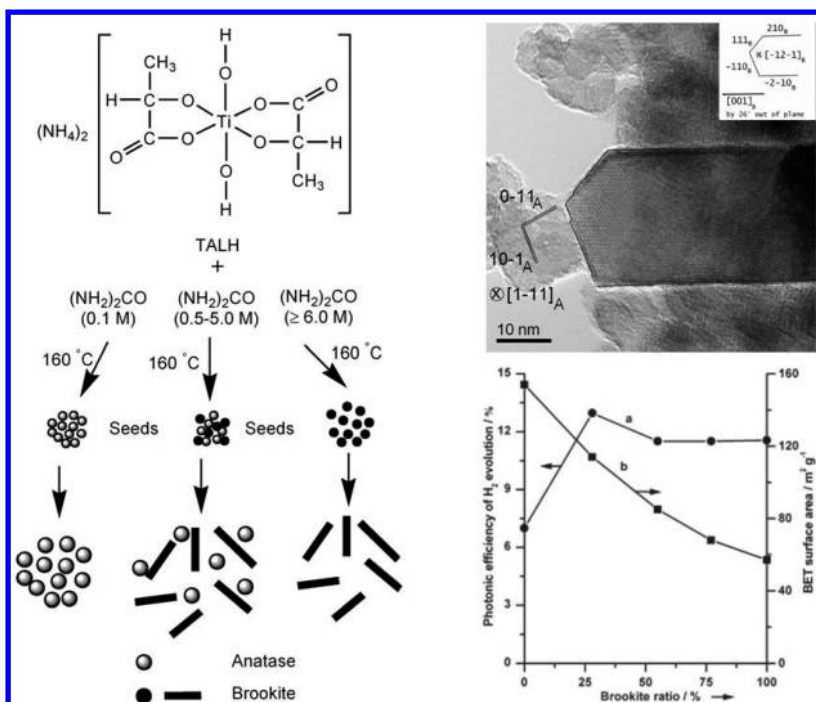


Figure 34. Proposed routes for the formation of anatase nanoparticles and brookite nanorods (left); HRTEM of as-synthesized nanocrystalline TiO_2 powder obtained by thermal hydrolysis of aqueous solutions of the TALC precursor at 160 °C for 24 h in the presence of urea. The rodlike particle of ca. 25 nm in diameter is brookite imaged along the $[1\bar{1}1]_B$ zone axis (see inset). The smaller particle of ca. 15 nm in size is anatase imaged along $[1\bar{1}1]_A$. The labels A and B refer to anatase and brookite, respectively. (upper right) Relation between (a) photonic efficiency, and (b) surface area and the content of brookite; conditions: 0.5 g/L catalyst, 75 mL aqueous methanol solution (4.93 mM), 0.5 wt % Pt (lower right). Adapted with permission from ref 245. Copyright 2010 American Chemical Society.

solution as well as by the degradation of dichloroacetic acid (DCA) in aqueous solution.²⁴⁵ The results indicate that the photocatalytic hydrogen evolution activity of anatase/brookite mixtures and of pure brookite is higher than that of pure anatase nanoparticles despite the lower surface area of the former (see Figure 34, lower right). This behavior has been explained by the fact that the conduction band edge of brookite phase TiO_2 is shifted more cathodically than that of anatase as experimentally evidenced under dark and UV–vis illumination conditions. On the contrary, in case of the photocatalytic degradation of DCA, anatase/brookite mixtures and pure brookite exhibit lower photocatalytic activity than pure anatase nanoparticles. This behavior correlates well with the surface area of the investigated powders.²⁴⁵

6. PREPARATION AND PROPERTIES OF DOPED TiO_2 PHOTOCATALYSTS

As an approach for the development of visible light-responsive titanium dioxide photocatalysts, various photosensitizing dyes adsorbed and/or supported on TiO_2 were investigated. In these systems, the photosensitizing dyes are, however, generally found to be thermally and/or photochemically not stable.^{247–251} On the other hand, in 1991, M. Grätzel reported his idea of constructing a solar cell using a dye's photosensitizing effect on a titanium dioxide electrode.²⁵² Since the first reports by Grätzel et al.²⁴⁷ and Bahnemann and Hoffmann,⁶⁶ various investigations have been carried out into the development of visible light-responsive photocatalysts by incorporating small amounts of components such as cations and metal oxides. However, these initial trials were found to have limitations.^{66,253–255} As an alternative preparation approach for doped TiO_2 , an advanced metal ion-implantation method has been applied to modify the

electronic properties of TiO_2 photocatalysts by bombarding them with high energy metal ions. In particular, the group of Anpo discovered that the implantation of TiO_2 with various transition metal ions such as V, Cr, Fe, Co, and Ni by high voltage acceleration in the range of 50–200 keV could enable a large shift in the absorption band of these photocatalysts toward visible light regions, with differing levels of effectiveness.^{256–262} In the following, the preparation of visible light-responsive TiO_2 photocatalysts by chemical doping methods to incorporate metals, nonmetals, and metal oxides as well as by metal ion-implantation to modify the electronic state of TiO_2 , that is, by physical doping, will be discussed in detail.

6.1. Preparation of Visible Light-Responsive TiO_2 Photocatalysts by Chemical Doping

To induce visible light activity into normally purely UV-active TiO_2 , thus enabling its activation for photocatalytic processes also by visible light, various modification methods such as impurity doping (chemical and physical), semiconductor coupling, dye sensitization, etc., have been employed in recent years. After these modifications, the TiO_2 showed an absorption band in the visible light region, and, in most cases, also an enhanced photocatalytic efficiency under visible light irradiation for various applications such as environmental depollution, fuel synthesis, and solar cells. Among the above-mentioned modifications, although the dye-sensitized photocatalysts are usually found to be unstable under UV irradiation, they are still widely applied for the preparation of solar cells, due to the dye-sensitized material's strong visible light absorption ability. In 1991, Michael Grätzel and Brian O'Regan described a photovoltaic cell, created from low-to-medium-purity materials through low-cost processes, which exhibited a commercially realistic energy-conversion efficiency.²⁶³ The device is based on a

Table 2. Doping Modified TiO₂ Photocatalysts Prepared by Different Chemical Methods

chemical doping method	doping elements	precursors	visible-light driven photocatalysis	ref
sol-gel	N	Ti source, TBOT/TTIP; N source, urea/NH ₄ Cl/thiourea/ethylmethylamine	photocatalytic degradation of methylene blue; effective agents against both bacteria and stearic acid using a white light source	320–324
	C	Ti source, TTIP/TiCl ₄ ; C source, carbon particle ethanol/melamine borate	photodegradation of gaseous toluene or 4-chlorophenol	325,326
	Fe	Ti source, TTIP/TBOT; Fe source, Fe(NO ₃) ₃ ·9H ₂ O	photodegradation of active yellow XRG or methyl orange	271,290
	B and N	Ti source, TTIP/TBOT; N source, NH ₄ OH/urea; B source, H ₃ BO ₃	hydrogen evolution from water splitting	327–329
	N	Ti source, TiN/TiCl ₄ ; N source, TiN/l-lysine	hydrogen evolution from water splitting; photocatalytic degradation of methyl orange	330,331
hydrothermal	Ti ³⁺	Ti source, titanium powder and hydrochloric acid/TBOT and NaBH ₄	H ₂ evolved under visible light; photodegradation of methyl orange	293,332
	C	Ti source, TBOT/TTIP; C source, ethanol	photocatalytic degradation of methyl orange	333
	B and N	Ti source, TTIP/TBOT; N source, NH ₄ OH/NH ₃ /urea; B source, H ₃ BO ₃	photodegradation for Rhodamine B or methyl orange	334,335
	Ga ³⁺ , Y ³⁺ , or Nb ⁵⁺	Ti source, TTIP; Ga ³⁺ source, gallium nitrate; Y ³⁺ source, yttrium chloride; Nb ⁵⁺ source, niobium pentachloride	dye-sensitized solar cells (DSSCs)	336
	Fe and N	Ti source, TBOT; N source, NH ₄ Cl; Fe source, Fe(NO ₃) ₃	photodegradation of Rhodamine B	337
microemulsion	La and C	Ti source, Ti(SO ₄) ₂ /TBOT/TTIP; La ³⁺ source, lanthanum nitrate; C source, glucose	photodegradation of methyl orange	282
	N	Ti source, TBOT; N source, triethylamine, urea, thiourea, and hydrazine hydrate	photodegradation of Rhodamine B and 2,4-dichlorophenol	338
	Ag	Ti source, TTIP; Ag source, silver nitrate	decomposition of phenol	339
	C	Ti source, TiCl ₄ ; C source, tetrabutyl ammonium hydroxide	photodegradation of 4-chlorophenol	340
	N	Ti source, TBOT/Ti(SO ₄) ₂ ; N source, NH ₄ OH, NH ₄ NO ₃	photodegradation rate of 2,4-DCP or toluene	324,341–343
chemical precipitation	F	Ti source, TTIP; F source, NH ₄ F	photocatalytic oxidation of acetone	344
	Fe	Ti source, K ₂ TiF ₆ ; Fe source, FeSO ₄ ·7H ₂ O	photocatalytic decomposition of bromocresol green	345
	oxygen vacancies	Ti source, TTIP (CVD method)	photodegradation of methylene blue	346
	Sn ⁴⁺	Ti source, TiCl ₄ ; Sn ⁴⁺ source, SnCl ₄ ; plasma-enhanced chemical vapor deposition (PCVD)	photodegradation of phenol	347
	Nb, Ta, or F	Ti source, titanium alkoxides/titanium sheets; Nb source, niobium ethoxide; Ta source, tantalum ethoxide; F source, <i>t</i> -butyl fluoride/NH ₄ F, chemical vapor deposition (PCVD)	photodegradation for methyl orange	348,349
impregnation	Fe	Ti source, P25/titanate nanotubes; Fe source, Fe(acac) ₃ /Fe ₂ (SO ₄) ₃ /FeCl ₃	photodegradation of oxalic acid or photocatalytic oxidation of acetone; photocatalytic degradation of acetophenone	350–352
	N and Fe	Ti source, Ti(SO ₄) ₂ ; N source, NH ₄ OH; Fe source, ferric chloride	photodegradation of methylene blue	353
	Co, Cr, Cu, Fe, Mo, V, or W	Ti source, titanium trichloride; Co source, Co(NO ₃) ₂ ·6H ₂ O; Cr source, Cr(NO ₃) ₃ ·9H ₂ O; Cu source, Cu(NO ₃) ₂ ·3H ₂ O; Fe source, Fe(NO ₃) ₃ ·9H ₂ O; Mo source, (NH ₄) ₆ Mo ₇ O ₂₄ ·4H ₂ O; V source, NH ₄ VO ₃ ; W source, (NH ₄) ₆ W ₁₂ O ₃₉ ·xH ₂ O	photooxidation of 4-nitrophenol	354
	H	TTIP/titanium butoxide, H ₂ atmosphere at 200/450 °C	methylene blue decomposition and hydrogen generation	355–358
	Ti ³⁺	TTIP, 2-ethylimidazole calcination at 500 °C	high visible-light photocatalytic activity for the generation of hydrogen gas from water	292
high-temperature calcination	Ti ³⁺ and N	rutile TiO ₂ and NH ₄ flow at 500 °C ₂ =	extension of the active spectrum and superior visible light water photo-oxidation activity	295
	C	Ti source, Ti metal sheet; C source, CO ₂ and steam (H ₂ O)	water splitting with a total conversion efficiency of 11% and a maximum photoconversion efficiency of 8.35% when illuminated at 40 milliwatts per square centimeter	359
	B	Ti source, TiCl ₄ ; B source, BH ₃ /THF-solution	photocatalytic decomposition of methyl tertiary butyl ether	360
	Ti ³⁺	TTIP/P25 in vacuum	photodegradation of methyl orange, phenol, or methylene blue; hydrogen evolution from water splitting	296,361
	Ti ³⁺ and F	Ti source, Ti(SO ₄) ₂ ; F source, NH ₄ F	photodegradation of Rhodamine B	310
thermal plasma	H	Ti source, commercial amorphous TiO ₂	photocatalytic methyl orange decomposition and photocatalytic H ₂ generation	362

10- μm -thick, optically transparent film made with TiO_2 particles being a few nanometres in size, coated with a monolayer of dye to sensitize the film for light harvesting. The overall light-to-electric energy conversion efficiency was then reported to be 7.1–7.9% for simulated solar light and 12% for diffuse daylight. The large current densities and the high stability of these dye-sensitized solar cells (DSSCs) are making practical applications very feasible. Since then, the record of energy conversion efficiency for the DSSCs is constantly improved year by year.^{264–270} An impressive efficiency of solar-to-electrical energy conversion has been measured using such films, but in all cases the photon-to-electron conversion efficiency of the incident monochromatic light remained low, especially when such films were used in conjunction with solid charge-transport materials. In 1998, a development of the solar cell based on dye-sensitized mesoporous TiO_2 films has been reported by Grätzel and co-workers to convert photons to electric current with a yield of 33%.²⁴³ At present, the photoelectric conversion efficiency of these TiO_2 -based solar cells has stabilized to be more than 10%, but its cost of manufacturing is still rather high.

Although the pure TiO_2 is an ideal material for the application in solar cells, its visible light response is mainly induced by the dye sensitization, which is, however, not stable enough in photocatalytic reaction systems such as environmental depollution and splitting water into H_2 and O_2 . In addition to the dye sensitization, other modifications of the TiO_2 matrix, for example, TiO_2 modified by impurity doping, were also found to exhibit visible light-responsive photocatalytic reactivity and show more stability upon UV irradiation. Consequently, this approach has also attracted much attention and has been applied for the photodegradation of organic pollutants and also for the water splitting reaction. Hence, in this section, different modification methods will be introduced related to the doping of trace impurities into TiO_2 , including chemical synthesis such as high temperature sintering in different atmospheres, wet chemical methods such as sol–gel processes, hydrothermal treatment, spray pyrolysis, and supercritical methods.

Various chemical synthesis methods used for the doping of TiO_2 are summarized in Table 2. As can be seen in this table, doped TiO_2 synthesized by different chemical preparation methods usually exhibits a considerable photocatalytic activity for the degradation of organic dye pollutants and even for water splitting upon visible light illumination. In addition to the division into different synthesis methods, the chemical doping modification of TiO_2 can also be divided into metal doping and nonmetal doping. In the metal doping method, a certain amount of metal ions such as Fe^{3+} ,^{271–275} Cr^{3+} ,^{183,276} Ru^{2+} ,^{277,278} Ce^{4+} ,^{279,280} La^{3+} ,^{281–283} and V^{5+} ,^{284–286} is introduced into the TiO_2 matrix (Table 2), where they most likely form active “small oxide islands”, thus increasing the lifetime of the photoformed electron/hole pairs as well as the rate of their transfer processes resulting in the observed increase in the photocatalytic activity of the doped TiO_2 . Furthermore, the impurities induced by metal doping into the TiO_2 could efficiently narrow its bandgap and extend the absorption edge into the visible light range. Many studies have demonstrated that metal doping could effectively improve the photocatalytic activity of TiO_2 under visible light irradiation.^{287–290} However, metal doping also showed several drawbacks: thermal instability of the doped TiO_2 , electron trapping by the metal centers, introduction of electron/hole recombination centers.²⁹¹ It is worth mentioning that, in addition to the above “traditional” impurity metal ion doping, more and more research has been focused in recent years on the

investigation of Ti^{3+} self-doped TiO_2 .^{292–296} It has, for example, been observed that excessive Ti^{3+} self-doping will not introduce electron/hole recombination centers in TiO_2 .²⁹³

On the other hand, nonmetal doping is another technology to modify TiO_2 , which could achieve the substitution of lattice oxygen by nonmetal elements.^{291,297–299} An early work by Asahi et al.³⁰⁰ in 2001 reported that nitrogen doping could enhance the photocatalytic activity of TiO_2 for the photodegradation of methylene blue and gaseous acetaldehyde upon visible light irradiation, while, however, the photocatalytic activity in the UV light region decreases. Since then, considerable research effort has been focused on various nonmetal-doped TiO_2 photocatalysts, such as N,^{41,42} B,^{301–304} C,^{282,305–307} F,^{308–312} S,^{313–317} and P.³¹⁸ Although nonmetal doping modification could change the band structure of TiO_2 and therefore affect the transfer of electrons and holes, the origin of its visible light photoactivity is still under debate,²⁹¹ especially concerning the photocatalytic mechanism of nitrogen doping. Recent experimental and theoretical studies suggest that N-doping does not cause a narrowing of the band gap of TiO_2 , but rather leads to the formation of localized midgap states above the valence band of TiO_2 , thereby enhancing its visible light response and photoactivity.^{291,319}

In this section, we mainly introduce and highlight the chemically synthesized visible light-responsive TiO_2 photocatalysts with doping modification, including metal doping, nonmetal doping, and codoping. The factors influencing the doping modification, the research development concerning the doping and underlying photocatalytic mechanism, and novel investigations of synergistic effects between different elements are also discussed in the following.

6.1.1. Metal Ion Doping. As shown in the reaction mechanisms of TiO_2 photocatalysis, the number of photoformed electrons and holes participating in the photoinduced redox reaction plays an important role for the photocatalytic performance of visible light-responsive TiO_2 . The irradiation of sunlight onto TiO_2 determines the number of photoformed electrons and holes, and the magnitude of the band gap of TiO_2 is one of the key factors to improve the efficiency of utilization of sunlight, especially for the visible light absorption regions. Thereby, the modification of the band gap of TiO_2 is expected to be remarkably responsible for the enhancement in the formation of electrons and holes. To achieve a fundamental enhancement of the quantum yield of a photocatalytic reaction initiated by TiO_2 upon visible light irradiation, two problems must be overcome. One issue is how to produce more photoformed electrons and holes; another issue is how to improve the separation efficiency of these electrons and holes. It is well-known that an appropriate amount of transition metal ions doped into TiO_2 can introduce electron capture centers and may as well change the crystallinity of TiO_2 , resulting in the production some defects and thereby a decrease in electron/hole recombination centers.^{272,287–290,293,294,363} Thus, doping by metal ions is recognized as an effective modification method to improve the reactivity of visible light-responsive TiO_2 .

The methods selected for an appropriate doping of metal ions into the TiO_2 matrix can be divided into three types. The first type involves the doping with transition metal ions. Early on, Choi et al.³⁶⁴ studied the photoactivity of TiO_2 doped with 21 transition metal ions by using as model reactions the photocatalytic oxidation of chloroform and the photocatalytic reduction of carbon tetrachloride. The researchers discovered that the doping with Fe^{3+} , Mo^{5+} , Ru^{3+} , Os^{3+} , Re^{5+} , V^{4+} , and Rn^{3+}

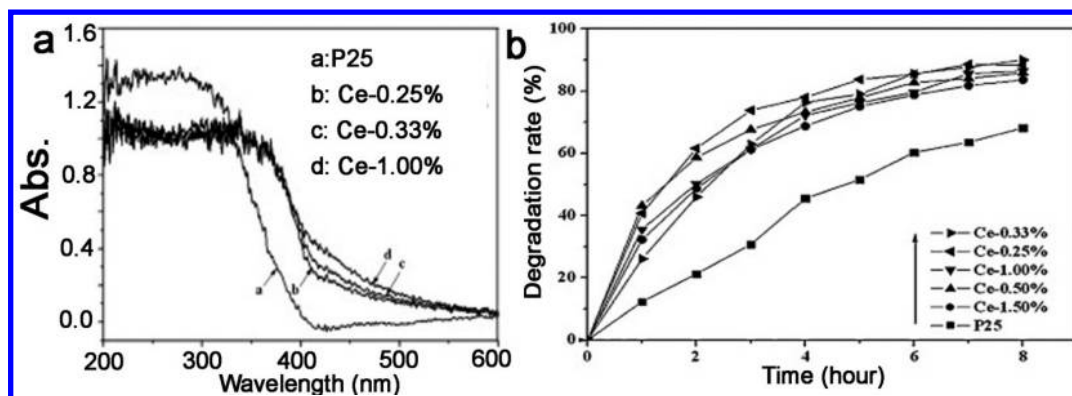


Figure 35. UV-vis absorption spectra of Ce-TiO₂ samples with different Ce ion doping concentrations (a). Curves showing the methylene blue degradation by Ce-TiO₂ samples with different Ce ion doping concentrations (b). Reprinted with permission from ref 365. Copyright 2012 Elsevier.

cations is beneficial as evinced by the enhancement of the photodegradation of chloroform. Recently, Yan et al.³⁶⁵ synthesized by a sol-gel method TiO₂ nanoparticles doped with different contents of cerium ions. The authors suggest that the Ce dopant ions generate additional electronic states in the bandgap of TiO₂ above the valence band acting by capturing the photoformed holes, thus decreasing the recombination rate of photogenerated electrons and holes. Additionally, electrons from these electronic states can be photoexcited directly into the conduction band of TiO₂, leading to a better visible light absorption and enhancing the photocatalytic degradation of methylene blue as compared to pure TiO₂ (Figure 35). Zhang and co-workers have also worked extensively on transition metal-doped TiO₂ and its application for various photocatalytic reactions.^{276,279,280,285,290,366–372} Iron ion-doped anatase TiO₂ was prepared by hydrothermal hydrolysis and crystallized in octanol-water solution.³⁷² The results employing the photodegradation of the active yellow XRG dye as model reaction indicated that the amount of dopant iron ions plays a significant role in affecting the photocatalytic activity and that iron doped at its optimum content enhances the photocatalytic activity considerably, especially under visible light irradiation. When the Fe³⁺ doped TiO₂ photocatalysts were prepared by combining a sol-gel method with a hydrothermal treatment,³⁶⁶ the Fe was found to exist in a trivalent ionic state, thus substituting Ti⁴⁺ in TiO₂ with its concentration being found to decrease from the surface to the deep bulk of TiO₂. As a result, the synthetic method of Fe doping in TiO₂ has a significant influence on the doping structures and concentration. In addition to iron, chromium and vanadium are also widely used as dopant elements into TiO₂. Because of the excitation of the 3d electrons of Cr³⁺ to the conduction band (CB) of TiO₂, Cr-TiO₂ always exhibits a good ability of absorbing visible light to induce the photodegradation of active yellow XRG dye.²⁷⁶ V⁴⁺ ions have also been successfully incorporated into TiO₂ by the flame spray pyrolysis (FSP) technique,²⁸⁵ by the sol-gel,^{286,373} as well as by other chemical methods.²⁸⁴ V-doping into TiO₂ leads to a change of the bandgap of TiO₂, resulting in an extension of the absorption edge to the visible light region and thereby in an improvement of the visible light-driven photocatalytic activity of TiO₂.²⁸⁶

The second type involves doping with rare-earth metals with lanthanide-doped TiO₂ accounting for the majority of examples published to date.^{282,283,374–376} Sun et al.³⁷⁴ investigated the effect of substitutional La-doping on the electronic structure and the photocatalytic activity of TiO₂ by the density function theory

(DFT) calculation method. Their calculations indicate that the enhanced absorption of La-TiO₂ in the visible light region can be attributed to the adsorption of La rather than to a substitutional La doping. On the contrary, Anandan et al.³⁷⁷ suggested that the rapid mineralization of monocrotophos over La-doped TiO₂ under visible light irradiation could be associated with the suppression of the electron/hole recombination by La³⁺ dopant cations present in the TiO₂ matrix and the subsequent generation of a higher number of •OH radicals by the surface trapping of excess holes. Recently, Zhang and co-workers have studied some other lanthanide metals such as Eu, Yb, and Sm as dopants for TiO₂ and the associated photocatalytic activities of the thus prepared materials under visible light irradiation.^{378–380}

Samarium-doped TiO₂ (Sm-TiO₂) was successfully prepared via a chemical coprecipitation method. The resulting Sm_{3d} XPS spectrum was found to exhibit two significant peaks³⁸⁰ with the peak at 1084.3 eV corresponding to the Sm-O bond and the peak at 1082.2 eV corresponding to the Sm-O-Ti bond. Although the ionic radius of Sm³⁺ (1.08 Å) is considerably larger than the ionic radius of Ti⁴⁺ (0.68 Å), thus preventing the Sm³⁺ ions from entering into the lattice of TiO₂, the Ti⁴⁺ ions may enter into the lattice of the Sm₂O₃ leading a change in the electronic field of Sm³⁺ and hence to an increase in the electron density and to a decrease in the binding energy of Sm³⁺. Well-ordered mesoporous TiO₂ doped with ytterbium has also successfully been synthesized by an evaporation-induced self-assembly process.³⁷⁸ The Yb dopant was beneficial in stabilizing the mesoporous structure and in reducing the recombination rate of photogenerated electrons and holes, resulting in an enhanced visible light-driven photoactivity. Europium-doped TiO₂ was synthesized by a precipitation-peptization method and used as photocatalyst to degrade salicylic acid.³⁷⁹ The results showed that the doping of Eu was beneficial for the adsorption of salicylic acid and the separation of photoformed holes and electrons.

In addition to the transition and the rare-earth metal ion doping, studies involving TiO₂ doped with some other metal ions have also been published, for example, Tin doping and Ti(III) self-doping. The dopant Sn⁴⁺ was found to substitute Ti⁴⁺ in the lattice of TiO₂, which was reflected in a lattice expansion in both the *a*- and the *c*-direction, and in a change in the binding energy.³⁸¹ Different from other metal ions, the doping of Sn⁴⁺ in anatase TiO₂ did result in a blue shift of the absorption edge, and was reported to enhance the amount of surface hydroxyl groups and oxygen vacancies absorbing in the UV light region. On the other hand, Sn doping has also been demonstrated as an effective modification method to enhance the visible light response of

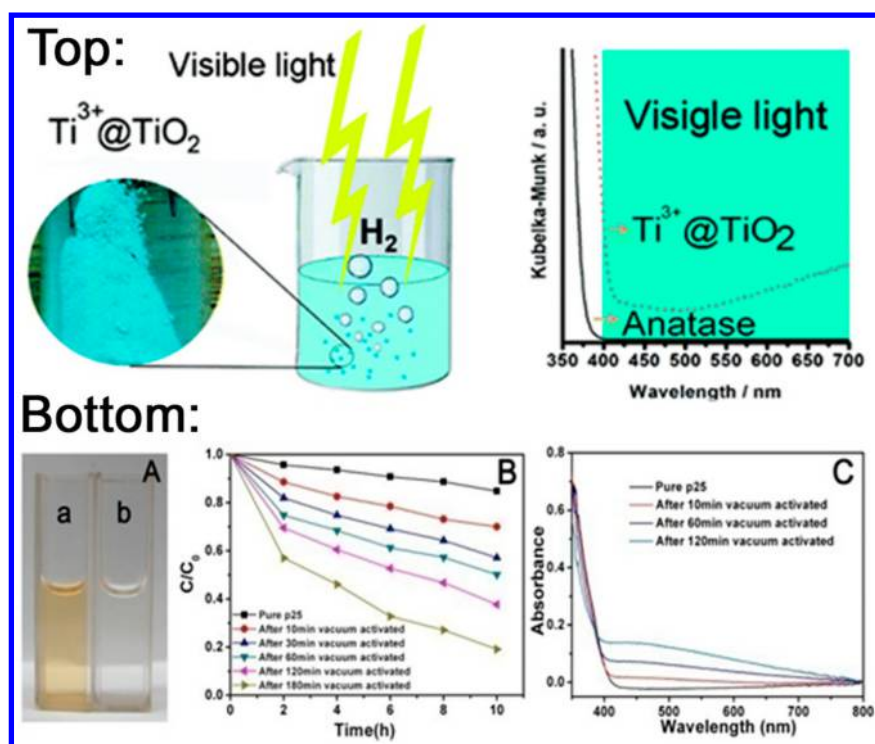


Figure 36. Top figure shows the time course of evolved H_2 under visible light (>400 nm) irradiation and the UV–visible diffuse reflectance spectra for commercial anatase TiO_2 (solid line) and Ti^{3+} -self-doped TiO_2 (dashed line) (top figures).²⁹² The bottom figure is (A) photo-oxidation of 5 mg L⁻¹ methyl orange before (a) and after (b) visible light (>420 nm) irradiation for 3 h by the sample after vacuum activation for 180 min (temperature of vacuum activation is 470 K); (B) photo-oxidation of 20 mg L⁻¹ phenol under visible light (>420 nm) irradiation for 10 h; and (C) UV–vis diffuse reflectance spectra of pure P25 and of the vacuum activated samples. Reproduced with permission from ref 296. Copyright 2011 The Royal Society of Chemistry.

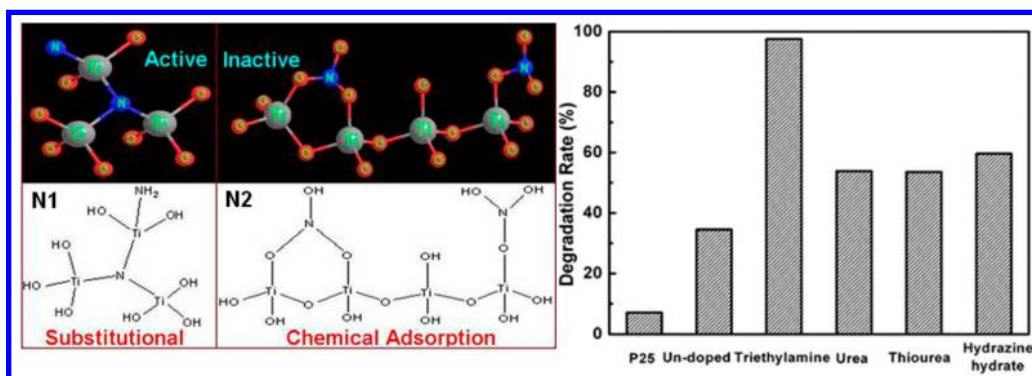


Figure 37. Left part of the figure shows how nitrogen may be present in N-doped TiO_2 ;³⁴² the right part of the figure shows the photocatalytic activities of N-doped TiO_2 prepared from different nitrogen sources at the respective optimal doping values. Adapted with permission from ref 338. Copyright 2007 American Chemical Society.

TiO_2 .³⁸² Tin has been reported to improve the photocatalytic activity of TiO_2 by enhancing the separation rate of photo-generated electrons and holes on the surface of TiO_2 . Because the Fermi level of SnO_2 is lower than that of TiO_2 , the photogenerated electrons can easily be transferred from TiO_2 to SnO_2 , resulting in a reduction of the number of photo-generated electrons on the surface of TiO_2 . In recent years, Ti^{3+} -doped TiO_2 has attracted much interest, since it has been demonstrated to exhibit visible-light absorption.^{383,384} Sasikala et al.³⁸⁴ have found that surfacial Ti^{3+} and oxygen vacancies may be responsible for the enhanced visible-light absorption of TiO_2 – SnO_2 composites. However, surfacial Ti^{3+} centers and oxygen defects are usually not stable on TiO_2 in air, because the Ti^{3+} centers are easily oxidized into Ti^{4+} by the oxygen dissolved in

water.^{292,385} Most research has therefore been focused on Ti^{3+} self-doped TiO_2 exhibiting better chemical stability and higher photocatalytic activity. Zuo et al.²⁹² have reported a one-step calcination method to synthesize Ti^{3+} self-doped TiO_2 exhibiting high stability, improved visible light absorption, and efficient photocatalytic hydrogen production capacity from water under visible-light irradiation (Figure 36, top). Furthermore, a vacuum activation method has been employed for the modification of P25 into Ti^{3+} self-doped TiO_2 with a high stability and photocatalytic reactivity under visible light irradiation (Figure 36, bottom).²⁶⁹ The EPR results for the vacuum-treated P25 also showed its stability under visible and UV light irradiation. In addition to the vacuum activation method, a simple one-step solvo-thermal method with low-cost NaBH_4 added as a reductant

has also been reported for the successful synthesis of a series of TiO_2 catalysts self-doped with Ti^{3+} also exhibiting strong visible light absorption and enhanced photocatalytic activity.²⁹³

6.1.2. Nonmetal Ion Doping. Although the metal ion doping of TiO_2 has been able to induce the desired spectral shifts into the visible light region, the presence of various metallic ions was also found to induce a reduced thermostability of TiO_2 and to introduce additional recombination centers, in particular, at increased doping levels. Following an early report of Asahi et al.⁵⁰ in 2001 that nitrogen-doped TiO_2 exhibits enhanced visible light absorption and photocatalytic activity, research concerning nonmetal ion doping of TiO_2 has become a rather hot research topic.

Taking into consideration the poor thermostability caused by metal ion doping and the associated rather high modification costs, in recent years an increasing number of nonmetal elements have been used as dopants aiming to modify the bandgap of TiO_2 . Nonmetal doping mainly consists of N, C, F, B, and some other elements having an atomic radius similar to that of the O atom. Among them, nitrogen has attracted much attention and has been widely studied. In some recent work,^{51,52} a new approach to synthesize N-doped TiO_2 nanocrystals was developed, and the relationship between the nitrogen dopant species and the respective visible light photoactivity was investigated. It was found that nitrogen present in the TiO_2 bulk is beneficial for the visible light-induced photodegradation of 2,4-dichlorophenol, while nitrogen species chemically adsorbed on the catalyst surface are harmful to the photoactivity, as shown in Figure 37.³⁴² Moreover, the nitrogen source also plays an important role for the N doping effect. Urea, triethylamine, thiourea, and hydrazine hydrate could all be used as the nitrogen source to prepare nitrogen-doped TiO_2 by a microemulsion-hydrothermal method.³³⁸ Among the above nitrogen sources, triethylamine was found to be most effective, yielding N-doped TiO_2 with the highest visible light photocatalytic degradation activity for Rhodamine B (Figure 37). Yates et al.³⁸⁶ showed that NH_3 gas can be successfully used as the nitrogen source to prepare the N-doped TiO_2 with enhanced visible light photoactivity by a calcination method, while TiO_2 treated by N_2 exhibited a decreased photoactivity, which was explained by a broadening of the bandgap of TiO_2 .

In addition to nitrogen, carbon has also been demonstrated to be an effective doping element to modify the visible light absorption and the photoactivity of TiO_2 . Using a sol-gel method, Nagaveni et al.³⁸⁷ successfully prepared C-doped TiO_2 exhibiting a high photodegradation activity for methylene blue under visible and UV light irradiation. Kamisaka et al.³⁸⁸ investigated the effect of C-doping on the structure and on the optical properties of TiO_2 by the density functional theory (DFT) calculation method. They assumed that the carbon atom may substitute four different sites of titanium and oxygen to obtain four corresponding C-doped structures. The results of these DFT calculations indicated that the substitution of C for Ti does not result in any visible light response of TiO_2 because of the formation of titanate anions. On the contrary, the substitution of C for O will be beneficial for the visible light absorption of TiO_2 and will not change its crystal structure. Recently, Bai et al.³⁶¹ prepared monodisperse, carbon-doped rutile TiO_2 single crystals having an exposed (110) facet, which possessed a hierarchical structure and were found to be highly efficient for the photocatalytic H_2 generation from water. Nearly 450 mL of H_2 was generated after 196 min of the reaction. The corresponding H_2 generation rate was found to increase in the

first 100 min and then remained constant at around 3 mL min^{-1} (22 mmol per hour per gram of photocatalyst). Yu et al.³⁸⁹ also synthesized novel carbon self-doped TiO_2 sheets with exposed (001) facets by hydrothermal treatment. The C-doped TiO_2 sheets showed enhanced absorption in the entire visible light region and a significant red-shift of the absorption edge. They also exhibited a high photocatalytic degradation activity for methylene blue under visible light irradiation. Lin et al.³⁹⁰ prepared visible light-sensitive C-doped mesoporous TiO_2 films by a sol-gel method combined with a hydrothermal treatment. These C-doped TiO_2 films had a high surface area and showed excellent photodegradation activities for the dye reactive brilliant Red X-3B upon UV and visible light irradiation.

Fluorine doping of TiO_2 has attracted considerable attention in recent years; however, employing conventional F-doped TiO_2 does not usually exhibit the desired enhanced UV and visible light photoactivity, and the underlying photocatalytic mechanism still remains controversial.^{391–393} Originally, NH_4F was used as a hydrophobic modifier and isopropanol as the solvent to prepare superhydrophobic mesoporous MCF loaded with fluorinated TiO_2 nanoparticles,³¹⁰ through a simple one-step solvothermal method (Figure 38, top). The prepared catalysts exhibited

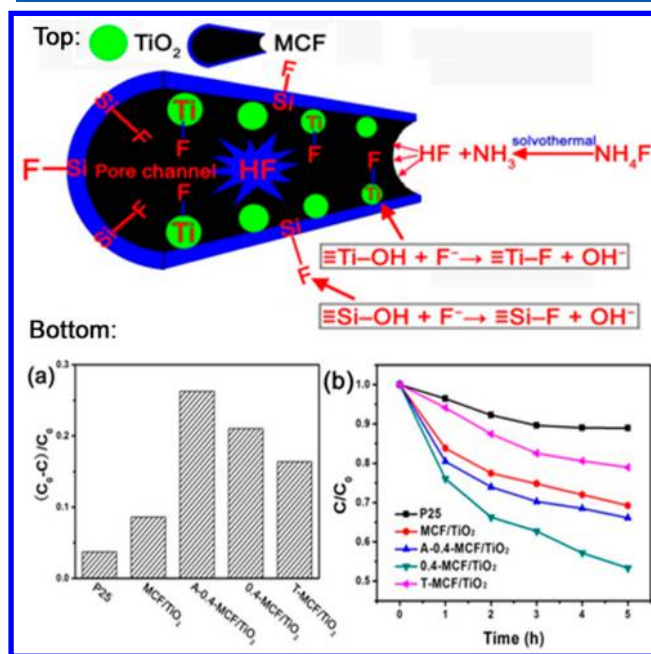


Figure 38. Top figure shows a schematic diagram of the fluorination reaction occurring in the pore channels of MCF; the bottom figure shows adsorption capacities of RhB (20 mg/L, catalyst concentration: 0.25 g/L) on different samples (a); visible light photocatalytic activities of different samples (b). Reprinted with permission from ref 310. Copyright 2012 Elsevier.

permanent and excellent superhydrophobic properties, high adsorption capacity, and considerable photocatalytic activity for Rhodamine B degradation (Figure 38, bottom). However, through the solvothermal method, the F^- anions can only be adsorbed at the surface of the catalyst but cannot be introduced into the TiO_2 lattice. Various research groups have also reported the preparation of F-doped TiO_2 exhibiting high photocatalytic activity.^{310,393} It has been proposed that the standard substitutional doping of TiO_2 with fluoride ions can be compared to the formation of F-doped SnO_2 , that is, with the generation of impurity levels close to the conduction band.^{394–396} However,

the exact electronic structure and the photocatalytic mechanism of F-doped TiO_2 are still unclear. It has been demonstrated by first-principles calculations that F substitution for lattice O can neither introduce impurity levels within the TiO_2 band gap, nor can it shift its absorption edge into the visible region.³⁹⁷ This might be explained by the fact that F substitution for oxygen vacancies has not been taken into account during this calculation process. Other studies have reported that F substitution for oxygen vacancies could indeed introduce acceptor impurity levels inside the ZnO or the SnO_2 bandgap.^{398,399} Hence, it was concluded that the achievement of abundant fluorine substitution for lattice oxygen vacancies plays a very important role for the diminishing of vacancy-induced recombination sites and also for the introduction of impurity levels inside the TiO_2 bandgap.³¹²

As compared to the nonmetal ion dopants discussed so far, studies on boron doping of TiO_2 have been relatively rare. On the one hand, it was suggested that the boron doping of TiO_2 could lead to a red-shift of the absorption band of TiO_2 toward the visible light region, resulting from an overlap of the boron impurity levels with the 2p electronic states of oxygen.^{400,401} On the other hand, however, other studies reported that the boron incorporation into the TiO_2 lattice could induce a blue shift rather than a red-shift of the TiO_2 absorption spectrum resulting from a decrease of the primary TiO_2 crystal size caused by the presence of B during the crystal growth (quantum size effect).^{402,403} To date, boron is mainly being used for the modification of TiO_2 as an important codopant together with other nonmetal ions. Hence, more and more researchers began to study the codoping modification of boron with other elements in TiO_2 .^{328,334,404,405}

6.1.3. Codoping of TiO_2 . To further improve the photocatalytic activity of TiO_2 and to enable a more effective use of sunlight in the visible light region, multicomponent modified TiO_2 , that is, TiO_2 codoped with different elements, has attracted considerable attention in the field of photocatalysis. Some studies reported that TiO_2 codoped with appropriate elements could exhibit a much higher photocatalytic activity than any singly doped photocatalyst, because of the existence of synergistic effects between the doping elements promoting the visible light absorption and facilitating the separation efficiency of photoformed electron/hole pairs.^{272,284,295,334,335,378,406–408} Herein, we will focus on a summary of the recent research status of the codoping modification of TiO_2 , the modification mechanism of codoping, and the synergistic effects existing in codoped TiO_2 .

According to the band theory of semiconductors, the conduction band of TiO_2 semiconductors is mainly determined by the Ti 3d orbital energy levels, while the valence band is mainly formed from the O 2p orbitals. As compared to the O 2p orbital, other nonmetal elements such as N, C, S, P have 2p orbitals exhibiting more negative energy levels; hence, the partial substitution of the impurity dopants N, C, S, P as well as other nonmetal elements for lattice oxygen will result in the formation of new energy bands above the TiO_2 valence band, thus enhancing the visible light photocatalytic activity of TiO_2 .

As soon as two different doping elements will be present in the TiO_2 matrix, their respective 2p orbital energy levels will both contribute to the creation of new energy states within the TiO_2 bandgap in a synergetic manner. As compared to other nonmetal elements, the codoping of titanium dioxide with carbon and nitrogen has been found to exhibit this synergistic effect in a most pronounced fashion resulting in a considerable visible light response of the respective codoped materials. Cong et al.⁴⁰⁹

proposed the energy level of N-doping to connect with the states of C-doping, thus facilitating the overlap of C 1s and N 1s with the VB states of TiO_2 , as shown in Figure 39. The codoping of N

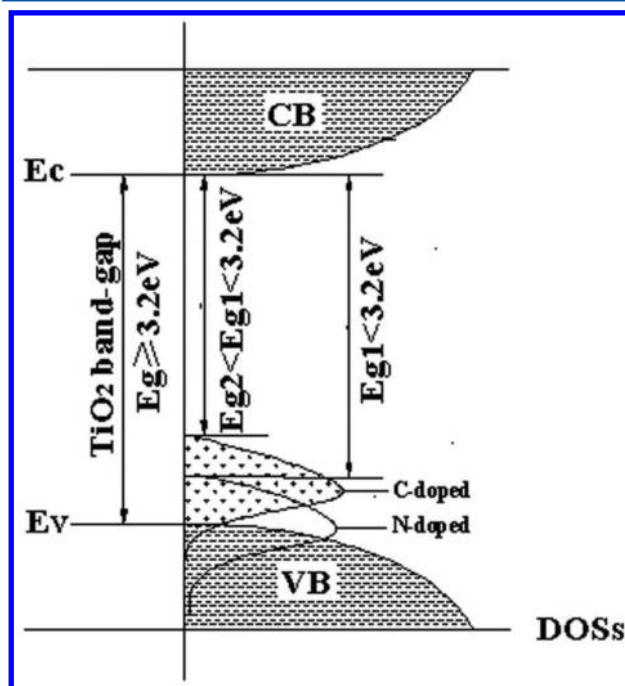


Figure 39. Formation of new energy bands in C–N codoped TiO_2 photocatalysts resulting in their visible light absorptivity. Reproduced with permission from refs 291,409. Copyright 2010, 2006 The Royal Society of Chemistry.

and C further narrows the band gap of TiO_2 and improves its visible light photocatalytic activity.⁴⁰⁹ Meanwhile, boron has also been used as an important codopant together with nitrogen for TiO_2 .^{327,334,335,360,404} In et al.³⁶⁰ and Liu et al.³³⁵ proposed that the fact that B and N codoped TiO_2 shows a high UV and visible light photocatalytic activity can probably be explained by the existence of a synergistic effect between boron and nitrogen forming Ti–B–N structures at the catalyst surface. However, there is still no detailed mechanistic understanding of the B–N synergistic effect and of its effect on the photocatalytic activity of TiO_2 . Xing et al.³³⁴ have attempted to analyze the exact role of this synergistic effect for the optical absorbance and for the photocatalytic activity of B and N codoped TiO_2 . Various codoped TiO_2 materials were systematically prepared by using a double hydrothermal method. Different new bonds (Ti–B–N–Ti and Ti–N–B–O) were formed on the surface of TiO_2 when the order of boron and nitrogen addition was changed, thus significantly affecting the photocatalytic activities of the materials. These experimental results have been further supported by DFT calculations. Gombac et al.⁴¹⁰ found that surfacial N-doping did not appreciably modify the TiO_2 structure or texture, while the boron incorporation in TiO_2 indeed inhibited the TiO_2 crystallite growth, thus increasing its surface area. Only when B was present in excess with respect to N could a remarkable photoactivity improvement be obtained. DFT calculations were used to interpret the observed behavior, suggesting that when B is present in molar excess with respect to N, Ti^{3+} sites are generated, which might further induce the generation of reactive superoxide species. Different from the surface-bound structures and the reactive Ti^{3+} sites induced by B

and N codoping, Czoska et al.³²⁸ proposed that lattice centers (labeled $[\text{NOB}]^{\bullet}$) based on the presence of interstitial N and B atoms both bound to the same lattice oxygen ion could induce new energy levels near the edge of VB of TiO_2 . $[\text{NOB}]^{\bullet}$ can easily trap one electron to produce a diamagnetic center at about 0.4 eV above the top of the valence band VB (Figure 40), which will contribute to the visible light photoactivity.

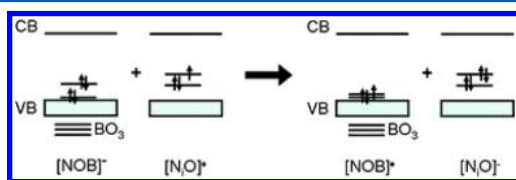


Figure 40. Schematic representation of the interplay between the $[\text{NOB}]^{\bullet}$ and $[\text{NiO}]^{\bullet}$ centers in N–B codoped TiO_2 . Reproduced with permission from ref 328. Copyright 2011 PCCP Owner Societies.

Recently, nitrogen and sulfur codoped TiO_2 was successfully immobilized on the surface of nitrified Ti substrates, and exhibited high photocatalytic activities for the degradation of methylene blue upon visible light irradiation.⁴¹¹ It was suggested that N, S codoping of the anodically formed TiO_2 narrowed its band gap and enhanced its visible light absorption and photocatalytic activity. To eliminate recombination centers induced in TiO_2 nanoparticles by their nonmetal doping, Yang et al.⁴¹² synthesized fluorine and sulfur codoped mesoporous TiO_2 . The ability to control both the morphology and the chemical composition of mesoporous TiO_2 could be beneficial to improve the light-harvesting capacity and to decrease the number of recombination centers. The F, S codoping in TiO_2 can red-shift the threshold of the TiO_2 absorption into the visible light region and improve the photocatalytic efficiency for the degradation of organic pollutants. Hence, various nonmetal codoped TiO_2 materials have been successfully synthesized and employed for the photodegradation of organic dyes under visible light irradiation. N, F codoped TiO_2 microspheres were prepared by the ethanol solvothermal method.⁴¹³ It was found that the mesoporous codoped catalyst exhibited a significant synergistic effect of N and F doping, leading to a high photocatalytic activity for the visible light-induced degradation of AO7. Moreover, carbon and boron codoped TiO_2 were also synthesized for the first time by a gel-hydrothermal method,⁴⁰⁵ that is, prepared through a sol–gel process followed by hydrothermal treatment in a glucose solution. The experimental results indicated that the coke carbon generated on the codoped catalyst surface acts as a photosensitizer inducing visible light activity. The boron doping, on the other hand, was found to effectively narrow the band gap of TiO_2 and to induce an easier transition of photoformed electrons from the boron dopant level to the Ti^{3+} level. The synergistic effect of B and C is responsible for the excellent visible light photocatalytic activity of this material.

Both metal and nonmetal doping will change the electronic structure of TiO_2 through the creation of new doping levels inside its band gap. Concerning the different positions of these doping levels, it is generally considered that the doping levels induced by the substitution of metal ions for Ti^{4+} are close to the CB of TiO_2 , while the impurity levels caused by the doping of nonmetal ions into oxygen vacancy sites will be close to the VB of TiO_2 . Doping levels located inside the band gap of TiO_2 can either accept photoformed electrons from the VB or absorb photons with longer wavelengths, thus extending the absorption

range of TiO_2 . These synergistic effects between metal and nonmetal dopants could promote the separation of electrons and holes, resulting in an improvement of the visible light photocatalytic activity of TiO_2 .

Generally speaking, the synergistic effect between metal and nonmetal dopants can be explained as follows: nonmetal doping ions can enhance the absorption of TiO_2 in the visible light region, while metal doping ions can introduce traps for electrons, thereby decreasing the electron/hole recombination rate. Vanadium and nitrogen codoped TiO_2 was, for example, synthesized by the sol–gel method, and the catalyst showed a high visible light photocatalytic activity for the degradation of RhB.³⁷³ The visible light absorption efficiency of V–N-codoped TiO_2 was better than that of V or N singly doped TiO_2 , because of the effective narrowing of the band gap induced by the simultaneous incorporation of V and N into the TiO_2 lattice, as shown in Figure 41. The energy levels inside the TiO_2 band gap

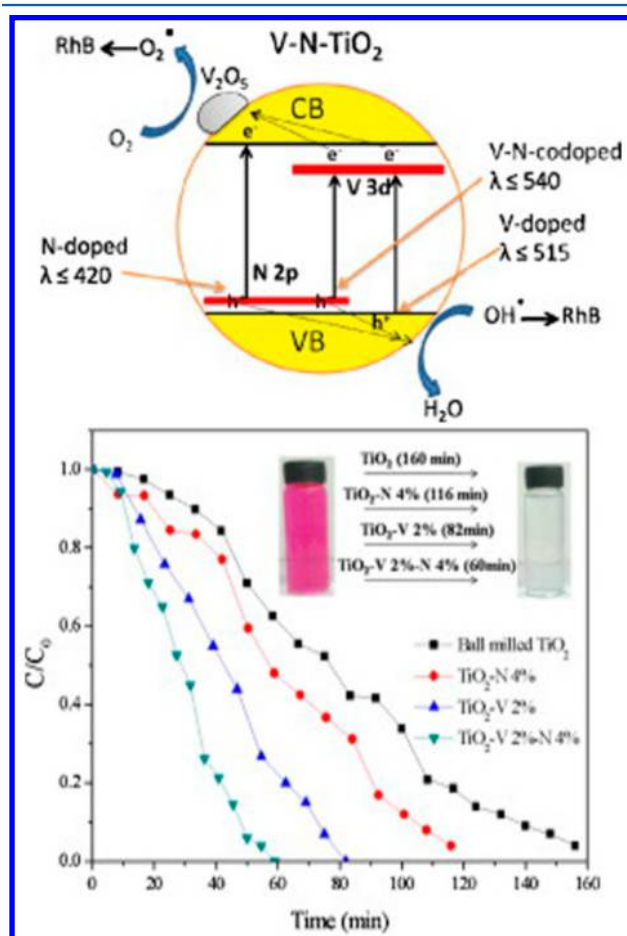


Figure 41. Schematic diagram illustrating the photocatalytic degradation of the RhB dye over V2–N4-codoped TiO_2 photocatalysts under visible light irradiation (upper part). Comparison of the photocatalytic degradation of RhB under visible light illumination in the presence of undoped, V2-doped, N4-doped, and V2–N4-codoped TiO_2 powders. Reprinted with permission from ref 373. Copyright 2012 Elsevier.

can act as traps for photoformed holes and electrons, thus decreasing the recombination rate between the photoformed charge carriers. It is the synergy between the narrowed band gap and the enhanced charge separation efficiency that improves the visible light photoactivity of the codoped TiO_2 . Wei et al.⁴¹⁴ argued that the synergistic effect between nitrogen and

lanthanum in La, N codoped TiO_2 is responsible for its high photocatalytic activity. The N doping decreased the band gap of TiO_2 and increased the absorption intensity of TiO_2 in the visible light region. The La^{3+} doping did not only increase the overall surface area of the material but did also restrain the recombination probability of electrons and holes, due to the electron capturing capacity of La^{3+} . To minimize the role of metal ions as recombination centers, Kim and co-workers synthesized boron and iron codoped TiO_2 using a modified sol–gel method. It was observed that the simultaneous presence of boron and iron causes a red-shift in the absorption band of TiO_2 .⁴¹⁵ Cong et al.³³⁷ also successfully prepared nanosized TiO_2 catalysts codoped with nitrogen and iron, which exhibited a higher photocatalytic activity under visible light irradiation than the singly doped catalyst. Employing a simple one-step hydrothermal method, Xing et al.²⁸² prepared highly dispersed carbon and lanthanum codoped TiO_2 crystals with exposed (001) facets by using glucose as the carbon-doping source and the (001)-facet-controlling agent. The C doping was found to be responsible for the strong absorption in the visible light region, while the La doping acted as electron capture center. The synergistic effect of C and La is used to explain the observed high visible light photocatalytic activity of this codoped TiO_2 .

However, in addition to the synergistic effects described so far, other forms of synergy between metal and nonmetal dopants in TiO_2 have also been reported, such as an increasing number of surface active species including hydroxyl groups and hydrogen peroxide. The role of surface-bound hydroxyl groups and hydrogen peroxide is mainly described by the following two aspects: their involvement in the reaction with the photoformed holes to generate hydroxyl radical intermediates; and their role in changing the adsorption form of different reactants and acting as active centers influencing the photocatalytic reaction of the reactant molecules. Wei and co-workers noted that the content of hydroxyl groups on the surface of sulfur and iron codoped TiO_2 was increased, as deduced from the respective XPS characterization,⁴¹⁶ and considered this to be beneficial for its visible light photocatalytic activity. The difference in the number of surface –OH groups between pure TiO_2 and singly doped TiO_2 was found to be very small, while the amount of surface –OH groups on Fe and S codoped TiO_2 was much higher than that measured for the singly doped catalyst, evincing the synergistic effect between Fe and S. Although the mechanism of an enhancement in the number of surface –OH groups by F and S doping is not clear yet, an increase in the number of surface –OH groups is quite possible to lead to an enhancement in the photocatalytic reactivity. Gomathi Devi et al.⁴¹⁷ prepared Ag and nitrogen codoped TiO_2 by grinding sol–gel titania with urea followed by a photoreduction process. The as-prepared $\text{Ag-TiO}_{2-x}\text{N}_x$ exhibited much higher visible light photocatalytic activity than the singly nitrogen doped TiO_2 , which can be accounted for by the synergistic effect of Ag loading with N doping. Strongly interacting electron-accepting hydrogen peroxide species at the catalyst surface have been proposed in this case to act as surface states enabling an inelastic transfer of electrons from the CB to the respective oxidizing species. Additionally, a synergistic effect was also suggested to explain the electron transfer between the codopant states. Hoang et al.²⁹⁵ reported a synergistic effect involving Ti^{3+} and nitrogen in TiO_2 nanowire arrays, which exhibited an enhanced water photooxidation performance upon visible light irradiation. The authors proposed a reversible electron transfer between the paramagnetic bulk N (N_b) species and the Ti^{3+} centers forming the diamagnetic bulk species N_b^-

and Ti^{4+} . This can readily be explained by the existence of an interaction between Ti^{3+} and N in TiO_2 (Figure 42). The lower

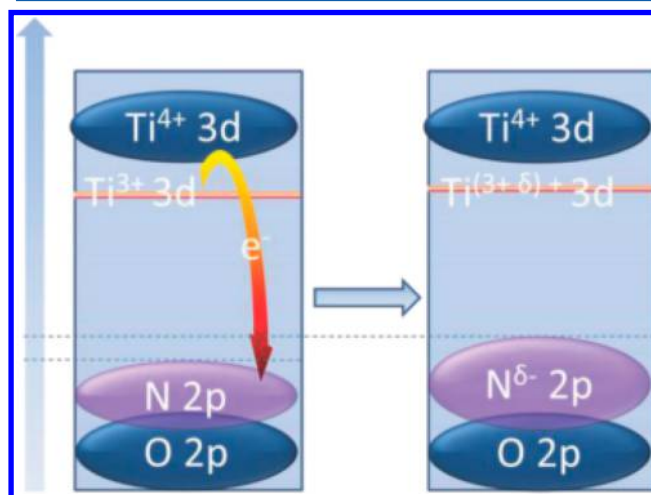


Figure 42. Proposed mechanism explaining the interaction between Ti^{3+} and substitutional N. Reprented with permission from ref 295. Copyright 2012 American Chemical Society.

oxidation states of the substitutional N in the codoped TiO_2 might result from an electron transfer with Ti^{3+} . Because of the Coulombic repulsion, the lower oxidation states of N in codoped TiO_2 are located at higher energy levels as compared to those of the singly N-doped TiO_2 , thus enabling excitation with photons of longer wavelengths.

6.2. Preparation of Visible Light-Responsive TiO_2 Photocatalysts by Doping Using Physical Methods

Besides the chemical doping methods discussed in the preceding paragraphs, it is also possible to employ physical doping methods to effectively incorporate anions or transition metal ions into TiO_2 to prepare visible light-responsive TiO_2 photocatalysts. In this section, the importance of physical doping methods to prepare visible light-responsive TiO_2 photocatalysts will be introduced by focusing on two different modes of ion-implantation techniques: (1) transition metal ion-implantation and (2) anion implantation.

6.2.1. Transition Metal Ion-Implantation. Anpo and co-workers have been very active in the area of TiO_2 doping through ion-implantation and succeeded to prepare various visible light-responsive photocatalysts by applying this technique.^{183,257–259,261,262,418–425} Metal ion-implantation employing various transition metal ions such as V, Cr, Mn, Fe, and Ni accelerated by high voltage leads to large shifts in the absorption band of the titanium oxide catalysts toward the visible light region. To achieve this implantation, transition metal ion vapors (M^+ ion: $\text{M} = \text{V}, \text{Cr}, \text{Mn}, \text{Fe}, \text{and Ni}$) are accelerated in a high voltage field, for example, at 150 keV, thus bombarding the TiO_2 samples, followed by the annealing in air at 723–823 K. Among the various kinds of ions tested here, Cr (Figure 43) and V were found to be especially effective to induce a red-shift of the absorption band of TiO_2 .^{257–259,418,422–425}

Ar, Mg, or Ti ion-implanted TiO_2 exhibited no spectral shift, evincing that such a shift is not caused by the high energy implantation process itself, but rather by the interaction of the transition metal ions with the TiO_2 matrix.^{257–259,418,422–425} Interestingly, TiO_2 chemically doped with Cr by an impregnation method shows a typical and distinct absorption shoulder around

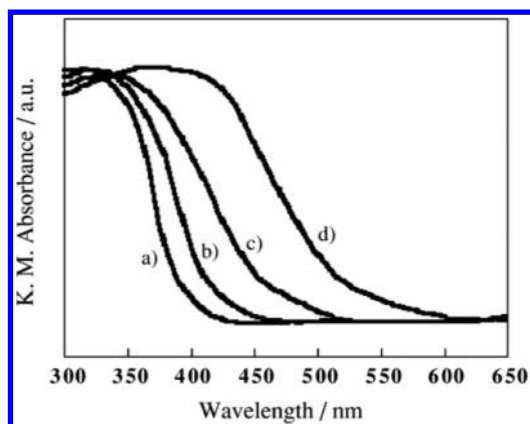


Figure 43. UV-vis absorption spectra (diffuse reflectance) of unimplanted original pure TiO_2 (a) and Cr ion-implanted TiO_2 catalysts (b–d) (amount of implanted Cr ions (in 10^{-7} mol/g), (b) 2.2, (c) 6.6, (d) 13). Reprinted with permission from ref 425. Copyright 2002 Elsevier.

450 nm, which has been explained by the formation of impurity energy levels within the semiconductor's band gap (Figure 44).^{257–259,418,422–425}

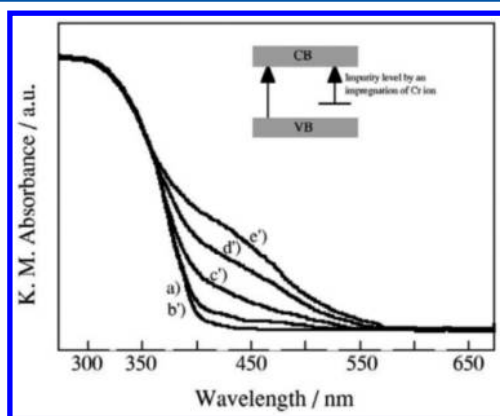


Figure 44. UV-vis absorption spectra (diffuse reflectance) of undoped original pure TiO_2 (a) and of TiO_2 photocatalysts chemically doped by Cr ions (b'–e'); the inset explains the formation of Cr impurity energy levels in the band gap of TiO_2 (amounts of Cr ions-chemically doped (in 10^{-7} mol/g), (b') 16, (c') 200, (d') 1000, (e') 2000). Reprinted with permission from ref 425. Copyright 2002 Elsevier.

The increase of the intensity of this absorption shoulder with an increasing amount of Cr ions present in the sample stands in clear contrast to the shift of the absorption onset into the visible region observed for Cr ions implanted into TiO_2 . Photocatalytic activities of TiO_2 and Cr-implanted TiO_2 have been investigated, for example, for the NO decomposition in the gas phase. Visible light irradiation ($\lambda > 450$ nm) of the Cr ion-implanted TiO_2 in the presence of NO at 275 K led to the decomposition of NO into N_2 , O_2 , and N_2O , while under the same conditions, pure TiO_2 or TiO_2 chemically doped with Cr (data not shown) showed no activity for this reaction as illustrated in Figure 45.⁴²⁴

Furthermore, it was found that under solar illumination Cr or V ion implanted TiO_2 shows more than 3 times higher activity for the removal of NO_x as compared to pure TiO_2 (see Figure 46).⁴²⁰

To elucidate the chemical structure of the Cr ions within the TiO_2 matrix, XAFS measurements were performed. Results

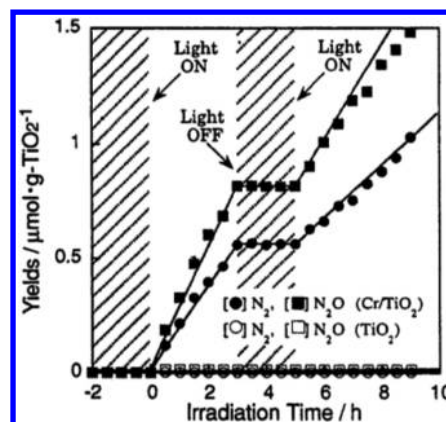


Figure 45. Reaction time profiles of the photocatalytic decomposition of NO into N_2 , O_2 , and N_2O on Cr ion-implanted TiO_2 and on pure TiO_2 under visible light irradiation ($\lambda > 450$ nm). Reprinted with permission from ref 424 (<http://dx.doi.org/10.1107/S0909049598017257>). Copyright 1999 International Union of Crystallography.

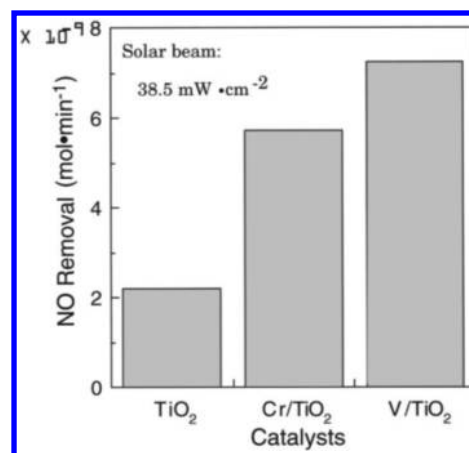


Figure 46. Photocatalytic decomposition on NO on unimplanted original TiO_2 and on V and Cr ion-implanted TiO_2 photocatalysts under outdoor solar irradiation. The data are averaged values observed from 9:00–16:00 on a sunny day with a solar irradiance of 38.5 mW cm^{-2} . Amount of catalyst, 3.6 g; flow rate of air, 18 L min^{-1} . Reprinted with permission from ref 420. Copyright 2004 Springer.

showed that the implanted Cr ions are located at the lattice position of TiO_2 and that they are stabilized as Cr^{3+} ion, while chemically doped Cr ions within TiO_2 (prepared by an impregnation method) exist as the mixture of tetrahedrally and octahedrally coordinated Cr–oxide species (Cr_2O_3 -like cluster) as shown in Figure 47.⁴²⁴

These results highlight the importance of the ion-implantation method (physical method), thus enabling the stabilization of implanted cations at lattice positions of TiO_2 as well as an efficient visible light absorption of the ion-implanted TiO_2 . Tekeuchi et al. also reported that Cr ion-implanted TiO_2 thin films prepared by an ionized cluster beam technique is effective for the visible light-induced photocatalytic decomposition of NO into N_2 , O_2 , and N_2O .⁴¹⁸ Ao et al. also reported the preparation of Cr ion-implanted sol–gel TiO_2 thin films (Cr/TiO_2) and their visible light photocatalytic activity for the decolorization of acid blue 80 employing a metal halide lamp ($\lambda > 470$ nm).^{426,427} XPS investigations of a sol–gel TiO_2 thin film implanted with Cr ion at a concentration of 1×10^{17} ions/ cm^2 revealed that the Cr ions exist within the film as Cr^{3+} . Visible light irradiation of Cr/TiO_2

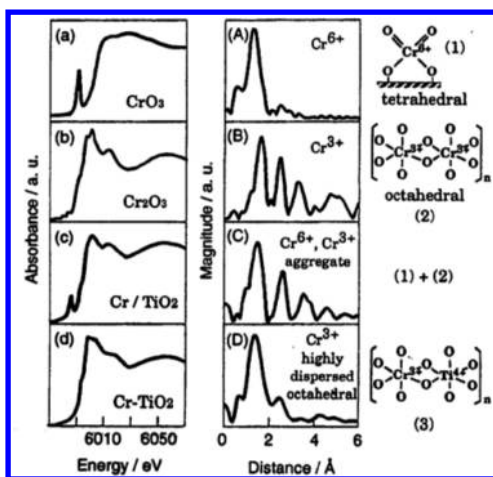


Figure 47. Cr K-edge XANES (a–d) and FT-EXAFS (A–D) spectra of CrO_3 (a, A), Cr_2O_3 (b, B), Cr ion impregnated TiO_2 (c, C), and Cr ion-implanted TiO_2 (d, D) as isolated Cr^{3+} . Reprinted with permission from ref 424. Copyright 2004 Springer.

led to a rapid decolorization of acid blue 80, while the decolorization proceeded very slowly on pure TiO_2 films, demonstrating the effectiveness of the ion-implantation technique to achieve visible light activity for TiO_2 . Ghicov et al. prepared Cr implanted TiO_2 nanotube electrodes by the anodization of Ti foil followed by Cr ion implantation at 60 keV.⁴²⁸

Cr implanted TiO_2 nanotube electrodes showed considerable photocurrents under visible light irradiation even above 520 nm (Figure 48), with the electrode that had been subjected to Cr ion-

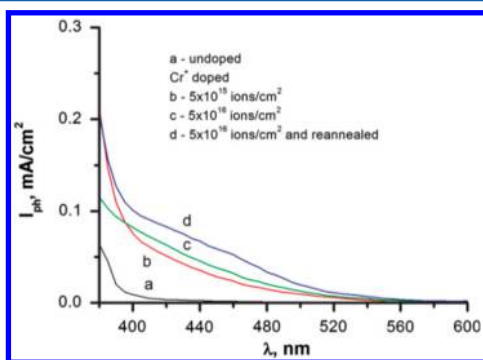


Figure 48. Wavelength dependence of photocurrent (photocurrent spectrum) observed for anatase TiO_2 nanotube layers before Cr ion-implantation as reference (a). The spectra of the nanotube layers following Cr^{+} ion-implantation with a nominal fluence of $5 \times 10^{15} \text{ cm}^{-2}$, with a nominal fluence of $5 \times 10^{16} \text{ cm}^{-2}$, and Cr^{+} ion-implantation with a nominal fluence of $5 \times 10^{16} \text{ cm}^{-2}$, and subsequent annealing at 450°C for 1 h in air are shown in (b), (c), and (d), respectively. Reprinted with permission from ref 428. Copyright 2007 Elsevier.

implantation at a concentration of $5 \times 10^{16} \text{ ions/cm}^2$ followed by annealing treatment at 723 K exhibiting the highest photocurrent in the wavelength region above 400 nm. Recombination kinetics in the Cr implanted TiO_2 nanotube were investigated by using a 10 s light pulse at $\lambda = 450 \text{ nm}$. As shown in Figure 49, the photocurrent transients of TiO_2 nanotubes prepared by Cr implantation ($5 \times 10^{16} \text{ ions/cm}^2$) and subsequent annealing treatment at 723 K showed more than 7 times higher photocurrents than before the annealing step. By the decay fitting analysis, recombination rate constants were determined to

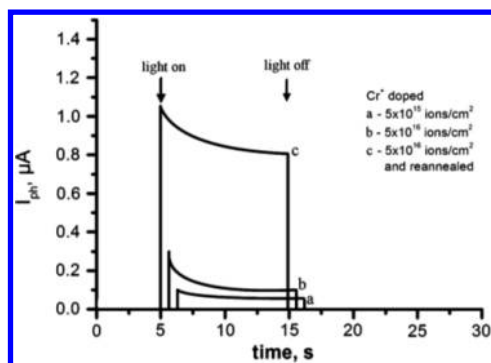


Figure 49. Photocurrent transients of Cr^{+} ion-implanted anatase TiO_2 nanotube electrodes with nominal concentrations of $5 \times 10^{15} \text{ ions/cm}^2$ (a) and $5 \times 10^{16} \text{ ions/cm}^2$ before (b) and after a subsequent thermal annealing step (c). Reprinted with permission from ref 428. Copyright 2007 Elsevier.

be 0.28 and 0.16 s^{-1} for Cr implanted TiO_2 nanotube electrodes before and after the annealing treatment, respectively, evincing the importance of defect elimination by thermal annealing to decrease the recombination rate constant of the photogenerated charge carriers.

Sumita et al. investigated the photoinduced surface charge separation of Cr implanted TiO_2 thin films.^{429,430} Figure 50 shows a schematic diagram of the employed photoinduced transient charge separation (PITCS) measurement setup.

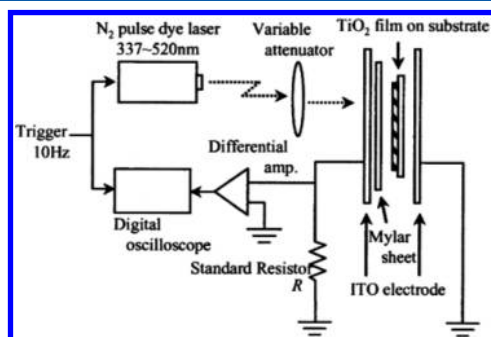


Figure 50. Schematic diagram of a photoinduced transient charge separation (PITCS) measurement setup. Reprinted with permission from ref 419. Copyright 2002 Elsevier.

For these measurements, the TiO_2 films mounted on a substrate were placed between two indium tin oxide electrodes with a Mylar sheet covering the front of the film to prevent carrier injection. A standard resistor R was also connected to the photoirradiated side. Pulsed laser irradiation led to the charge separation within the TiO_2 thin film producing a transient electric charge attributed to surface band bending. After the laser irradiation, this electric charge was subsequently discharged through R . By monitoring the time-resolved voltage drop, the number of carriers transported toward the surface can be calculated. Figure 51 shows the discharge waveforms obtained by these PITCS measurements for an anatase film and the charge separation efficiency ($h^+/\text{photon} \%$) derived from the analysis of such signals as a function of the employed laser wavelength for various TiO_2 films including Cr implanted and doped rutile films.

Cr implanted rutile TiO_2 (Cr ion implantation: 150 keV with $5 \times 10^{15} \text{ ions/cm}^2$) having a Cr concentration gradient shows a higher charge separation efficiency in the visible light region as compared to Cr doped TiO_2 exhibiting a uniform Cr distribution.

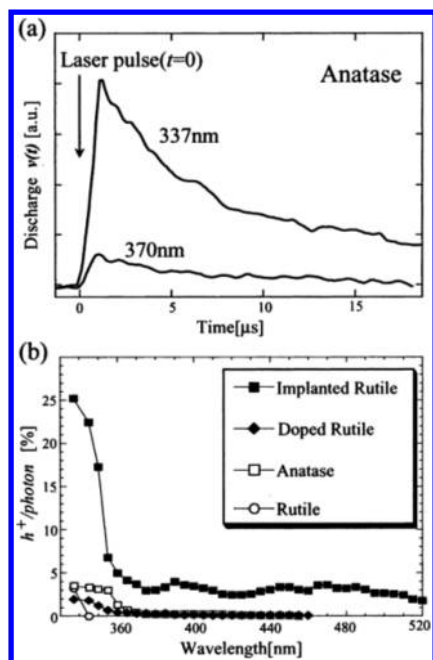


Figure 51. (a) Typical discharge waveforms obtained by PITCS measurements for an anatase film at room temperature. (b) The charge separation efficiency (h^+ /photon %) measured by PITCS as a function of the employed laser wavelength (photon energy) for implanted rutile (with a Cr concentration gradient); doped rutile (with a uniform Cr distribution); undoped highly oriented anatase; and virgin rutile films. Reprinted with permission from ref 419. Copyright 2002 Elsevier.

These results illustrate that a graded Cr distribution in rutile is an important factor resulting in the desired charge separation.

Hou et al. reported the preparation of V ion-implanted TiO_2 films. V ions were implanted within the TiO_2 thin films at 40 keV with various ion fluences: 3×10^{15} , 6×10^{15} , 1×10^{16} , 3×10^{16} , and 6×10^{16} ions/ cm^2 , followed by an annealing of the implanted films at 723 K.⁴³¹ The V ion-implanted TiO_2 films exhibit a visible absorption band above 400 nm with its intensity increasing upon an increase of the ion concentration. The V ion-implanted TiO_2 films were found to readily decompose methyl orange in aqueous solution upon visible light irradiation using a 15 W lamp, with the optimum V ion fluence having been determined to be 6×10^{16} ions/ cm^2 .

In addition to the implantation of Cr and V ions, Fe ion-implantation was also found to be efficient for the preparation of visible light-responsive TiO_2 . Yamashita et al. reported that Fe^+ ion-implantation (at 150 keV) in TiO_2 followed by calcination under O_2 atmosphere at 723 K led to a shift of the absorption edge of TiO_2 to around 600 nm.⁴¹⁹ As in the case of the Cr ion-implantation method, the implanted Fe ions are present as isolated octahedrally coordinated Fe^{3+} species located at a lattice position of TiO_2 . The thus-prepared Fe ion-implanted TiO_2 showed photocatalytic activity for the decomposition of 2-propanol in water into CO_2 through the intermediate formation of acetone under visible light irradiation above 450 nm, while almost no reaction proceeded under the same conditions when pure TiO_2 was used as photocatalyst. Yen et al. also reported the preparation of visible light-responsive photocatalysts by applying the metal plasma ion implantation (MPII) technique to incorporate Fe ions into TiO_2 .^{432,433} MPII can operate at an accelerating energy range of 20–80 keV involving a beamline ion implantation process and enabling an effective ion–solid interaction near the surfaces without excessive radiation

damage.⁴³³ The absorption band of TiO_2 was shifted to the visible light region by Fe ion-implantation at a concentration level of 5×10^{15} ions/ cm^2 , while XPS investigations indicated that some of the lattice Ti^{4+} ions are substituted by Fe^{3+} ions. First-principle calculations based on the density functional theory showed that impurity levels (Fe 3d) are created below the conduction band (Ti 3d) after the Fe ion implantation process, leading to the experimentally observed decrease in the band gap energy of TiO_2 . This Fe ion-doped TiO_2 exhibited a more than 3 times higher photocatalytic activity as compared to pure TiO_2 for the methylene blue decolorization under irradiation from a fluorescent lamp. Furthermore, the photocatalytic activity of Fe ion-doped TiO_2 was enhanced by annealing treatment in an N_2 atmosphere at 773 K for 3 h ((Fe, N) codeposited TiO_2), accompanied by a further increase in the visible absorption band.⁴³² Yao et al. applied Fe ion-implanted TiO_2 to measure the antimicrobial photocatalytic activity under visible light irradiation using a fluorescence lamp.⁴³⁴ Here, the Fe ion-implantation into TiO_2 (TiO_2/Fe) was performed by a metal plasma ion implantation (MPII) technique at 20 keV with 1×10^{16} ions/ cm^2 . The viability of the bacteria *E. carotovora* subsp. *carotovora* ZL1 was tested using the antibacterial drop-test method. The results showed that the survival rate of *E. carotovora* subsp. *carotovora* ZL1 under visible light illumination was dramatically decreased after Fe ion-implantation. Furthermore, as shown in Figure 52, SEM image measurements revealed that the cellular

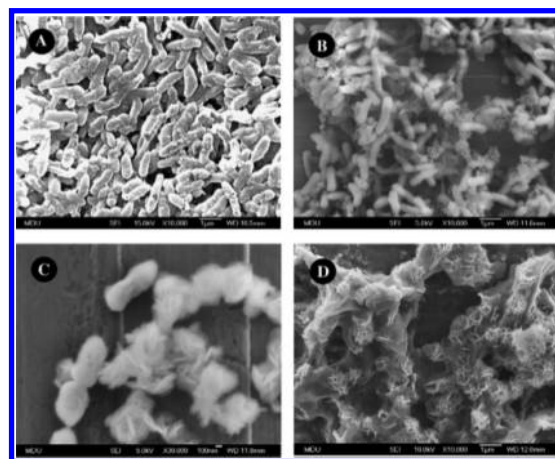


Figure 52. SEM images of the ultrastructure of *Erwinia carotovora* subsp. *carotovora* ZL1 obtained with and/or without TiO_2/Fe thin films after 60 min irradiation. The bacteria were illuminated on an undoped TiO_2/Fe thin film using visible light (N450 nm) irradiation (A). The control sample was kept on a doped TiO_2/Fe thin film in the dark (B), whereas the test samples were illuminated on the doped TiO_2/Fe thin film by visible light (C), and by UV-A light (D). Reprinted with permission from ref 434. Copyright 2007 Elsevier.

surface shape of the *E. carotovora* subsp. *carotovora* ZL1 cells was completely destroyed and shrunk after the illumination, indicating that cell death takes place by the disruption of the cells.

6.2.2. Anion-Implantation. As compared to the transition metal ion-implantation, only rather few examples are known to date of the anion-implantation for the preparation of visible light-responsive TiO_2 with the kind of anions that have been implanted almost being limited to the nitrogen anion. For example, Ghicov et al. have reported the preparation of N implanted TiO_2 nanotubes and their photocurrent response under visible light irradiation.⁴³⁵ TiO_2 nanotube layers were prepared by the anodization of Ti foil and then annealed at 723 K

to convert the nanotube layers into the anatase structure. Nitrogen ions have subsequently been implanted into these samples at 60 keV, attaining a nitrogen concentration of 1×10^{16} ions/cm². Thereafter, the foils have been reannealed at 723 K. XRD results show that this ion implantation process led to an amorphization of the anatase TiO₂ nanotube structure, which, however, was recovered after the reannealing at 723 K. Figure 53

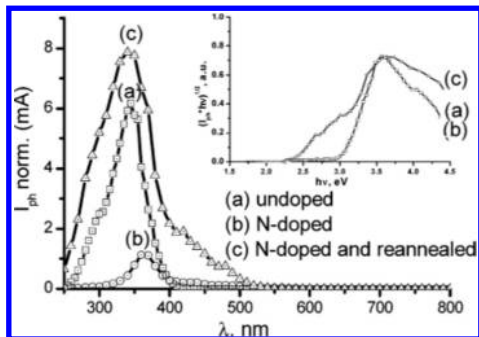


Figure 53. Photocurrent spectra of TiO₂ nanotube layers before N ion-implantation (a), after N ion-implantation (b), and after annealing of the N ion-implanted layer at 723 K for 3 h (c). The inset shows a replot of the spectra with a horizontal axis in the unit of eV. Reprinted with permission from ref 435. Copyright 2006 American Chemical Society.

shows the photocurrent spectra of the TiO₂ nanotube layers, as well as of the N ion-implanted TiO₂ nanotube layers before and after reannealing. It is apparent that the TiO₂ nanotube layers only show a photoresponse in the UV light region below 400 nm and that the photocurrent intensity even decreases upon the subsequent N ion-implantation. However, the reannealing treatment of N ion-implanted TiO₂ nanotube layers led to a remarkable increase in the photocurrent response as well as to a clear appearance of a photocurrent response in the visible light region above 400 nm. These findings show that ion-implantation initially introduces a high number of defect sites within the TiO₂ nanotube structure acting as charge recombination centers. The subsequent reannealing step is therefore required to rebuild the original (anatase) crystal structure and to eliminate these defect sites. The N 1s XPS spectrum of the reannealed N ion-implanted TiO₂ nanotube layer showed two distinct peaks, that is, a peak at 396 eV exhibiting a strong intensity and another peak at 400 eV with low intensity. While the peak at 400 eV could be assigned to adsorbed nitrogen species, the peak at 396 eV has been assigned to atomic N species existing in a state similar to that in TiN, evincing that N ion-implantation and subsequent annealing is an effective method to dope atomic nitrogen species into the TiO₂ matrix, thus realizing visible light absorption and photoresponse.

Gomez et al. have reported that N ion-implanted TiO₂ thin films show a decrease in the water contact angle under visible light irradiation.⁴³⁶ In these studies, the TiO₂ thin films (sample A) were prepared by plasma enhanced chemical vapor deposition at 523 K. These films then were exposed to a high energy nitrogen (N⁺) ion beam employing a particle accelerator at 60 keV with an ion concentration of 2.4×10^{17} ions/cm² at two different substrate temperatures, that is, at ambient temperature (sample B) and at 673 K (sample C). Rutherford backscattering spectroscopy (RBS) measurements showed that sample A was fully stoichiometric, while samples B and C consisted of three different zones: a few surface layers exhibiting TiO₂ stoichiometry and containing some nitrogen species (zone 1), followed by a second zone depleted in oxygen (zone 2) and a third zone

consisting again of stoichiometric TiO₂ (zone 3). Samples B and C showed XPS spectra consisting of broad and strong bands at around 396.2 eV assigned to diamagnetic N(III) species substituting O(II) sites and weak bands at around 398.8 and 401.2 eV assigned to interstitial N species, possibly bound to lattice oxygen forming some kind of NO-like units. The changes in water contact angle were investigated under visible light irradiation ($\lambda > 380$ nm). Sample A (stoichiometric TiO₂) did not show any contact angle change under these conditions. However, samples B and C clearly showed a decrease in the water contact angle under visible light irradiation with the magnitude of this decrease being particularly remarkable for sample C. It should, however, be noted that the water contact angle of sample C did not decrease below 20° under visible light irradiation and that UV light irradiation is indispensable to attain super-hydrophilic surfaces with water contact angles below 10°. Borrás et al. reported a similar water contact change of N ion-implanted TiO₂ thin films (N₂⁺: 50 keV with $0.3\text{--}1.2 \times 10^{17}$ ions/cm²).⁴³⁷ These results indicate that N ion-implanted TiO₂ surely exhibits a visible light response, that is, photocurrent generation or surface wettability changes.

6.3. Preparation of Visible Light-Responsive TiO₂ Photocatalysts by Other Doping Methods: Plasmon Enhanced Photocatalysis and Metal Organic Frameworks (MOF)

Recently, in addition to the above-described attempts to decrease the band gap energy of TiO₂ by chemical or physical doping methods, the sensitizing effect of the surface plasmon resonance absorption by metal nanoparticles has been considered to also be a promising approach for the development of visible light-responsive TiO₂ photocatalysts. Furthermore, a new class of inorganic–organic materials called metal–organic frameworks (MOFs) or porous coordination polymers (PCPs) has emerged, and attention has been focused on their photocatalytic properties under visible light irradiation. These topics will therefore be discussed in the following section.

6.3.1. Plasmon Enhanced Photocatalysis with TiO₂.

Gold nanoparticles have been intensely investigated due to their unique magnetic, electronic, and optical properties based on the surface plasmon resonance (SPR) effect. These properties are strongly dependent on individual differences in the size and shape of the employed nanoparticles. Recently, the unique visible–light SPR absorption characteristics have been applied to design visible-light active photocatalytic systems for processes such as H₂ evolution from water splitting, organic synthesis, and decomposition of pollutants. For example, C.G. Silva et al. have reported that gold nanoparticles supported on TiO₂ (Au/TiO₂) exhibit photocatalytic activity for H₂ or O₂ evolution from water containing the respective sacrificial reagents under UV and visible light irradiation.⁴³⁸ They prepared the Au/TiO₂ by using a deposition–precipitation method and determined the photocatalytic activity of Au/TiO₂ for H₂ or O₂ evolution from water containing EDTA (ethylenediamine tetraacetic acid) or AgNO₃ as sacrificial electron donor or acceptor, respectively. Both H₂ and O₂ evolution over Au/TiO₂ was observed upon visible light illumination; however, the evolution rates were found to be low as compared to the rates obtained upon UV irradiation. This study also investigated the optimum size of gold nanoparticles in the Au/TiO₂ assemblies to achieve the maximum enhancement of the photocatalytic activity with relatively high quantum yields obtained for H₂ and O₂ evolution, respectively, under visible–light irradiation at 560 nm ($\Phi_{\text{H}_2} = 7.5\%$, $\Phi_{\text{O}_2} = 5.0\%$,

respectively) by the use of Au/TiO₂ containing 0.2 wt % gold with an average particle size of 1.87 nm. In addition, Kominami et al. also clearly demonstrated the important role of the particle size in the SPR-induced photocatalytic activity of Au/TiO₂ for the H₂ evolution from aqueous solutions containing various biomass-related compounds (2-propanol, methanol, ethanol, ammonia, and benzyl alcohol) under irradiation of visible light at around 550 nm.⁴³⁹

These authors reported that large particle sizes of gold (13 nm) on TiO₂ prepared by a multi-step (MS) photodeposition method exhibit much stronger photoabsorption at 550 nm than small particle sizes (1.2 nm) prepared by a single-step (SS) photodeposition method (Figure S4). These results are a

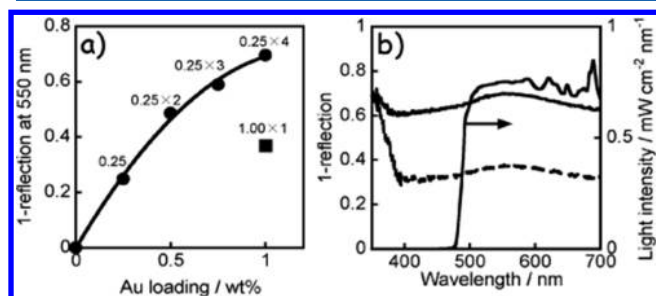


Figure S4. (a) Intensity of photoabsorption of MS-Au/TiO₂ at 550 nm as a function of the different Au loadings (●) and for SS-(1.00)Au/TiO₂ (■), (b) absorption spectra of SS-(1.00)Au/TiO₂ (broken line) and SS-(1.00)Au/TiO₂ (solid line) and light intensity of visible light used for the irradiation employing a Xe lamp with a Y-48 filter (right axis). Au was loaded by repeating 0.25 wt % loading of Au (0.25, 0.25 × 2, 3, 4 times) or 1.0 wt % at one time (1.00 × 1). Values in the figure represent the amount and the frequency of Au loading.⁴³⁹ Reprinted with permission from ref 439. Copyright 2012 Royal Society of Chemistry.

contrast to the report by Silva et al., although the preparation method and the materials used by the two groups were different. Regarding the SPR-induced photocatalytic activity of Au/TiO₂, E. Kowalska and co-workers have observed that the activity depended strongly on the properties of gold and TiO₂, such as particle size and shape, surface area, and crystalline form.^{440,441} They have investigated and evaluated the visible-light-induced photocatalytic activity of different sizes and shapes of Au/TiO₂ particles prepared by the photodeposition of gold nanoparticles on various commercial TiO₂ powders. Their results revealed that the size and shape of the photodeposited gold nanoparticles of Au/TiO₂ are strictly dependent on the TiO₂ particle properties (i.e., fine gold particles are generated on fine TiO₂ particles, while larger gold particles are mainly formed on large TiO₂ particles.). Moreover, the photocatalytic reaction rates roughly increased linearly with increasing particle sizes of gold and TiO₂ (Figure S5).

However, these data have not been obtained with TiO₂ powders being uniform in particle size. Therefore, to unambiguously evaluate the correlation between particle size and shape of the gold nanoparticles and the SPR-induced photocatalytic activity, the development of a deposition method for the formation of uniformly sized gold nanoparticles on differently sized TiO₂ particles will be important.

As for the mechanism of SPR-induced photocatalytic systems, T. Tatsuma and co-workers have suggested a SPR-induced charge separation scheme.¹⁸⁹ They propose that the charge separation is accomplished by electron transfer from the excited gold nanoparticles to the conduction band of TiO₂, while the

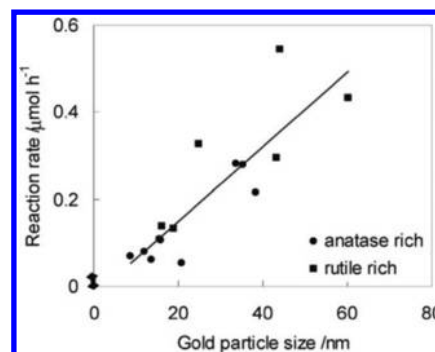


Figure S5. Acetone generation under visible-light irradiation (>450 nm) on Au modified titania powders (line indicates the range of activities of bare samples). Reprinted with permission from ref 440. Copyright 2009 Royal Society of Chemistry.

thus transferred electrons are replaced directly from a suitable donor to the excited gold nanoparticles (Figure S6). Likewise,

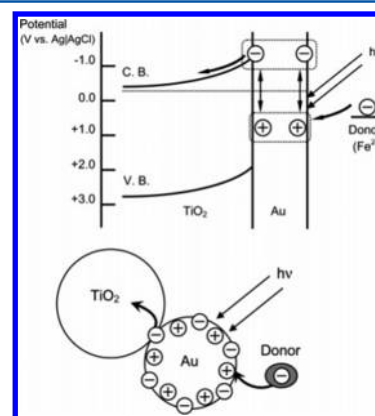


Figure S6. Proposed mechanism explaining the processes occurring in a SPR-induced photocatalytic system. Charges are separated at the interface between the visible-light-irradiated gold nanoparticle and the TiO₂ particle. Reprinted with permission from ref 189. Copyright 2005 American Chemical Society.

the H₂ and the O₂ evolution mechanisms have been described by C. G. Silva et al. on the basis of charge separation schemes.⁴³⁸ In this report, they proposed, for example, for the mechanism of molecular hydrogen formation that the gold nanoparticles absorb photons in the SPR wavelength region and subsequently inject the SPR-induced electrons into the semiconductor conduction band of TiO₂ as shown in Figure S7.

Furthermore, the SPR-induced photocatalytic reaction sites of Au/TiO₂ have been identified by T. Majima and co-workers.^{442,443} They observed the photocatalytic reduction sites of

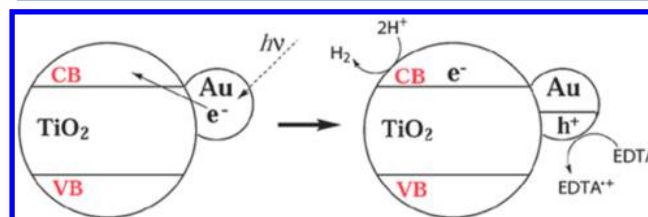


Figure S7. Proposed rationalization of the photocatalytic H₂ formation activity in EDTA-containing aqueous suspensions of Au/TiO₂ upon excitation of the gold surface plasmon band. Reprinted with permission from ref 438. Copyright 2011 American Chemical Society.

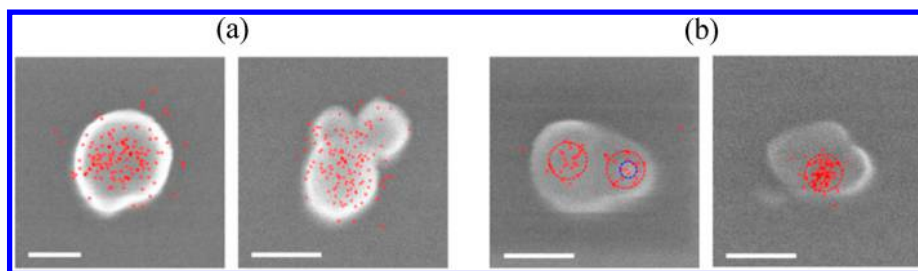


Figure 58. Spatial distribution of fluorescence spots (red dots, >50 spots) collected from TiO₂ (a) and from 14 nm Au/TiO₂ particles. (b) The SEM images of the particles analyzed are shown. Scale bars are 100 nm. The locations of the reactive sites and of the Au nanoparticles are surrounded with dashed lines in red and blue, respectively. Reprinted with permission from ref 415. Copyright 2013 American Chemical Society.

Au/TiO₂ by using water-soluble fluorescent probe molecules. As compared to pure TiO₂, where the reduction sites appear to be rather evenly distributed across the surface of the TiO₂ particle, for Au/TiO₂ the reduction sites seem to exist mainly at or around the gold nanoparticles (Figure 58).

These results indicate that the SPR-induced photocatalytic reduction takes place on the surface of TiO₂ in the vicinity of the gold nanoparticles. Thus, both photocatalytic reduction and photocatalytic oxidation occur at or at least around the gold nanoparticles on the TiO₂ surface. Therefore, to enhance the photocatalytic activity of plasmonic Au/TiO₂ systems, it might be necessary to control rather short deposition distances of the individual gold nanoparticles on TiO₂.

6.3.2. Metal Organic Frameworks (MOF). Metal organic frameworks (MOFs) and porous coordination polymers (PCPs) are hybrid organic–inorganic porous materials consisting of organic linkers and metal–oxo clusters. Their various applications as adsorbents, separation materials, ion conductive materials, or catalysts are currently active areas of research.^{444–446} Additionally, in recent years an increasing number of studies have explored the possibility to employ MOFs as platforms for the integration of different functional molecular components to achieve light harvesting and to drive various photocatalytic reactions.^{447–451} As compared to other photocatalytic systems, these integrated MOF photocatalytic–catalytic systems have the advantage that the possible range of combinations of metal–oxo clusters and bridging organic linkers allows for a fine-tuning and a rational design of these photocatalysts at the molecular level. Furthermore, the intrinsic porosity of MOFs facilitates the diffusion of substrates and products through the open framework structures. Herein, we introduce visible-light-responsive Ti-based MOF photocatalysts, the organic linkers of which act as light-harvesting units. In 2009, Férey and co-workers reported the synthesis of a Ti-based MOF (MIL-125(Ti), Ti₈O₈(OH)₄–(O₂C–C₆H₄–CO₂)₆) consisting of Ti–oxo clusters and 1,4-benzenedicarboxylic acid (H₂BDC), here denoted as Ti–MOF.⁴⁵² As described in Figure 59, its 3D pseudocubic structure consists of cyclic octameric inorganic subunits of edge- and corner-sharing TiO₅(OH) octahedra connected through an organic linker (BDC). Ti–MOF shows also a high thermal stability (633 K) and porosity ($S_{\text{BET}} \approx 1550 \text{ m}^2 \text{ g}^{-1}$, $V_p \approx 0.6 \text{ cm}^3 \text{ g}^{-1}$) with two types of cages corresponding to the octahedral (12.55 Å) and the tetrahedral vacancies (6.13 Å) of a cc packing accessible through triangular narrow windows (5–7 Å). It was also reported that Ti–MOF exhibits photocatalytic activity for the oxidation of alcohols to aldehydes under UV-light irradiation.

More recently, Li and co-workers described the successful tuning of the optical properties of Ti-based MOFs by synthesizing a visible-light-responsive Ti-based MOF photo-

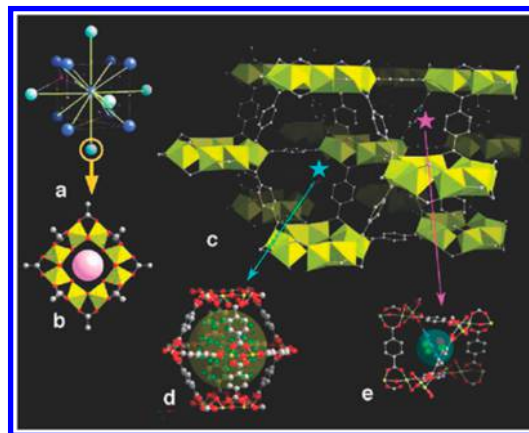


Figure 59. (a) Perspective view of a centered cubic (cc) arrangement; the 12-fold coordination is evidenced by yellow lines. Purple and orange dots indicate the positions of the centers of the tetrahedral and octahedral vacancies. (b) View of the perforated cyclic octamer with edge- and corner-sharing Ti octahedra; it corresponds to the atom with an orange circle of the classical cc packing through the SBU augmentation. (c) Perspective view of Ti–MOF with the central octamer surrounded by 12 others; the pink and blue stars indicate the centers of the tetrahedral and octahedral vacancies in Ti–MOF. (d) Ball and stick representation of the octahedral vacancy, filled by water molecules (in green); the large yellow sphere represents the effective accessible volume of the cage. (e) The tetrahedral vacancy; in (d) and (e) the color code is as follows: carbon, gray; oxygen, red; water, green; titanium, yellow. Reprinted with permission from ref 452. Copyright 2009 American Chemical Society.

catalyst with 2-amino-benzenedicarboxylic acid (H₂BDC–NH₂) as an organic linker (MIL–125(Ti)–NH₂), here denoted as Ti–MOF–NH₂, and its application as a photocatalyst for CO₂ reduction to form formate anions (HCOO[−]) under visible-light irradiation ($\lambda > 420 \text{ nm}$).⁴⁵³ The photocatalytic reduction of CO₂ was performed in acetonitrile with triethanolamine (TEOA) as sacrificial agent. The amount of produced HCOO[−] reached 8.14 μmol after a 10 h period of the photocatalytic reaction, while Ti–MOF or a mixture of TiO₂ and H₂BDC–NH₂ showed no photocatalytic activity under the same conditions (Figure 60). The results obtained from several control reactions revealed that the light irradiation as well as the presence of Ti–MOF–NH₂ and of TEOA as sacrificial electron donor are essential for the progress of the reaction. Furthermore, employing isotopically labeled ¹³CO₂ revealed that the produced HCOO[−] indeed originates from CO₂.

Matsuoka and co-workers also reported that Ti–MOF–NH₂ behaves as an effective photocatalyst for the visible-light-driven hydrogen production as well as for the respective reduction of nitrobenzene.^{454,455} They also elucidated the reaction mecha-

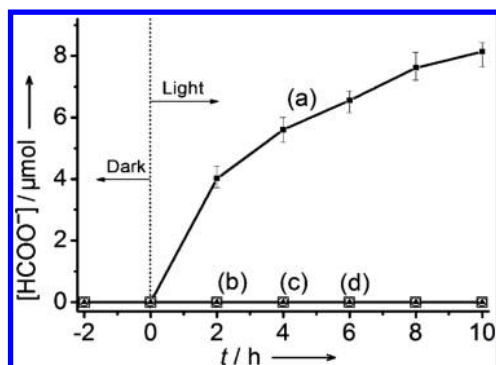


Figure 60. Amount of HCOO^- produced as a function of the time of irradiation over (a) Ti-MOF- NH_2 (■), (b) Ti-MOF (□), (c) a mixture of TiO_2 and $\text{H}_2\text{BDC-NH}_2$ (19 mg + 32 mg) (○), and (d) visible light irradiation without a sample (▲). The solutions were irradiated using a Xe lamp with filters producing light in the range of 420–800 nm. Photocatalysts: 50 mg, MeCN/TEOA (5:1); solution volume, 60 mL. Reprinted with permission from ref 453. Copyright 2012 Wiley.

nism of Ti-MOF- NH_2 -catalyzed reactions under visible-light irradiation by obtaining action spectra and using in situ ESR techniques. The apparent quantum yields were observed to depend strongly on the illumination wavelength in a manner that correlates with respective absorption intensities in the visible spectrum of Ti-MOF- NH_2 (Figure 61).

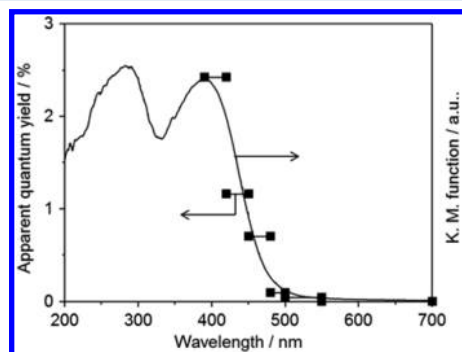


Figure 61. Action spectrum for hydrogen evolution from water containing TEOA as a sacrificial electron donor over Ti-MOF- NH_2 . Reproduced with permission from ref 445. Copyright 2008 The Royal Society of Chemistry.

The longest wavelength available to initiate photocatalytic reactions was shown to be 500 nm. In addition, similar results were obtained by photoelectrochemical measurements and for the photocatalytic reduction of nitrobenzene. For ESR measurements, Ti-MOF- NH_2 was immersed in an aqueous solution of 0.01 M TEOA, and this suspension was evacuated at 77 K. Following irradiation by visible light ($\lambda > 420$ nm) for 3 h at room temperature, the ESR spectrum was recorded at 77 K. This ESR spectrum contained signals, the parameters of which are characteristic of paramagnetic Ti^{3+} centers in a distorted rhombic oxygen ligand field ($g_x = 1.994$, $g_y = 1.958$, and $g_z = 1.904$). The combined results from the action spectra and the ESR measurements clearly suggest that the reaction proceeds through light absorption by the organic linker (i.e., the BDC- NH_2 group) followed by electron transfer to the conduction band of the catalytically active titanium-oxo cluster, as shown in Figure 62.

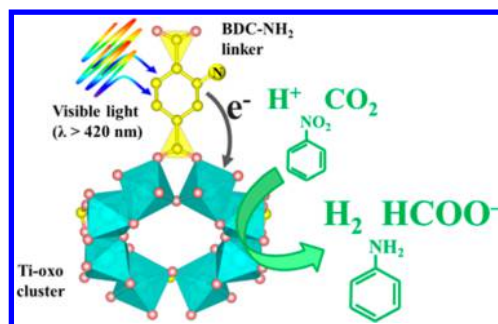


Figure 62. Schematic illustration of the mechanism of the photocatalytic hydrogen production reaction (or other photocatalytic reduction reactions, such as nitrobenzene reduction) over Ti-MOF- NH_2 upon visible-light irradiation ($\lambda > 420$ nm).

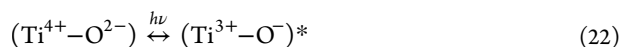
Subsequently, Garcia and co-workers further confirmed by laser flash photolysis measurements the ability of Ti-MOF- NH_2 to undergo photoinduced charge separation.⁴⁵⁶ The spectroscopic data obtained during the laser flash photolysis of Ti-MOF- NH_2 showed a transient signal compatible with the photoinduced charge separation leading to the generation of electrons and holes. The use of methylviologen as electron acceptor and of tetramethylphenylenediamine as electron donor confirmed that the irradiation of Ti-MOF- NH_2 can serve to simultaneously promote reduction and oxidation reactions, depending on the redox potentials of the probe molecules. In addition, Walsh et al. elucidated the specific role of the - NH_2 group of the BDC- NH_2 linker in lowering the optical band gap of Ti-MOF- NH_2 (ca. 2.6 eV) through a combination of experimental and theoretical approaches.⁴⁵⁷ They confirmed that electronic modifications of the aromatic moiety are localized and are thus able to directly control the optical properties through modifications of the valence band. The optical band gap decrease observed when the BDC- NH_2 linker was used arises from the donation of the N 2p electrons to the aromatic linking unit, resulting in a red-shifted band above the valence-band edge of Ti-MOF. Walsh and co-workers further studied silico-Ti-based MOFs with a diaminated linker ($\text{BDC}-(\text{NH}_2)_2$) and other functional groups (-OH, - CH_3 , -Cl) as alternative substitutions to control the optical response. The BDC- $(\text{NH}_2)_2$ linking unit was predicted to lower the band gap of Ti-based MOFs to 1.28 eV, and this was experimentally confirmed through the synthesis of the Ti-MOF- $(\text{NH}_2)_2$.

As described in this section, the accurate combination of metal-oxo clusters and organic linkers is of extreme importance for the development of more efficient MOF photocatalysts. The methods described here can be further extended to the large range of organic linkers used in MOF synthesis, which should enable accurate control of optical properties in tailored frameworks.

7. TITANIUM-BASED SINGLE-SITE PHOTOCATALYSTS

Titanium oxide moieties isolated at the atomic level within, for example, silica matrixes of zeolites or mesoporous silica show unique and efficient photocatalytic properties, which can often not be realized by bulk TiO_2 photocatalysts.^{60,458,459} This type of photocatalyst is called “single-site photocatalyst”. Single-site photocatalysts can be prepared by various techniques typified as hydrothermal synthesis, sol-gel method, ion-exchange method, and chemical vapor deposition method. Besides Ti, various types of transition metals, such as V, Cr, Mo, and W, can be incorporated into silica matrixes,⁴⁶⁰ and in many cases, the

atomic ratio of the silicon atom and the incorporating transition metal atom within a single-site photocatalyst is more than 30 for the formation of the monomeric metal oxide moieties. In the case of bulk TiO_2 photocatalysts, photoirradiation leads to optical excitation across the band gap resulting in charge separation within the particles; that is, the excitation of electrons into the conduction band and the accompanying hole generation in the valence band take place upon light irradiation. These photoformed electrons and holes act as electron donors and acceptors, respectively, on the photocatalyst surface, thus enabling the photocatalytic process to proceed. In contrast, the light irradiation of a single-site photocatalyst induces the formation of a charge-transfer excited state via a ligand-to-metal charge-transfer transition from the oxygen anion (O^{2-}) to the titanium cation (Ti^{4+}) in an isolated TiO_4 moiety (eq 22). The excited electron–hole pair localizes quite near to each other as compared to that produced in semiconducting materials and plays most likely a significant role in various photocatalytic reactions. In this section, we introduce structural characterizations and various applications of mainly Ti-based single-site photocatalysts.



7.1. Local Structure of a Single-Site Photocatalyst

An explanation of the local structure of a Ti-based single-site photocatalyst will be given here. As shown in Figure 63, the incorporated Ti–oxide moiety within silica matrixes of Ti-based single-site photocatalysts exists in a tetrahedrally coordinated state.

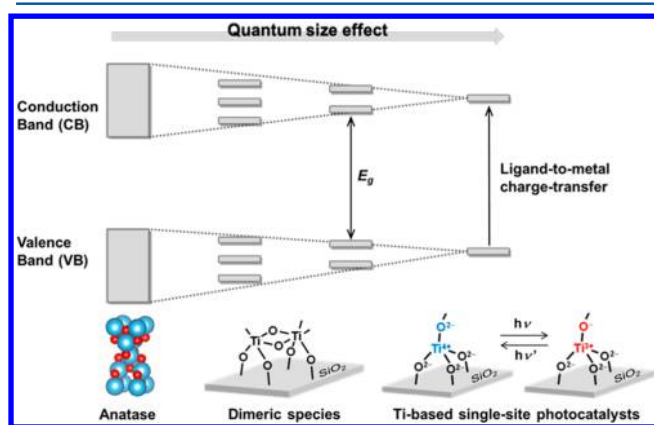


Figure 63. Illustration of various titanium species and their corresponding electronic states.

This local structure around the titanium center has been confirmed, among others, by diffuse reflectance UV–vis (DRUV–vis), photoluminescence, XAFS, and FT-IR measurements.^{461–466} Figure 64A shows typical DRUV–vis spectra of Ti-MCM-41 (Ti-MCM-41), with different titanium content.⁴⁶⁷ The spectrum of Ti-MCM-41 with a Ti content of 0.5 wt % shows a sharp absorption band at 215 nm assignable to a charge transfer from O^{2-} to Ti^{4+} of tetrahedrally coordinated Ti–oxide moieties dispersed in the mesoporous silica framework, which is completely different from the bulk TiO_2 powder spectrum showing a broad absorption band at 200–400 nm due to band gap excitation. Upon increase in the Ti content within Ti-MCM-41, an absorption shoulder at 260 nm appears and grows. This band is explained by HOMO–LUMO absorptions within

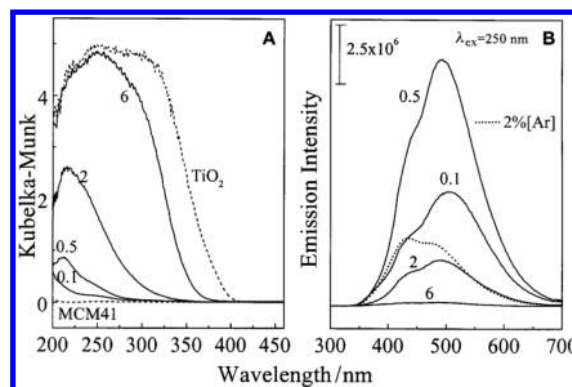


Figure 64. (A) DRUV–vis spectra of Ti-MCM-41 with different titanium content (0.1, 0.5, 2, 4, and 6 wt %) and bulk TiO_2 . (B) Photoluminescence spectra (excitation at 250 nm) of Ti-MCM-41 with different titanium content (0.1, 0.5, 2, and 6 wt %). 2% [Ar] represents that the sample containing 2 wt % Ti was prepared under argon using Schlenk techniques with a surface dehydration step under high vacuum (453 K, 1 h) for spectroscopic comparisons. Prior to the measurements, oxidation in 100 Torr at 823 K and evacuation at the same temperature were conducted. Reproduced with permission from ref 467. Copyright 1999 The Royal Society of Chemistry.

oligomers and/or TiO_2 -like clusters, that is, octahedrally coordinated Ti–oxide species. Moreover, a fluorescence emission corresponding to a radiative decay process from the excited charge-transfer state to the ground state is observed in the PL spectra of Ti-based single-site photocatalysts. As can be seen from Figure 64B, a characteristic emission band is detected at 490 nm upon excitation at 250 nm.

XAFS measurements are also very sensitive to detect the presence of isolated and tetrahedrally coordinated Ti–oxide moieties.^{468,469} Figure 65 displays the Ti K-edge XANES (left)

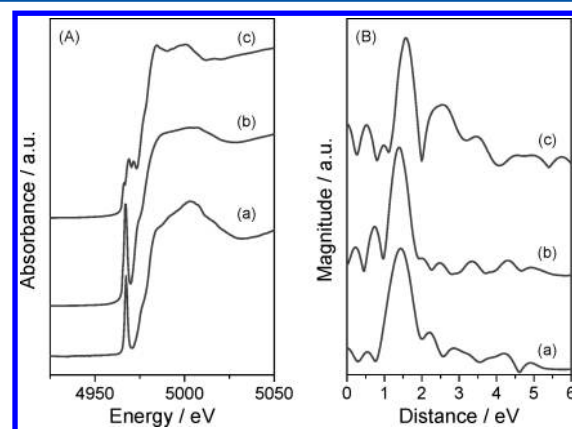


Figure 65. Ti K-edge (A) XANES and (B) Fourier transform of EXAFS spectra of (a) Ti-MCM-41, (b) tetraisopropyl orthotitanate ($\text{Ti}(\text{O}^i\text{Pr})_4$), and (c) anatase TiO_2 powder.

and the Fourier transform of the EXAFS spectra (right) of Ti-MCM-41 together with tetraisopropyl orthotitanate ($\text{Ti}(\text{O}^i\text{Pr})_4$) and anatase TiO_2 powder as reference samples.

In the XANES spectrum of TiO_2 powder, several well-defined pre-edge peaks are observed, which are assigned to titanium in a symmetric octahedral environment. In contrast, Ti-MCM-41 and tetraisopropyl orthotitanate both exhibit a sharp single pre-edge peak at 4968 eV attributed to the $1s$ – $3d$ transition, indicating the presence of tetrahedrally coordinated Ti–oxide moieties. In the Fourier transform of the EXAFS data, TiO_2

powder shows a peak at around 2.5 Å corresponding to a contiguous Ti–O–Ti bond. On the other hand, in the data of Ti-MCM-41 and tetraisopropyl orthotitanate, only a strong peak at around 1.5 Å corresponding to neighboring oxygen atoms (Ti–O bond) can be observed. These findings reveal that Ti-MCM-41 possesses monomeric TiO_4 moieties.

FT-IR spectra of Ti-based single-site photocatalysts show an obvious band at 960 cm^{-1} attributed to the Si–O–Ti stretching frequency, the intensity of which grows with an increase in the Ti content. However, even in the spectrum of pure silicate materials, this band can be observed exhibiting a very low intensity. In pure silicate materials, the band at 960 cm^{-1} is assigned to the Si–O stretching vibrations of $\text{Si-O}^-\text{H}^+$ groups. Thus, although this band should not be regarded as a complete proof because its origin and interpretation can be ambiguous,^{461,470} it could be the one result that indicates the presence of isolated Ti–oxide moieties within their silica framework when combined with the other characterization techniques described above.

7.2. Decomposition of Harmful Organic Compounds

The photocatalytic decomposition of harmful organic compounds in water or air is a promising process for environmental remediation. Although a wide range of organic pollutants can be oxidized into CO_2 and H_2O under light irradiation by using bulk photocatalysts, there are several advantages in the use of single-site photocatalysts. As depicted in Figure 63, the oxidation and reduction power of single-site photocatalysts induced by light irradiation is enhanced due to the discretization of energy levels. Moreover, because most single-site photocatalysts are synthesized by employing silica-based porous materials, they are expected to show adsorptive enrichment effects, thus facilitating substance diffusion. In fact, Zhuang et al. demonstrated that Ti-containing hexagonal mesoporous silica (Ti-HMS) exhibits better photocatalytic activity for the decomposition of benzene in the gas phase than commercial powdered TiO_2 (P 25) as shown in Figure 66.⁴⁷¹ After 1 h of reaction, the average conversion ratio

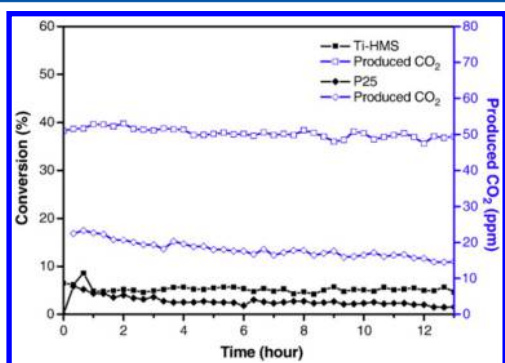


Figure 66. Time course of the photocatalytic activity of Ti-HMS and P25 for the decomposition of benzene. Reprinted with permission from ref 471. Copyright 2010 Elsevier.

had reached 5.2% by using the Ti-HMS photocatalyst while producing ca. 50 ppm of CO_2 from ca. 250 ppm benzene. This finding corresponds to an average mineralization ratio of 65.4%. Moreover, no obvious deactivation was observed for the degradation of benzene during 12 h of reaction over the Ti-HMS photocatalyst. In contrast, the photocatalytic activity observed by using P 25 is lower and not stable. After 12 h of reaction, the conversion ratio over P 25 was found to decrease to 1.5% along with the production of 15 ppm of CO_2 . Such deactivation of TiO_2 photocatalysts is often observed for the

degradation of volatile aromatic compounds, and can usually be explained by the deposition of the stable reaction intermediates and/or polymeric species on the surface of TiO_2 .⁴⁷²

Furthermore, Kosuge et al. achieved much higher photocatalytic activity for the decomposition of acetic acid in the liquid phase than with commercially available anatase TiO_2 (Ishihara-Sangyo Co., Ltd., ST-01) by using a Ti-containing mesoporous silica, in which the Ti-containing mesoporous silica yielded 39 times higher TON than ST-01 (Figure 67).⁴⁷³

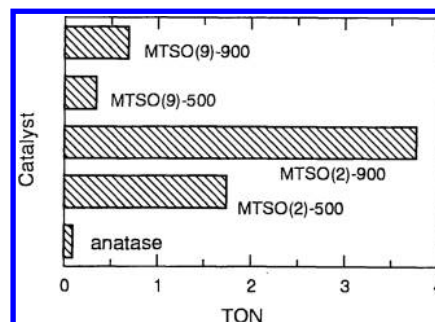


Figure 67. Photocatalytic activities for acetic acid decomposition by using various photocatalysts. The prepared Ti-containing mesoporous silicas are designated as MTSO(*x*)-*T*, where *x* and *T* are the Ti mol % and calcination temperature, respectively. Reprinted with permission from ref 473. Copyright 1998 The Chemical Society of Japan.

Lee et al. applied titanium silicalite (TS-1) for the photocatalytic decomposition of 4-nitrophenol in water.⁴⁷⁴ The photocatalytic decomposition rate of TS-1 was found to be improved by the addition of H_2O_2 , especially under acidic conditions. It has been concluded from these results that $\cdot\text{OH}$ radicals are efficiently generated from titanium–hydroperoxide species formed through an interaction of framework titanium in TS-1 with H_2O_2 under UV-light irradiation. Ti-based single-site photocatalysts are also effective for the decomposition of ethylene as reported by Fu and co-workers.⁴⁷⁵ Figure 68 shows

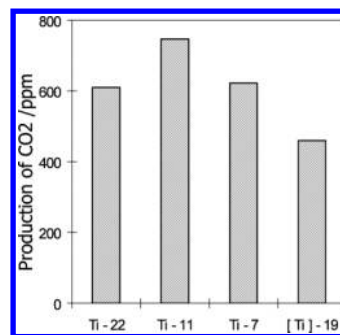


Figure 68. Yields of CO_2 produced during the photocatalytic ethylene decomposition by using various Ti-MCM-41 photocatalysts. Reprinted with permission from ref 475. Copyright 2006 Elsevier.

yields of CO_2 formed during the photocatalytic ethylene decomposition in the presence of various Ti-MCM-41 photocatalysts. Herein, Ti-*X* stands for Ti-MCM-41 photocatalysts with different Ti content (*X* is the Si/Ti molar ratio) prepared by a chemical vapor deposition technique, and [Ti]-19 means Ti-MCM-41 photocatalysts with Si/Ti molar ratio of 19 prepared by a conventional sol–gel process. As the titanium concentration increases, the photocatalytic activity is found to increase to its maximum level followed by a slow decrease. These findings imply

that isolated and tetrahedrally coordinated Ti–oxide moieties are the main active species for the photocatalytic decomposition of ethylene, and that titanium oxide clusters formed when higher amounts of titanium are incorporated apparently inactivate the reaction. Moreover, Ti-22, which was prepared by a chemical vapor deposition technique, showed higher photocatalytic activity than the material prepared by a sol–gel process ([Ti]-19) despite its almost identical titanium content. This can be rationalized by the fact that in Ti-22 the entire amount of titanium is located on the mesoporous silica surface, while part of the titanium content in [Ti]-19 is embedded in the silica wall and can therefore not interact with the ethylene. As described above, distinct photocatalytic processes for the decomposition of organics can be attained by using Ti-based single-site photocatalysts.

7.3. Decomposition of NO

Nitrogen oxides (NO_x) are among the most harmful atmospheric pollutants and a major contributor to acid rain and photochemical smog, both of which pose a serious problem worldwide. Therefore, much attention has been paid to the removal of nitrogen oxides (NO_x : NO , N_2O , NO_2) from the atmosphere via their direct decomposition into N_2 and O_2 using photocatalysts. Moreover, concomitantly, the photochemistry of nitrogen oxides on the TiO_2 surface has also been intensively investigated.^{476,477} Against this background, Anpo and co-workers have thoroughly studied the applicability of single-site photocatalysts for the photocatalytic NO_x decomposition reaction.^{478–485} Figure 69

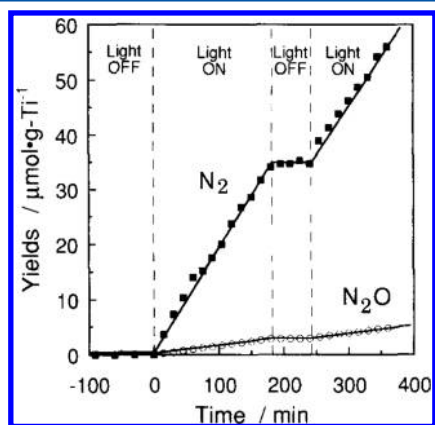


Figure 69. Reaction time profile of the photocatalytic decomposition of NO into N_2 and N_2O on Ex-Ti/Y-zeolite. Reprinted with permission from ref 486. Copyright 1997 Elsevier.

shows the reaction time profile of the photocatalytic decomposition of NO into N_2 and N_2O on Ti–oxide species-anchored Y-zeolite (Ex-Ti/Y-zeolite), which was prepared by an ion-exchange method from an aqueous titanium ammonium oxalate solution.⁴⁸⁶

The yields of N_2 and N_2O were found to increase linearly with the irradiation time, and as soon as the illumination is stopped, the reaction also immediately ceases. This result indicates that Ex-Ti oxide/Y-zeolite photocatalytically promotes the decomposition of NO into N_2 and N_2O under UV-light irradiation. Although this reaction also proceeds by using other Ti-based photocatalysts, its reactivity, and especially its product selectivity, is largely different. As shown in Table 3, N_2 is produced with high selectivity over Ex-Ti/Y-zeolite, whereas TiO_2 powder as well as Ti–oxide-loaded Y-zeolites prepared by using an impregnation method (Imp-Ti/Y-zeolites) yield N_2O as the major product.

Table 3. Photocatalytic Decomposition of NO into N_2 and N_2O over Various Ti-Based Photocatalysts^a

catalyst	Ti content [wt % as TiO_2]	yield [$\mu\text{mol g}_{\text{cat}}^{-1} \text{h}^{-1}$]			selectivity [%]	
		N_2	N_2O	total	N_2	N_2O
Ex-Ti/Y-zeolite	1.1	14	1	15	91	9
Imp-Ti/Y-zeolite	1.1	7	10	17	41	59
Imp-Ti/Y-zeolite	10	5	22	27	19	81
TiO_2 powder	100	2	6	8	25	75

^aReprinted with permission from ref 486. Copyright 1997 Elsevier.

In this NO decomposition reaction, the high selectivity of its photocatalytic transformation to harmless N_2 realized by using Ex-Ti/Y-zeolite is significantly important and beneficial for the practical application to environmental remediation. These selectivity differences can be related to the local structure around the titanium atom. From XAFS investigations, the Ti–oxide moieties within the Ex-Ti/Y-zeolite are revealed to exist in isolated and tetrahedrally coordinated states; that is, they are single-site photocatalysts. On the other hand, Imp-Ti/Y-zeolites contain aggregated and octahedrally coordinated Ti–oxide species. These findings imply that the titanium oxide moieties with tetrahedral coordination play an important role for the enhancement of the N_2 selectivity during the photocatalytic decomposition of NO. On the basis of these considerations, the relationship between the selectivity of the NO conversion to N_2 and the coordination number of the Ti–oxide species within various photocatalysts was investigated. The results summarized in Figure 70 demonstrate a clear dependence of the N_2 selectivity

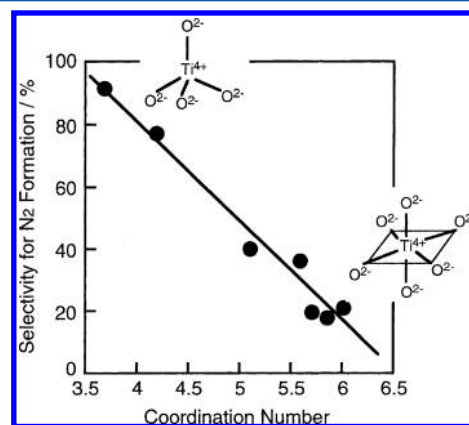


Figure 70. Dependence of the NO to N_2 conversion selectivity for the photocatalytic NO decomposition on the coordination number of various Ti-based photocatalysts. Reprinted with permission from ref 60. Copyright 2003 Elsevier.

on the coordination number, in which the selectivity of the conversion to N_2 increases with a lowering of the coordination number of titanium oxide species from 6 (octahedral coordination) to 4 (tetrahedral coordination).

Subsequently, the reaction mechanism between photoexcited tetrahedrally coordinated titanium oxide moieties and NO molecules was analyzed by photoluminescence measurements. The PL spectrum of Ex-Ti/Y-zeolite observed by excitation at 290 nm at 77 K in vacuo shows a typical emission band around 490 nm attributable to a radiative decay process from the excited charge-transfer state of tetrahedrally coordinated Ti–oxide moieties ($(\text{Ti}^{3+}-\text{O}^-)^*$). When NO was added to the measure-

ment system, a significant quenching of the PL spectrum was observed. Moreover, the lifetime of the excited charge-transfer state is shortened as the amount of NO added increases. These findings demonstrate that NO molecules have access to the tetrahedrally coordinated Ti–oxide moieties and can interact easily with their excited charge-transfer states. Figure 71 displays

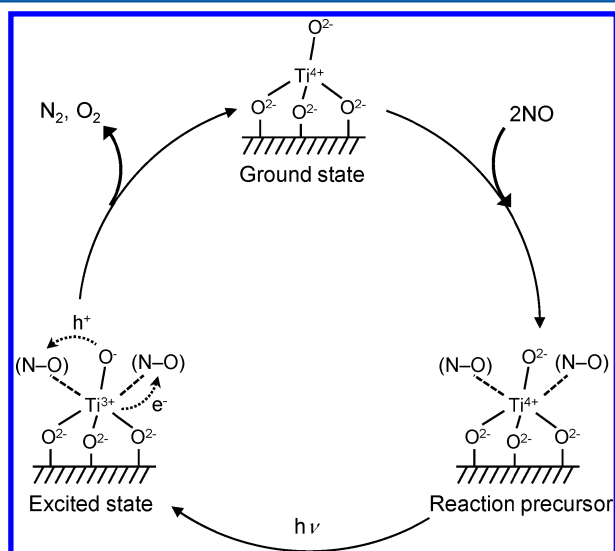


Figure 71. Proposed reaction mechanism of the photocatalytic NO decomposition reaction induced by Ex-Ti/Y-zeolite under UV-light irradiation.

the proposed reaction pathway based on the above results. First, NO molecules are adsorbed to tetrahedrally coordinated Ti–oxide moieties as weak ligands to form the reaction precursors. Upon irradiation by UV light, these reaction precursors are converted into the respective excited charge-transfer complexes, $(\text{Ti}^{3+}-\text{O}^-)^*$, followed by an electron transfer from Ti^{3+} to the antibonding π -orbital of NO. Simultaneously, an electron transfer proceeds from the π -bonding orbital of another NO into the trapped hole center, O^- . It is through these two simultaneous electron transfer processes that the direct decomposition of two NO molecules into N_2 and O_2 can progress on one excited $(\text{Ti}^{3+}-\text{O}^-)^*$ site under UV-irradiation even at 275 K. On the other hand, the simultaneous activation of two NO molecules on the same active site does not take place by

using bulk TiO_2 photocatalysts because the photoformed holes and electrons rapidly separate from each other, quickly attaining rather large distances between them. As a result, N_2O and NO_2 are formed through the reaction of decomposed N and O species with NO on different sites.

7.4. Photocatalytic Reduction of CO_2 with H_2O

Chemical fixation of carbon dioxide using photocatalysis is increasingly becoming an important research area in the face of ongoing fossil-fuel shortage and global warming. This photocatalytic chemical process does not only allow a decrease in atmospheric CO_2 concentration but also the direct conversion of CO_2 and water into valuable carbon-containing compounds, such as carbon monoxide (CO), formaldehyde (HCHO), formic acid (HCOOH), methanol (CH_3OH), and methane (CH_4), at room temperature and ambient pressure.

The pioneering work on photocatalytic CO_2 reduction was conducted by Halmann in 1978, in which photoelectrochemical CO_2 reduction to HCOOH, HCHO, and CH_3OH was attained by using a p-type GaP electrode.⁴⁸⁷ Inoue et al. also reported that various semiconducting photocatalysts, such as TiO_2 , ZnO, CdS, GaP, and SiC, can promote the photoelectrochemical CO_2 reduction.⁴⁸⁸ Work concerning the photocatalytic CO_2 reduction continued thereafter; however, the overall efficiency remained at a low level. Hence, the development of effective photocatalysts for this reaction is still highly desired. In the following, the potential of single-site photocatalysts that might possess unique local structures and effective electronic states based on the quantum size effect for CO_2 reduction will be discussed.

Intense studies concerning the CO_2 reduction with H_2O by using single-site photocatalysts have been conducted by Anpo and co-workers.^{489,490} When the above-described Ex-Ti/Y-zeolite with isolated and tetrahedrally coordinated Ti–oxide moieties (see section 7.3) was employed, the reaction efficiently proceeded under UV-light irradiation to form CH_4 and CH_3OH as the main products (Figure 72A).⁴⁹¹ It is noteworthy that the activity and the product selectivity were found to be completely different when bulk TiO_2 photocatalysts or Ti-based photocatalysts with aggregated Ti–oxide species were employed. Figure 72B summarizes the yields of CH_4 and CH_3OH per unit weight of TiO_2 for the different photocatalysts. Ex-Ti/Y-zeolite exhibits higher photocatalytic activity per unit weight of TiO_2 than bulk TiO_2 photocatalysts or Ti-based photocatalysts with aggregated Ti–oxide species (Imp-Ti/Y-zeolites). These find-

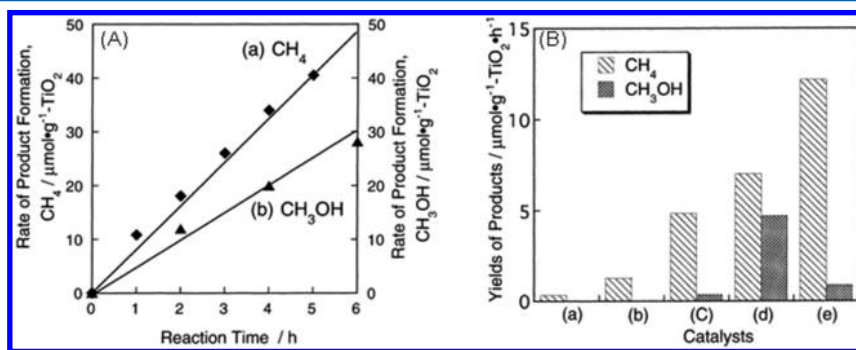


Figure 72. (A) Time course of the yields of (a) CH_4 and (b) CH_3OH during the photocatalytic CO_2 reduction with H_2O over Ex-Ti/Y-zeolite and (B) the yields of CH_4 and CH_3OH per unit weight of TiO_2 for different photocatalysts ((a) anatase TiO_2 powder, (b) Imp-Ti/Y-zeolite (10 wt % as TiO_2), (c) Imp-Ti/Y-zeolite (1.0 wt % as TiO_2), (d) Ex-Ti/Y-zeolite (1.1 wt % as TiO_2), and (e) Pt-loaded Ex-Ti/Y-zeolite (1.1 wt % as TiO_2)). The reaction was carried out with the catalysts in a quartz cell with a flat bottom under UV irradiation conditions from a high-pressure Hg lamp ($\lambda > 280 \text{ nm}$) at 328 K. Reprinted with permission from ref 491. Copyright 1998 Elsevier.

ings indicate that the isolated and tetrahedrally coordinated Ti–oxide moieties within Ex-Ti/Y-zeolite are more active than the aggregated ones. Moreover, the Ex-Ti/Y-zeolite photocatalyst yields CH_3OH with relatively high selectivity as compared to the other photocatalysts explored in this study.

The interaction between the isolated and tetrahedrally coordinated Ti–oxide moieties and CO_2 or H_2O can be confirmed by photoluminescence and ESR measurements. As shown in Figure 73, the emission band at 490 nm corresponding

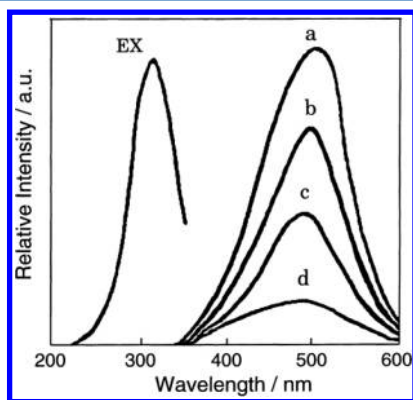


Figure 73. Photoluminescence spectra (excitation at 290 nm) of (a–c) EX-Ti/Y-zeolite observed (a) under vacuum, (b) in the presence of CO_2 ($8.5 \mu\text{mol g}^{-1}$), (c) in the presence of H_2O ($2.9 \mu\text{mol g}^{-1}$), and (d) Pt-loaded EX-Ti/Y-zeolite under vacuum. EX represents the excitation spectrum of EX-Ti/Y-zeolite monitored at 490 nm emission. All spectra were measured at 77 K. Reprinted with permission from ref 491. Copyright 1998 Elsevier.

to the radiative decay process from the excited charge-transfer state of tetrahedrally coordinated Ti–oxide moieties undergoes significant quenching by the addition of CO_2 or H_2O to the measurement system. Furthermore, UV-light irradiation of Ex-Ti/Y-zeolite in the presence of CO_2 and H_2O at 77 K leads to the appearance of characteristic ESR signals derived from Ti^{3+} ions, H atoms, and carbon centered radicals, respectively. On the basis of these results, the reaction mechanism of the photocatalytic reduction of CO_2 with H_2O on the isolated and tetrahedrally coordinated Ti–oxide moieties has been proposed. First, CO_2 and H_2O molecules interact with the excited state, that is, the photoformed $(\text{Ti}^{3+}-\text{O}^-)^*$ species, resulting in the reduction of CO_2 and the decomposition of H_2O , competitively. Subsequently, H atoms and OH^\bullet radicals formed from H_2O react with the carbon species formed from CO_2 to produce CH_4 and CH_3OH .

The CO_2 reduction with H_2O is also promoted by other Ti-based single-site photocatalysts, such as Ti-containing mesoporous silica and TS-1 zeolite, with a similar trend on the reactivity and selectivity being observed.^{492,493} Figure 74 shows the photocatalytic activities for the CO_2 reduction reaction in the presence of H_2O over various Ti-based single-site photocatalysts. UV-irradiation of Ti-mesoporous silica (Ti-MCM-41 and Ti-MCM-48) and TS-1 zeolite in the presence of CO_2 and H_2O also induces the formation of CH_3OH and CH_4 as the main products. Among those explored, Ti-MCM-48 exhibits the highest photocatalytic activity. These reactivity differences can be related to differences in their respective pore structures and the associated differences of substance diffusion. TS-1 zeolite has a smaller pore size (ca. 5.7 \AA) and a three-dimensional channel structure. On the other hand, although Ti-MCM-41 has a large pore size ($>20 \text{ \AA}$), its pore structure consists of one-dimensional,

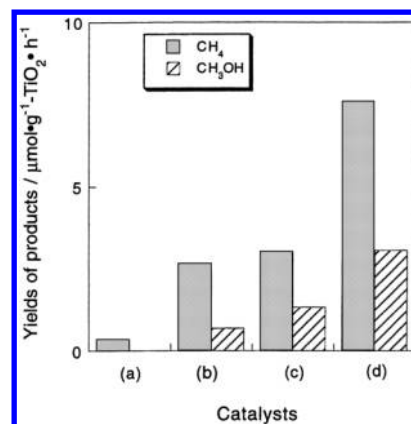


Figure 74. Yields of CH_4 and CH_3OH per unit weight of TiO_2 for different employed photocatalysts ((a) anatase TiO_2 powder, (b) TS-1 zeolite, (c) Ti-MCM-41, and (d) Ti-MCM-48). Reprinted with permission from ref 493. Copyright 1998 Elsevier.

cylindrical pores. Ti-MCM-48 has both a large pore size ($>20 \text{ \AA}$) and three-dimensional channels. Thus, the high reactivity and high selectivity for the formation of CH_3OH observed with the Ti-MCM-48 as compared to the other catalysts are hence attributed to the combined contribution of the high dispersion state of the Ti oxide species and the large pore size with a three-dimensional channel structure. These findings clearly show that highly dispersed Ti–oxide moieties in their silica matrixes can behave as effective photocatalysts for the photoreduction of CO_2 with H_2O .

On the other hand, the loading with Pt nanoparticles was found to lead to an enhancement of specific photocatalytic activity but simultaneously to a significant decrease in the CH_3OH production yield (Figure 72B(e)). Considering that an effective quenching of the photoluminescence from Ex-Ti/Y-zeolite has been noted after Pt loading (Figure 73d), electron transfer from the photoexcited Ti–oxide moieties to the Pt metal islands existing in the neighborhood appears to progress easily, resulting in an efficient charge separation of electrons and holes. Thereby, on the Pt-loaded Ti-containing zeolite catalyst, photocatalytic reactions that proceed in the same manner as on bulk TiO_2 catalysts become predominant; that is, the reduction reaction by electrons and the oxidation reaction by holes occur separately from each other on different sites. This also explains the selective formation of CH_4 , although the possibility that the selectivity difference comes from different modes of adsorption in two systems cannot be excluded.

Isolated titanate species on the appropriate supports are still among the most promising materials known for the photocatalytic carbon dioxide fixation. In their recent work, G. Mul and co-workers have proposed a mechanism for the photocatalytic CO_2 reduction involving the formation of CO in the initial stages followed by the formation of formaldehyde.⁴⁹⁴ Subsequently, the latter compound is then converted into CH_4 , C_2H_4 , and C_2H_6 , most likely by the reaction with hydroxyl radical intermediates formed in the photocatalytic process.⁴⁹⁴

Even though they did not observe any stable CO_2 adsorption at these isolated titanate species,⁴⁹⁵ Strunk and co-workers also observed the formation of methane during the photocatalytic CO_2 reduction over titanate species in SBA-15 followed by that of (para)formaldehyde, in particular, as the water content of the reaction mixture was decreased.⁴⁹⁶ These authors reported that the photocatalytic activity of these single-site systems can be

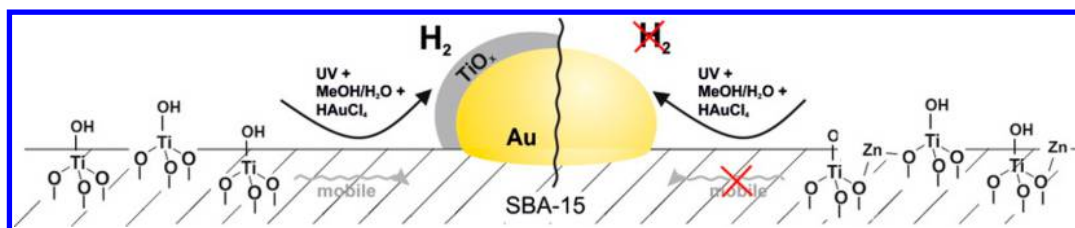


Figure 75. Schematic illustration showing that the photocatalytic reduction product H_2 is efficiently formed on photodeposited core/shell TiO_2 /gold nanoparticles deposited onto titanate-loaded SBA-15 ($\text{Ti}(x)/\text{SBA-15}$) but not on the free Au nanoparticle surface. Reprinted with permission from ref 497. Copyright 2013 American Chemical Society.

readily increased by the photodeposition of gold nanoparticles on titanate/SBA-15.⁴⁹⁷ The isolated titanate species were found to be highly mobile during this photodeposition process, resulting in the formation of titanium-rich shells around the gold nanoparticles, and often even in the formation of core/shell Au/TiO_x structures. As shown in Figure 75, these core/shell structures are suggested to play a crucial role in the electron transfer process. This behavior resembles typical processes observed due to strong metal–support interactions. Hole transfer, on the contrary, does not seem to be influenced by the presence of these shells and is instead found to scale with the amount of $\text{Ti}-\text{O}-\text{Si}$ bonds in the samples.⁴⁹⁷

7.5. Other Single-Site Photocatalysts with Different Metal Centers

Along with the Ti-based single-site photocatalysts described above, the development of single-site photocatalysts based on other transition metal oxide species has also been reported. Herein, only a brief introduction into this topic will be given because this Review focuses on Ti-based photocatalyst materials.

Tanaka and co-workers have designed and developed isolated V–oxide photocatalysts dispersed on SiO_2 or Al_2O_3 .^{498–501} The former (i.e., $\text{V}_2\text{O}_5/\text{SiO}_2$) have been found to catalyze the photoepoxidation of propene with O_2 to afford partial oxidation products, especially propene oxide and ethanol, under UV-light irradiation in a flow reactor system.⁵⁰² The latter (i.e., $\text{V}_2\text{O}_5/\text{Al}_2\text{O}_3$) exhibits a high selectivity for the formation of partial oxidation compounds (cyclohexanol and cyclohexanone) during the photo-oxidation of cyclohexane in the liquid phase.⁵⁰³ The synthesis of a Mo-based single-site photocatalyst has also been reported by Anpo et al.^{504,505} This photocatalyst consists of isolated Mo–oxide moieties loaded on silica or mesoporous silica and was reported to promote the photocatalytic reduction of NO with CO to produce N_2 via N_2O as an intermediate product.⁵⁰⁶ On the other hand, when a single-site photocatalyst with isolated V–oxide moieties was used, the NO reduction reaction still proceeded, however, producing N_2O as final product under UV-light irradiation. Details concerning the photocatalytic reduction of NO with CO over various single-site photocatalysts as well as the associated reaction mechanisms have been summarized in ref 506. Moreover, Cr-based single-site photocatalysts can act as visible-light-responsive photocatalysts.⁵⁰⁷ For example, Cr-containing hexagonal mesoporous silica has been successfully used for the photocatalytic decomposition of NO and the partial oxidation of propane with molecular oxygen under visible light irradiation ($\lambda > 450 \text{ nm}$).⁵⁰⁸

In addition, metal ion-exchanged ZSM-5 catalysts ($\text{M}^{n+}/\text{ZSM-5}$) also behave as effective photocatalysts. $\text{Cu}^{2+}/\text{ZSM-5}$ and $\text{Ag}^+/\text{ZSM-5}$ was, for example, found to induce the photocatalytic decomposition of NO_x into N_2 and O_2 under UV-light irradiation.^{509–513} This reaction has been revealed to progress through a local electron transfer from the excited Cu^+ or Ag^+ ions

to the π -antibonding orbital of NO_x and the simultaneous electron transfer from the π -bonding orbitals of another NO_x to the vacant orbital of the Cu^+ or Ag^+ ions.

7.6. Surface Functionality of Single-Site Photocatalyst Thin Films

The use of single-site photocatalysts in a thin film form should enable the development of photocatalyst films with unique functional surfaces for practical applications. Yamashita and co-workers reported the synthesis of mesoporous silica thin films containing isolated and tetrahedrally coordinated Ti–oxide moieties (Ti-MS thin film) and possessing remarkably high affinity for water.^{514–518} This type of thin film material can be prepared on various substrates by spin-coating. Figure 76

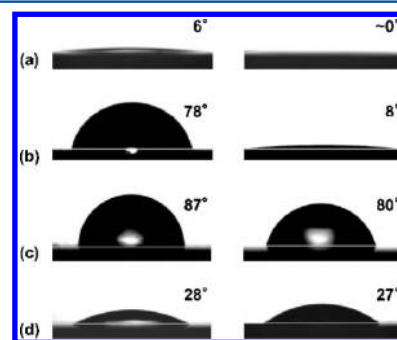


Figure 76. Photographic images of a water droplet on (a) a Ti-MS thin film, (b) a pure TiO_2 thin film, (c) a Ti-containing silica thin film, and (d) a pure mesoporous silica thin film before (left) and after (right) UV-light irradiation. The inset values show the corresponding water contact angles. Reprinted with permission from ref 519. Copyright 2011 Elsevier.

displays photographic images of water droplets on various thin film surfaces.⁵¹⁹ Although pure TiO_2 thin films exhibit photoinduced superhydrophilicity under UV-light irradiation (Figure 76b, right),⁵²⁰ their affinity for water is found to be low before UV-light irradiation (Figure 76b, left). In contrast, the water droplet spreads evenly on a Ti-MS thin film ($\text{Ti}/\text{Si} = 0.02$) even before UV light irradiation (Figure 76a, left). This high dark hydrophilicity is considered to be crucial for various practical applications. Given that Ti-containing silica thin films without mesoporous structure (Figure 76c, left) as well as pure mesoporous silica thin films (Figure 76d, left) do not exhibit high affinity for water, the formation of both the mesoporous structure and isolated Ti–oxide moieties appears to be an important factor for the appearance of hydrophilic characteristics. The physical basis of this effect will be explained in the following. The mesoporous silica matrix contains a large amount of silanol ($\text{Si}-\text{OH}$) groups, on which atmospheric water molecules adsorb efficiently, and which is also known to induce

capillary action. Moreover, the isolated Ti–oxide moieties in the silica matrix serve as strong adsorption sites for water due to their ability to induce electron localization.

Upon UV-light irradiation of the Ti-MS thin film, self-cleaning properties based on the combined effect of photoinduced superhydrophilicity and photocatalytic organic degradation ability can be observed. As is obvious from the images in Figure 76a (right), the water contact angle on the Ti-MS thin film becomes smaller, almost reaching 0° upon UV light irradiation, indicating the appearance of photoinduced superhydrophilicity. Subsequently, to evaluate the photocatalytic organic degradation ability, the surface of the Ti-MS thin film has been soiled with oleic acid and then irradiated with UV-light for 48 h. Following this procedure, the water contact angle is found to decrease again under UV-light irradiation and finally reaches 3° , suggesting the successful decomposition of oleic acid on its surface (Figure 77A). The complete removal of oleic acid has also been

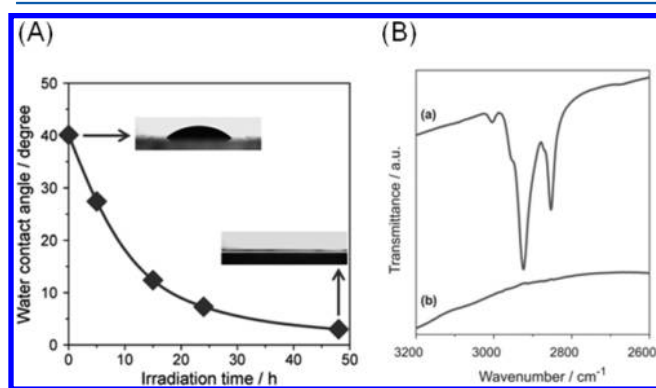


Figure 77. (A) Time course of the change in the water contact angle on a Ti-MS thin film soiled with oleic acid under UV-light irradiation. The inset images show the corresponding photographs of a water droplet on the film. (B) FT-IR spectra of Ti-MS thin film soiled with oleic acid before (a) and after (b) UV-light irradiation for 48 h. Reprinted with permission from ref 519. Copyright 2011 Elsevier.

confirmed by FT-IR measurements. As shown in Figure 77B, the peaks corresponding to C–H stretching vibration of the alkyl groups in oleic acid covering the Ti-MS thin film disappear after UV-light irradiation. These results suggest that the Ti-MS thin film can degrade organic compounds photocatalytically under UV-light irradiation and will be applicable as a self-cleaning material.

Mesoporous silica thin films incorporating various isolated transition metal oxide moieties (M-MS thin film; M = V, Cr, Mo, and W) also show a high affinity for water without UV-light irradiation, as shown in Figure 78.⁵²¹ This finding implies that the incorporation of isolated transition metal oxide moieties within the mesoporous silica matrixes leads to the improvement of their hydrophilic properties by the formation of new water adsorption sites due to electron localization, as has been explained for the case of the Ti-MS thin film. Among those explored, the W-MS thin film is found to show the highest hydrophilic properties with a water contact angle below 5° without UV-light irradiation. Interestingly, the superhydrophilic surface formed by this W-MS thin film under UV-light irradiation retains its superhydrophilicity for 10 days in the dark, and its superhydrophilic surface immediately recovers by UV-light irradiation even after 3 months dark storage.

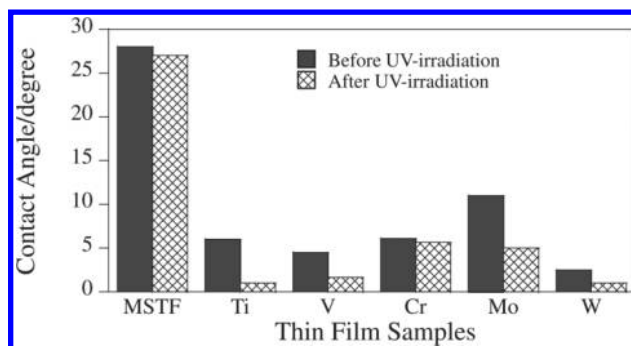


Figure 78. Water contact angles of various mesoporous silica thin films. MSTF means pure mesoporous silica thin film, and Ti, V, Cr, Mo, and W describe the kind of transition metal species incorporated into the MS thin film. Reprinted with permission from ref 521. Copyright 2008 The Chemical Society of Japan.

7.7. Platform for the Formation of Fine Metal Nanoparticles

Single-site photocatalysts can also be employed as a unique platform for the formation of fine metal nanoparticles. In the case of bulk semiconducting photocatalysts, the photodeposition method is often used to immobilize metal nanoparticles on their surfaces. Under light irradiation in the presence of metal precursors and hole scavengers (e.g., methanol), the photoformed electrons in the photocatalysts can reduce metal precursors to the metallic state while photoformed holes are consumed by the reaction with the hole scavenger, resulting in the formation of metal nanoparticles on the photocatalyst surfaces. This kind of photodeposition method has also been used for the quantification of the photoeffect on TiO_2 .⁵²² In this line, Yamashita and co-workers have proposed a novel photoassisted deposition (PAD) method combined with Ti-based single-site photocatalysts, such as TS-1 zeolite, Ti-HMS, and Ti-MCM-41, as photoresponsive catalyst supports.^{63,64,523–527} The UV light irradiation of Ti-based single-site photocatalysts results in an electron transfer from the oxygen to the Ti^{4+} ions within the silica framework, leading to the formation of pairs of trapped hole (O^-) and electron centers (Ti^{3+}), which can serve as anchor sites for the deposition of metal precursors. Because tetrahedrally coordinated Ti–oxide moieties within Ti-based single-site photocatalysts exist in highly dispersed states, the thus deposited metal nanoparticles tend to be uniform and highly dispersed without aggregation. In fact, fine Pt nanoparticles have been successfully deposited on Ti-HMS under UV-light irradiation, with the catalytic activity of the resulting Pt-loaded catalyst for CO oxidation exceeding that of catalysts prepared by conventional impregnation methods (Figure 79).

This PAD method using single-site photocatalysts can also conveniently be applied for the formation of bimetallic nanoparticles.^{65,528,529} As shown in Figure 80A, the formation of Pd–Au bimetallic nanoparticles onto a TS-1 zeolite has been achieved by using the PAD method in the presence of PdCl_2 and HAuCl_4 as respective precursors (PAD-PdAu/TS-1). Figure 80B shows the summary of the catalytic activity for direct H_2O_2 formation from H_2 and O_2 of various metal-loaded catalysts. The bimetallic nanoparticle-loaded catalysts show an improvement in the catalytic efficiency as compared to single Pd nanoparticle-loaded catalysts prepared in the same manner. Furthermore, the PAD-PdAu/TS-1 catalyst can also act as an efficient unique bifunctional catalyst. In the presence of H_2 and O_2 , partial oxidation of phenol proceeds over the PAD-PdAu/TS-1 catalyst

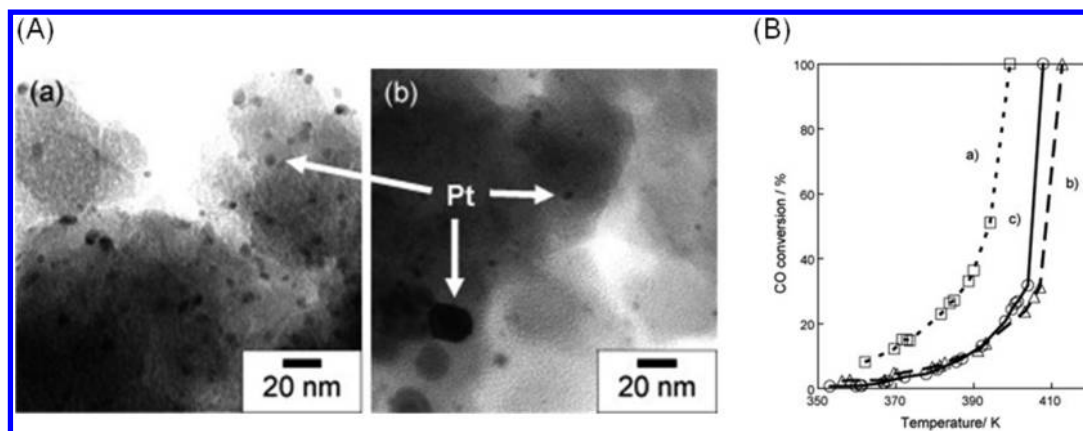


Figure 79. (A) TEM images of Pt-loaded Ti-HMS catalysts prepared by (a) PAD method and (b) impregnation method. (B) CO oxidation reaction over (a,b) Pt-loaded Ti-HMS and (c) Pt-loaded pure silica HMS prepared by (a) PAD method and (b,c) impregnation method. Reprinted with permission from ref 527. Copyright 2008 Elsevier.

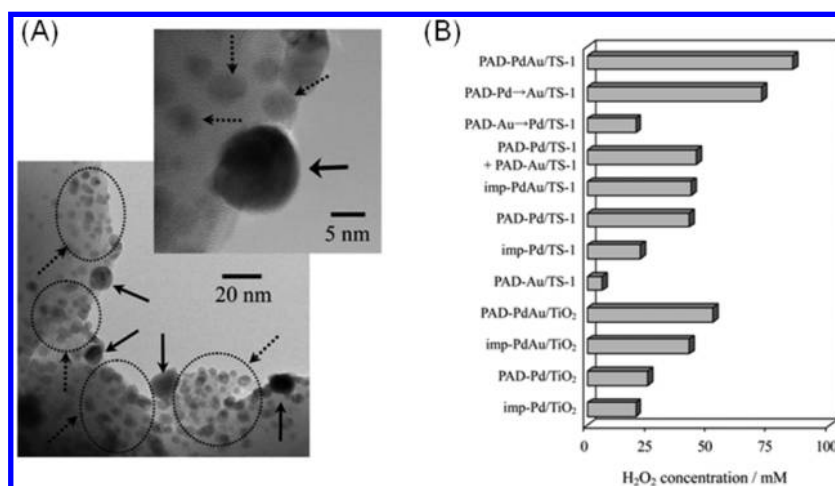
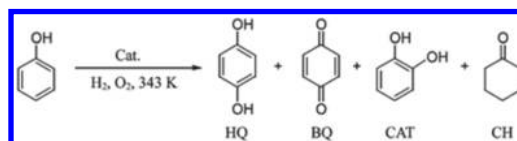


Figure 80. (A) TEM images of PAD-Pd-Au/TS-1. The larger nanoparticles indicated by the solid line arrows are Pd-Au alloys having 20 mol % Pd and 80 mol % Au compositions, while the smaller nanoparticles indicated by the dotted line arrows consist of pure Pd. (B) Effect of catalysts on concentration of H_2O_2 generated. Reaction conditions: catalyst (0.1 g), 0.01 M HCl (50 mL), 293 K, 6 h, H_2 and O_2 (80 mL min^{-1} , $\text{H}_2:\text{O}_2 = 1:1$). Reprinted with permission from ref 65. Copyright 2009 American Chemical Society.

Table 4. Oxidation of Phenol in a Flow of H_2 and O_2 ^a



entry	catalyst	solvent	$\text{H}_2/\text{mL min}^{-1}$	$\text{O}_2/\text{mL min}^{-1}$	yield %	selectivity/%			
						HQ ^b	BQ ^c	CAT ^d	CH ^e
1	TS-1	CH_3CN	40	40	0				
2	PAD-Pd/TS-1	CH_3CN	0	40	0				
3	PAD-Pd/TS-1	MeOH	40	40	6.4	1	0	2	97
4	imp-Pd/TS-1	MeOH	40	40	1.7	13	3	35	48
5	PAD-Au/TS-1	CH_3CN	40	40	0.3	15	0	85	0
6	PAD-Pd/TS-1	CH_3CN	40	40	7.0	17	0	83	0
7	imp-Pd/TS-1	CH_3CN	40	40	2.0	20	5	75	0
8	PAD-PdAu/TS-1	CH_3CN	40	40	13.3	8	31	9	52
9	imp-PdAu/TS-1	CH_3CN	40	40	7.7	9	23	13	55
10	PAD-PdAu/TS-1	CH_3CN	20	40	11.2	11	23	57	9
11	imp-PdAu/TS-1	CH_3CN	20	40	6.0	13	26	50	11

^aReprinted with permission from ref 65. Copyright 2009 American Chemical Society. Reaction conditions: catalyst (0.1 g), solvent (30 mL), 0.01 M HCl (15 mL), phenol (1.0 g), 343 K, 6 h. ^bHQ: hydroquinone. ^cBQ: benzoquinone. ^dCAT: cathecol. ^eCH: cyclohexanone.

by utilizing in situ generated H_2O_2 as the oxidant. That is, loaded Pd–Au bimetallic nanoparticles catalyze the H_2O_2 generation from H_2 and O_2 , and, subsequently, tetrahedrally coordinated TiO_4 moieties in TS-1 zeolite promote the partial phenol oxidation using in situ generated H_2O_2 as oxidant in a single reactor. It is noteworthy that this catalytic system using the PAD-PdAu/TS-1 catalyst in the presence of H_2 and O_2 as H_2O_2 source gives a 13.3% total yield of partial oxidation products, which is much higher than that generated by the original TS-1 catalyst in the presence of aqueous H_2O_2 (2% of total yield) as summarized in Table 4. This can be explained by the cooperative action between loaded nanoparticles and the Ti–oxide moieties, where the H_2O_2 generated on the nanoparticle can smoothly react with the neighboring Ti–oxide moieties without its decomposition before contribution to the oxidation reaction as an oxidant.

8. APPLICATIONS OF VISIBLE LIGHT-RESPONSIVE TiO_2 THIN FILMS: SOLAR WATER SPLITTING, SOLAR CELLS, AND PHOTOFUEL CELLS

Solar water splitting using visible light-responsive photocatalysts to produce molecular hydrogen and oxygen has been intensively investigated as one of the most promising environmentally benign energy conversion and storage systems. However, most visible light-responsive photocatalysts developed are present in powder form and thus have limitations for practical or industrial applications. The development of stable and easily applicable thin film photocatalysts is therefore strongly desired. The utilization of thin film photocatalysts for water splitting also allows the design of reactor concepts for the separate evolution of hydrogen and oxygen, thus enabling the elimination of additional separation processes for commercial applications. Moreover, visible light-responsive thin film photocatalysts can also be employed for other solar energy conversion devices, such as thin film solar cells without the need to use any dye sensitization or photofuel cells. In this section, the development of visible light-responsive TiO_2 thin film photocatalysts based on a magnetron sputtering method and their applications for solar energy conversion systems including water splitting, thin film solar cells, and photofuel cells will be highlighted.

8.1. Visible Light-Responsive TiO_2 Photocatalyst Thin Films

Various techniques, such as the sol–gel method, sputtering deposition, atomic layer deposition, and electrophoresis, have been employed to prepare thin film photocatalysts for practical applications. In this line, Anpo et al. reported the synthesis of novel and unique visible light-responsive TiO_2 photocatalyst (vis- TiO_2) thin films by using a radio frequency magnetron sputtering deposition method.^{530–533} The employed sputtering system was equipped with a substrate (quartz or Ti foil) centrally positioned in parallel just above the source material, that is, a calcined TiO_2 plate. Various sputtering parameters have been found to affect the optical characteristics of the prepared films strongly as will be described below.

Figure 81 shows the UV–vis transmission spectra of TiO_2 thin films prepared on quartz substrates employing different substrate temperatures (T_s) and target-to-substrate distances (D_{T-S}). The effect of the substrate temperature during the sputtering deposition is displayed in Figure 81a,b,d. It is obvious that TiO_2 thin films prepared at $T_s = 473$ K exhibit no absorption above 380 nm (denoted as UV- TiO_2 thin film), while the TiO_2 thin films prepared at 673 and 873 K are yellow-colored with light absorption bands in the visible wavelength region above 380 nm (denoted as vis- TiO_2 thin films). These findings imply that

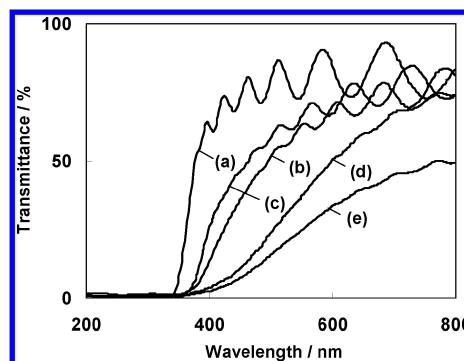


Figure 81. UV–vis transmission spectra of TiO_2 thin films prepared at different substrate temperatures of (a) 473, (b) 673, and (c–e) 873 K and target-to-substrate distances of (c) 90, (a,b,d) 80, and (e) 70 mm. Reprinted with permission from ref 533. Copyright 2010 Springer.

the control of the substrate temperature during the simple one-step TiO_2 deposition process enables a fine-tuning of the visible light absorption. Furthermore, the target-to-substrate distance (D_{T-S}) has also an influence on the absorption characteristics. The absorption spectra of TiO_2 thin films prepared at 873 K shift toward longer wavelengths upon decreasing D_{T-S} from 90 to 70 mm (Figure 81c–e). This effect of the target-to-substrate distance has been explained by the amount and the kinetic energy of sputtered atoms reaching the substrate. Because the sputtered atoms from the target material experience many collisions with the sputtering gas molecules before they reach the substrate, the amount of sputtered atoms that reach the substrate and their kinetic energy will increase with decreasing target-to-substrate distances, leading to a reduction of the thus-formed TiO_2 thin films.

SIMS measurements provided information concerning the origin of the visible light absorption characteristics of the TiO_2 thin films prepared at high substrate temperatures and short target-to-substrate distances. As shown in Figure 82, the SIMS

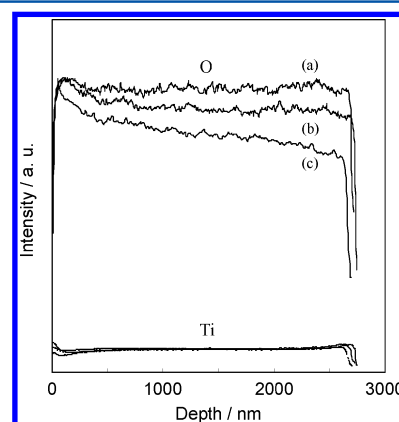


Figure 82. SIMS depth profiles for O and Ti for TiO_2 thin films prepared at different substrate temperatures of (a) 473 and (b,c) 873 K and target-to-substrate distances of (a,b) 80 and (c) 70 mm. Reprinted with permission from ref 533. Copyright 2010 Springer.

depth profile of the TiO_2 thin films prepared at 873 K indicates that the concentration of O^{2-} ions in these samples gradually decreases from the top surface (O/Ti ratio of 2.00 ± 0.01) to the inside bulk. The O/Ti values of the inside bulk for vis- TiO_2 prepared at $T_s = 873$ K and D_{T-S} of 80 mm and for vis- TiO_2 prepared at $T_s = 873$ K and D_{T-S} of 70 mm are found to be 1.93

and 1.70, respectively. In contrast, no significant changes can be observed for UV-TiO₂, the O/Ti value of which coincides with the stoichiometric value of TiO₂ (2.00 ± 0.01) across the entire depth profile. These results clearly indicate that the higher is the kinetic energy of the sputtered atoms, the lower will be the O/Ti ratio of the TiO₂ thin films, accompanied by a large shift in their absorption band toward visible light regions. Such a unique anisotropic structure may be responsible for the modification of the electronic properties, resulting in the appearance of visible light absorption.

The energy band diagrams of the vis-TiO₂ thin films have been determined by photoelectrochemical measurements under visible light illumination in aqueous 0.05 M NaOH solution for films prepared on Ti foil substrates. An anodic photocurrent was observed under visible light irradiation up to 520 nm, determining the band gap energy to be about 2.5 eV. Moreover, current–voltage measurements provided information concerning the flat band potential, with the zero current potential of UV-TiO₂ (−0.91 V vs SCE at pH 12.3) found to be more negative than that of vis-TiO₂ (−0.82 vs SCE at pH 12.3). This potential is equivalent to the flat band potential (E_{FB}) in polycrystalline semiconductors, thus allowing one to evaluate the conduction band edge (E_{CB}), which was estimated to be ca. −1.11 V vs SCE for UV-TiO₂ and −1.02 V vs SCE for vis-TiO₂ at pH 12.3, assuming an energy difference between E_{CB} and E_{FB} of 0.2 eV for oxide semiconductors. The proposed energy band diagrams of vis-TiO₂ and UV-TiO₂ thin films are displayed in Figure 83.

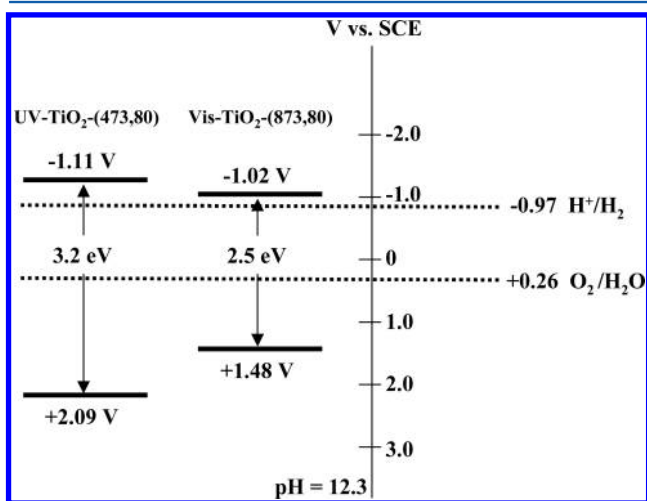


Figure 83. Proposed energy band diagrams of vis-TiO₂ and UV-TiO₂ thin films. Reprinted with permission from ref 533. Copyright 2010 Springer.

8.2. Evolution of H₂ and O₂ by Visible Light-Induced Water Splitting

Photoelectrochemical cells based on visible light-responsive thin film photocatalysts offer the chance to develop molecular hydrogen and oxygen in two separated compartments, thus avoiding subsequent gas separation steps. The basic concept of a suitable photoelectrochemical cell is displayed in Figure 84. When light is absorbed by the visible light-responsive thin film photocatalyst used as a photoanode, electrons are excited to the conduction band level and move to the platinum cathode (this process is often supported by applying an external bias) where they reduce protons to produce molecular hydrogen. The associated holes oxidize water directly at the surface of the

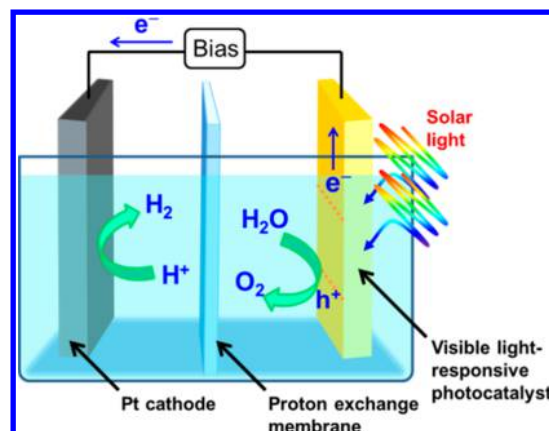


Figure 84. Basic concept of a photoelectrochemical cell based on a visible light-responsive thin film photocatalyst to produce H₂ and O₂ separately.

photoanode to produce molecular oxygen. Thus, the separated production of H₂ and O₂ will be attained.

On the basis of this concept, a unique H-type reactor for the separate evolution of H₂ and O₂ under solar irradiation was developed by Anpo and co-workers.^{534–540} As shown in Figure 85, the H-type reactor has a structure in which a TiO₂ thin film

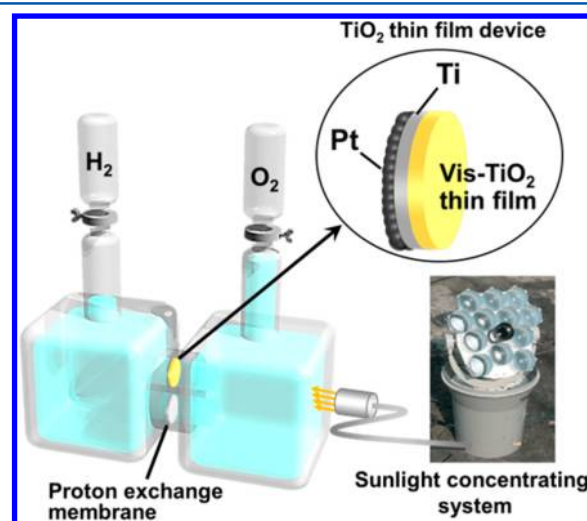


Figure 85. Schematic illustration of an H-type reactor based on vis-TiO₂ thin films to produce H₂ and O₂ separately from water under solar illumination.

device and a proton exchange membrane are sandwiched between two glass containers. The TiO₂ thin film device consists of a Ti foil with 50 μm thickness on which a vis-TiO₂ thin film is deposited on one side and Pt nanoparticles on the other side, with the latter being prepared by a RF-MS method.

Figure 86A shows the time course of the solar water splitting reaction to produce H₂ and O₂ separately by using this H-type reactor system. This reaction has been carried out in 1.0 M NaOH_{aq} for the TiO₂ side and 0.5 M H₂SO_{4aq} for the Pt side, thus attaining a chemical bias of ca. 0.83 V to assist the electron transfer from TiO₂ to Pt. This H-type reactor system has been reported to achieve an efficient photocatalytic water splitting reaction to produce stoichiometric H₂ and O₂ separately employing vis-TiO₂, while almost no reaction proceeded employing UV-TiO₂. These findings suggested that the visible-

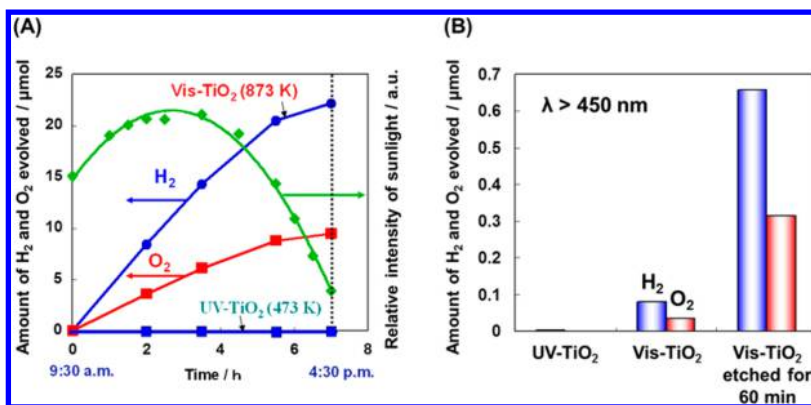


Figure 86. (A) Time course evincing the separate evolution of H₂ and O₂ under solar light irradiation by using the H-type reactor based on vis-TiO₂ or UV-TiO₂ thin films. The TiO₂ side of the glass container contained 1.0 M NaOH_{aq} and the Pt side contained 0.5 M H₂SO_{4aq}, resulting in a chemical bias of ca. 0.83 V. The device was irradiated by solar light from the TiO₂ side. Reprinted with permission from ref 540. Copyright 2007 Elsevier. (B) Effect of HF treatment on the photocatalytic performance of the vis-TiO₂ film in the H-type reactor for the separate evolution of H₂ and O₂ under visible-light irradiation ($\lambda > 450$ nm). The reactions were performed under the same conditions as (A) except using a different light source.

light absorption characteristics of the vis-TiO₂ thin films play a significant role to enable the water splitting reaction under solar irradiation.

Further enhancement of the photocatalytic activities have been achieved by chemical etching of the vis-TiO₂ thin film with HF solution.^{541,542} The photocurrent of the vis-TiO₂ thin film observed in an aqueous HClO₄ solution under both UV- and visible-light irradiation conditions increases dramatically by HF treatment, showing that the efficiency of the photooxidation of water improves with HF treatment. The highest photocurrent has been observed for vis-TiO₂ thin films etched for 60 min, with IPCE (incident photon-to-current conversion efficiency) values (+0.1 V vs SCE) under UV- and visible-light irradiation determined to be 66% and 9.4%, respectively. It has been suggested that the increases in the surface roughness and in the surface area of the vis-TiO₂ thin film following the HF treatment are responsible for the enhancement of the photocatalytic activities. When a vis-TiO₂ thin film etched for 60 min was employed, the reaction rate of the evolution of H₂ and O₂ under visible-light irradiation was considerably enhanced as compared to the nontreated vis-TiO₂ films (Figure 86B). Furthermore, the solar light conversion efficiency of the system employing the vis-TiO₂ thin film etched for 60 min and a solar concentrating system was determined to be 0.38% based on the H₂ evolution rate.

8.3. Design of Solid Thin Film Solar Cell without Use of Any Dye Sensitization

TiO₂ is usually employed in dye-sensitized solar cells (DSSCs) as transparent electrode material.^{263,543} DSSCs have attracted much attention due to their low production cost and high solar-to-electric energy conversion efficiency. For example, Grätzel et al. have reported the fabrication of DSSCs using a porous TiO₂ working electrode sensitized with a ruthenium dye complex, attaining a solar-to-electric energy conversion efficiency of up to 11%.⁵⁴⁴

The utilization of visible light-responsive thin film photocatalysts as working electrodes in DSSCs would enable a unique design of solar cells without the need to employ any dye sensitization, because the visible light-responsive thin film photocatalysts themselves should be able to act as light absorbers. This type of solar cells has been called solid thin film solar cells (STFSCs). Anpo et al. have developed STFSCs based on visible light-responsive TiO₂ photocatalysts thin films prepared on an

ITO substrate (vis-TiO₂/ITO) by an RF-MS method.⁵⁴⁵ As shown in Figure 87, the STFSC based on vis-TiO₂/ITO

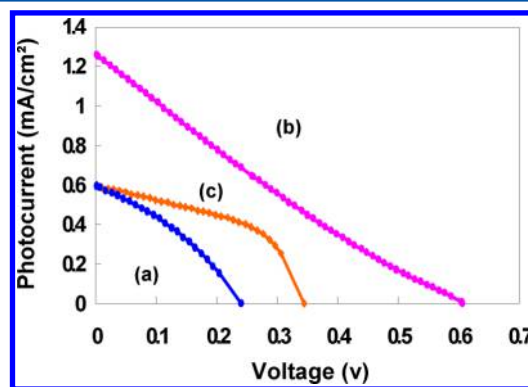


Figure 87. *I*–*V* curves of solid thin film solar cells constructed with (a,b) Cu₂O/vis-TiO₂/ITO electrodes calcined in (a) vacuum, in (b) ammonia, and for (c) a bare vis-TiO₂/ITO electrode, observed in 0.5 M NaI and 0.025 M I₂ aq under simulated solar light irradiation (100 mW/cm²). Reprinted with permission from ref 545. Copyright 2010 Springer.

exhibited a photovoltaic performance under simulated solar light irradiation, with the short-circuit photocurrent density (J_{sc}), the open-circuit photovoltage (V_{oc}), the fill factor (FF), and the solar energy conversion efficiency (η) being 0.6 mA cm⁻², 0.35 mV, 0.48, and 0.1%, respectively. Although the conversion efficiency of the STFSC is much lower than that of conventional DSSC systems employing dyes, a system without any dye would offer advantages of low cost and high durability. Moreover, an improvement of the photovoltaic performance has been attained by the deposition of Cu₂O on vis-TiO₂/ITO. The electrode with Cu₂O (Cu₂O/vis-TiO₂/ITO) was prepared by an electrodeposition method followed by calcination in vacuum or in ammonia atmosphere. The STFSC constructed with the Cu₂O/vis-TiO₂/ITO calcined in ammonia shows a considerably higher photovoltaic performance ($J_{sc} = 1.3$ mA cm⁻², $V_{oc} = 0.61$ mV, $FF = 0.22$, and $\eta = 1.7\%$) than the one constructed with bare vis-TiO₂/ITO, evincing that the calcination treatment of the Cu₂O/vis-TiO₂/ITO in ammonia is quite effective in enhancing the cell performance of the solar cells. This has been explained by the fact that the Cu₂O thin layer acts as an effective inorganic sensitizer to

improve the visible light absorption of the device. However, unfortunately, the cell performance of the solar cell based on the $\text{Cu}_2\text{O}/\text{vis-TiO}_2/\text{ITO}$ calcined in vacuum was found to be significantly lower.

8.4. Photofuel Cells Based on Vis- TiO_2

There has been intensive interest in the utilization of biomass and its derivatives as carbon-neutral feedstocks for the development of new energy production technologies from clean and renewable resources. For example, Kaneko et al. developed a new TiO_2 -based device enabling the production of electricity using various biomass and biorelated compounds as fuels.^{546,547}

This device is called photofuel cells (PFCs) and is comprised of a nanoporous TiO_2 thin film photoanode, a Pt cathode for O_2 reduction, and an electrolyte containing various biomass and biorelated compounds as fuels as shown in Figure 88. Upon

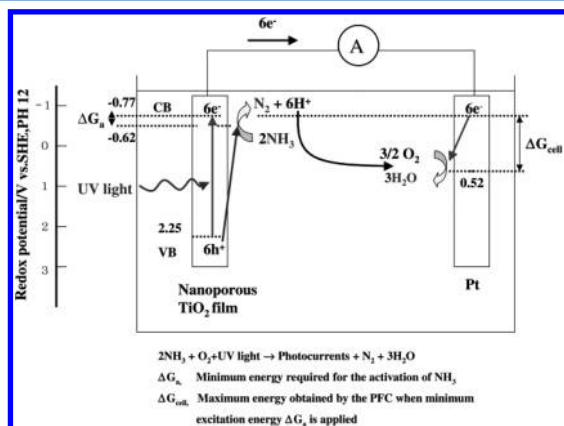
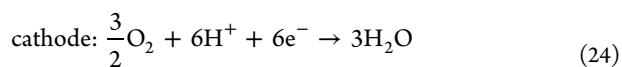
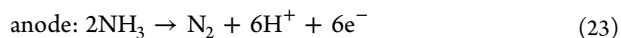


Figure 88. Energy diagram of an ammonia converting PFC (at pH 12) using a nanoporous TiO_2 film photoanode and a Pt cathode soaked in an aqueous ammonia solution. Reprinted with permission from ref 547. Copyright 2006 Elsevier.

illumination, the photoformed holes in the nanoporous TiO_2 thin film oxidize the biomass and the biorelated compounds, while the photoformed electrons are transferred to the cathode through the external circuit where they reduce O_2 to form H_2O . When ammonia is used as the fuel, the following oxidation and reduction reactions take place at the anode and at the cathode, respectively.



As a result, PFC systems allow for the production of electric energy from solar light and biomass. However, because the reported conversion efficiencies of such devices are still rather low, much effort has been devoted to their improvement. Nishikiori et al. reported that the hybridization of a clay mineral, allophane, with a TiO_2 electrode by using a sol-gel process leads to an enhancement of cell performance of the PFC (Figure 89).⁵⁴⁸ This is because allophane can effectively adsorb fuels and then transport them to the photocatalytically active TiO_2 . Matsuoka et al. have devised a new device that is based on the use of a separator-type photofuel cell (SPFC).⁵⁴⁹ In this device, two different electrolytes containing biomass derivatives as fuels and redox couples to promote the reduction reaction are used in the respective separated anode and cathode compartments as shown in Figure 90. Additionally, the above-described visible light-

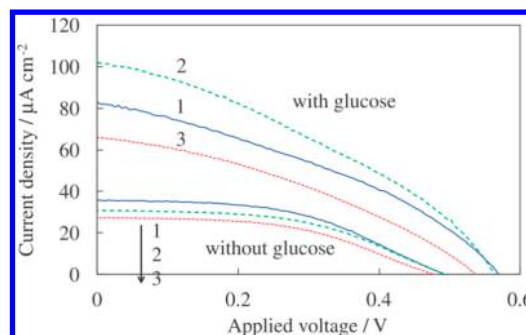


Figure 89. I - V curves of the (1) titania electrode and the allophane-titania composite electrodes containing (2) 0.10% and (3) 1.0% allophane observed using the electrolyte solutions with and without glucose during UV irradiation. Reprinted with permission from ref 548. Copyright 2012 The Chemical Society of Japan.

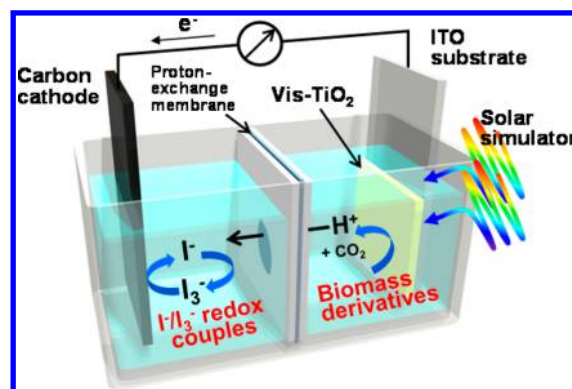


Figure 90. Schematic illustration of a separator-type photofuel cell (SPFC) based on a vis- TiO_2 photoanode and a carbon cathode. Reproduced with permission from ref 62. Copyright 2013 PCCP Owner societies.

responsive TiO_2 thin film materials, vis- TiO_2 , have been used in the SPFC, attaining an efficient utilization of solar light. Details of the SPFC system will be described below.

Figure 91 shows the photovoltaic performances of various SPFCs based on vis- TiO_2 observed under simulated solar irradiation from a PEC-L 11 solar simulator at AM 1.5 (100 mW cm^{-2}). When the effect of the addition of iodine redox couples into the cathode electrolyte on photovoltaic performances of SPFCs was investigated, in the presence of methanol in the anode electrolyte solution as fuel (Figure 91A), a significant improvement of the photovoltaic performances has been observed after addition of iodine redox couples. These results suggested that, in the presence of I_3^-/I^- redox couples, the reduction reaction of I_3^- ions to I^- ions (eq 25) rather than the oxygen reduction reaction takes place at the cathode (eq 26).



Moreover, interestingly, the device employing a carbon cathode exhibits almost the same performance as that employing a Pt cathode in the presence of the I_3^-/I^- redox couples. This finding indicates that cost-efficient carbon electrodes can be used as alternatives to Pt electrodes. When UV- TiO_2 , which is a UV-light active TiO_2 thin film prepared by an RF-MS method, was used as the photoanode in the SPFC device, a significant decrease of the cell performance was observed. This performance difference was

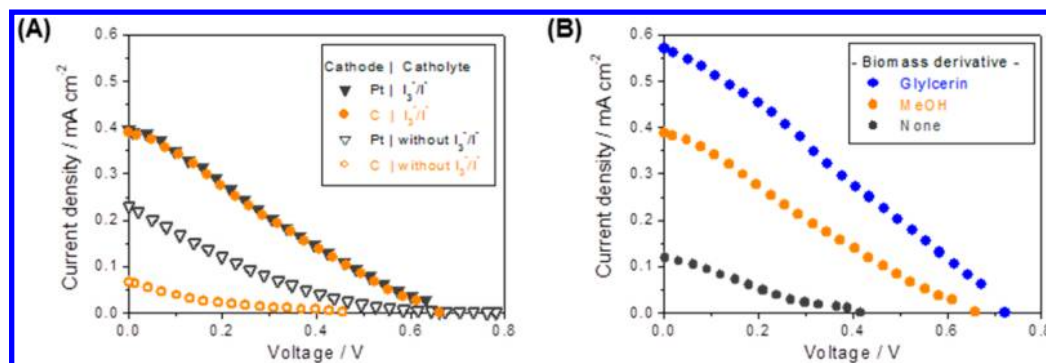


Figure 91. *I*–*V* curves of SPFCs under simulated solar light irradiation at AM 1.5 observed at various conditions. Effect of the addition of (A) iodine redox couples and (B) biomass derivatives on photovoltaic performances of SPFCs. Reproduced with permission from ref 62. Copyright 2013 PCCP Owner Societies.

readily explained by the good visible light responsivity of vis-TiO₂ revealing that the efficient utilization of visible solar light can be achieved by using vis-TiO₂ for the photoanode of the SPFC. The range of biomass derivatives tested so far is summarized in Figure 91B and Table 5. Various biomass

Table 5. Photovoltaic Performances of SPFCs with or without Biomass Derivatives under Simulated Solar Light Irradiation at AM 1.5^a

biomass derivatives	<i>V</i> _{OC} [V]	<i>J</i> _{SC} [mA cm ^{−2}]	<i>FF</i>	<i>η</i> [%]
none	0.42	0.10	0.22	0.009
methanol (10 vol %)	0.66	0.39	0.24	0.062
ethanol (10 vol %)	0.65	0.33	0.20	0.043
ethylene glycol (10 vol %)	0.68	0.52	0.28	0.099
glycerin (10 vol %)	0.72	0.57	0.27	0.111
glucose (9 wt %)	0.68	0.41	0.26	0.073

^aReproduced with permission from ref 62. Copyright 2013 PCCP Owner Societies.

derivatives can be used as fuels, and among those explored, the device employing glycerin as the fuel was found to show the best cell performance. It can thus be expected that more efficient biomass derivatives for SPFCs will be discovered by investigations concerning the adsorption properties and the redox potentials of various biomass derivatives.

Further improvement of the cell performance of SPFCs has been attained by modifications of the vis-TiO₂ photoanode. For example, the loading of Rh³⁺ ions onto vis-TiO₂ led to an enhancement of the cell performance of the respective SPFCs.⁵⁵⁰ This has been explained by the improvement of the visible light absorption properties combined with an increase in the electron donor density of the employed vis-TiO₂ by the loading with Rh³⁺ ions. Furthermore, HF treatment of vis-TiO₂ was found to enhance the solar energy conversion efficiency from 0.11% to 0.15% due to the enhanced conductivity as well as to the increase in surface area and in surface roughness.⁵⁵¹

9. PHOTOINDUCED SURFACE WETTABILITY CHANGES

9.1. Introduction

The discovery of the photoinduced superhydrophilicity of TiO₂ films⁵⁵² has opened various new applications of TiO₂ photocatalysts as self-cleaning, antifogging, and antibacterial materials.^{553,554} To apply TiO₂ photocatalysts for the purification of polluted water and air, a robust fixation of the TiO₂ powders onto various substrates is in most cases strongly desired. Frequently,

suitable TiO₂ films have been prepared by wet chemical processes such as sol–gel, dip-coating, or spin-coating methods.^{553,554} For a strong enough adhesion of the films onto the substrates, these wet preparation methods usually require a postcalcination step at high temperatures after the coating of the precursor solutions. In contrast, dry processes such as ion-engineering techniques possess some potential advantages: (i) because the films are prepared in a high vacuum chamber, contamination with impurities can be prevented; (ii) because no organic solvents are used for the preparation of the films, these methods are environmentally safe; (iii) thin films exhibiting high crystallinity and strong adhesion to the substrates can be readily prepared without calcination at high temperatures; and (iv) the physical and chemical properties of the films can be easily controlled. In particular, ion-engineering techniques, such as ionized cluster beam (ICB)^{418,555–558} and RF-magnetron sputtering^{532,559,560} deposition methods, were successfully applied for the dry preparation of such transparent TiO₂-based photocatalyst films.

9.2. Preparation of TiO₂ and TiO₂-Based Binary Oxide Films by the Ionized Cluster Beam (ICB) Deposition Method

A schematic diagram of the ionized cluster beam (ICB) deposition method is shown in Figure 92. For the preparation of TiO₂ by this technique, Ti vapor obtained by heating Ti metal

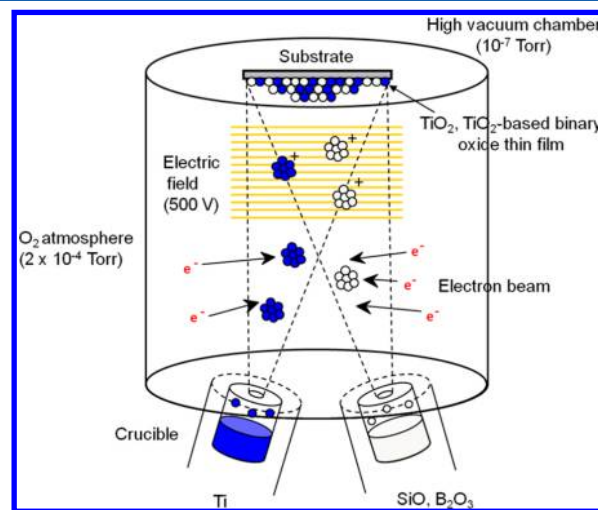


Figure 92. Schematic diagram of the ionized cluster beam (ICB) deposition method with multi ion sources. Reprinted with permission from ref 556. Copyright 2003 American Chemical Society.

(the source material) at ca. 2200 K is introduced into an O₂ atmosphere, thus forming stoichiometric TiO₂ clusters in the high vacuum chamber. These TiO₂ clusters are ionized by electron beam irradiation, accelerated by an electric field of 0.5 kV, and then bombarded onto the substrates. TiO₂-based binary oxide films (TiO₂/SiO₂ or TiO₂/B₂O₃) having different Ti-oxide contents can be prepared by using multi ion sources such as SiO₂ or B₂O₃.^{45,556,561,562}

Figure 93 shows the XRD patterns and SEM images of TiO₂ films prepared by the ICB deposition method with different

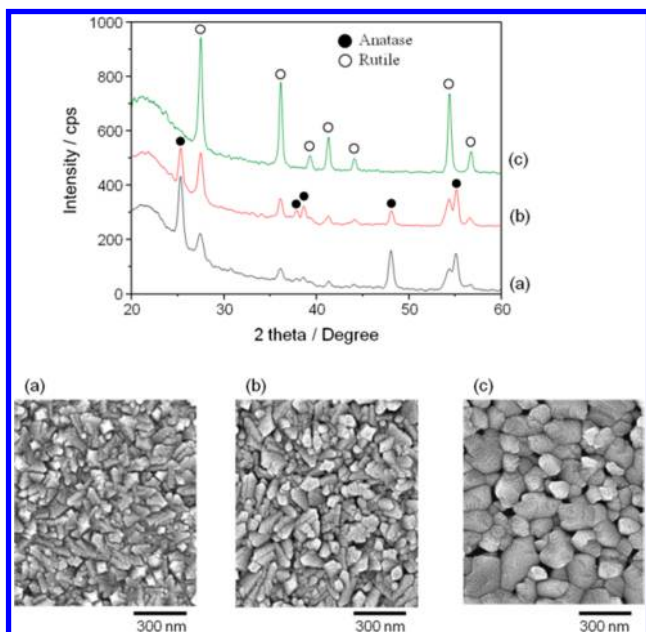


Figure 93. XRD patterns and SEM images of TiO₂ films prepared by the ICB method: (a) as-prepared; (b) calcined at 823 K; and (c) calcined at 973 K. Reprinted with permission from ref 563. Copyright 2009 Springer Science+Business Media, LCC.

postcalcination temperatures. The thin film deposited at 623 K without postcalcination showed a mixed structure of both anatase and rutile phases. The TiO₂ grain sizes of this as-prepared film (a) were ca. 20–50 nm. When film (a) was calcined at 823 K, the ratio anatase/rutile decreased to ca. 40%. However, the surface morphology of film (b) was almost identical to that of the as-prepared film. In contrast, when film (a) was calcined at 973 K, the crystal structure completely changed to the rutile phase. The small TiO₂ particles aggregated to large grain sizes in the range of 100–150 nm, and the surface morphology became much smoother as compared to that of film (a). These results clearly indicate that the ICB deposition method has the potential to prepare highly crystalline TiO₂ films even at relatively low temperatures.

Figure 94 shows the wettability changes observed on these TiO₂ films under UV light irradiation employing a commercial fluorescent lamp (light intensity: 10–20 μW/cm²). The films prepared at 623 K (a) and calcined at 823 K (b) showed a UV light-driven high wettability with water contact angles of less than 5°. On the other hand, the film calcined at 973 K (c) showed a low wettability even under UV light irradiation. Moreover, the TiO₂ films exhibiting mainly the anatase phase showed high photocatalytic activity for the oxidation of acetaldehyde by O₂ as well as efficient photoluminescence, assigned to deep-trapped holes,^{33,151} under UV irradiation.

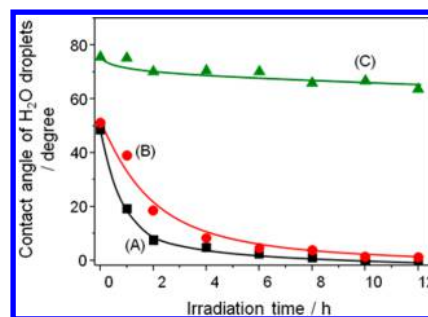


Figure 94. Surface wettability changes of the TiO₂ films prepared by the ICB method under UV light irradiation: (A) as-prepared; (B) calcined at 823 K; and (C) calcined at 973 K. Reprinted with permission from ref 563. Copyright 2009 Springer Science+Business Media, LCC.

9.3. Photoinduced Surface Wettability of TiO₂-Based Binary Oxide Thin Films

The addition of SiO₂ particles⁵⁶⁴ or SiO₂ thin layers⁵⁶⁵ to a TiO₂ surface is known to improve its surface wettability. Therefore, it was interesting to investigate the surface wettability of TiO₂-based binary oxide films containing highly dispersed tetrahedral TiO₄ units within SiO₂ or B₂O₃ matrixes. Figure 95 shows the

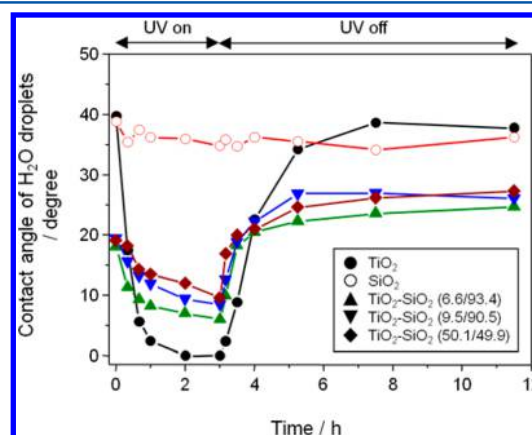


Figure 95. Time courses of water contact angle changes on TiO₂-SiO₂, TiO₂, and SiO₂ films prepared by the ICB deposition method under UV light irradiation followed by dark conditions. Adapted with permission from ref 539. Copyright 2003 American Chemical Society.

time courses of the water contact angle changes observed upon illumination of the TiO₂-SiO₂ thin films and of a bare SiO₂ thin film prepared by the ICB method equipped with multi ion sources. The water contact angle on the bare TiO₂ film reached 0° within 2 h of UV irradiation. In contrast, the contact angles of water droplets on the TiO₂-SiO₂ binary oxide films leveled off at ca. 10° under UV irradiation. However, because the pure SiO₂ film did not show a high degree of wettability under UV light irradiation, the tetrahedral TiO₄ species dispersed within the SiO₂ matrixes obviously showed a photoresponse inducing the observed surface wettability. Moreover, the TiO₂-SiO₂ binary films maintained the highly wettable state under dark conditions for a prolonged period as compared to the bare TiO₂ film. Similar features have been obtained for TiO₂-B₂O₃ binary films prepared by the same ICB method.^{45,556,561,562}

9.4. Proposed Mechanism of Photoinduced Wettability Changes on TiO₂ Photocatalyst Surfaces

The photoinduced superhydrophilicity of TiO₂ surfaces was initially explained by an increase in the amount of hydroxyl

groups on the TiO_2 surfaces formed by the UV light irradiation.^{566–568} It was also discussed that no direct correlation exists between the photocatalytic reactivity and the photo-induced high wettability of TiO_2 surfaces.⁵⁶⁹ In recent years, the origin of the highly wettable state of a TiO_2 surface has been proposed to be a metastable surface with increased tensile stress induced by a dissociative adsorption of H_2O molecules.⁵⁷⁰ However, the mechanism of this UV light driven phenomenon has yet to be clarified by further detailed experimental results. The volume (V) and the contact area (S) of a H_2O droplet on solid surfaces (θ , contact angle; r , radius of a H_2O droplet as one part of a sphere) can be calculated as shown in Figure 96.

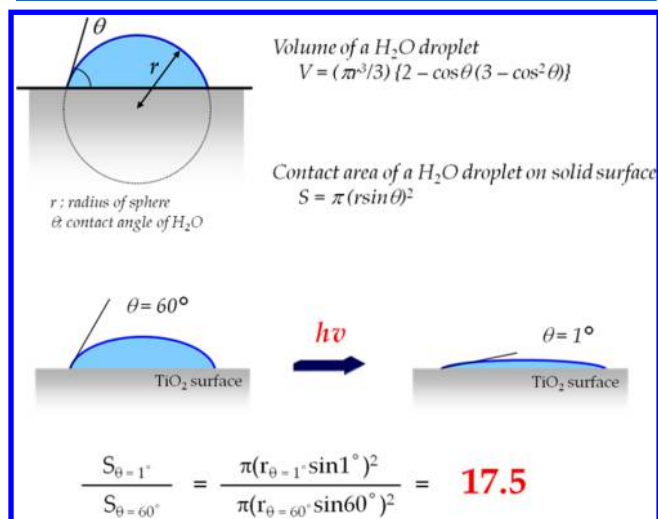


Figure 96. Relationship between the contact angle (θ), the volume (V), and the contact area (S) of a water droplet on a solid surface.

When the contact angle of a water droplet changes from 60° to 1° , the contact area (S) between the solid surface and the water droplet must increase up to 17.5 times. Although this phenomenon can be explained by a two-dimensional capillary effect,⁵⁶⁶ the density of the hydroxyl groups on the respective TiO_2 surface must increase at least several times by UV light irradiation. However, clear experimental evidence that the hydroxyl group density of the TiO_2 surface increases by UV light irradiation has not been reported since the discovery of this phenomenon. Furthermore, as shown in Figure 97, when the TiO_2 film showing a contact angle of 0° was stored under dark condition, the highly wettable state gradually recovers to eventually reach the initial state. On the other hand, when the TiO_2 film showing a contact angle of 0° was outgassed at room temperature (rt) for only 5 min, the highly wettable state immediately disappeared.⁵²⁹ These results can not simply be explained by the formation or disappearance of hydroxyl groups on the TiO_2 surface. Carrying out TPD analyses of TiO_2 single crystals under ultrahigh vacuum conditions, White et al. concluded that the dissociation of H_2O to form OH groups is not required to induce wetting phenomena because neither the dissociation of H_2O molecules nor the absence or presence of oxygen vacancies appear to control the hydrophilicity.⁵⁷¹ Moreover, the results shown in Figure 97 indicate that analyses under high vacuum conditions may not clarify the origin of the photoinduced superhydrophilic properties of TiO_2 surfaces. The chemical states of the hydroxyl groups and the adsorption states of H_2O molecules on the TiO_2 surface have thus been investigated under ambient conditions by near-infrared (NIR)

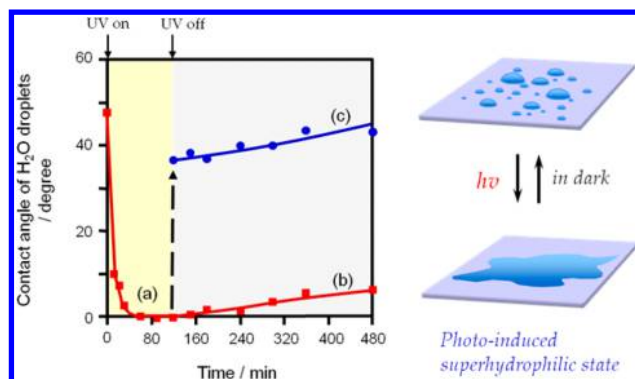


Figure 97. Time courses of water contact angle changes on TiO_2 films: (a) under UV light irradiation (ca. $1.0\text{ mW}/\text{cm}^2$), (b) when the samples were stored in the dark, and (c) after the samples in (a) were degassed at rt and then stored under dark conditions. Reprinted with permission from ref 572. Copyright 2005 American Chemical Society.

absorption spectroscopy.⁵²⁹ The mechanism of the photo-induced wettability changes at the TiO_2 surface was then discussed with regard to hydrogen-bond structures of H_2O clusters adsorbed on the TiO_2 surface (vide infra).

9.4.1. Effect of UV Irradiation on the Microstructure of H_2O Clusters Adsorbed on the TiO_2 Surface. In general, light irradiation will always lead to a temperature increase of the solid surfaces as an incidental consequence; that is, the entropy of the surface always increases during light irradiation. For example, when a TiO_2 sample was irradiated with UV light from a medium pressure Hg lamp (intensity, ca. $1\text{--}2\text{ mW}/\text{cm}^2$; distance, 30 cm), a temperature increase up to a maximum of 328 K was observed (initial temperature: ca. 298 K).^{572,573} Just after the Hg lamp was turned off, the temperature of the sample was quickly decreased followed by a gradual recovery of the initial state. On the basis of thermodynamic considerations, the adsorption of H_2O can never be increased on surfaces warmed by illumination. Actually, Munuera et al.⁵⁷⁴ and Bahnemann et al.²²⁹ even reported that H_2O desorbs from TiO_2 surfaces during UV light irradiation.

The NIR spectra of H_2O molecules adsorbed on TiO_2 surfaces measured during UV light irradiation are shown in Figure 98. The absorption band around 1940 nm has been assigned to a combination ($\delta + \nu_{\text{asym}}$) band (δ , bending; ν_{asym} , asymmetric stretching of H_2O molecule).^{575–580} Because this absorption band disappeared by outgassing the sample at 473 K, the spectral features observed in the NIR have been assigned to physisorbed H_2O molecules rather than to hydroxyl groups of the TiO_2 surfaces. Moreover, the peak positions are known to be closely related to differences in the hydrogen-bond networks, such as liquid water, ice, and water vapor.^{572,575–580} Assuming hydrogen-bond networks within the H_2O clusters, the absorption bands at 1940 and 1890 nm (as a shoulder) have been assigned to “hydrogen-bonded H_2O ” and “less- or non-hydrogen-bonded H_2O ”, respectively. When the TiO_2 sample was irradiated by UV light, the NIR absorption band at ca. 1940 nm assigned to hydrogen-bonded H_2O was found to decrease, increasing again upon storage in the dark, in particular, at lower temperatures. These results clearly indicate that the H_2O molecules on the TiO_2 surface desorb during UV light irradiation and adsorb again on the TiO_2 surfaces after UV light irradiation is ceased, depending on the temperature changes of the sample.

The detailed adsorption states of H_2O molecules adsorbed on the TiO_2 surface before and after UV light irradiation have been discussed from the viewpoint of hydrogen-bond networks

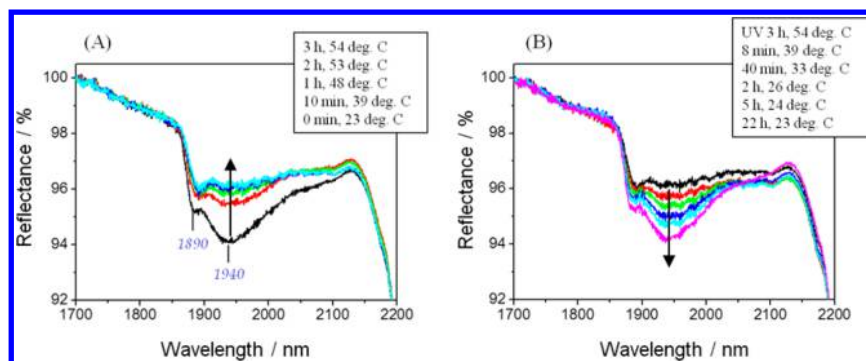


Figure 98. Near-infrared absorption spectra of H₂O adsorbed on TiO₂ surfaces: (A) under UV light irradiation for 0, 10, 60, 120, and 180 min (from bottom to top), (B) after the samples from (A) were stored in the dark for 0, 8, 40, 120, 300, and 1320 min (from top to bottom). Reprinted with permission from ref 572. Copyright 2005 American Chemical Society.

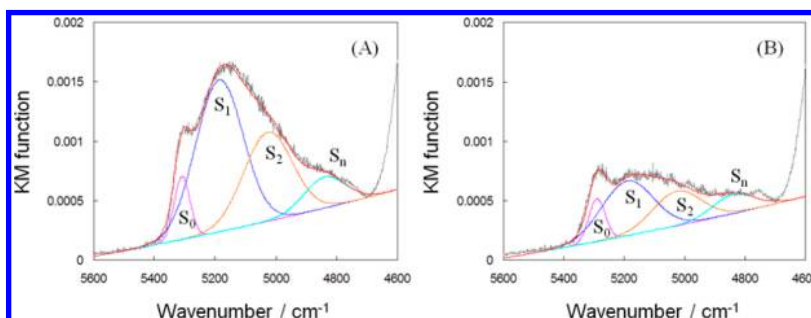


Figure 99. Deconvoluted spectra of the combination ($\delta + \nu_{\text{asym}}$) bands of H₂O molecules adsorbed on the TiO₂ surface: (A) before UV light irradiation and (B) after UV light irradiation for 3 h. Reprinted with permission from ref 572. Copyright 2005 American Chemical Society.

formed in the H₂O clusters. Figure 99 shows the deconvolution of the NIR absorption spectra around 1940 nm. The spectra could be deconvoluted into four components, assigned to different states of hydrogen bonds. When a H₂O molecule (A) interacts with another one (B) as shown in Figure 100, the

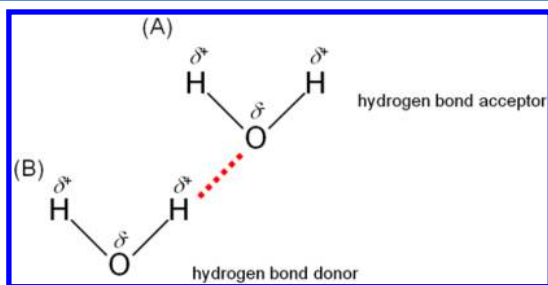


Figure 100. Interaction between two H₂O molecules through a hydrogen bond: (A) hydrogen-bond acceptor; (B) hydrogen-bond donor. Reprinted with permission from ref 573. Copyright 2005 American Chemical Society.

molecules (A) and (B) can be regarded as hydrogen-bond acceptor and donor, respectively.^{572,573} The O atom of molecule (A) strongly attracts not only the H atom of molecule (A) but also the H atom of the neighboring molecule (B) due to its high electronegativity. During this interaction, the hydrogen bond strongly perturbs the OH bond of molecule (B) but not the OH bond of molecule (A). Hence, the hydrogen-bond donor may show a large shift in the chemical states of the H₂O molecule as compared to a hydrogen-bond acceptor. According to this model, hydrogen-bond donors and acceptors are forming “active hydrogen bonds” and “passive hydrogen bonds”, respectively. Each H₂O molecule can possess a maximum of four hydrogen

bonds (two active and two passive), with the active hydrogen bonds playing a more important role in the hydrogen-bond networks within the H₂O clusters as compared to the passive bonds. However, it is difficult to experimentally distinguish between these two types of intermolecular hydrogen bonds.

The details of this spectral analysis, such as wavenumbers, wavelengths, and relative peak areas of the four components, are summarized in Table 6. Because H₂O vapor is known to show an

Table 6. Different Chemical States of the H₂O Molecules Depending on the Number of Hydrogen Bonds on the TiO₂ Surface before and after UV Light Irradiation^a

	wavenumber/cm ⁻¹ (wavelength/nm)			
	before UV light irradiation		after UV light irradiation for 3 h	
S ₀	5309 cm ⁻¹ (1884 nm)	6.3%	5290 cm ⁻¹ (1890 nm)	11.3%
S ₁	5186 cm ⁻¹ (1928 nm)	50.3%	5190 cm ⁻¹ (1927 nm)	45.4%
S ₂	5028 cm ⁻¹ (1989 nm)	32.4%	5056 cm ⁻¹ (1990 nm)	28.8%
S _n	4840 cm ⁻¹ (2076 nm)	11.0%	4839 cm ⁻¹ (2067 nm)	14.5%

^aReprinted with permission from ref 572. Copyright 2005 American Chemical Society. S₀: H₂O without active H-bonds. S₁: H₂O with 1 active H-bond. S₂: H₂O with 2 active H-bonds. S_n: H₂O with 2 active H-bonds and 1 (or 2) passive H-bond(s) (polymeric-chained H₂O molecules).

intense peak at 1875 nm, the component S₀ has been assigned to “hydrogen bond-free and/or less hydrogen-bonded H₂O molecules”. On the other hand, three components (S₁, S₂, and S_n) were assigned to “hydrogen-bonded H₂O molecules”, because H₂O in liquid and solid phase is known to show broad NIR absorption bands at 1938 and 1988 nm, respectively. It is of particular importance that the S₀ component increased from 6.3% to 11.3% by UV light irradiation of the TiO₂ layer.

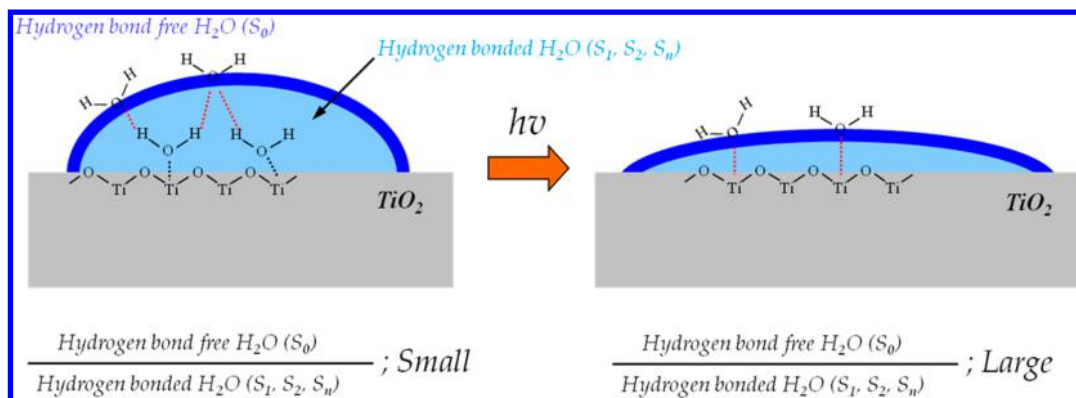


Figure 101. Schematic diagrams of different shapes of microsized H_2O clusters on the TiO_2 surface before and after UV light irradiation. Reprinted with permission from ref 572. Copyright 2005 American Chemical Society.

Apparently, the distribution of hydrogen bonds in the H_2O clusters decreased during UV light irradiation. The structure model proposed for the H_2O clusters on the TiO_2 surface before and after UV light irradiation is shown in Figure 101. According to this model, the decrease of the hydrogen-bond network between the H_2O molecules by UV light irradiation of the TiO_2 surface is closely related to a decreasing surface tension of the microsized H_2O clusters. These changes in the surface tension of the H_2O clusters can be associated with a thermodynamic driving force resulting in their spreading out on the TiO_2 surfaces to show a high wettability. In fact, when the TiO_2 sample was heated to 323 K in the dark, the NIR absorption bands of H_2O adsorbed on the TiO_2 surface clearly decreased (vaporization), while the water contact angles decreased to approximately 30° and then leveled off. Although the TiO_2 surface did not reach the so-called “superhydrophilic” state, its wettability was improved only by heating at 323 K without any UV light irradiation. Because possible hydrocarbon contaminants adsorbed on the TiO_2 surface could hardly be decomposed by heating at ca. 323 K, the observed hydrophilic conversion upon heating has been associated with the desorption of the H_2O molecules from the TiO_2 surface.

9.4.2. Photocatalytic Reactivity versus Wettability Control of TiO_2 Surfaces. To elucidate the role of UV light irradiation for the wettability control of TiO_2 surfaces, the wettability changes of a TiO_2 surface under UV light irradiation were investigated in different atmospheres. As shown in Figure 102, when the TiO_2 films were irradiated with UV light under O_2 (purity >99.9%) or synthetic air ($\text{O}_2/\text{N}_2 = 1/4$) flow, they showed high wettability. However, when the TiO_2 films were irradiated under N_2 flow (purity >99.9%), the contact angles of the H_2O droplets did not change at all. Moreover, when the O_2 flow was changed to N_2 , the hydrophilic conversion of the TiO_2 surface stopped and leveled off. The role of O_2 for the wettability of TiO_2 surfaces was then discussed in the context of the photocatalytic decomposition of hydrocarbons in the presence of O_2 or N_2 . The amounts of hydrocarbons adsorbed on the TiO_2 films were estimated by the C 1s XPS spectra, as shown in Figure 103. The C 1s peak intensity decreased only when the TiO_2 films were irradiated with UV light in O_2 atmosphere. Moreover, the TiO_2 films generally showed higher photocatalytic reactivity in O_2 than in N_2 atmosphere.

The effects of various surface treatments on the surface wettability of TiO_2 and the amounts of hydrocarbons determined from the C 1s XPS peak intensities are summarized in Table 7. TiO_2 films calcined at 723 K for 1 h showed 0° contact angle of

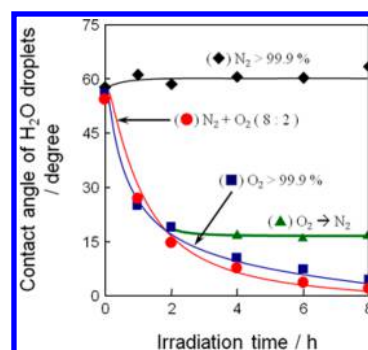


Figure 102. Effects of atmospheric gases on the changes in water contact angles on TiO_2 films under UV light irradiation (24 W fluorescent valve; ca. $25\text{--}30\ \mu\text{W}/\text{cm}^2$): (a) in synthetic air ($\text{N}_2/\text{O}_2 = 4/1$), (b) in O_2 (purity >99.9%), (c) in N_2 (purity >99.9%), and (d) when O_2 flow was switched to N_2 . Reprinted with permission from ref 572. Copyright 2005 American Chemical Society.

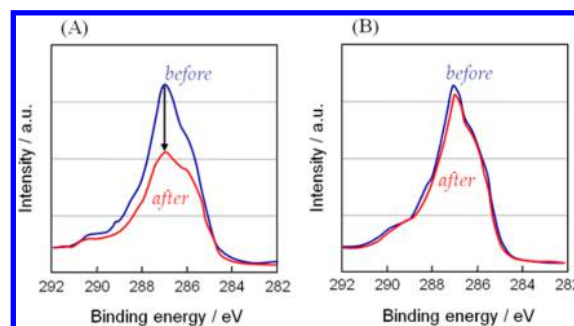


Figure 103. C 1s XPS spectra of the TiO_2 films before and after UV light irradiation (24 W fluorescent valve; ca. $25\text{--}30\ \mu\text{W}/\text{cm}^2$) for 8 h in the presence of (A) O_2 and (B) N_2 . Reprinted with permission from ref 572. Copyright 2005 American Chemical Society.

H_2O droplets with the removal of more than one-half of the initial amount of hydrocarbons having been confirmed. The TiO_2 films rinsed in 2 M NaOH solution at 323 K showed a contact angle of 11° and a removal of about 30% of the hydrocarbons. These results clearly suggest that the wettability of TiO_2 surfaces can be controlled by the removal of hydrocarbonous contaminants, also by nonphotocatalytic treatments. In fact, it has been reported that the surface wettability of nonalkaline silica glass could be controlled by vacuum UV light (172 nm) irradiation in O_3 atmosphere because of the efficient removal of hydrocarbons from its surface.^{581,582} SiO_2 surfaces

Table 7. Effects of Various Treatments on the Wettability Changes of TiO₂ Surfaces and Relative Amounts of Hydrocarbons Determined by the C 1s XPS Spectra^a

	pretreatments	contact angle of H ₂ O (deg)	relative intensity of C 1s peak at 286.4 eV ^b
(1)	before treatment	49.3	100
(2)	washed by distilled H ₂ O for 1 min	20.1	98.5
(3)	rinsed in NaOH (2 M, 323 K) soln for 1 min	11.2	71.2
(4)	calcination at 723 K for 1 h	0	40.1
(5)	UV light irradiation for 3 h (1 mW/cm ²)	0	64.7

^aReprinted with permission from ref 572. Copyright 2005 American Chemical Society. ^bThe influence of hydrocarbons from XPS apparatus was not subtracted.

generally do not show any photocatalytic reactivity for the degradation of hydrocarbons; however, the hydrocarbons adsorbed on the silica surface have been reported to be decomposed by vacuum UV light (172 nm) irradiation in O₃ or O₂ atmospheres, leading to an improvement of the surface wettability.

9.4.3. Mechanism of the Wettability Control on TiO₂ Surfaces. The proposed mechanism explaining the photo-induced wettability conversion on TiO₂ surfaces is shown in Figure 104. When, for example, the TiO₂ surface is heated at ca.

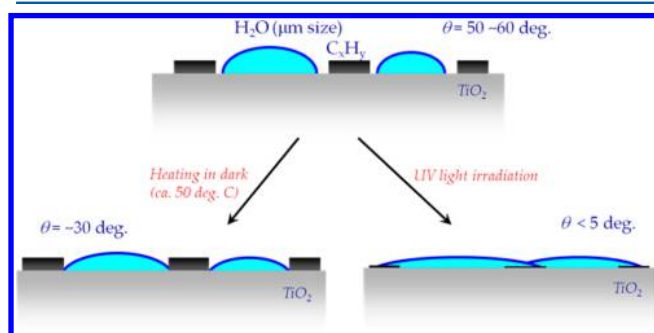


Figure 104. Schematic diagram explaining heat- and photoinduced wettability changes of the TiO₂ photocatalyst surface under UV light irradiation. Reprinted with permission from ref 572. Copyright 2005 American Chemical Society.

323 K in the dark, H₂O molecules desorb from the surface; however, adsorbed hydrocarbon molecules are not decomposed at this temperature, resulting in minimal water contact angles of ca. 30°. In contrast, when the TiO₂ surface is irradiated with UV light, the H₂O molecules also desorb from the surface most probably by the heating effect from the light source while, at the same time, parts of the hydrocarbons present on the TiO₂ surface are photocatalytically decomposed. This partial removal of the hydrocarbons from the TiO₂ surface combined with the decrease in the distribution of hydrogen bonds in the H₂O clusters on the surface will lead to an efficient spillover of H₂O molecules onto free spaces of the surfaces, resulting in the formation of H₂O mono- and/or multilayers. As soon as some stains such as hydrocarbons are removed from the TiO₂ surface and the amount of H₂O molecules is decreased, the surface exhibits high wettability toward water.

10. CONCLUSIONS

The research field of photocatalysis has seen well over 40 years of active research now and currently appears to be in its heydays. Many industrial applications of this technology are already available on the market today such as air and water cleaning devices, self-cleaning surfaces, solar cells, and even solar fuel generators. However, as shown in this Review, several even of the most basic principles of photocatalysis are still far from being understood today. While not aiming to be comprehensive, this overview focuses on some, at least in the eyes of the authors, important and crucial features of TiO₂ photocatalytic systems.

Time-resolved analytical tools such as transient optical spectroscopy seem to be ideally suited to study the generation, trapping, and transfer of electrons and holes, that is, the “initiators” of all photocatalytic processes, in particular, when different detection methods such as transient optical spectroscopy and microwave conductivity measurements are combined. The respective data analysis is found to be very complex, and it has been highlighted that photoelectrochemical concepts involving band bending and particle–particle contacts need to be considered in depth. While the generally accepted mechanistic picture uses a single photocatalyst particle excited by a single photon to explain the entire photocatalytic world, recent research results have created the need of more elaborate mechanisms involving, for example, three-dimensional self-assembled particle agglomerates acting as antenna and charge-transfer systems, for their comprehensive interpretation. It is through these ensemble and cooperative properties that even widely used effects such as the photoinduced superhydrophilicity are currently being explained, even though considerable scientific controversies still exist today as to the (only) correct model.

This Review also highlights several current concepts for the preparation of materials suitable as photocatalysts. Interesting quantum-size effects are encountered during the synthesis of TiO₂ nanoparticles from their respective molecular precursors, while different synthetic approaches for the preparation of “doped” visible-light active TiO₂-based photocatalysts have been presented and compared here. Single-site photocatalysts present another group of currently investigated materials, the photocatalytic activities of which have been found to be both significant and stable. Finally, some examples are given here for devices employing TiO₂ photocatalysis, that is, for solar water splitting, in solar or in photofuel cells.

AUTHOR INFORMATION

Corresponding Authors

*E-mail: bahnmann@iftc.uni-hannover.de.

*E-mail: schneid@iftc.uni-hannover.de.

Notes

The authors declare no competing financial interest.

Biographies



Jenny Schneider received her M.Sc. degree in Material- and Nano-chemistry in 2011 from the Gottfried Wilhelm Leibniz University Hannover. She is currently a Ph.D. student with Prof. Bahnemann at the Gottfried Wilhelm Leibniz University Hannover, investigating the reaction dynamics of photogenerated charge carriers in different photocatalysts by means of laser flash photolysis spectroscopy. Her research interests include the mechanism(s) of photocatalysis, the detailed understanding of photocatalytically induced chemical conversions, as well as theoretical simulations of photocatalytic processes.



Masaya Matsuoka was born in 1969 in Osaka, Japan. He studied at the Osaka Prefecture University, where he obtained his Ph.D. in applied chemistry studying the photocatalysis on the transition metal ion exchanged zeolites in 1997. During 1997, he worked as a postdoctoral fellow at the Université Pierre et Marie Curie, Paris. In 1998 he again joined the Osaka Prefecture University as an assistant professor and is presently a professor at the same university. His current research interests include the development of the visible light-responsive photocatalysts, PCP/MOF photocatalysts, and their applications for the environmental purifications as well as the H₂ production from water.



Masato Takeuchi is currently an associate professor in the graduate school of engineering at Osaka Prefecture University (OPU). He received his Ph.D. degree at OPU in 2002. Prior to working in OPU, he was JSPS postdoctoral fellow in OPU (Prof. Anpo) and Torino University (Profs. Collucia and Martra) from 2002–2004. His major interest is the NIR investigations on the hydrogen-bond networks in water, alcohol, and ammonia clusters adsorbed on catalyst surfaces.



Prof. Jinlong Zhang studied Fine Chemicals at East China University of Science and Technology, China, where he received a Ph.D. in Applied Chemistry in 1993. In 1996 he received the Award of the JSPS and then studied at Osaka Prefecture University, Japan as a postdoctoral. He became a full professor in 2000. He has published over 300 original papers, and serves as the editor of *Research on Chemical Intermediates* and on editorial boards of several international journals, for example, *Applied Catalysis B: Environmental*, *Dyes and Pigments*, and *Photographic Science and Photochemistry*. His research interests include photocatalysis, mesoporous materials, and materials science.



Yu Horiuchi was born in 1984 in Shizuoka, Japan. He received his Ph.D. from Osaka University in 2011. During the period 2010–2011, he

worked in Professor Hiromi Yamashita's laboratory at Osaka University as a JSPS research fellow. In 2011 he joined Osaka Prefecture University as an Assistant Professor in Chemistry. His research interests include the development of visible-light-responsive photocatalysts for water splitting and solar energy conversion, and the rational design and application of metal–organic frameworks for heterogeneous catalysts and photocatalysts.



Masakazu Anpo is presently an Advisor of the President (ex-Vice President and Executive Director) and Director of the R&D Center for the Plant Factory of Osaka Prefecture University. He is a pioneer in the study of photochemical reactions on solid surfaces including catalysts, and published the first Japanese book, "Photocatalysis" in 1988. An English book, "Photochemistry on Solid Surfaces", was published in 1989 from Elsevier. He has published more than 100 books. Dr. Anpo has received 7 awards including the award of Japan Photochemical Society, Catalysis Society of Japan, Chemical Society of Japan, and Ministry of Education of Japan, etc. He has published 500 original papers and been cited more than 17 000 times, served on the editorial boards of numerous international journals, and is Editor-in-Chief of the international journal, *Research on Chemical Intermediates* (Springer). Dr. Anpo has been elected as one of only a few members of the Academia Europaea from Asia, and is also a member of the Science Council of Japan. Dr. Anpo's current research topics deal with the development of highly efficient visible-light-responsive TiO₂ thin films as well as the design of highly active single-site oxide catalysts within zeolites and mesoporous materials as photocatalysts for environmental remediation, preservation processes, and the production of clean energies by using sunlight energy. His dream is the establishment of solar chemistry as a new environmentally friendly science and technology.



Prof. Dr. rer. nat. habil. Detlef Bahnemann received his Ph.D. in Chemistry from the Technical University Berlin in 1981 and his Habilitation in the area of Technical Chemistry from the Leibniz

University Hannover in 2012. He is currently the Head of the Research Unit "Photocatalysis and Nanotechnology" at the Institute of Technical Chemistry of the Leibniz University Hannover in Germany and also the Director of the Research Institute on Nanocomposite Materials for Photonic Applications at Saint Petersburg State University in Russia. His main research topics include photocatalysis, photoelectrochemistry, solar chemistry, and photochemistry focussed on the synthesis and the detailed investigation of the physical-chemical properties of semiconductor and metal nanoparticles. He holds an Honorary Professorship at the Robert Gordon University in Aberdeen/Scotland (United Kingdom), an Honorary Professorship at the Xinjiang Technical Institute of Physics and Chemistry (Chinese Academy of Sciences) in Urumqi (China), the Erudite Professorship at the Mahatma Gandhi University in Kottayam (India), a Guest Professorship of Tianjin University (China), and is DeTao Master of Photocatalysis, Nanomaterials and Energy Applications (China). Prof. Bahnemann is the lead author of more than 260 publications in peer reviewed journals that have been cited more than 21 000 times (h-index: 58 according to ISI, 64 according to Google Scholar Citations) and has edited 2 scientific books.

ACKNOWLEDGMENTS

We gratefully acknowledge, in particular, the work performed by our respective research groups in Japan and Germany during the past decades. Without the continuous support of all of the undergraduate, graduate, and Ph.D. students, postdocs, and visiting scientists, our knowledge in this research field would not have reached its present level. Thank you all very much indeed! J.S. gratefully acknowledges financial support from the German Ministry of Science and Technology (BMBF), grant no. 033RC1012C (Neue Katalysatoren und Technologien für die solarchemische Wasserstoffherzeugung, HyCats).

REFERENCES

- (1) Kennedy, D. R.; Ritchie, M.; Mackenzie, J. *Trans. Faraday Soc.* **1958**, *54*, 119.
- (2) Fujita, Y.; Kwan, T. *Bull. Chem. Soc. Jpn.* **1958**, *31*, 379.
- (3) Barry, T. I.; Stone, F. S. *Proc. R. Soc. London, Ser. A* **1960**, *255*, 124.
- (4) Doerfler, W.; Hauffe, K. *J. Catal.* **1964**, *3*, 156.
- (5) Kato, K.; Masuo, F. *Kogyo Kagaku Zasshi* **1964**, *67*, 1136.
- (6) Steinbach, F. *Nature* **1967**, *215*, 152.
- (7) Formenti, M.; Juillet, F.; Meriaude, P.; Teichner, S. *J. Chem. Technol.* **1971**, 680.
- (8) Tanaka, K.; Blyholde, G. *J. Phys. Chem.* **1972**, *76*, 1807.
- (9) Yoneyama, H.; Tamura, H.; Toyoguchi, Y. *J. Phys. Chem.* **1972**, *76*, 3460.
- (10) Volkenstein, F. F. *Adv. Catal.* **1973**, *23*, 157.
- (11) Bickley, R. I.; Stone, F. S. *J. Catal.* **1973**, *31*, 389.
- (12) Fujishima, A.; Honda, K. *Nature* **1972**, *238*, 37.
- (13) Schrauzer, G. N.; Guth, T. D. *J. Am. Chem. Soc.* **1977**, *99*, 7189.
- (14) Frank, S. N.; Bard, A. J. *J. Am. Chem. Soc.* **1977**, *99*, 303.
- (15) Halmann, M. *Nature* **1978**, *275*, 115.
- (16) Anpo, M.; Chiba, K.; Tomonari, M.; Coluccia, S.; Che, M.; Fox, M. A. *Bull. Chem. Soc. Jpn.* **1991**, *64*, 543.
- (17) Yoneyama, H.; Koizumi, M.; Tamura, H. *Bull. Chem. Soc. Jpn.* **1979**, *52*, 3449.
- (18) Kiwi, J.; Gratzel, M. *J. Am. Chem. Soc.* **1979**, *101*, 7214.
- (19) Kawai, T.; Sakata, T. *Chem. Phys. Lett.* **1980**, *72*, 87.
- (20) Kawai, T.; Sakata, T. *Nature* **1980**, *286*, 474.
- (21) Sato, S.; White, J. M. *J. Am. Chem. Soc.* **1980**, *102*, 7206.
- (22) Domen, K.; Naito, S.; Soma, M.; Onishi, T.; Tamaru, K. *J. Chem. Soc., Chem. Commun.* **1980**, 543.
- (23) Boonstra, A. H.; Mutsaers, C. *J. Phys. Chem.* **1975**, *79*, 1694.
- (24) Yun, C.; Anpo, M.; Kubokawa, Y. *J. Chem. Soc., Chem. Commun.* **1980**, 609.

- (25) Graetzel, M. *Energy Resources through Photochemistry and Catalysis*; Academic Press: New York, 1983.
- (26) Schiavello, M.; Reidel, D. *Photoelectrochemistry, Photocatalysis and Photoreactions*; D. Reidel: Dordrecht, 1985.
- (27) Kuczyński, J. P.; Milosavljević, B. H.; Thomas, J. K. *J. Phys. Chem.* **1984**, *88*, 980.
- (28) Duonghong, D.; Ramsden, J.; Gratzel, M. *J. Am. Chem. Soc.* **1982**, *104*, 2977.
- (29) Moser, J.; Gratzel, M. *J. Am. Chem. Soc.* **1983**, *105*, 6547.
- (30) Weller, H.; Koch, U.; Gutierrez, M.; Henglein, A. *Ber. Bunsen-Ges. Phys. Chem.* **1984**, *88*, 649.
- (31) Fojtik, A.; Weller, H.; Koch, U.; Henglein, A. *Ber. Bunsen-Ges. Phys. Chem.* **1984**, *88*, 969.
- (32) Rossetti, R.; Ellison, J. L.; Gibson, J. M.; Brus, L. E. *J. Chem. Phys.* **1984**, *80*, 4464.
- (33) Bahnemann, D.; Henglein, A.; Lilie, J.; Spanhel, L. *J. Phys. Chem.* **1984**, *88*, 709.
- (34) Nozik, A. J.; Williams, F.; Nenadovic, M. T.; Rajh, T.; Micic, O. I. *J. Phys. Chem.* **1985**, *89*, 397.
- (35) Anpo, M.; Shima, T.; Kodama, S.; Kubokawa, Y. *J. Phys. Chem.* **1987**, *91*, 4305.
- (36) Hong, A. P.; Bahnemann, D. W.; Hoffmann, M. R. *J. Phys. Chem.* **1987**, *91*, 6245.
- (37) Anpo, M. *Chem. Intermed.* **1988**, *11*, 67.
- (38) Mau, A. W. H.; Huang, C. B.; Kakuta, N.; Bard, A. J.; Campion, A.; Fox, M. A.; White, J. M.; Webber, S. E. *J. Am. Chem. Soc.* **1984**, *106*, 6537.
- (39) Kuczyński, J.; Thomas, J. K. *J. Phys. Chem.* **1985**, *89*, 2720.
- (40) Anpo, M.; Zhang, S. G.; Higashimoto, S.; Matsuoka, M.; Yamashita, H.; Ichihashi, Y.; Matsumura, Y.; Souma, Y. *J. Phys. Chem. B* **1999**, *103*, 9295.
- (41) Zhang, J. L.; Minagawa, M.; Matsuoka, M.; Yamashita, H.; Anpo, M. *Catal. Lett.* **2000**, *66*, 241.
- (42) Zhang, J. L.; Matsuoka, M.; Yamashita, H.; Anpo, M. *J. Synchrotron Radiat.* **2001**, *8*, 637.
- (43) Anpo, M.; Nakaya, H.; Kodama, S.; Kubokawa, Y.; Domen, K.; Onishi, T. *J. Phys. Chem.* **1986**, *90*, 1633.
- (44) Anpo, M.; Kawamura, T.; Kodama, S.; Maruya, K.; Onishi, T. *J. Phys. Chem.* **1988**, *92*, 438.
- (45) Dohshi, S.; Takeuchi, M.; Anpo, M. *J. Nanosci. Nanotechnol.* **2001**, *1*, 337.
- (46) Anpo, M.; Che, M.; Werner, O. Haag, B. C. G.; Knoezinger, H. *Advances in Catalysis*; Academic Press: New York, 1999.
- (47) Anpo, M.; Dzwigaj, S.; Che, M.; Bruce, C. G.; Knoezinger, H. *Advances in Catalysis*; Academic Press: New York, 2009.
- (48) Anpo, M.; Matsuoka, M.; Takeuchi, M. In *Nanoscale Materials in Chemistry*; Klabunde, J. K., Richards, R. M., Eds.; John Wiley & Sons, Inc.: New York, 2009.
- (49) Matsuoka, M.; Anpo, M. *Heterogeneous Catalysis*. In *Green Catalysis*; Anastas, P. T., Crabtree, R. H., Eds.; Wiley-VCH: New York, 2009.
- (50) Matsuoka, M.; Saito, M. In *Characterization of Solid Materials and Heterogeneous Catalysts*; Che, M., Vedrine, J. C., Eds.; Wiley-VCH: New York, 2012.
- (51) Anpo, M.; Aikawa, N.; Kubokawa, Y.; Che, M.; Louis, C.; Giamello, E. *J. Phys. Chem.* **1985**, *89*, 5689.
- (52) Gritscov, A. M.; Shvets, V. A.; Kazansky, V. B. *Chem. Phys. Lett.* **1975**, *35*, 511.
- (53) Anpo, M.; Tanahashi, I.; Kubokawa, Y. *J. Phys. Chem.* **1980**, *84*, 3440.
- (54) Anpo, M.; Sunamoto, M.; Che, M. *J. Phys. Chem.* **1989**, *93*, 1187.
- (55) Anpo, M.; Kubokawa, Y. *J. Catal.* **1982**, *75*, 204.
- (56) Anpo, M.; Tanahashi, I.; Kubokawa, Y. *J. Chem. Soc., Faraday Trans.* **1982**, *78*, 2121.
- (57) Anpo, M.; Kondo, M.; Coluccia, S.; Louis, C.; Che, M. *J. Am. Chem. Soc.* **1989**, *111*, 8791.
- (58) Anpo, M.; Tanahashi, I.; Kubokawa, Y. *J. Phys. Chem.* **1982**, *86*, 1.
- (59) Anpo, M. *Sol. Energy Mater. Sol. Cells* **1995**, *38*, 221.
- (60) Matsuoka, M.; Anpo, M. *J. Photochem. Photobiol., C* **2003**, *3*, 225.
- (61) Anpo, M.; Thomas, J. M. *Chem. Commun.* **2006**, 3273.
- (62) Horiuchi, Y.; Toyao, T.; Takeuchi, M.; Matsuoka, M.; Anpo, M. *Phys. Chem. Phys.* **2013**, *15*, 13243.
- (63) Yamashita, H.; Mori, K. *Chem. Lett.* **2007**, *36*, 348.
- (64) Yamashita, H.; Mori, K.; Shironita, S.; Horiuchi, Y. *Catal. Surv. Asia* **2008**, *12*, 88.
- (65) Mori, K.; Miura, Y.; Shironita, S.; Yamashita, H. *Langmuir* **2009**, *25*, 11180.
- (66) Hoffmann, M. R.; Martin, S. T.; Choi, W.; Bahnemann, D. W. *Chem. Rev.* **1995**, *95*, 69.
- (67) Alfano, O. M.; Bahnemann, D.; Cassano, A. E.; Dillert, R.; Goslich, R. *Catal. Today* **2000**, *58*, 199.
- (68) Zhang, H.; Chen, G.; Bahnemann, D. W. *J. Mater. Chem.* **2009**, *19*, 5089.
- (69) Bloh, J. Z.; Wagner, S.; Bahnemann, D. W.; Scheper, T.; Kasper, C. *Chem. Ing. Tech.* **2010**, *82*, 335.
- (70) Khataee, A. R.; Kasiri, M. B. *J. Mol. Catal. A: Chem.* **2010**, *328*, 8.
- (71) Maeda, K.; Domen, K. *J. Phys. Chem. Lett.* **2010**, *1*, 2655.
- (72) Abe, R. *J. Photochem. Photobiol., C* **2010**, *11*, 179.
- (73) Knox, V. *Am. Ceram. Soc. Bull.* **2010**, *89*, 31.
- (74) Boddy, P. J. *Surf. Sci.* **1966**, *4*, 320.
- (75) Memming, R. *Semiconductor Electrochemistry*; Wiley-VCH: Weinheim, 2001.
- (76) Hardman, P. J.; Raikar, G. N.; Muryn, C. A.; Vanderlaan, G.; Wincott, P. L.; Thornton, G.; Bullett, D. W.; Dale, P. *Phys. Rev. B* **1994**, *49*, 7170.
- (77) Lindan, P. J. D.; Harrison, N. M.; Gillan, M. J.; White, J. A. *Phys. Rev. B* **1997**, *55*, 15919.
- (78) Chretien, S.; Metiu, H. *J. Phys. Chem. C* **2011**, *115*, 4696.
- (79) Diebold, U. *Surf. Sci. Rep.* **2003**, *48*, 53.
- (80) Deskins, N. A.; Rousseau, R.; Dupuis, M. *J. Phys. Chem. C* **2010**, *114*, 5891.
- (81) Martinez, U.; Hammer, B. *J. Chem. Phys.* **2011**, *134*, 194703.
- (82) Zhang, Z.; Yates, J. T., Jr. *Chem. Rev.* **2012**, *112*, 5520.
- (83) Onda, K.; Li, B.; Petek, H. *Phys. Rev. B* **2004**, *70*, 045415.
- (84) Pearson, R. G. *Inorg. Chem.* **1988**, *27*, 734.
- (85) Pang, C. L.; Lindsay, R.; Thornton, G. *Chem. Rev.* **2013**, *113*, 3887.
- (86) Sun, C. H.; Liu, L. M.; Selloni, A.; Lu, G. Q.; Smith, S. C. *J. Mater. Chem.* **2010**, *20*, 10319.
- (87) Redfern, P. C.; Zapol, P.; Curtiss, L. A.; Rajh, T.; Thurnauer, M. C. *J. Phys. Chem. B* **2003**, *107*, 11419.
- (88) He, Y. B.; Dulub, O.; Cheng, H. Z.; Selloni, A.; Diebold, U. *Phys. Rev. Lett.* **2009**, *102*, 106105.
- (89) Shi, W. J.; Xiong, S. J. *Surf. Sci.* **2010**, *604*, 1987.
- (90) Wendt, S.; Matthiesen, J.; Schaub, R.; Vestergaard, E. K.; Laegsgaard, E.; Besenbacher, F.; Hammer, B. *Phys. Rev. Lett.* **2006**, *96*, 066107.
- (91) Bikondoa, O.; Pang, C. L.; Ithnin, R.; Muryn, C. A.; Onishi, H.; Thornton, G. *Nat. Mater.* **2006**, *5*, 189.
- (92) Ketteler, G.; Yamamoto, S.; Bluhm, H.; Andersson, K.; Starr, D. E.; Ogletree, D. F.; Ogasawara, H.; Nilsson, A.; Salmeron, M. *J. Phys. Chem. C* **2007**, *111*, 8278.
- (93) Tilocca, A.; Selloni, A. *J. Phys. Chem. B* **2004**, *108*, 4743.
- (94) Eagles, D. M. *J. Phys. Chem. Solids* **1964**, *25*, 1243.
- (95) Sell, K.; Barke, I.; Polei, S.; Schumann, C.; von Oeynhausen, V.; Meiwes-Broer, K. H. *Phys. Status Solidi B* **2010**, *247*, 1087.
- (96) Stevanovic, A.; Yates, J. T. *J. Phys. Chem. C* **2013**, *117*, 24189.
- (97) Komiyama, M.; Yin, D. H.; Li, Y. J. In *Science and Technology in Catalysis 2002*; Anpo, M., Onaka, M., Yamashita, H., Eds.; Elsevier: New York, 2003.
- (98) Komiyama, M.; Li, Y. J.; Yin, D. H. *Jpn. J. Appl. Phys., Part 1* **2002**, *41*, 4936.
- (99) Lantz, J. M.; Corn, R. M. *J. Phys. Chem.* **1994**, *98*, 4899.
- (100) Lantz, J. M.; Corn, R. M. *J. Phys. Chem.* **1994**, *98*, 9387.
- (101) Ohtani, B. *Catalysts* **2013**, *3*, 942.
- (102) Serpone, N.; Lawless, D.; Khairutdinov, R.; Pelizzetti, E. *J. Phys. Chem.* **1995**, *99*, 16655.
- (103) Boschloo, G. K.; Goossens, A. *J. Phys. Chem.* **1996**, *100*, 19489.

- (104) Wang, X. L.; Feng, Z. C.; Shi, J. Y.; Jia, G. Q.; Shen, S. A.; Zhou, J.; Li, C. *Phys. Chem. Chem. Phys.* **2010**, *12*, 7083.
- (105) Emeline, A. V.; Ryabchuk, V. K.; Serpone, N. *J. Phys. Chem. B* **2005**, *109*, 18515.
- (106) Tang, H.; Levy, F.; Berger, H.; Schmid, P. E. *Phys. Rev. B* **1995**, *52*, 7771.
- (107) Tang, H.; Prasad, K.; Sanjines, R.; Schmid, P. E.; Levy, F. *J. Appl. Phys.* **1994**, *75*, 2042.
- (108) Stevanovic, A.; Buettner, M.; Zhang, Z.; Yates, J. T., Jr. *J. Am. Chem. Soc.* **2012**, *134*, 324.
- (109) Murakami, M.; Matsumoto, Y.; Nakajima, K.; Makino, T.; Segawa, Y.; Chikyow, T.; Ahmet, P.; Kawasaki, M.; Koinuma, H. *Appl. Phys. Lett.* **2001**, *78*, 2664.
- (110) Nakato, Y.; Akanuma, H.; Magari, Y.; Yae, S.; Shimizu, J. I.; Mori, H. *J. Phys. Chem. B* **1997**, *101*, 4934.
- (111) Shi, J.; Chen, J.; Feng, Z.; Chen, T.; Lian, Y.; Wang, X.; Li, C. *J. Phys. Chem. C* **2007**, *111*, 693.
- (112) Knorr, F. J.; Mercado, C. C.; McHale, J. L. *J. Phys. Chem. C* **2008**, *112*, 12786.
- (113) Yamada, Y.; Kanemitsu, Y. *Appl. Phys. Lett.* **2012**, *101*, 133907.
- (114) Dozzi, M. V.; D'Andrea, C.; Ohtani, B.; Valentini, G.; Selli, E. *J. Phys. Chem. C* **2013**, *117*, 25586.
- (115) Leytner, S.; Hupp, J. T. *Chem. Phys. Lett.* **2000**, *330*, 231.
- (116) Stopper, K.; Dohrmann, J. K. *Z. Phys. Chem.* **2000**, *214*, 555.
- (117) Pagel, R.; Dohrmann, J. K. *J. Phys. Chem. C* **2007**, *111*, 4458.
- (118) Mendive, C. B.; Hansmann, D.; Bredow, T.; Bahnemann, D. *J. Phys. Chem. C* **2011**, *115*, 19676.
- (119) Yoshihara, T.; Katoh, R.; Furube, A.; Tamaki, Y.; Murai, M.; Hara, K.; Murata, S.; Arakawa, H.; Tachiya, M. *J. Phys. Chem. B* **2004**, *108*, 3817.
- (120) Skinner, D. E.; Colombo, D. P.; Cavaleri, J. J.; Bowman, R. M. *J. Phys. Chem.* **1995**, *99*, 7853.
- (121) Yamakata, A.; Ishibashi, T.; Onishi, H. *Chem. Phys. Lett.* **2001**, *333*, 271.
- (122) Peiro, A. M.; Colombo, C.; Doyle, G.; Nelson, J.; Mills, A.; Durrant, J. R. *J. Phys. Chem. B* **2006**, *110*, 23255.
- (123) Haque, S. A.; Tachibana, Y.; Willis, R. L.; Moser, J. E.; Gratzel, M.; Klug, D. R.; Durrant, J. R. *J. Phys. Chem. B* **2000**, *104*, 538.
- (124) Colombo, D. P.; Bowman, R. M. *J. Phys. Chem.* **1996**, *100*, 18445.
- (125) Katoh, R.; Furube, A. *J. Phys. Chem. Lett.* **2011**, *2*, 1888.
- (126) Rothenberger, G.; Moser, J.; Gratzel, M.; Serpone, N.; Sharma, D. K. *J. Am. Chem. Soc.* **1985**, *107*, 8054.
- (127) Henderson, M. A. *Surf. Sci. Rep.* **2011**, *66*, 185.
- (128) Lawless, D.; Serpone, N.; Meisel, D. *J. Phys. Chem.* **1991**, *95*, 5166.
- (129) Rajh, T.; Saponjic, Z. V.; Micic, O. I. *Langmuir* **1992**, *8*, 1265.
- (130) Di Iorio, Y.; Aguirre, M. E.; Brusa, M. A.; Grela, M. A. *J. Phys. Chem. C* **2012**, *116*, 9646.
- (131) Jaeger, C. D.; Bard, A. J. *J. Phys. Chem.* **1979**, *83*, 3146.
- (132) Anpo, M.; Shima, T.; Kubokawa, Y. *Chem. Lett.* **1985**, 1799.
- (133) Wardman, P. *J. Phys. Chem. Ref. Data* **1989**, *18*, 1637.
- (134) Cheng, J.; VandeVondele, J.; Sprik, M. *J. Phys. Chem. C* **2014**, *118*, 5437.
- (135) Bredow, T.; Jug, K. *J. Phys. Chem.* **1995**, *99*, 285.
- (136) Diesen, V.; Jonsson, M. *J. Phys. Chem. C* **2014**, *118*, 10083.
- (137) Imanishi, A.; Okamura, T.; Ohashi, N.; Nakamura, R.; Nakato, Y. *J. Am. Chem. Soc.* **2007**, *129*, 11569.
- (138) Delahay, P.; Vonburg, K. *Chem. Phys. Lett.* **1981**, *83*, 250.
- (139) Nakamura, R.; Nakato, Y. *J. Am. Chem. Soc.* **2004**, *126*, 1290.
- (140) Berger, T.; Sterrer, M.; Diwald, O.; Knozinger, E.; Panayotov, D.; Thompson, T. L.; Yates, J. T. *J. Phys. Chem. B* **2005**, *109*, 6061.
- (141) Micic, O. I.; Zhang, Y. N.; Cromack, K. R.; Trifunac, A. D.; Thurnauer, M. C. *J. Phys. Chem.* **1993**, *97*, 7277.
- (142) Ishibashi, K.; Fujishima, A.; Watanabe, T.; Hashimoto, K. *J. Photochem. Photobiol., A* **2000**, *134*, 139.
- (143) Howe, R. F.; Gratzel, M. *J. Phys. Chem.* **1987**, *91*, 3906.
- (144) Salvador, P. *J. Phys. Chem. C* **2007**, *111*, 17038.
- (145) Zhang, H. Z.; Penn, R. L.; Hamers, R. J.; Banfield, J. F. *J. Phys. Chem. B* **1999**, *103*, 4656.
- (146) Jug, K.; Nair, N. N.; Bredow, T. *Surf. Sci.* **2005**, *596*, 108.
- (147) Shapovalov, V.; Stefanovich, E. V.; Truong, T. N. *Surf. Sci.* **2002**, *498*, L103.
- (148) Ji, Y. F.; Wang, B.; Luo, Y. *J. Phys. Chem. C* **2012**, *116*, 7863.
- (149) Gadaczek, I.; Hintze, K. J.; Bredow, T. *Phys. Chem. Chem. Phys.* **2012**, *14*, 741.
- (150) Hug, G. L. *Optical Spectra of Nonmetallic Inorganic Transient Species in Aqueous Solution*; NSRDS-NBS: 1981.
- (151) Bahnemann, D. W.; Hilgendorff, M.; Memming, R. *J. Phys. Chem. B* **1997**, *101*, 4265.
- (152) Arbour, C.; Sharma, D. K.; Langford, C. H. *J. Phys. Chem.* **1990**, *94*, 331.
- (153) Tamaki, Y.; Furube, A.; Murai, M.; Hara, K.; Katoh, R.; Tachiya, M. *Phys. Chem. Chem. Phys.* **2007**, *9*, 1453.
- (154) Murakami, Y.; Nishino, J.; Mesaki, T.; Nosaka, Y. *Spectrosc. Lett.* **2011**, *44*, 88.
- (155) Yang, X. J.; Tamai, N. *Phys. Chem. Chem. Phys.* **2001**, *3*, 3393.
- (156) Tamaki, Y.; Furube, A.; Katoh, R.; Murai, M.; Hara, K.; Arakawa, H.; Tachiya, M. *C. R. Chim.* **2006**, *9*, 268.
- (157) Yoshihara, T.; Tamaki, Y.; Furube, A.; Murai, M.; Hara, K.; Katoh, R. *Chem. Phys. Lett.* **2007**, *438*, 268.
- (158) Katoh, R.; Murai, M.; Furube, A. *Chem. Phys. Lett.* **2010**, *500*, 309.
- (159) Tang, J.; Cowan, A. J.; Durrant, J. R.; Klug, D. R. *J. Phys. Chem. C* **2011**, *115*, 3143.
- (160) Jing, L.; Zhou, J.; Durrant, J. R.; Tang, J.; Liu, D.; Fu, H. *Energy Environ. Sci.* **2012**, *5*, 6552.
- (161) Tachikawa, T.; Tojo, S.; Kawai, K.; Endo, M.; Fujitsuka, M.; Ohno, T.; Nishijima, K.; Miyamoto, Z.; Majima, T. *J. Phys. Chem. B* **2004**, *108*, 19299.
- (162) Zawadzki, P. *J. Phys. Chem. C* **2013**, *117*, 8647.
- (163) Kowalski, P. M.; Camellone, M. F.; Nair, N. N.; Meyer, B.; Marx, D. *Phys. Rev. Lett.* **2010**, *105*, 146405.
- (164) Di Valentin, C.; Pacchioni, G.; Selloni, A. *Phys. Rev. Lett.* **2006**, *97*, 166803/1.
- (165) Di Valentin, C.; Selloni, A. *J. Phys. Chem. Lett.* **2011**, *2*, 2223.
- (166) Graetzel, M. *Heterogeneous Photochemical Electron Transfer Reactions*; CRC Press: Boca Raton, FL, 1987.
- (167) Kuznetsov, A. I.; Kameneva, O.; Alexandrov, A.; Bityurin, N.; Marteau, P.; Chhor, K.; Sanchez, C.; Kanaev, A. *Phys. Rev. E* **2005**, *71*, 021403.
- (168) Fonash, S. J. *Solar Cell Device Physics*; Academic Press: New York, London, 1981.
- (169) Colbeau-Justin, C.; Valenzuela, M. A. *Rev. Mex. Fis.* **2013**, *59*, 191.
- (170) Colbeau-Justin, C.; Kunst, M.; Huguenin, D. *J. Mater. Sci.* **2003**, *38*, 2429.
- (171) Carneiro, J. T.; Savenije, T. J.; Moulijn, J. A.; Mul, G. *J. Phys. Chem. C* **2011**, *115*, 2211.
- (172) Schindler, K. M.; Kunst, M. *J. Phys. Chem.* **1990**, *94*, 8222.
- (173) Martin, S. T.; Herrmann, H.; Choi, W. Y.; Hoffmann, M. R. *J. Chem. Soc., Faraday Trans.* **1994**, *90*, 3315.
- (174) Martin, S. T.; Herrmann, H.; Hoffmann, M. R. *J. Chem. Soc., Faraday Trans.* **1994**, *90*, 3323.
- (175) Carneiro, J. T.; Savenije, T. J.; Moulijn, J. A.; Mul, G. *J. Phys. Chem. C* **2010**, *114*, 327.
- (176) Serpone, N.; Emeline, A. V. *Int. J. Photoenergy* **2002**, *4*, 91.
- (177) Enright, B.; Fitzmaurice, D. *J. Phys. Chem.* **1996**, *100*, 1027.
- (178) Grätzel, M.; Frank, A. J. *J. Phys. Chem.* **1982**, *86*, 2964.
- (179) Warman, J. M.; Dehaas, M. P.; Pichat, P.; Koster, T. P. M.; Vanderzouwenassink, E. A.; Mackor, A.; Cooper, R. *Radiat. Phys. Chem.* **1991**, *37*, 433.
- (180) Mohamed, H. H.; Mendive, C. B.; Dillert, R.; Bahnemann, D. W. *J. Phys. Chem. A* **2011**, *115*, 2139.
- (181) Mohamed, H. H.; Dillert, R.; Bahnemann, D. W. *Chem.—Eur. J.* **2012**, *18*, 4314.
- (182) Huang, L. H.; Chan, Q. Z.; Zhang, B.; Wu, X. J.; Gao, P.; Jiao, Z. B.; Liu, Y. L. *Chin. J. Catal.* **2011**, *32*, 1822.
- (183) Anpo, M.; Takeuchi, M. *J. Catal.* **2003**, *216*, 505.

- (184) Furube, A.; Asahi, T.; Masuhara, H.; Yamashita, H.; Anpo, M. *Chem. Phys. Lett.* **2001**, 336, 424.
- (185) Iwata, K.; Takaya, T.; Hamaguchi, H.; Yamakata, A.; Ishibashi, T. A.; Onishi, H.; Kuroda, H. *J. Phys. Chem. B* **2004**, 108, 20233.
- (186) Emilio, C. A.; Litter, M. I.; Kunst, M.; Bouchard, M.; Colbeau-Justin, C. *Langmuir* **2006**, 22, 3606.
- (187) Kowalska, E.; Remita, H.; Colbeau-Justin, C.; Hupka, J.; Belloni, J. *J. Phys. Chem. C* **2008**, 112, 1124.
- (188) Daniel, M.-C.; Astruc, D. *Chem. Rev.* **2003**, 104, 293.
- (189) Tian, Y.; Tatsuma, T. *J. Am. Chem. Soc.* **2005**, 127, 7632.
- (190) Ingram, D. B.; Linic, S. *J. Am. Chem. Soc.* **2011**, 133, 5202.
- (191) Fang, J.; Cao, S. W.; Wang, Z.; Shahjamali, M. M.; Loo, S. C. J.; Barber, J.; Xue, C. *Int. J. Hydrogen Energy* **2012**, 37, 17853.
- (192) Du, L. C.; Furube, A.; Hara, K.; Katoh, R.; Tachiya, M. *J. Photochem. Photobiol., A* **2013**, 15, 21.
- (193) Tamaki, Y.; Furube, A.; Murai, M.; Hara, K.; Katoh, R.; Tachiya, M. *J. Am. Chem. Soc.* **2006**, 128, 416.
- (194) Muir, J. N.; Choi, Y.; Idriss, H. *Phys. Chem. Chem. Phys.* **2012**, 14, 11910.
- (195) Zhao, J.; Yang, J. L.; Petek, H. *Phys. Rev. B* **2009**, 80.
- (196) Panayotov, D. A.; Burrows, S. P.; Morris, J. R. *J. Phys. Chem. C* **2012**, 116, 6623.
- (197) Lilie, J.; Beck, G.; Henglein, A. *Ber. Bunsen-Ges. Phys. Chem.* **1971**, 75, 458.
- (198) Memming, R. In *Electron Transfer I*; Mattay, J., Ed.; Springer-Verlag: Berlin Heidelberg, 1994.
- (199) Hykaway, N.; Sears, W. M.; Morisaki, H.; Morrison, S. R. *J. Phys. Chem.* **1986**, 90, 6663.
- (200) Nakabayashi, S.; Komuro, S.; Aoyagi, Y.; Kira, A. *J. Phys. Chem.* **1987**, 91, 1696.
- (201) Pukies, J.; Roebke, W.; Henglein, A. *Ber. Bunsen-Ges. Phys. Chem.* **1968**, 72, 842.
- (202) Henglein, A. *Ber. Bunsen-Ges. Phys. Chem.* **1990**, 94, 600.
- (203) Shen, M.; Henderson, M. A. *J. Phys. Chem. C* **2012**, 116, 18788.
- (204) Montoya, J. F.; Ivanova, I.; Dillert, R.; Bahnemann, D. W.; Salvador, P.; Peral, J. *J. Phys. Chem. Lett.* **2013**, 4, 1415.
- (205) Montoya, J. F.; Bahnemann, D. W.; Peral, J.; Salvador, P. *ChemPhysChem* **2014**, 15, 2311.
- (206) Szczepankiewicz, S. H.; Colussi, A. J.; Hoffmann, M. R. *J. Phys. Chem. B* **2000**, 104, 9842.
- (207) Furube, A.; Asahi, T.; Masuhara, H.; Yamashita, H.; Anpo, M. *Res. Chem. Intermed.* **2001**, 27, 177.
- (208) Hush, N. S. *Trans. Faraday Soc.* **1961**, 57, 557.
- (209) Marcus, R. A. *Annu. Rev. Phys. Chem.* **1964**, 15, 155.
- (210) Kuciauskas, D.; Freund, M. S.; Gray, H. B.; Winkler, J. R.; Lewis, N. S. *J. Phys. Chem. B* **2001**, 105, 392.
- (211) Gaal, D. A.; Hupp, J. T. *J. Am. Chem. Soc.* **2000**, 122, 10956.
- (212) Yan, S. G.; Prieskorn, J. S.; Kim, Y. J.; Hupp, J. T. *J. Phys. Chem. B* **2000**, 104, 10871.
- (213) Gao, R. M.; Safrany, A.; Rabani, J. *Radiat. Phys. Chem.* **2003**, 67, 25.
- (214) Moser, J.; Punchihewa, S.; Infelta, P. P.; Grätzel, M. *Langmuir* **1991**, 7, 3012.
- (215) Wang, C. Y.; Bahnemann, D. W.; Dohrmann, J. K. *Chem. Commun.* **2000**, 1539.
- (216) Wang, C.; Bahnemann, D. W.; Dohrmann, J. K. *Water Sci. Technol.* **2001**, 44, 279.
- (217) Wang, C. Y.; Rabani, J.; Bahnemann, D. W.; Dohrmann, J. K. *J. Photochem. Photobiol., A* **2002**, 148, 169.
- (218) Wang, C. Y.; Bottcher, C.; Bahnemann, D. W.; Dohrmann, J. K. *J. Mater. Chem.* **2003**, 13, 2322.
- (219) Wang, C. Y.; Bottcher, C.; Bahnemann, D. W.; Dohrmann, J. K. *J. Nanopart. Res.* **2004**, 6, 119.
- (220) Wang, C. Y.; Pagel, R.; Bahnemann, D. W.; Dohrmann, J. K. *J. Phys. Chem. B* **2004**, 108, 14082.
- (221) Wang, C. Y.; Pagel, R.; Dohrmann, J. K.; Bahnemann, D. W. *C. R. Chim.* **2006**, 9, 761.
- (222) Ismail, A. A.; Bahnemann, D. W.; Robben, L.; Yarovy, V.; Wark, M. *Chem. Mater.* **2010**, 22, 108.
- (223) Moss, J. A.; Szczepankiewicz, S. H.; Park, E.; Hoffmann, M. R. *J. Phys. Chem. B* **2005**, 109, 19779.
- (224) Szczepankiewicz, S. H.; Moss, J. A.; Hoffmann, M. R. *J. Phys. Chem. B* **2002**, 106, 2922.
- (225) Szczepankiewicz, S. H.; Moss, J. A.; Hoffmann, M. R. *J. Phys. Chem. B* **2002**, 106, 7654.
- (226) Araujo, P. Z.; Mendive, C. B.; Rodenas, L. A. G.; Morando, P. J.; Regazzoni, A. E.; Blesa, M. A.; Bahnemann, D. *Colloids Surf., A* **2005**, 265, 73.
- (227) Mendive, C. B.; Bahnemann, D. W.; Blesa, M. A. *Catal. Today* **2005**, 101, 237.
- (228) Hug, S. J.; Bahnemann, D. *J. Electron Spectrosc. Relat. Phenom.* **2006**, 150, 208.
- (229) Mendive, C. B.; Bredow, T.; Blesa, M. A.; Bahnemann, D. W. *Phys. Chem. Chem. Phys.* **2006**, 8, 3232.
- (230) Feldhoff, A.; Mendive, C.; Bredow, T.; Bahnemann, D. *ChemPhysChem* **2007**, 8, 805.
- (231) Mendive, C. B.; Blesa, M. A.; Bahnemann, D. *Water Sci. Technol.* **2007**, 55, 139.
- (232) Mendive, C. B.; Bredow, T.; Feldhoff, A.; Blesa, M.; Bahnemann, D. *Phys. Chem. Chem. Phys.* **2008**, 10, 1960.
- (233) Mendive, C. B.; Bredow, T.; Feldhoff, A.; Blesa, M. A.; Bahnemann, D. *Phys. Chem. Chem. Phys.* **2009**, 11, 1794.
- (234) Baumanis, C.; Bahnemann, D. W. *J. Phys. Chem. C* **2008**, 112, 19097.
- (235) Meier, A.; Selmarten, D.; Hanna, M.; Nozik, A.; Siemoneit, K.; Reineke-Koch, R.; Memming, R. *Z. Phys. Chem.* **1999**, 213, 117.
- (236) Siemoneit, K.; Reineke-Koch, R.; Meier, A.; Memming, R. *Electrochim. Acta* **2000**, 45, 4577.
- (237) Kormann, C.; Bahnemann, D. W.; Hoffmann, M. R. *J. Phys. Chem.* **1988**, 92, 5196.
- (238) Bahnemann, D. W.; Kormann, C.; Hoffmann, M. R. *J. Phys. Chem.* **1987**, 91, 3789.
- (239) Bahnemann, D. W. *Res. Chem. Intermed.* **2000**, 26, 207.
- (240) Hufschmidt, D.; Bahnemann, D.; Testa, J. J.; Emilio, C. A.; Litter, M. I. *J. Photochem. Photobiol., A* **2002**, 148, 223.
- (241) Hidalgo, M. C.; Sakthivel, S.; Bahnemann, D. *Appl. Catal., A* **2004**, 277, 183.
- (242) Hidalgo, M. C.; Bahnemann, D. *Appl. Catal., B* **2005**, 61, 259.
- (243) Ismail, A. A.; Bahnemann, D. W. *J. Adv. Oxid. Technol.* **2009**, 12, 9.
- (244) Kandiel, T. A.; Dillert, R.; Bahnemann, D. W. *Photochem. Photobiol. Sci.* **2009**, 8, 683.
- (245) Kandiel, T. A.; Feldhoff, A.; Robben, L.; Dillert, R.; Bahnemann, D. W. *Chem. Mater.* **2010**, 22, 2050.
- (246) Kandiel, T. A.; Dillert, R.; Feldhoff, A.; Bahnemann, D. W. *J. Phys. Chem. C* **2010**, 114, 4909.
- (247) Kalyanasundaram, K.; Gratzel, M. *Angew. Chem., Int. Ed. Engl.* **1979**, 18, 701.
- (248) Borgarello, E.; Kiwi, J.; Gratzel, M.; Pelizzetti, E.; Visca, M. *J. Am. Chem. Soc.* **1982**, 104, 2996.
- (249) Kamat, P. V.; Fox, M. A. *Chem. Phys. Lett.* **1983**, 102, 379.
- (250) Tachibana, Y.; Moser, J. E.; Gratzel, M.; Klug, D. R.; Durrant, J. R. *J. Phys. Chem.* **1996**, 100, 20056.
- (251) Islam, A.; Sugihara, H.; Hara, K.; Singh, L. P.; Katoh, R.; Yanagida, M.; Takahashi, Y.; Murata, S.; Arakawa, H. *J. Photochem. Photobiol., A* **2001**, 145, 135.
- (252) Oregan, B.; Gratzel, M. *Nature* **1991**, 353, 737.
- (253) Ghosh, A. K.; Maruska, H. P. *J. Electrochem. Soc.* **1977**, 124, 1516.
- (254) Maruska, H. P.; Ghosh, A. K. *Sol. Energy Mater.* **1979**, 1, 237.
- (255) Herrmann, J. M.; Disdier, J.; Pichat, P. *Chem. Phys. Lett.* **1984**, 108, 618.
- (256) Anpo, M.; Yamashita, H.; Ishibashi, Y. *Optronics* **1997**, 186, 161.
- (257) Anpo, M.; Ichihashi, Y.; Takeuchi, M.; Yamashita, H. *Res. Chem. Intermed.* **1998**, 24, 143.
- (258) Anpo, M. *Pure Appl. Chem.* **2000**, 72, 1787.
- (259) Anpo, M.; Kishiguchi, S.; Ichihashi, Y.; Takeuchi, M.; Yamashita, H.; Ikeue, K.; Morin, B.; Davidson, A.; Che, M. *Res. Chem. Intermed.* **2001**, 27, 459.

- (260) Anpo, M.; Takeuchi, M.; Yamashita, H.; Kishiguchi, S.; Davidson, A.; Che, M. In *Semiconductor Photochemistry and Photophysics*; Ramamurthy, V., Schanze, K., Dekker, S. M., Eds.; CRC Press: New York, 2003.
- (261) Anpo, M. *Bull. Chem. Soc. Jpn.* **2004**, *77*, 1427.
- (262) Stepanov, A. L. *Rev. Adv. Mater. Sci.* **2012**, *30*, 150.
- (263) O'Regan, B.; Gratzel, M. *Nature* **1991**, *353*, 737.
- (264) Ito, S.; Chen, P.; Comte, P.; Nazeeruddin, M. K.; Liska, P.; Pechy, P.; Gratzel, M. *Prog. Photovoltaics* **2007**, *15*, 603.
- (265) Ito, S.; Zakeeruddin, S. M.; Humphry-Baker, R.; Liska, P.; Charvet, R.; Comte, P.; Nazeeruddin, M. K.; Pechy, P.; Takata, M.; Miura, H.; Uchida, S.; Gratzel, M. *Adv. Mater.* **2006**, *18*, 1202.
- (266) Kuang, D.; Brillet, J.; Chen, P.; Takata, M.; Uchida, S.; Miura, H.; Sumioka, K.; Zakeeruddin, S. M.; Gratzel, M. *ACS Nano* **2008**, *2*, 1113.
- (267) Nazeeruddin, M. K.; Humphry-Baker, R.; Liska, P.; Gratzel, M. *J. Phys. Chem. B* **2003**, *107*, 8981.
- (268) Nazeeruddin, M. K.; Pechy, P.; Renouard, T.; Zakeeruddin, S. M.; Humphry-Baker, R.; Comte, P.; Liska, P.; Cevey, L.; Costa, E.; Shklover, V.; Spiccia, L.; Deacon, G. B.; Bignozzi, C. A.; Gratzel, M. *J. Am. Chem. Soc.* **2001**, *123*, 1613.
- (269) Wang, P.; Zakeeruddin, S. M.; Comte, P.; Charvet, R.; Humphry-Baker, R.; Gratzel, M. *J. Phys. Chem. B* **2003**, *107*, 14336.
- (270) Zukalova, M.; Zukal, A.; Kavan, L.; Nazeeruddin, M. K.; Liska, P.; Gratzel, M. *Nano Lett.* **2005**, *5*, 1789.
- (271) Zhu, J. F.; Chen, F.; Zhang, J. L.; Chen, H. J.; Anpo, M. *J. Photochem. Photobiol. A* **2006**, *180*, 196.
- (272) Yang, Y.; Tian, C. X. *Photochem. Photobiol.* **2012**, *88*, 816.
- (273) Shi, J.-W.; Zheng, J.-T.; Hu, Y.; Zhao, Y.-C. *Mater. Chem. Phys.* **2007**, *106*, 247.
- (274) Zhu, J.; Zheng, W.; He, B.; Zhang, J.; Anpo, M. *J. Mol. Catal. A: Chem.* **2004**, *216*, 35.
- (275) Tong, T.; Zhang, J.; Tian, B.; Chen, F.; He, D. *J. Hazard. Mater.* **2008**, *155*, 572.
- (276) Zhu, J. F.; Deng, Z. G.; Chen, F.; Zhang, J. L.; Chen, H. J.; Anpo, M.; Huang, J. Z.; Zhang, L. Z. *Appl. Catal., B* **2006**, *62*, 329.
- (277) Hamzah, N.; Nordin, N. M.; Nadzri, A. H. A.; Nik, Y. A.; Kassim, M. B.; Yarmo, M. A. *Appl. Catal., A* **2012**, *419–420*, 133.
- (278) Panagiotopoulou, P.; Kondarides, D. I.; Vaykios, X. E. *J. Phys. Chem. C* **2011**, *115*, 1202.
- (279) Yuan, S.; Chen, Y.; Shi, L. Y.; Fang, J. H.; Zhang, J. P.; Zhang, J. L.; Yamashita, H. *Mater. Lett.* **2007**, *61*, 4283.
- (280) Tong, T. Z.; Zhang, J. L.; Tian, B. Z.; Chen, F.; He, D. N.; Anpo, M. *J. Colloid Interface Sci.* **2007**, *315*, 382.
- (281) Gao, H. T.; Liu, W. C.; Lu, B.; Liu, F. F. *J. Nanosci. Nanotechnol.* **2012**, *12*, 3959.
- (282) Xing, M. Y.; Qi, D. Y.; Zhang, J. L.; Chen, F. *Chem.—Eur. J.* **2011**, *17*, 11432.
- (283) Yuan, S.; Sheng, Q. R.; Zhang, J. L.; Chen, F.; Anpo, M.; Zhang, Q. H. *Microporous Mesoporous Mater.* **2005**, *79*, 93.
- (284) Liu, H. B.; Wu, Y. M.; Zhang, J. L. *ACS Appl. Mater. Interfaces* **2011**, *3*, 1757.
- (285) Tian, B. Z.; Li, C. Z.; Gu, F.; Jiang, H. B.; Hu, Y. J.; Zhang, J. L. *Chem. Eng. J.* **2009**, *151*, 220.
- (286) Lin, W. C.; Lin, Y. J. *Environ. Eng. Sci.* **2012**, *29*, 447.
- (287) Cong, Y.; Tian, B. Z.; Zhang, J. L. *Appl. Catal., B* **2011**, *101*, 376.
- (288) Sajjad, S.; Leghari, S. A. K.; Chen, F.; Zhang, J. L. *Chem.—Eur. J.* **2010**, *16*, 13795.
- (289) Wang, W. J.; Zhang, J. L.; Chen, F.; Anpo, M.; He, D. N. *Res. Chem. Intermed.* **2010**, *36*, 163.
- (290) Yuan, X. L.; Zhang, J. L.; Anpo, M.; He, D. N. *Res. Chem. Intermed.* **2010**, *36*, 83.
- (291) Zhang, J.; Wu, Y.; Xing, M.; Leghari, S. A. K.; Sajjad, S. *Energy Environ. Sci.* **2010**, *3*, 715.
- (292) Zuo, F.; Wang, L.; Wu, T.; Zhang, Z.; Borchardt, D.; Feng, P. *J. Am. Chem. Soc.* **2010**, *132*, 11856.
- (293) Xing, M.; Fang, W.; Nasir, M.; Ma, Y.; Zhang, J.; Anpo, M. *J. Catal.* **2013**, *297*, 236.
- (294) Zheng, Z.; Huang, B.; Meng, X.; Wang, J.; Wang, S.; Lou, Z.; Wang, Z.; Qin, X.; Zhang, X.; Dai, Y. *Chem. Commun.* **2013**.
- (295) Hoang, S.; Berglund, S. P.; Hahn, N. T.; Bard, A. J.; Mullins, C. B. *J. Am. Chem. Soc.* **2012**, *134*, 3659.
- (296) Xing, M.; Zhang, J.; Chen, F.; Tian, B. *Chem. Commun.* **2011**, *47*, 4947.
- (297) Liu, G. L.; Han, C.; Pelaez, M.; Zhu, D. W.; Liao, S. J.; Likodimos, V.; Ioannidis, N.; Kontos, A. G.; Falaras, P.; Dunlop, P. S. M.; Byrne, J. A.; Dionysiou, D. D. *Nanotechnology* **2012**, *23*.
- (298) Selvam, K.; Swaminathan, M. *RSC Adv.* **2012**, *2*, 2848.
- (299) Zhang, W. J.; Yang, B.; Chen, J. L. *Int. J. Photoenergy* **2012**.
- (300) Asahi, R.; Morikawa, T.; Ohwaki, T.; Aoki, K.; Taga, Y. *Science* **2001**, *293*, 269.
- (301) Wang, X. D.; Blackford, M.; Prince, K.; Caruso, R. A. *ACS Appl. Mater. Interfaces* **2012**, *4*, 476.
- (302) Wu, Y. M.; Xing, M. Y.; Zhang, J. L.; Chen, F. *Appl. Catal., B* **2010**, *97*, 182.
- (303) Lu, X. N.; Tian, B. Z.; Chen, F.; Zhang, J. L. *Thin Solid Films* **2010**, *519*, 111.
- (304) Tang, Y.-B.; Yin, L.-C.; Yang, Y.; Bo, X.-H.; Cao, Y.-L.; Wang, H.-E.; Zhang, W.-J.; Bello, I.; Lee, S.-T.; Cheng, H.-M.; Lee, C.-S. *ACS Nano* **2012**, *6*, 1970.
- (305) Wu, Y. M.; Zhang, J. L.; Xiao, L.; Chen, F. *Appl. Surf. Sci.* **2010**, *256*, 4260.
- (306) Parayil, S. K.; Kibombo, H. S.; Wu, C. M.; Peng, R.; Baltrusaitis, J.; Koodali, R. T. *Int. J. Hydrogen Energy* **2012**, *37*, 8257.
- (307) Zhong, J.; Chen, F.; Zhang, J. L. *J. Phys. Chem. C* **2010**, *114*, 933.
- (308) Kuwahara, Y.; Maki, K.; Matsumura, Y.; Kamegawa, T.; Mori, K.; Yamashita, H. *J. Phys. Chem. C* **2009**, *113*, 1552.
- (309) Tosoni, S.; Fernandez Hevia, D.; González Díaz, Ó.; Illas, F. *J. Phys. Chem. Lett.* **2012**, *3*, 2269.
- (310) Xing, M. Y.; Qi, D. Y.; Zhang, J. L.; Chen, F.; Tian, B. Z.; Bagwas, S.; Anpo, M. *J. Catal.* **2012**, *294*, 37.
- (311) Liu, S. W.; Yu, J. G.; Cheng, B.; Jaroniec, M. *Adv. Colloid Interface Sci.* **2012**, *173*, 35.
- (312) Seo, H.; Baker, L. R.; Hervier, A.; Kim, J.; Whitten, J. L.; Somorjai, G. A. *Nano Lett.* **2011**, *11*, 751.
- (313) Dozzi, M. V.; Livraghi, S.; Giamello, E.; Selli, E. *Photochem. Photobiol. Sci.* **2011**, *10*, 343.
- (314) Niu, Y.; Xing, M.; Tian, B.; Zhang, J. *Appl. Catal., B* **2012**, *115–116*, 253.
- (315) Xu, P.; Xu, T.; Lu, J.; Gao, S.; Hosmane, N. S.; Huang, B.; Dai, Y.; Wang, Y. *Energy Environ. Sci.* **2010**, *3*, 1128.
- (316) Bidaye, P.; Khushalani, D.; Fernandes, J. B. *Catal. Lett.* **2010**, *134*, 169.
- (317) He, H. Y. *Res. Chem. Intermed.* **2010**, *36*, 155.
- (318) Yang, K.; Dai, Y.; Huang, B. *J. Phys. Chem. C* **2007**, *111*, 18985.
- (319) Di Valentin, C.; Pacchioni, G.; Selloni, A.; Livraghi, S.; Giamello, E. *J. Phys. Chem. B* **2005**, *109*, 11414.
- (320) Jagadale, T. C.; Takale, S. P.; Sonawane, R. S.; Joshi, H. M.; Patil, S. I.; Kale, B. B.; Ogale, S. B. *J. Phys. Chem. C* **2008**, *112*, 14595.
- (321) Hao, H.; Zhang, J. *Microporous Mesoporous Mater.* **2009**, *121*, 52.
- (322) Livraghi, S.; Paganini, M. C.; Giamello, E.; Selloni, A.; Di Valentin, C.; Pacchioni, G. *J. Am. Chem. Soc.* **2006**, *128*, 15666.
- (323) Caratto, V.; Setti, L.; Campodonico, S.; Carnasciali, M. M.; Botter, R.; Ferretti, M. *J. Sol-Gel Sci. Technol.* **2012**, *63*, 16.
- (324) Dong, F.; Zhao, W. R.; Wu, Z. B.; Guo, S. *J. Hazard. Mater.* **2009**, *162*, 763.
- (325) Kim, M.-S.; Liu, G.; Nam, W. K.; Kim, B.-W. *J. Ind. Eng. Chem.* **2011**, *17*, 223.
- (326) Neville, E. M.; Mattle, M. J.; Loughrey, D.; Rajesh, B.; Rahman, M.; MacElroy, J. M. D.; Sullivan, J. A.; Thampi, K. R. *J. Phys. Chem. C* **2012**, *116*, 16511.
- (327) Gopal, N. O.; Lo, H.-H.; Ke, S.-C. *J. Am. Chem. Soc.* **2008**, *130*, 2760.
- (328) Czoska, A. M.; Livraghi, S.; Paganini, M. C.; Giamello, E.; Di Valentin, C.; Pacchioni, G. *Phys. Chem. Chem. Phys.* **2011**, *13*, 136.
- (329) Li, Y.; Ma, G.; Peng, S.; Lu, G.; Li, S. *Appl. Surf. Sci.* **2008**, *254*, 6831.
- (330) Liu, G.; Yang, H. G.; Wang, X.; Cheng, L.; Pan, J.; Lu, G. Q.; Cheng, H.-M. *J. Am. Chem. Soc.* **2009**, *131*, 12868.

- (331) Wang, D.-H.; Jia, L.; Wu, X.-L.; Lu, L.-Q.; Xu, A.-W. *Nanoscale* **2012**, *4*, 576.
- (332) Zuo, F.; Bozhilov, K.; Dillon, R. J.; Wang, L.; Smith, P.; Zhao, X.; Bardeen, C.; Feng, P. *Angew. Chem., Int. Ed.* **2012**, *51*, 6223.
- (333) Zhao, L.; Chen, X.; Wang, X.; Zhang, Y.; Wei, W.; Sun, Y.; Antonietti, M.; Titirici, M.-M. *Adv. Mater.* **2010**, *22*, 3317.
- (334) Xing, M.-Y.; Li, W.-K.; Wu, Y.-M.; Zhang, J.-L.; Gong, X.-Q. *J. Phys. Chem. C* **2011**, *115*, 7858.
- (335) Liu, G.; Zhao, Y.; Sun, C.; Li, F.; Lu, G. Q.; Cheng, H.-M. *Angew. Chem., Int. Ed.* **2008**, *47*, 4516.
- (336) Hopper, E. M.; Sauvage, F.; Chandiran, A. K.; Grätzel, M.; Poeppelmeier, K. R.; Mason, T. O. *J. Am. Ceram. Soc.* **2012**, *95*, 3192.
- (337) Cong, Y.; Zhang, J.; Chen, F.; Anpo, M.; He, D. *J. Phys. Chem. C* **2007**, *111*, 10618.
- (338) Cong, Y.; Zhang, J. L.; Chen, F.; Anpo, M. *J. Phys. Chem. C* **2007**, *111*, 6976.
- (339) Zielińska, A.; Kowalska, E.; Sobczak, J. W.; Łacka, I.; Gazda, M.; Ohtani, B.; Hupka, J.; Zaleska, A. *Sep. Purif. Technol.* **2010**, *72*, 309.
- (340) Sakthivel, S.; Kisch, H. *Angew. Chem., Int. Ed.* **2003**, *42*, 4908.
- (341) Xing, M.; Zhang, J.; Chen, F. *J. Phys. Chem. C* **2009**, *113*, 12848.
- (342) Xing, M.; Zhang, J.; Chen, F. *Appl. Catal., B* **2009**, *89*, 563.
- (343) Wu, Y. M.; Liti, H. B.; Zhang, J. L.; Chen, F. *J. Phys. Chem. C* **2009**, *113*, 14689.
- (344) Yu, J. C.; Yu, J.; Ho, W.; Jiang, Z.; Zhang, L. *Chem. Mater.* **2002**, *14*, 3808.
- (345) Goswami, P.; Ganguli, J. N. *Mater. Res. Bull.* **2012**, *47*, 2077.
- (346) Justicia, I.; Ordejón, P.; Canto, G.; Mozos, J. L.; Fraxedas, J.; Battiston, G. A.; Gerbasí, R.; Figueras, A. *Adv. Mater.* **2002**, *14*, 1399.
- (347) Cao, Y.; Yang, W.; Zhang, W.; Liu, G.; Yue, P. *New J. Chem.* **2004**, *28*, 218.
- (348) Kurtz, S. R.; Gordon, R. G. *Thin Solid Films* **1987**, *147*, 167.
- (349) Su, Y.; Zhang, X.; Han, S.; Chen, X.; Lei, L. *Electrochem. Commun.* **2007**, *9*, 2291.
- (350) Yu, J.; Xiang, Q.; Zhou, M. *Appl. Catal., B* **2009**, *90*, 595.
- (351) Navío, J.; Colón, G.; Litter, M. I.; Bianco, G. N. *J. Mol. Catal. A: Chem.* **1996**, *106*, 267.
- (352) Suroliá, P. K.; Tayade, R. J.; Jasra, R. V. *Ind. Eng. Chem. Res.* **2007**, *46*, 6196.
- (353) Xing, M.; Zhang, J.; Chen, F. *J. Phys. Chem. C* **2009**, *113*, 12848.
- (354) Di Paola, A.; Marci, G.; Palmisano, L.; Schiavello, M.; Uosaki, K.; Ikeda, S.; Ohtani, B. *J. Phys. Chem. B* **2001**, *106*, 637.
- (355) Xia, T.; Zhang, C.; Oyler, N. A.; Chen, X. *Adv. Mater.* **2013**, *25*, 6905.
- (356) Chen, X.; Liu, L.; Yu, P. Y.; Mao, S. S. *Science* **2011**, *331*, 746.
- (357) Naldoni, A.; Alliet, M.; Santangelo, S.; Marelli, M.; Fabbri, F.; Cappelli, S.; Bianchi, C. L.; Psaro, R.; Dal Santo, V. *J. Am. Chem. Soc.* **2012**, *134*, 7600.
- (358) Chen, X.; Liu, L.; Liu, Z.; Marcus, M. A.; Wang, W.-C.; Oyler, N. A.; Grass, M. E.; Mao, B.; Glans, P.-A.; Yu, P. Y.; Guo, J.; Mao, S. S. *Sci. Rep.* **2013**, *3*, 1510.
- (359) Khan, S. U. M.; Al-Shahry, M.; Ingler, W. B., Jr. *Science* **2002**, *297*, 2243.
- (360) In, S.; Orlov, A.; Berg, R.; Garcia, F.; Pedrosa-Jimenez, S.; Tikhov, M. S.; Wright, D. S.; Lambert, R. M. *J. Am. Chem. Soc.* **2007**, *129*, 13790.
- (361) Xia, T.; Zhang, W.; Murowchick, J. B.; Liu, G.; Chen, X. *Adv. Energy Mater.* **2013**, DOI: 10.1002/aenm.201300294.
- (362) Wang, Z.; Yang, C.; Lin, T.; Yin, H.; Chen, P.; Wan, D.; Xu, F.; Huang, F.; Lin, J.; Xie, X.; Jiang, M. *Adv. Funct. Mater.* **2013**, *23*, 5444.
- (363) Wu, H.-C.; Li, S.-H.; Lin, S.-W. *Int. J. Photoenergy* **2012**, DOI: 10.1155/2012/823498.
- (364) Choi, W.; Termin, A.; Hoffmann, M. R. *J. Phys. Chem.* **1994**, *98*, 13669.
- (365) Yan, N. N.; Zhu, Z. Q.; Zhang, J.; Zhao, Z. Y.; Liu, Q. J. *Mater. Res. Bull.* **2012**, *47*, 1869.
- (366) Zhu, J. F.; Chen, F.; Zhang, J. L.; Chen, H. J.; Anpo, M. *J. Photochem. Photobiol., A* **2006**, *180*, 196.
- (367) Xiao, L.; Zhang, J. L.; Cong, Y.; Tian, B. Z.; Chen, F.; Anpo, M. *Catal. Lett.* **2006**, *111*, 207.
- (368) Tong, T. Z.; Zhang, J. L.; Tian, B. Z.; Chen, F.; He, D. N. *J. Hazard. Mater.* **2008**, *155*, 572.
- (369) You, X.; Chen, F.; Zhang, J.; Anpo, M. *Catal. Lett.* **2005**, *102*, 247.
- (370) Wang, W.; Zhang, J.; Chen, F.; He, D.; Anpo, M. *J. Colloid Interface Sci.* **2008**, *323*, 182.
- (371) Wu, Y. M.; Zhang, J. L.; Xiao, L.; Chen, F. *Appl. Catal., B* **2009**, *88*, 525.
- (372) Zhu, J. F.; Zheng, W.; Bin, H. E.; Zhang, J. L.; Anpo, M. *J. Mol. Catal. A: Chem.* **2004**, *216*, 35.
- (373) Jaiswal, R.; Patel, N.; Kothari, D. C.; Miotello, A. *Appl. Catal., B* **2012**, *126*, 47.
- (374) Sun, L.; Zhao, X.; Cheng, X.; Sun, H.; Li, Y.; Li, P.; Fan, W. *Langmuir* **2012**, *28*, 5882.
- (375) Yuan, S.; Sheng, Q. R.; Zhang, J. L.; Chen, F.; Anpo, M.; Dai, W. L. *Catal. Lett.* **2006**, *107*, 19.
- (376) Chen, Q. L.; Wang, Y.; Zhong, C. Y.; Guo, Y. In *Advanced Materials, Pts 1–4*; Cao, Z., Cao, X. Q., Sun, L., He, Y. H., Eds.; Wiley: New York, 2011.
- (377) Anandan, S.; Ikuma, Y.; Murugesan, V. *Int. J. Photoenergy* **2012**, *2012*, 921412.
- (378) Ma, Y. F.; Xing, M. Y.; Zhang, J. L.; Tian, B. Z.; Chen, F. *Microporous Mesoporous Mater.* **2012**, *156*, 145.
- (379) Ma, Y. F.; Zhang, J. L.; Tian, B. Z.; Chen, F.; Bao, S. Y.; Anpo, M. *Res. Chem. Intermed.* **2012**, *38*, 1947.
- (380) Ma, Y. F.; Zhang, J. L.; Tian, B. Z.; Chen, F.; Wang, L. Z. *J. Hazard. Mater.* **2010**, *182*, 386.
- (381) Zhao, Y.; Liu, J.; Shi, L.; Yuan, S.; Fang, J.; Wang, Z.; Zhang, M. *Appl. Catal., B* **2011**, *103*, 436.
- (382) Zhou, X.; Lu, J.; Li, L.; Wang, Z. *J. Nanomater.* **2011**, 2011.
- (383) Lu, G.; Linsebigler, A.; Yates, J. T. *J. Phys. Chem.* **1994**, *98*, 11733.
- (384) Sasikala, R.; Shirole, A.; Sudarsan, V.; Sakuntala, T.; Sudakar, C.; Naik, R.; Bharadwaj, S. R. *Int. J. Hydrogen Energy* **2009**, *34*, 3621.
- (385) Nakamura, I.; Negishi, N.; Kutsuna, S.; Ihara, T.; Sugihara, S.; Takeuchi, K. *J. Mol. Catal. A: Chem.* **2000**, *161*, 205.
- (386) Linsebigler, A. L.; Lu, G.; Yates, J. T. *Chem. Rev.* **1995**, *95*, 735.
- (387) Nagaveni, K.; Hegde, M. S.; Ravishankar, N.; Subbanna, G. N.; Madras, G. *Langmuir* **2004**, *20*, 2900.
- (388) Kamisaka, H.; Adachi, T.; Yamashita, K. *J. Chem. Phys.* **2005**, *123*, 084704.
- (389) Yu, J.; Dai, G.; Xiang, Q.; Jaroniec, M. *J. Mater. Chem.* **2011**, *21*, 1049.
- (390) Lin, X.; Rong, F.; Ji, X.; Fu, D. *Microporous Mesoporous Mater.* **2011**, *142*, 276.
- (391) Fattori, A.; Peter, L. M.; Wang, H.; Miura, H.; Marken, F. *J. Phys. Chem. C* **2010**, *114*, 11822.
- (392) Czoska, A. M.; Livraghi, S.; Chiesa, M.; Giamello, E.; Agnoli, S.; Granozzi, G.; Finazzi, E.; Valentin, C. D.; Pacchioni, G. *J. Phys. Chem. C* **2008**, *112*, 8951.
- (393) Chen, S.; Yang, Y.; Liu, W. *J. Hazard. Mater.* **2010**, *186*, 1560.
- (394) Ma, H. L.; Zhang, D. H.; Win, S. Z.; Li, S. Y.; Chen, Y. P. *Sol. Energy Mater. Sol. Cells* **1996**, *40*, 371.
- (395) Minami, T. *MRS Bull.* **2000**, *25*, 38.
- (396) Rakhshani, A. E.; Makdisi, Y.; Ramazaniyan, H. A. *J. Appl. Phys.* **1998**, *83*, 1049.
- (397) Cui, Y.; Du, H.; Wen, L. *Mater. Sci. Forum* **2009**, *620–622*, 647.
- (398) Liu, B.; Gu, M.; Liu, X.; Huang, S.; Ni, C. *Appl. Phys. Lett.* **2010**, *97*, 122101.
- (399) Gonzalez-Hernandez, R.; Martinez, A. I.; Falcony, C.; Lopez, A. A.; Pech-Canul, M. I.; Hdz-Garcia, H. M. *Mater. Lett.* **2010**, *64*, 1493.
- (400) Zhao, W.; Ma, W.; Chen, C.; Zhao, J.; Shuai, Z. *J. Am. Chem. Soc.* **2004**, *126*, 4782.
- (401) Moon, S. C.; Mametsuka, H.; Suzuki, E.; Nakahara, Y. *Catal. Today* **1998**, *45*, 79.
- (402) Chen, D.; Yang, D.; Wang, Q.; Jiang, Z. *Ind. Eng. Chem. Res.* **2006**, *45*, 4110.
- (403) Jung, K. Y.; Park, S. B.; Ihm, S.-K. *Appl. Catal., B* **2004**, *51*, 239.
- (404) Xing, M. Y.; Wu, Y. M.; Zhang, J. L.; Chen, F. *Nanoscale* **2010**, *2*, 1233.

- (405) Wu, Y. M.; Xing, M. Y.; Zhang, J. L. *J. Hazard. Mater.* **2011**, 192, 368.
- (406) Sun, L. M.; Zhao, X.; Cheng, X. F.; Sun, H. G.; Li, Y. L.; Li, P.; Fan, W. L. *Langmuir* **2012**, 28, 5882.
- (407) Wang, W.; Lu, C. H.; Ni, Y. R.; Su, M. X.; Huang, W. J.; Xu, Z. Z. *Appl. Surf. Sci.* **2012**, 258, 8696.
- (408) Naik, B.; Parida, K. M. *Ind. Eng. Chem. Res.* **2010**, 49, 8339.
- (409) Cong, Y.; Chen, F.; Zhang, J.; Anpo, M. *Chem. Lett.* **2006**, 35, 800.
- (410) Gombac, V.; De Rogatis, L.; Gasparotto, A.; Vicario, G.; Montini, T.; Barreca, D.; Balducci, G.; Fornasiero, P.; Tondello, E.; Graziani, M. *Chem. Phys.* **2007**, 339, 111.
- (411) Komai, Y.; Okitsu, K.; Nishimura, R.; Ohtsu, N.; Miyamoto, G.; Furuhashi, T.; Semboshi, S.; Mizukoshi, Y.; Masahashi, N. *Catal. Today* **2011**, 164, 399.
- (412) Yang, G.; Xiao, T.; Sloan, J.; Li, G.; Yan, Z. *Chem.—Eur. J.* **2011**, 17, 1096.
- (413) Wu, Y. M.; Xing, M. Y.; Tian, B. Z.; Zhang, J. L.; Chen, F. *Chem. Eng. J.* **2010**, 162, 710.
- (414) Wei, H.; Wu, Y.; Lun, N.; Zhao, F. *J. Mater. Sci.* **2004**, 39, 1305.
- (415) Khan, R.; Kim, S. W.; Kim, T.-J.; Nam, C.-M. *Mater. Chem. Phys.* **2008**, 112, 167.
- (416) Fengyu, W.; Tong, Z. *Appl. Chem. Ind.* **2007**, 36, 421.
- (417) Devi, L. G.; Nagaraj, B.; Rajashekhar, K. E. *Chem. Eng. J.* **2012**, 181–182, 259.
- (418) Takeuchi, M.; Yamashita, H.; Matsuoka, M.; Anpo, M.; Hirao, T.; Itoh, N.; Iwamoto, N. *Catal. Lett.* **2000**, 67, 135.
- (419) Yamashita, H.; Harada, M.; Misaka, J.; Takeuchi, M.; Neppolian, B.; Anpo, M. *Catal. Today* **2003**, 84, 191.
- (420) Yamashita, H.; Anpo, M. *Catal. Surv. Asia* **2004**, 8, 35.
- (421) Anpo, M.; Dohshi, S.; Kitano, M.; Hu, Y.; Takeuchi, M.; Matsuoka, M. *Annu. Rev. Mater. Res.* **2005**.
- (422) Yamashita, H.; Harada, M.; Misaka, J.; Takeuchi, M.; Ichihashi, Y.; Goto, F.; Ishida, M.; Sasaki, T.; Anpo, M. *J. Synchrotron Radiat.* **2001**, 8, 569.
- (423) Yamashita, H.; Harada, M.; Misaka, J.; Takeuchi, M.; Ikeue, K.; Anpo, M. *J. Photochem. Photobiol., A* **2002**, 148, 257.
- (424) Yamashita, H.; Ichihashi, Y.; Takeuchi, M.; Kishiguchi, S.; Anpo, M. *J. Synchrotron Radiat.* **1999**, 6, 451.
- (425) Anpo, M.; Takeuchi, M.; Ikeue, K.; Dohshi, S. *Curr. Opin. Solid State Mater. Sci.* **2002**, 6, 381.
- (426) Ao, C. H.; Leung, M. K. H.; Lam, R. C. W.; Leung, D. Y. C.; Vrijmoed, L. L. P.; Yam, W. C.; Ng, S. P. *Chem. Eng. J.* **2007**, 129, 153.
- (427) Lam, R. C. W.; Leung, M. K. H.; Leung, D. Y. C.; Vrijmoed, L. L. P.; Yam, W. C.; Ng, S. P. *Sol. Energy Mater. Sol. Cells* **2007**, 91, 54.
- (428) Ghicov, A.; Schmidt, B.; Kunze, J.; Schmuki, P. *Chem. Phys. Lett.* **2007**, 433, 323.
- (429) Sumita, T.; Yamaki, T.; Yamamoto, S.; Miyashita, A. *Thin Solid Films* **2002**, 416, 80.
- (430) Sumita, T.; Yamaki, T.; Yamamoto, S.; Miyashita, A. *Nucl. Instrum. Methods Phys. Res., Sect. B* **2003**, 206, 245.
- (431) Hou, X. G.; Hao, F. H.; Fan, B.; Gu, X. N.; Wu, X. Y.; Liu, A. D. *Nucl. Instrum. Methods Phys. Res., Sect. B* **2006**, 243, 99.
- (432) Yen, C. C.; Wang, D. Y.; Chang, L. S.; Shih, H. C. *J. Solid State Chem.* **2011**, 184, 2053.
- (433) Yen, C. C.; Wang, D. Y.; Shih, M. H.; Chang, L. S.; Shih, H. C. *Appl. Surf. Sci.* **2010**, 256, 6865.
- (434) Yao, K. S.; Wang, D. Y.; Yan, J. J.; Yang, L. Y.; Chen, W. S. *Surf. Coat. Technol.* **2007**, 201, 6882.
- (435) Ghicov, A.; Macak, J. M.; Tsuchiya, H.; Kunze, J.; Haeublein, V.; Frey, L.; Schmuki, P. *Nano Lett.* **2006**, 6, 1080.
- (436) Romero-Gomez, P.; Lopez-Santos, C.; Borrás, A.; Espinos, J. P.; Palmero, A.; Gonzalez-Eliphe, A. R. *Chem. Phys. Lett.* **2013**, 582, 95.
- (437) Borrás, A.; Lopez, C.; Rico, V.; Gracia, F.; Gonzalez-Eliphe, A. R.; Richter, E.; Battiston, G.; Gerbasí, R.; McSparran, N.; Sauthier, G.; Gyorgy, E.; Figueras, A. *J. Phys. Chem. C* **2007**, 111, 1801.
- (438) Silva, C. G.; Juárez, R.; Marino, T.; Molinari, R.; Garcia, H. *J. Am. Chem. Soc.* **2011**, 133, 595.
- (439) Tanaka, A.; Sakaguchi, S.; Hashimoto, K.; Kominami, H. *Catal. Sci. Technol.* **2012**, 2, 907.
- (440) Kowalska, E.; Abe, R.; Ohtani, B. *Chem. Commun.* **2009**, 241.
- (441) Kowalska, E.; Mahaney, O. O. P.; Abe, R.; Ohtani, B. *Phys. Chem. Chem. Phys.* **2010**, 12, 2344.
- (442) Wang, N.; Tachikawa, T.; Majima, T. *Chem. Sci.* **2011**, 2, 891.
- (443) Tachikawa, T.; Yonezawa, T.; Majima, T. *ACS Nano* **2013**, 7, 263.
- (444) Yaghi, O. M.; O’Keeffe, M.; Ockwig, N. W.; Chae, H. K.; Eddaoudi, M.; Kim, J. *Nature* **2003**, 423, 705.
- (445) Ferey, G. *Chem. Soc. Rev.* **2008**, 37, 191.
- (446) Kitagawa, S.; Kitaura, R.; Noro, S. *Angew. Chem., Int. Ed.* **2004**, 43, 2334.
- (447) Alvaro, M.; Carbonell, E.; Ferrer, B.; Xamena, F.; Garcia, H. *Chem.—Eur. J.* **2007**, 13, 5106.
- (448) Tachikawa, T.; Choi, J. R.; Fujitsuka, M.; Majima, T. *J. Phys. Chem. C* **2008**, 112, 14090.
- (449) Kent, C. A.; Liu, D.; Meyer, T. J.; Lin, W. J. *Am. Chem. Soc.* **2012**, 134, 3991.
- (450) Silva, C. G.; Luz, I.; Xamena, F.; Corma, A.; Garcia, H. *Chem.—Eur. J.* **2010**, 16, 11133.
- (451) Fateeva, A.; Chater, P. A.; Ireland, C. P.; Tahir, A. A.; Khimiyak, Y. Z.; Wiper, P. V.; Darwent, J. R.; Rosseinsky, M. J. *Angew. Chem., Int. Ed.* **2012**, 51, 7440.
- (452) Dan-Hardi, M.; Serre, C.; Frot, T.; Rozes, L.; Maurin, G.; Sanchez, C.; Ferey, G. *J. Am. Chem. Soc.* **2009**, 131, 10857.
- (453) Fu, Y. H.; Sun, D. R.; Chen, Y. J.; Huang, R. K.; Ding, Z. X.; Fu, X. Z.; Li, Z. H. *Angew. Chem., Int. Ed.* **2012**, 51, 3364.
- (454) Horiuchi, Y.; Toyao, T.; Saito, M.; Mochizuki, K.; Iwata, M.; Higashimura, H.; Anpo, M.; Matsuoka, M. *J. Phys. Chem. C* **2012**, 116, 20848.
- (455) Toyao, T.; Saito, M.; Horiuchi, Y.; Mochizuki, K.; Iwata, M.; Higashimura, H.; Matsuoka, M. *Catal. Sci. Technol.* **2013**, 3, 2092.
- (456) De Miguel, M.; Ragon, F.; Devic, T.; Serre, C.; Horcajada, P.; Garcia, H. *ChemPhysChem* **2012**, 13, 3651.
- (457) Hendon, C. H.; Tiana, D.; Fontecave, M.; Sanchez, C.; D’Arras, L.; Sasse, C.; Rozes, L.; Mellot-Draznieks, C.; Walsh, A. *J. Am. Chem. Soc.* **2013**, 135, 10942.
- (458) Yamashita, H.; Anpo, M. *Curr. Opin. Solid State Mater. Sci.* **2003**, 7, 471.
- (459) Panayotov, D. A.; Paul, D. K.; Yates, J. T. *J. Phys. Chem. B* **2003**, 107, 10571.
- (460) Anpo, M.; Kim, T.-H.; Matsuoka, M. *Catal. Today* **2009**, 142, 114.
- (461) Blasco, T.; Corma, A.; Navarro, M. T.; Pariente, J. P. *J. Catal.* **1995**, 156, 65.
- (462) Blasco, T.; Camblor, M. A.; Corma, A.; Perez-Pariente, J. *J. Am. Chem. Soc.* **1993**, 115, 11806.
- (463) Ricciardi, G.; Damin, A.; Bordiga, S.; Lamberti, C.; Spanò, G.; Rivetti, F.; Zecchina, A. *J. Am. Chem. Soc.* **2001**, 123, 11409.
- (464) Farges, F.; Brown, G. E., Jr.; Rehr, J. J. *Geochim. Cosmochim. Acta* **1996**, 60, 3023.
- (465) Bordiga, S.; Coluccia, S.; Lamberti, C.; Marchese, L.; Zecchina, A.; Boscherini, F.; Buffa, F.; Genoni, F.; Leofanti, G. *J. Phys. Chem.* **1994**, 98, 4125.
- (466) Morishita, M.; Shiraishi, Y.; Hirai, T. *J. Phys. Chem. B* **2006**, 110, 17898.
- (467) Marchese, L.; Gianotti, E.; Dellarocca, V.; Maschmeyer, T.; Rey, F.; Coluccia, S.; M. Thomas, J. *Phys. Chem. Chem. Phys.* **1999**, 1, 585.
- (468) Sankar, G.; Thomas, J. M.; Catlow, C. R. A.; Barker, C. M.; Gleeson, D.; Kaltsoyannis, N. *J. Phys. Chem. B* **2001**, 105, 9028.
- (469) Thomas, J. M.; Sankar, G. *Acc. Chem. Res.* **2001**, 34, 571.
- (470) Bhaumik, A.; Tatsumi, T. *J. Catal.* **2000**, 189, 31.
- (471) Zhuang, Y.; Song, H.-Y.; Li, G.; Xu, Y.-J. *Mater. Lett.* **2010**, 64, 2491.
- (472) Einaga, H.; Futamura, S.; Ibusuki, T. *Environ. Sci. Technol.* **2001**, 35, 1880.
- (473) Kosuge, K.; Singh, P. S. *Chem. Lett.* **1999**, 28, 9.

- (474) Lee, G. D.; Jung, S. K.; Jeong, Y. J.; Park, J. H.; Lim, K. T.; Ahn, B. H.; Hong, S. S. *Appl. Catal., A* **2003**, 239, 197.
- (475) Wang, X.; Lian, W.; Fu, X.; Basset, J.-M.; Lefebvre, F. *J. Catal.* **2006**, 238, 13.
- (476) Rusu, C. N.; Yates, J. T. *J. Phys. Chem. B* **2001**, 105, 2596.
- (477) Rusu, C. N.; Yates, J. T. *J. Phys. Chem. B* **2000**, 104, 1729.
- (478) Anpo, M.; Zhang, S. G.; Mishima, H.; Matsuoka, M.; Yamashita, H. *Catal. Today* **1997**, 39, 159.
- (479) Hu, Y.; Higashimoto, S.; Martra, G.; Zhang, J.; Matsuoka, M.; Coluccia, S.; Anpo, M. *Catal. Lett.* **2003**, 90, 161.
- (480) Yamashita, H.; Ichihashi, Y.; Anpo, M.; Hashimoto, M.; Louis, C.; Che, M. *J. Phys. Chem.* **1996**, 100, 16041.
- (481) Zhang, J.; Hu, Y.; Matsuoka, M.; Yamashita, H.; Minagawa, M.; Hidaka, H.; Anpo, M. *J. Phys. Chem. B* **2001**, 105, 8395.
- (482) Zhang, J.; Minagawa, M.; Ayusawa, T.; Natarajan, S.; Yamashita, H.; Matsuoka, M.; Anpo, M. *J. Phys. Chem. B* **2000**, 104, 11501.
- (483) Zhang, J.; Minagawa, M.; Matsuoka, M.; Yamashita, H.; Anpo, M. *Catal. Lett.* **2000**, 66, 241.
- (484) Zhang, S. G.; Ichihashi, Y.; Yamashita, H.; Tatsumi, T.; Anpo, M. *Chem. Lett.* **1996**, 25, 895.
- (485) Ichihashi, Y.; Yamashita, H.; Anpo, M. *Stud. Surf. Sci. Catal.* **1997**, 105, 1609.
- (486) Yamashita, H.; Ichihashi, Y.; Zhang, S. G.; Matsumura, Y.; Souma, Y.; Tatsumi, T.; Anpo, M. *Appl. Surf. Sci.* **1997**, 121–122, 305.
- (487) Halmann, M. *Nature* **1978**, 275, 115.
- (488) Inoue, T.; Fujishima, A.; Konichi, S.; Honda, K. *Nature* **1979**, 277, 637.
- (489) Anpo, M. *J. CO₂ Util.* **2013**, 1, 8.
- (490) Anpo, M.; Yamashita, H.; Ichihashi, Y.; Fujii, Y.; Honda, M. *J. Phys. Chem. B* **1997**, 101, 2632.
- (491) Yamashita, H.; Fujii, Y.; Ichihashi, Y.; Zhang, S. G.; Ikeue, K.; Park, D. R.; Koyano, K.; Tatsumi, T.; Anpo, M. *Catal. Today* **1998**, 45, 221.
- (492) Zhang, S. G.; Fujii, Y.; Yamashita, H.; Koyano, K.; Tatsumi, T.; Anpo, M. *Chem. Lett.* **1997**, 26, 659.
- (493) Anpo, M.; Yamashita, H.; Ikeue, K.; Fujii, Y.; Zhang, S. G.; Ichihashi, Y.; Park, D. R.; Suzuki, Y.; Koyano, K.; Tatsumi, T. *Catal. Today* **1998**, 44, 327.
- (494) Yang, C. C.; Vernimmen, J.; Meynen, V.; Cool, P.; Mul, G. *J. Catal.* **2011**, 284, 1.
- (495) Mei, B.; Becerikli, A.; Pougin, A.; Heeskens, D.; Sinev, I.; Grunert, W.; Muhler, M.; Strunk, J. *J. Phys. Chem. C* **2012**, 116, 14318.
- (496) Mei, B.; Pougin, A.; Strunk, J. *J. Catal.* **2013**, 306, 184.
- (497) Mei, B.; Wiktor, C.; Turner, S.; Pougin, A.; van Tendeloo, G.; Fischer, R. A.; Muhler, M.; Strunk, J. *ACS Catal.* **2013**, 3, 3041.
- (498) Tanaka, T.; Nishimura, Y.; Kawasaki, S.-i.; Ooe, M.; Funabiki, T.; Yoshida, S. *J. Catal.* **1989**, 118, 327.
- (499) Takenaka, S.; Kuriyama, T.; Tanaka, T.; Funabiki, T.; Yoshida, S. *J. Catal.* **1995**, 155, 196.
- (500) Teramura, K.; Tanaka, T.; Hosokawa, T.; Ohuchi, T.; Kani, M.; Funabiki, T. *Catal. Today* **2004**, 96, 205.
- (501) Tanaka, T.; Ito, T.; Takenaka, S.; Funabiki, T.; Yoshida, S. *Catal. Today* **2000**, 61, 109.
- (502) Amano, F.; Tanaka, T.; Funabiki, T. *Langmuir* **2004**, 20, 4236.
- (503) Teramura, K.; Tanaka, T.; Kani, M.; Hosokawa, T.; Funabiki, T. *J. Mol. Catal. A: Chem.* **2004**, 208, 299.
- (504) Higashimoto, S.; Tsumura, R.; Matsuoka, M.; Yamashita, H.; Che, M.; Anpo, M. *Stud. Surf. Sci. Catal.* **2001**, 140, 315.
- (505) Matsuoka, M.; Kamegawa, T.; Takeuchi, R.; Anpo, M. *Catal. Today* **2007**, 122, 39.
- (506) Toyao, T.; Morishima, J.; Saito, M.; Horiuchi, Y.; Kamegawa, T.; Martra, G.; Coluccia, S.; Matsuoka, M.; Anpo, M. *J. Catal.* **2013**, 299, 232.
- (507) Ohshiro, S.; Chiyoda, O.; Maekawa, K.; Masui, Y.; Anpo, M.; Yamashita, H. *C. R. Chim.* **2006**, 9, 846.
- (508) Yamashita, H.; Yoshizawa, K.; Ariyuki, M.; Higashimoto, S.; Che, M.; Anpo, M. *Chem. Commun.* **2001**, 435.
- (509) Matsuoka, M.; Matsuda, E.; Tsuji, K.; Yamashita, H.; Anpo, M. *J. Mol. Catal. A: Chem.* **1996**, 107, 399.
- (510) Ju, W.-S.; Matsuoka, M.; Iino, K.; Yamashita, H.; Anpo, M. *J. Phys. Chem. B* **2004**, 108, 2128.
- (511) Kanan, S. M.; Omary, M. A.; Patterson, H. H.; Matsuoka, M.; Anpo, M. *J. Phys. Chem. B* **2000**, 104, 3507.
- (512) Anpo, M.; Matsuoka, M.; Yamashita, H. *Catal. Today* **1997**, 35, 177.
- (513) Anpo, M.; Matsuoka, M.; Hanou, K.; Mishima, H.; Yamashita, H.; Patterson, H. H. *Coord. Chem. Rev.* **1998**, 171, 175.
- (514) Kamegawa, T.; Masuda, Y.; Suzuki, N.; Horiuchi, Y.; Yamashita, H. *ACS Appl. Mater. Interfaces* **2011**, 3, 4561.
- (515) Horiuchi, Y.; Ura, H.; Kamegawa, T.; Mori, K.; Yamashita, H. *J. Phys. Chem. C* **2011**, 115, 15410.
- (516) Horiuchi, Y.; Ura, H.; Kamegawa, T.; Mori, K.; Yamashita, H. *J. Mater. Chem.* **2011**, 21, 236.
- (517) Horiuchi, Y.; Ura, H.; Kamegawa, T.; Mori, K.; Yamashita, H. *Appl. Catal., A: Gen.* **2010**, 387, 95.
- (518) Horiuchi, Y.; Mori, K.; Nishiyama, N.; Yamashita, H. *Stud. Surf. Sci. Catal.* **2008**, 174, 635.
- (519) Horiuchi, Y.; Yamashita, H. *Appl. Catal., A* **2011**, 400, 1.
- (520) Zubkov, T.; Stahl, D.; Thompson, T. L.; Panayotov, D.; Diwald, O.; Yates, J. T. *J. Phys. Chem. B* **2005**, 109, 15454.
- (521) Horiuchi, Y.; Mori, K.; Nishiyama, N.; Yamashita, H. *Chem. Lett.* **2008**, 37, 748.
- (522) Diwald, O.; Thompson, T. L.; Zubkov, T.; Goralski, E. G.; Walck, S. D.; Yates, J. T. *J. Phys. Chem. B* **2004**, 108, 6004.
- (523) Horiuchi, Y.; Shimada, M.; Kamegawa, T.; Mori, K.; Yamashita, H. *J. Mater. Chem.* **2009**, 19, 6745.
- (524) Mori, K.; Shimada, M.; Horiuchi, Y.; Ohmichi, T.; Nishiyama, N.; Fujii, H.; Yamashita, H. *Res. Chem. Intermed.* **2008**, 34, 495.
- (525) Shironita, S.; Takasaki, T.; Kamegawa, T.; Mori, K.; Yamashita, H. *Top. Catal.* **2010**, 53, 218.
- (526) Shironita, S.; Mori, K.; Ohmichi, T.; Taguchi, E.; Mori, H.; Yamashita, H. *J. Nanosci. Nanotechnol.* **2009**, 9, 557.
- (527) Shironita, S.; Mori, K.; Shimizu, T.; Ohmichi, T.; Mimura, N.; Yamashita, H. *Appl. Surf. Sci.* **2008**, 254, 7604.
- (528) Mori, K.; Araki, T.; Shironita, S.; Sonoda, J.; Yamashita, H. *Catal. Lett.* **2009**, 131, 337.
- (529) Mori, K.; Araki, T.; Takasaki, T.; Shironita, S.; Yamashita, H. *Photochem. Photobiol. Sci.* **2009**, 8, 652.
- (530) Fukumoto, S.; Kitano, M.; Takeuchi, M.; Matsuoka, M.; Anpo, M. *Catal. Lett.* **2009**, 127, 39.
- (531) Kikuchi, H.; Kitano, M.; Takeuchi, M.; Matsuoka, M.; Anpo, M.; Kamat, P. V. *J. Phys. Chem. B* **2006**, 110, 5537.
- (532) Kitano, M.; Takeuchi, M.; Matsuoka, M.; Thomas, J. M.; Anpo, M. *Chem. Lett.* **2005**, 34, 616.
- (533) Kitano, M.; Takeuchi, M.; Matsuoka, M.; Ueshima, M.; Anpo, M. In *Environmentally Benign Photocatalysts: Applications of Titanium Oxide-based Materials*; Anpo, M., Kamat, P. V., Eds.; Springer: New York, 2010.
- (534) Kitano, M.; Takeuchi, M.; Matsuoka, M.; Thomas, J. M.; Anpo, M. *Catal. Today* **2007**, 120, 133.
- (535) Kitano, M.; Tsujimaru, K.; Anpo, M. *Appl. Catal., A: Gen.* **2006**, 314, 179.
- (536) Matsuoka, M.; Ebrahimi, A.; Nakagawa, M.; Kim, T.-H.; Kitano, M.; Takeuchi, M.; Anpo, M. *Res. Chem. Intermed.* **2009**, 35, 997.
- (537) Matsuoka, M.; Kitano, M.; Fukumoto, S.; Iyatani, K.; Takeuchi, M.; Anpo, M. *Catal. Today* **2008**, 132, 159.
- (538) Matsuoka, M.; Kitano, M.; Takeuchi, M.; Anpo, M.; Thomas, J. M. *Top. Catal.* **2005**, 35, 305.
- (539) Tode, R.; Ebrahimi, A.; Fukumoto, S.; Iyatani, K.; Takeuchi, M.; Matsuoka, M.; Lee, C.; Jiang, C.-S.; Anpo, M. *Catal. Lett.* **2010**, 135, 10.
- (540) Matsuoka, M.; Kitano, M.; Takeuchi, M.; Tsujimaru, K.; Anpo, M.; Thomas, J. M. *Catal. Today* **2007**, 122, 51.
- (541) Kitano, M.; Iyatani, K.; Tsujimaru, K.; Matsuoka, M.; Takeuchi, M.; Ueshima, M.; Thomas, J. M.; Anpo, M. *Top. Catal.* **2008**, 49, 24.
- (542) Kitano, M.; Matsuoka, M.; Hosoda, T.; Ueshima, M.; Anpo, M. *Res. Chem. Intermed.* **2008**, 34, 577.

- (543) Nazeeruddin, M. K.; Kay, A.; Rodicio, I.; Humphrybaker, R.; Muller, E.; Liska, P.; Vlachopoulos, N.; Gratzel, M. *J. Am. Chem. Soc.* **1993**, *115*, 6382.
- (544) Nazeeruddin, M. K.; De Angelis, F.; Fantacci, S.; Selloni, A.; Viscardi, G.; Liska, P.; Ito, S.; Bessho, T.; Gratzel, M. *J. Am. Chem. Soc.* **2005**, *127*, 16835.
- (545) Matsuoka, M.; Minakata, M.; Ebrahimi, A.; Anpo, M.; Chen, H.-C.; Lin, W.-T. In *Environmentally Benign Photocatalysts: Applications of Titanium Oxide-based Materials*; Anpo, M., Kamat, P. V., Eds.; Springer: New York, 2010.
- (546) Kaneko, M.; Gokan, N.; Katakura, N.; Takei, Y.; Hoshino, M. *Chem. Commun.* **2005**, 1625.
- (547) Kaneko, M.; Nemoto, J.; Ueno, H.; Gokan, N.; Ohnuki, K.; Horikawa, M.; Saito, R.; Shibata, T. *Electrochem. Commun.* **2006**, *8*, 336.
- (548) Nishikiori, H.; Ito, M.; Setiawan, R. A.; Kikuchi, A.; Yamakami, T.; Fujii, T. *Chem. Lett.* **2012**, *41*, 725.
- (549) Iyatani, K.; Horiuchi, Y.; Moriyasu, M.; Fukumoto, S.; Cho, S.-H.; Takeuchi, M.; Matsuoka, M.; Anpo, M. *J. Mater. Chem.* **2012**, *22*, 10460.
- (550) Toyao, T.; Iyatani, K.; Horiuchi, Y.; Moriyasu, M.; Cho, S.-H.; Takeuchi, M.; Matsuoka, M.; Anpo, M. *Res. Chem. Intermed.* **2013**, *39*, 1603.
- (551) Iyatani, K.; Horiuchi, Y.; Fukumoto, S.; Takeuchi, M.; Anpo, M.; Matsuoka, M. *Appl. Catal., A* **2013**, *458*, 162.
- (552) Wang, R.; Hashimoto, K.; Fujishima, A.; Chikuni, M.; Kojima, E.; Kitamura, A.; Shimohigoshi, M.; Watanabe, T. *Nature* **1997**, *388*, 431.
- (553) Fujishima, A.; Rao, T. N.; Tryk, D. A. *J. Photochem. Photobiol., C* **2000**, *1*, 1.
- (554) Fujishima, A.; Hashimoto, K.; Watanabe, T. *TiO₂ Photocatalysis Fundamentals and Applications*; BKC, Inc.: 1999.
- (555) Yamashita, H.; Harada, M.; Misaka, J.; Nakao, H.; Takeuchi, M.; Anpo, M. *Nucl. Instrum. Methods Phys. Res., Sect. B* **2003**, *206*, 889.
- (556) Takeuchi, M.; Dohshi, S.; Eura, T.; Anpo, M. *J. Phys. Chem. B* **2003**, *107*, 14278.
- (557) Takeuchi, M.; Yamashita, H.; Matsuoka, M.; Anpo, M.; Hirao, T.; Itoh, N.; Iwamoto, N. *Catal. Lett.* **2000**, *66*, 185.
- (558) Zhou, J. K.; Takeuchi, M.; Zhao, X. S.; Ray, A. K.; Anpo, M. *Catal. Lett.* **2006**, *106*, 67.
- (559) Takeuchi, M.; Yamashita, H.; Matsuoka, M.; Anpo, M.; Hirao, T.; Itoh, N.; Iwamoto, N. *Surf. Sci. Jpn.* **2001**, *22*, 561.
- (560) Takeuchi, M.; Yamasaki, T.; Tsujimaru, K.; Anpo, M. *Chem. Lett.* **2006**, *35*, 904.
- (561) Takeuchi, M.; Matsuoka, M.; Yamashita, H.; Anpo, M. *J. Synchrotron Radiat.* **2001**, *8*, 643.
- (562) Dohshi, S.; Takeuchi, M.; Anpo, M. *Catal. Today* **2003**, *85*, 199.
- (563) Takeuchi, M.; Sakamoto, K.; Tsujimaru, K.; Anpo, M. *Catal. Lett.* **2009**, *131*, 189.
- (564) Machida, M.; Norimoto, K.; Watanabe, T.; Hashimoto, K.; Fujishima, A. *J. Mater. Sci.* **1999**, *34*, 2569.
- (565) Jpn. Kokai Tokkyo Koho JP, 10 36144 [98 36144] (Japan).
- (566) Wang, R.; Hashimoto, K.; Fujishima, A.; Chikuni, M.; Kojima, E.; Kitamura, A.; Shimohigoshi, M.; Watanabe, T. *Adv. Mater.* **1998**, *10*, 135.
- (567) Sakai, N.; Wang, R.; Fujishima, A.; Watanabe, T.; Hashimoto, K. *Langmuir* **1998**, *14*, 5918.
- (568) Wang, R.; Sakai, N.; Fujishima, A.; Watanabe, T.; Hashimoto, K. *J. Phys. Chem. B* **1999**, *103*, 2188.
- (569) Miyauchi, M.; Nakajima, A.; Fujishima, A.; Hashimoto, K.; Watanabe, T. *Chem. Mater.* **2000**, *12*, 3.
- (570) Shibata, T.; Irie, H.; Hashimoto, K. *J. Phys. Chem. B* **2003**, *107*, 10696.
- (571) White, J. M.; Szanyi, J.; Henderson, M. A. *J. Phys. Chem. B* **2003**, *107*, 9029.
- (572) Takeuchi, M.; Sakamoto, K.; Martra, G.; Coluccia, S.; Anpo, M. *J. Phys. Chem. B* **2005**, *109*, 15422.
- (573) Takeuchi, M.; Martra, G.; Coluccia, S.; Anpo, M. *J. Phys. Chem. B* **2005**, *109*, 7387.
- (574) Munuera, G.; Rivesarnau, V.; Saucedo, A. *J. Chem. Soc., Faraday Trans. 1* **1979**, *75*, 736.
- (575) McCabe, W. C.; Subraman, S.; Fisher, H. F. *J. Phys. Chem.* **1970**, *74*, 4360.
- (576) Fornes, V.; Chaussidon, J. *J. Chem. Phys.* **1978**, *68*, 4667.
- (577) Chalmers, J. M.; Griffiths, P. R. *Handbook of Vibrational Spectroscopy*; Wiley: New York, 2002.
- (578) Ozaki, Y.; Kawata, S. *Near Infrared Spectroscopy (Kin-Sekigai-Bunko)*; Japan Scientific Societies Press: Tokyo, 1996.
- (579) Buijs, K.; Choppin, G. R. *J. Chem. Phys.* **1963**, *39*, 2035.
- (580) Garbassi, F.; Morra, M.; Occhiello, E. *Polymer Surfaces From Physics to Technology*; John Wiley & Sons: New York, 1994.
- (581) Iso, S.; Igarashi, T.; Matsuo, H. *J. Illum. Eng. Inst. Jpn.* **1999**, *83*, 273.
- (582) Vig, J. R.; Lebus, J. W. *IEEE Trans. Parts, Hybrids, Packag.* **1976**, *12*, 365.